ITU-Schriftenreihe, 2021
Institut für Technischen Umweltschutz

44

Neue thermoanalytische Verfahren zur Feststoffcharakterisierung im Kontext von Mikroverunreinigungen in Wasser

Detektion von Mikroplastik und Charakterisierung von Aktivkohle und Adsorbaten

Daniel Dittmann

Technische Universität Berlin

Neue thermoanalytische Verfahren zur Feststoffcharakterisierung im Kontext von Mikroverunreinigungen in Wasser

Detektion von Mikroplastik und Charakterisierung von Aktivkohle und Adsorbaten

vorgelegt von
M.Sc.
Daniel Dittmann
ORCID: 0000-0003-2793-7787

von der Fakultät III - Prozesswissenschaften
der Technischen Universität Berlin
zur Erlangung des akademischen Grades

Doktor der Ingenieurwissenschaften
-Dr.-Ing.-

genehmigte Dissertation

Promotionsausschuss:

Vorsitzender: Prof. Dr. Ferdi L. Hellweger
Gutachter: Prof. Dr.-Ing. Martin Jekel
Gutachter: Prof. Dr.-Ing. Stefan Panglisch

Tag der wissenschaftlichen Aussprache: 30. September 2021

Berlin 2021

Zusammenfassung

Thermoanalytische Verfahren mit Zersetzungsgasanalyse wurden in dieser kumulativen Dissertation auf aktuelle Fragestellungen zu Wasserqualität und Wasseraufbereitung angewendet. Es wird gezeigt, dass sich diese neuen analytischen Perspektiven praxisnah als auch forschungsorientiert einsetzen lassen und zu vielfältigem Erkenntnisgewinn beitragen.

Mit dem Befund von Mikroplastik in der aquatischen Umwelt erforderten diese neuen Mikroverunreinigungen auch neue analytische Nachweismethoden. Anders als organische Spurenstoffe sind Mikroplastikpartikel nicht gelöst, sondern liegen als Feststoffe im Wasser vor. Ausgehend von einem Ringversuch für den Nachweis von Mikroplastikgehalten in einer Schwebstoffmatrix werden verschiedene auf Thermogravimetrie basierende Analyseverfahren vorgestellt. In der Anwendung der pyrolytischen Zersetzung einer Feststoffprobe zeigt sich, wie durch unterschiedliche apparative Umsetzung deutlich andere Informationen generiert werden. Für die Mikroplastikdetektion erwies sich die bereits etablierte TED-GC/MS als das zu bevorzugende Verfahren. Die vergleichsweise einfacheren Gerätekonfigurationen TGA-FTIR, TGA-MS und MCC zeigten jedoch für spezifische Fragestellungen individuelle Vorteile und können ebenfalls gewinnbringend eingesetzt werden.

Der zweite Anwendungsschwerpunkt ist die Charakterisierung von frischer sowie beladener Aktivkohle, die als Feststoff in der Wasseraufbereitung zur adsorptiven Entfernung gelöster Mikroverunreinigungen eingesetzt wird. Die Herstellung von Aktivkohle basiert auf Pyrolyseprozessen, wodurch sich Parallelen mit der Anwendung der analytischen Pyrolyse ergeben. Diese Informationen werden bereits durch thermogravimetrische Analyse erfasst und konnten auf wichtige Materialeigenschaften übersetzt werden. So fanden sich bei frischen Aktivkohlen Korrelationen mit dem Kohlenstoff- und Sauerstoffgehalt als auch dem Point-of-zero-charge. Durch Zersetzungsgasanalyse gelang außerdem die qualitative und quantitative Bestimmung sechs verschiedener funktioneller Gruppen für eine Vielzahl von Aktivkohleprodukten. Es wird gezeigt, wie stark sich Aktivkohlen nicht nur in ihren physikalischen Eigenschaften (z. B. Porosität und spezifische innere Oberfläche), sondern auch in ihren chemischen Eigenschaften (z. B. Sauerstoffgehalt von 0,5 % bis zu extremen 17,6 %) unterscheiden können.

Schließlich wird das pyrolytische Zersetzungsverhalten beladener Aktivkohle mit Carbamazepin beschrieben, welches erstmals Rückschlüsse auf Adsorptionsplätze und -zustände zuließ. Adsorbate verschiedener Aktivkohlen zeigten zudem unterschiedliche Zersetzungsprodukte in Abhängigkeit ihres C/H-Verhältnisses sowie des Schwefelgehalts. Carbamazepin kann thermisch nicht wieder vollständig von der Aktivkohle getrennt werden, es blieben indirekt proportional zur Beladung 42 % bis 74 % sorbiert. Die komplementären Informationen aus den eingesetzten thermoanalytischen Verfahren deuten darauf hin, dass sich durch thermische Regeneration der Graphitisierungsgrad der Aktivkohle erhöht. Diese Arbeit leistet damit einen Beitrag für die Bestimmung und das Verständnis zur Wasseraufbereitung von Mikroverunreinigungen in den Wasserkreisläufen.

Abstract

In this cumulative dissertation, *thermoanalytical methods with evolved gas analysis* were applied to current water quality control issues. It will be shown that these new analytical perspectives on solid samples can contribute to multiple knowledge gains in practical as well as for research purposes.

With the finding of microplastic particles in the aquatic environment, these new micro-contaminants also required new analytical techniques for detection. Unlike dissolved organic micropollutants, microplastic particles are present as solids in water. Based on an interlaboratory test for the detection of microplastic contents in a suspended matter matrix, different techniques based on thermogravimetry are introduced. Pyrolytic decomposition of a solid sample provides a demonstration of how significantly different information can be generated by different instrumental implementations. The already established TED-GC/MS proved to be the most suitable method for the detection of microplastic. However, the comparatively simpler instrument configurations TGA-FTIR, TGA-MS and MCC showed individual advantages for specific tasks.

Another application is the characterization of virgin and loaded activated carbon, which is used as a solid in water treatment for the adsorptive removal of dissolved organic micropollutants. The production of activated carbon is based on pyrolysis processes, which can be exploited in analytical pyrolysis. This information is already obtained by thermogravimetric analysis and could be transferred to important properties for adsorption. Thus, correlations with carbon and oxygen content as well as with the point of zero charge were found for virgin activated carbons. Evolved gas analysis also successfully led to the qualitative and quantitative determination of six oxygen-containing functional groups for a variety of activated carbon products. The extent to which activated carbons can vary not only in their physical properties (e.g., porosity and specific surface area) but also in their chemical properties (e.g., oxygen content from 0.5% to extreme 17.6%) is demonstrated.

Finally, the pyrolytic decomposition behavior of loaded activated carbon with carbamazepine was examined, which for the first time allowed conclusions to be drawn about adsorption sites and states. Adsorbates of different activated carbons also showed different decomposition products depending on their C/H ratio and sulfur content. Carbamazepine could not be completely separated by pyrolysis from the activated carbons; indirectly proportional to the carbamazepine loadings, 42% to 74% of it remained sorbed. The complementary information from the thermoanalytical methods used indicates that thermal regeneration increases the degree of graphitization of the activated carbon. This work contributes to the determination and understanding of water treatment processes for microcontaminants in water cycles.

Activated carbons could be the Cinderella of the carbon family.
Over decades they have purified measureless tonnes of sugar, cleaned up oceans of water,
and enormous amounts of food, pharmaceuticals and fine chemicals.
But, they were never taken to The Ball.

Harry Marsh, 1997 [1]

Danksagung

Grundlage für die Anfertigung dieser Dissertation war die Kooperation zwischen Technischer Universität Berlin und Bundesanstalt für Materialforschung und -prüfung. Für diese Möglichkeit danke ich den Institutionen, aber besonders *Prof. Martin Jekel, Aki S. Ruhl und Ulrike Braun*, die mich in den letzten vier Jahren unermüdlich betreut haben und gleichzeitig frei forschen ließen. Ihre Interpretationen von wissenschaftlichem Wirken habe ich als vorbildhaft und ungemein unterstützend erfahren, wofür ich mich ausdrücklich bedanke und worüber ich nach wie vor sehr glücklich bin.

Großer Dank gilt zudem Fatima El-Athman, Caroline Goedecke und Maren Meurer, mit ihnen als Büro-Kolleginnen den Forschungsalltag zu teilen, war erfrischend und bereichernd zugleich. So haben sie meine Promotionszeit geprägt und mit ihren Perspektiven die entstandenen Arbeiten direkt beeinflusst.

Das Fachgebiet Wasserreinhaltung und die Arbeitsgruppe Braun waren zwei kreative und interdisziplinär-anregende Orte wissenschaftlichen Arbeitens. Dafür und für die darüber hinausgehenden Freundschaften danke ich Paul, Korinna, Erik, Maren, Yosri, Maria, Axel, Simone, Sven, Johanna, Philipp, Dominique, Lukas, Lars, Inga, Fredo, Geert, Pia, Luisa, Stefan, Josi und Yuki sowie Yannick, Leon und Kay. Für ihre große Hilfsbereitschaft und hohe Fachkompetenz danke ich Jutta, Anke, Ulrike, Gisela, Katrin, Katharina, Maike, Frank, Christiane, Fabian, Sergej, Carsten, Dominik, Ute Kalbe, Heike und Dana.

Darüber hinaus möchte ich Lucas Landwehrkamp, Thomas Lucke, Gabriel Sigmund und Frederik Zietzschmann für ihre Hinweise, Anregungen und den fachlichen Austausch danken. Ihre Arbeiten mit und Perspektiven auf Aktivkohle haben meine eigene Sicht erweitert und die Entwicklung des hier behandelten Themas stark vorangebracht.

Meiner Frau Theresa danke ich, dass sie diese Jahre mitgetragen hat und mir durch ihre kluge und immer vorwärts-gewandte Art die denkbar beste Heimat ist, die ich mir wünschen könnte. Meiner ganzen Familie danke ich für das uneingeschränkte Vertrauen, dass sie mir seit jeher zukommen lässt. Insbesondere Alexander, Eva, meinen Eltern und Schwiegereltern gilt für die vielen Stunden Dank, in denen sie sich um unseren Sohn Adrian gekümmert haben.

Publikationen

In dieser Dissertation sind folgenden Publikationen enthalten.

Daniel Dittmann, Paul Eisentraut, Caroline Goedecke, Yosri Wiesner, Martin Jekel, Aki Sebastian Ruhl und Ulrike Braun. „Specific Adsorption Sites and Conditions Derived by Thermal Decomposition of Activated Carbons and Adsorbed Carbamazepine“. *Scientific Reports* 10, Nr. 1 (2020): 6695. doi: 10.1038/s41598-020-63481-y. Akzeptiertes Manuskript als Kapitel 4.

Caroline Goedecke[1], Daniel Dittmann[1], Paul Eisentraut, Yosri Wiesner, Bernhard Schartel, Patrick Klack und Ulrike Braun. „Evaluation of Thermoanalytical Methods Equipped with Evolved Gas Analysis for the Detection of Microplastic in Environmental Samples“. *Journal of Analytical and Applied Pyrolysis* 152 (2020): 104961. doi: 10.1016/j.jaap.2020.104961. Akzeptiertes Manuskript als Kapitel 2.

Daniel Dittmann, Leon Saal, Frederik Zietzschmann, Maike Mai, Korinna Altmann, Dominik Al-Sabbagh, Pia Schumann, Aki Sebastian Ruhl, Martin Jekel und Ulrike Braun. „Material characterization of activated carbons of different raw materials and in-depth analyses of oxygen-containing surface groups“. *Water Research X*. Eingereichtes Manuskript als Kapitel 3.

Zwischen Juni 2017 und Juli 2021 sind weiterhin folgende Veröffentlichungen entstanden.

Daniel Dittmann, Ulrike Braun, Martin Jekel und Aki Sebastian Ruhl. „Quantification and characterisation of activated carbon in activated sludge by thermogravimetric and evolved gas analyses“. *Journal of Environmental Chemical Engineering* 6, Nr. 2 (2018): 2222–31. doi: 10.1016/j.jece.2018.03.010.

Dominique Lörchner, Daniel Dittmann, Ulrike Braun, Lothar W. Kroh und Robert Köppen. „Investigation of two triazine-based heterocyclic brominated flame retardants by coupled thermogravimetry-Fourier transform infrared spectroscopy“. *Journal of Analytical and Applied Pyrolysis* 141 (2019): 104635. doi: 10.1016/j.jaap.2019.104635.

[1] Beide Autoren trugen gleichermaßen zur Veröffentlichung bei.

Frederik Zietzschmann, Stefan Dittmar, Lydia Splettstößer, Jonas Hunsicker, Daniel Dittmann, Felix Meinel, Annette Rößler, Steffen Metzger, Martin Jekel und Aki Sebastian Ruhl. „Fast empirical lab method for performance projections of large-scale powdered activated carbon re-circulation plants“. *Chemosphere* 215 (2019): 563–73. doi: 10.1016/j.chemosphere.2018.10.055.

Daniel Dittmann, Thomas Lucke, Aki S. Ruhl, Rudi Winzenbacher, Martin Jekel und Ulrike Braun. „Untersuchungen zu biologischen, organischen und anorganischen Veränderungen granulierter Aktivkohlen während der Trinkwasseraufbereitung“. *Vom Wasser* 118, Nr. 2 (2020): 47–50.

Maria Kittner, Paul Eisentraut, Daniel Dittmann und Ulrike Braun. „Decomposability versus detectability: First validation of TED-GC/MS for microplastic detection in different environmental matrices“. *Journal of Chromatography A*, eingereicht 2021.

Außerdem wurden diese Abschlussarbeiten angefertigt.

Maria Kittner. „Analyses of Microplastics from Sediments of Lake Tegel“. *Bachelorarbeit*, Technische Universität Berlin (2018).

Yannick Dahm. „Charakterisierung des Einflusses der Ionenstärke auf die Adsorption organischer Spurenstoffe an Aktivkohle“. *Bachelorarbeit*, Technische Universität Berlin (2018).

Maria Kittner. „Screening of freshwater sediments for microplastics by means of thermoanalytical methods“. *Masterarbeit*, Technische Universität Berlin (2019).

Leon Saal. „Development of a thermoanalytical method for the determination of the oxygen surface groups of activated carbons“. *Masterarbeit*, Technische Universität Berlin (2020).

Kay Matzdorf. „Untersuchung von Adsorptionseigenschaften organischer Spurenstoffe an Aktivkohlen und ihr thermisches Zersetzungsverhalten nach cyclischer Beladung und Regeneration“. *Bachelorarbeit*, Beuth Hochschule für Technik Berlin (2021).

Inhaltsverzeichnis

1 Einleitung **1**
1.1 Mikroverunreinigung in den Wasserkreisläufen . . . 2
1.2 Mikroplastik als neue Umweltkontamination . . . 4
1.3 Aktivkohle für die Wasseraufbereitung . . . 9
1.4 Pyrolyse organischen Materials . . . 16
1.5 Zielstellung . . . 20

2 Evaluation of thermoanalytical methods for the detection of microplastic **21**
2.1 Introduction . . . 22
2.2 Materials and methods . . . 25
2.3 Results and discussion . . . 27
2.4 Conclusion . . . 38

3 Characterization of activated carbon products for water treatment **41**
3.1 Introduction . . . 42
3.2 Materials and methods . . . 43
3.3 Results and discussion . . . 46
3.4 Conclusion . . . 54

4 Specific adsorption sites and conditions of carbamazepine **57**
4.1 Introduction . . . 58
4.2 Materials and methods . . . 59
4.3 Results . . . 62
4.4 Discussion . . . 71

5 Zusammenfassung und Schlussfolgerungen **75**

Literatur **79**

Verzeichnisse **105**

Appendix A Supplementary information on chapter 3 (Methods) **113**

Appendix B Supplementary information on chapter 3 (Results) **127**

Appendix C Supplementary information on chapter 4 **167**

1 Einleitung

Wasser ist die Grundlage allen Lebens. Auf der Erde fließt es in Kreisläufen, sichtbar und unsichtbar. Sauberes Wasser ist für den Menschen unverzichtbar, das wird in der DIN 2000 eindringlich und unmissverständlich auf den Punkt gebracht: „Trinkwasser ist das wichtigste Lebensmittel, es kann nicht ersetzt werden.“ [2]. Das internationale Menschenrecht auf Zugang zu sauberem Wasser, wird damit begründet, dass es essenziell für den vollen Genuss des Lebens und für die Wahrnehmung *aller* Menschenrechte ist [3]. Daher ist eine nachhaltige Bewirtschaftung der Ressource Wasser für die Daseinsvorsorge von herausragender Bedeutung und spiegelt sich vielfältig in den 17 Zielen für nachhaltige Entwicklung der Vereinten Nationen wider [4].

Es gibt nur noch wenige naturbelassene Gewässer, bei denen sich kein anthropogener Einfluss nachweisen lässt. Menschliches Handeln hat Auswirkungen auf die aquatische Umwelt und beeinflusst über die Wasserkreisläufe auch unsere eigenen — unersetzlichen — Trinkwasserressourcen. Dies veranschaulicht der Begriff des *teilgeschlossenen Wasserkreislaufs* und der damit verbundenen Arzneimittelwirkstoffe, die sich in Spurenkonzentrationen im städtischen Trinkwasser wiederfinden [5]. Stoffe, die in sehr niedrigen Gehalten im Wasser vorhanden sind, damit aber potenziell „negative Auswirkungen auf Mensch, Umwelt oder die Trinkwassergewinnung haben können“, nennen wir *Mikroverunreinigungen* [6]. Deren Entwicklung zu beobachten, zu bewerten und gegebenenfalls zu kontrollieren ist wesentlich für die Aufgabe der Daseinsvorsorge und erfordert kontinuierliche Forschungsbemühungen.

Zu den Mikroverunreinigungen zählten lange Zeit nur gelöste, organische Spurenstoffe anthropogenen Ursprungs wie Pharmaka, Röntgenkontrastmittel, Biozide, Pflanzenschutzmittel und weitere Anwendungschemikalien wie Reinigungs- oder Korrosionsschutzmittel. Mit der intensivierten Forschung zu Mikroplastik wurde die Definition um diese ungelösten Polymerpartikel erweitert und es musste eine bereits ubiquitäre Verbreitung dieser neuen Kontaminante festgestellt werden. Auch wenn ihre potenziell negativen Auswirkungen heute noch nicht abschließend bewertet werden können, hat die Suche nach diesen kleinen Partikeln das Spektrum der apparativen Analytik im Wasserfach deutlich erweitert [7].

Zur Charakterisierung der ungelösten Wasserbestandteile (Schwimm- und Schwebstoffe) werden hochmoderne Mikroskopspektroskopie und Thermoanalysemethoden eingesetzt [8]. Bei Letzteren wird die Feststoffprobe unter hohen Temperaturen und Sauerstoffausschluss

pyrolysiert und aus den entstehenden Zersetzungsgasen werden Rückschlüsse auf die Probenzusammensetzung und Mikroplastikgehalte gezogen [9]. Die Nutzung der Pyrolyse als analytische Methode eröffnet mit der Feststoffcharakterisierung zudem weitere Einsatzgebiete in der Wasseraufbereitung [10, 11].

So wird Aktivkohle in Wasserwerken und Kläranlagen eingesetzt, um gelöste Spurenstoffe aus dem Wasser zu filtern. Im Vergleich zu den Spurenstoffkonzentrationen wird sie aber nur nachrangig charakterisiert. Der Adsorptionsprozess an der riesigen inneren Oberfläche von Aktivkohlekörnern ist seit über 100 Jahren bekannt und wird großtechnisch auch in der Lebensmittelindustrie, bei der Rauchgasreinigung oder zur Dekontamination von Böden und Grundwasser eingesetzt [1]. Die möglichen Wechselwirkungen zwischen Aktivkohleoberfläche und gelösten Spurenstoffen sind jedoch komplex, weshalb in der Praxis noch keine Prognose der zu erwartenden individuellen Spurenstoffentfernung möglich ist [12].

Das Einleitungskapitel beschreibt im Folgenden Eintragspfade und die Bedeutung der Mikroverunreinigungen in den Wasserkreisläufen. Des weiteren vertieft es die neuerliche Problematik der Mikroplastik sowie dessen thermoanalytische Bestimmung. Ausführlich wird auf das Material Aktivkohle eingegangen und dessen Einsatz, Herstellung sowie seine Eigenschaften erklärt. Es folgen Details zur pyrolytischen Zersetzung organischen Materials und den dabei ablaufenden Prozessen. Dieses Einleitungskapitel schließt mit der konkretisierten Zielstellung und der Formulierung der Forschungsfragen. Die vorliegende kumulative Dissertation wird diese in den darauffolgenden drei englischsprachigen Kapiteln beantworten. Dabei werden Thermoanalysen mit Zersetzungsgasanalyse für die Problematik der Mikroverunreinigungen angewendet und ihr Potenzial für die Wasseraufbereitung und -forschung dargelegt.

1.1 Mikroverunreinigung in den Wasserkreisläufen

Je nach Art und Ursprung gelangen Chemikalien auf unterschiedlichen Wegen in die Umwelt und die Wasserkreisläufe [6, 13]. In Abbildung 1.1 sind typische Eintragspfade dargestellt. Unvollständig metabolisierte Arzneimittel gelangen über Urin oder Fäzes in die Kanalisation und durch Kläranlagen oder Mischwasserüberläufe in die Gewässer. Pflanzenschutzmittel hingegen können durch Regenabschwemmung von Feldern in Gewässer gespült oder durch Versickerung direkt ins Grundwasser verlagert werden. Aber auch der Eintrag über nasse Deposition kann eine signifikante Eintragsquelle sein, wie die kürzlich erschienene Studie von Freeling et al. (2020) zur Konzentration von Trifluoressigsäure (TFA) in Niederschlagswasser zeigt [14]. Zu berücksichtigen sind auch Transformationsprodukte und Metabolite der Ausgangssubstanzen, die innerhalb der Wasserkreisläufe durch mikrobielle Aktivität, Photolyse oder technische Verfahren gebildet werden können [15, 16]. Diese Moleküle haben andere Eigenschaften und können zudem toxischer als ihre Vorläufersubstanzen sein [17, 18].

Kläranlagen tragen als Punktquellen mit die höchsten Spurenstofffrachten in Gewässer ein [6]. Dazu fanden Loos et al. (2013) an 90 Kläranlagenabläufen in Europa mit den höchsten Median-Konzentrationen die Süßungsmittel Acesulfam (14,3 μg L^{-1}) und Sucralose (1,7 μg L^{-1}), das Korrosionsschutzmittel Benzotriazol (2,7 μg L^{-1}), das Antiepileptikum Carbamazepin (0,8 μg L^{-1}), das Flammschutzmittel Tris(2-chlorisopropyl)phosphat (TCPP, 0,6 μg L^{-1}), das Opioid Tramadol (0,2 μg L^{-1}) sowie das Insektenabwehrmittel Diethyltoluamid (DEET, 0,2 μg L^{-1}) [19].

Abbildung 1.1: Quellen und Eintragspfade von organischen Spurenstoffen anthropogenen Ursprungs in die Umwelt und Wasserkreisläufe. Aus Abegglen und Siegrist (2012)[13].

Durch derartige Einträge finden sich im Mündungsdelta des Jangtsekiang in China 37 ng L^{-1} DEET [20]. In den Fließgewässern der USA sind es vergleichbare 31 ng L^{-1} DEET als Median-Konzentration sowie 70 ng L^{-1} Carbamazepin, 150 ng L^{-1} Tramadol und 1 μg L^{-1} Methyl-Benzotriazol-Derivate [21]. Flusswasser dient vielerorts als Rohwasser zur Trinkwassergewinnung, weshalb Tröger et al. (2021) dieses an 13 Wasserwerken in Europa und Asien untersuchten [22]. Im Mittel wurden dabei von den obigen Beispielsubstanzen 3 ng L^{-1} DEET, 90 ng L^{-1} Tramadol und 630 ng L^{-1} Sucralose detektiert, die sich durch die Trinkwasseraufbereitung im Mittel auf 1, 3 und 190 ng L^{-1} senken ließen. Die Trinkwassergewinnung aus Grundwasser hat durch die zusätzliche Barriere der Bodenpassage oder Uferfiltration ein niedrigeres Risiko erhöhte Spurenstoffkonzentrationen aufzuweisen. Dennoch wurden auch schon in Grundwasser Benzotriazol, Carbamazepin und DEET nachgewiesen [23].

Die aufgeführten Screening-Studien bestimmten teils mehrere hundert Substanzen über Target- und Suspect-Listen, was jedoch nur einem (kleinen) Teil der unbekannten Menge an Mikroverunreinigungen entspricht. Die verfügbaren analytischen Methoden sind durch die chromatographische Trennung ebenso diskriminierend wie die meist nötige Probenvorbereitung mittels Festphasenextraktion. Auch bei Non-Target Screenings mit teils über eintausend gleichzeitig bestimmten Features bleibt es dabei, dass wir nur ein unvollständiges und verzerrtes Bild über die vorhandenen Mikroverunreinigungen in unseren Wasserkreisläufen erhalten [24, 25].

Es gibt Bemühungen diese „analytical gap“[24] zu verkleinern als auch die Forschungsanstrengungen auf die potenziell gefährlichsten Spurenstoffe zu fokussieren. Eine Selektion wird beispielsweise anhand der Substanzkriterien Persistenz (P), Bioakkumulationspotenzial (B),

Toxizität (T) und Mobilität (M) vorgenommen. Das M-Kriterium wurde erst von Neumann (2017) vorgeschlagen und wird aus chemisch-physikalischen Eigenschaften (Wasserlöslichkeit und K_{OC}) abgeleitet [26]. Es reflektiert damit die Polarität einer Substanz und ermöglicht zusammen mit dem P-Kriterium die Bewertung, wie weit bzw. wie lange sich ein Stoff in den Wasserkreisläufen bewegt und möglicherweise akkumuliert.

Regulatorische Bestrebungen in Europa folgen dem Vorsorgeprinzip, wodurch vorausschauend anthropogene Einträge in Gewässer vermieden und auf das Nötigste begrenzt werden sollen. So wird durch die REACH-Verordnung der ungeprüfte und nicht-bestimmungsgemäße Gebrauch von Produkten und den darin enthaltenen Chemikalien schon vor Inverkehrbringen eingeschränkt [27]. Nach der Wasserrahmenrichtlinie (WFD, Water Framework Directive) [28] und ihrer Erweiterung, der Richtlinie zu Umweltqualitätsnormen (EQSD, Environmental Quality Standard Directive) [29], werden regelmäßig aktualisierte Substanzlisten (priority substances [30], watch list [31]) zusammengestellt, die in den Gewässern der Mitgliedsstaaten zu überwachen sind.

Mit dem gesundheitlichen Orientierungswert (GOW) gibt es in Deutschland ein zusätzliches Instrumentarium, das vorsieht, noch nicht bewertete oder bewertbare Spurenstoffe im Trinkwasser auf $< 0{,}1\,\mu g\,L^{-1}$ zu regulieren [32]. Um die Spurenstoffkonzentrationen in Trink- und Oberflächenwasser nicht nur regulatorisch zu beschränken, sondern die Einträge vorsorglich zu minimieren, wurde 2016 der Stakeholder-Dialog „Spurenstoffstrategie des Bundes“ ins Leben gerufen [33]. Dadurch sollten auf allen Ebenen des Lebenszyklus potenzieller Mikroschadstoffe Einzelmaßnahmen ausgelotet und ein breiter Konsens zur Reduzierung mit gemeinsamer Verantwortung geschaffen werden. Eine Maßnahme als erweiterte Abwasserbehandlung auf Kläranlagen wird in Abschnitt 1.3.1 detaillierter vorgestellt.

1.2 Mikroplastik als neue Umweltkontamination

Im vorigen Abschnitt wurde Mikroplastik (MP) als Mikroverunreinigung noch nicht berücksichtigt, da das Wissen um diese neuen partikulären Kontaminanten noch weit hinter dem der organischen Spurenstoffe zurückliegt. Im Spurenstoffdialog [33] wird dies als offene Frage festgehalten. Einzelmaßnahmen und Lösungsvorschläge werden noch nicht gegeben, auch wenn in teils emotional geführten öffentlichen Debatten die potenzielle Gefahr oft als evident eingeschätzt wird [34].

Es gibt nach wie vor keine einheitliche Definition und Handhabung von Mikroplastik als Mikroverunreinigung. Hartmann et al. (2019) schlugen als Definition und Klassifizierung für Mikroplastik alle festen, unlöslichen Polymerpartikel einer Größe von 1-1000 μm vor [35]. Die ISO/TR 21960 folgt diesem Vorschlag, ergänzt aber die Kategorie große Mikroplastik (1-5 mm) und schließt wegen der Zuständigkeit anderer Normengremien Gummi und Fasern explizit aus [36]. Obwohl klar ist, dass auch diese polymerbasierten Mikropartikel in der Umwelt gefunden werden. Die ECHA verwendet in den aktuellen Einschätzungen zum REACH Dossier von MP eine weiter gefasste Definition mit Größen von (0,1)-5000 μm, inkl. Gummi und Fasern [37]. Auch das spiegelt das noch in vielen Teilen nicht harmonisierte Verständnis zu Mikroplastik wider, welches bei der Erforschung einer neuen und so populären Kontaminante angestrebt wird [38, 39, 7, 40, 41]. Abbildung 1.2 zeigt die Größenbereiche von Nano- und Mikroplastik im Vergleich mit anderen Größen- und Substanzklassen zwischen 1 Å und 1 cm.

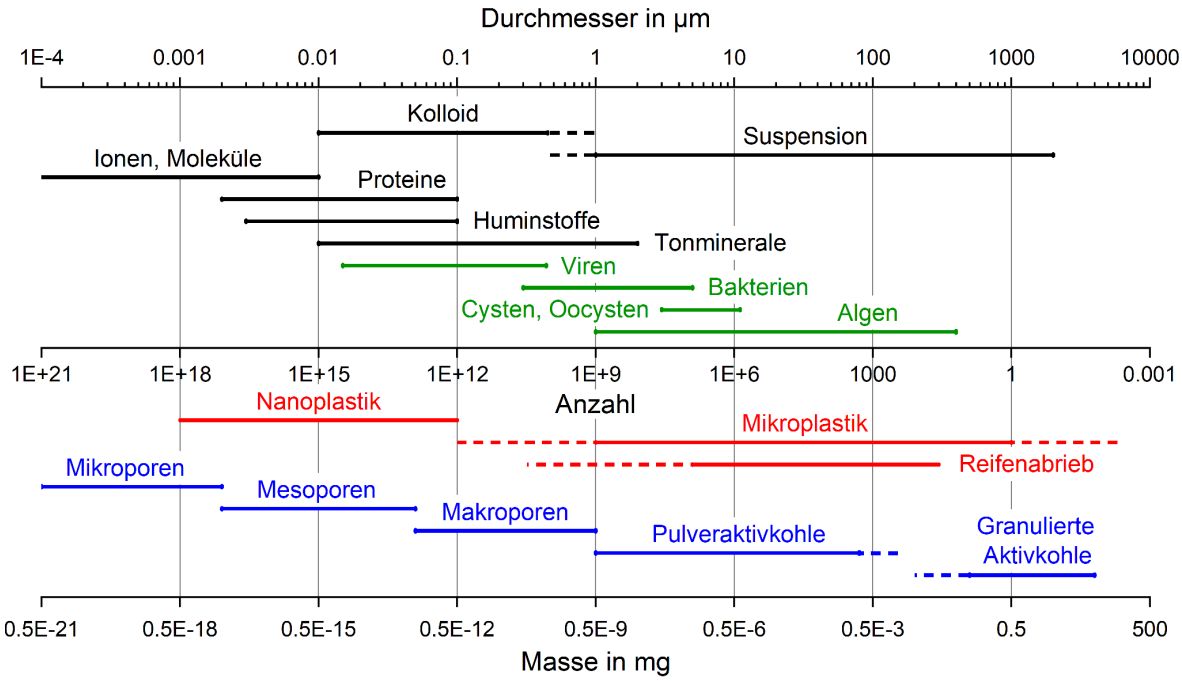

Abbildung 1.2: Gegenüberstellung von Größenspektren aus der unbelebten und belebten Natur, Nano- und Mikroplastik sowie Aktivkohleformen und ihrer Porenweiten. Die zusätzliche Skala zur Partikelanzahl entsteht relativ zu einer Sphäre mit 1 mm Durchmesser. Die Masse-Skala repräsentiert einen Partikel entsprechender Größe mit der Dichte 0,955 g cm^{-3} (z. B. PE-HD). Abbildung angelehnt an Jekel (1987)[42], Wagner et al. (2018)[43] und Braun et al. (2020)[7].

1.2.1 Eintragspfade und Einordnung zwischen Makro- und Nano-plastik

Kleine Kunststoff- oder Polymerpartikel können zum einen direkt in Produkten eingesetzt werden (z. B. als Peeling in Duschgels oder als Füllmaterial in Kunstrasenplätzen) oder entstehen durch die Fragmentierung größerer Kunststoffteile, sogenannter Makroplastik (z. B. aus Folien/Tüten oder aus Kleidung mit synthetischen Fasern). Diese können achtlos oder versehentlich in die Umwelt gelangt sein, aber auch gezielt auf Ackerflächen als Folie oder moderne Düngemittel eingesetzt werden. Letztere sind für eine langsamere Düngerabgabe mit einer dünnen Kunststoffhülle umschlossen sind. Demnach unterscheiden sich die Eintragspfade für MP deutlich von denen der gelösten organischen Spurenstoffe.

Kläranlagen als Punktquellen (z. B. durch Wäschewaschen im Haushalt oder Regenabfluss durch die Kanalisation) halten MP-Partikel zwar effizient zurück (98 %), die großen behandelten Wassermengen führen dennoch zu einem signifikanten Eintrag in die Gewässer [44]. Dafür wird durch die Akkumulation in Klärschlamm, dieser zu einem umso größeren Eintragspfad für MP auf landwirtschaftlich genutzten Flächen [45]. In absoluten Zahlen wird das Plastikproblem deutlich größer für Böden als für die Gewässer eingeschätzt [46], auch weil die größte MP-Fraktion in der Umwelt Reifenabrieb zu sein scheint, der nur zu 20 % in Gewässer abgespült wird [43]. Ein weiterer Eintragspfad und Forschungsbereich sind Niederschläge, die besonders in Städten erhöhte MP-Anteile aufweisen [47, 48, 49]. Aber auch die Raumluft ist mit MP-Fasern belastet, was direkt die menschliche Gesundheit betreffen kann [50]. Bei der Bewertung von MP steht die Akkumulation der Partikel in den Nahrungsnetzen im Vordergrund, auch wenn die Effekte von MP-Partikeln durch die Nahrungskette hindurch noch weitestgehend unklar sind.

Es wird vermutet, dass besonders kleine Partikel, auch Nano-Plastik, negative Auswirkungen auf Organismen haben können, da Partikel unter ca. 1 μm in der Lage sind, die Darmwand zu passieren, größere MP-Partikel aber nicht durch die Verdauung angegriffen werden [51]. Neben der Partikelgröße können auch die Polymerart die Wirkung beeinflussen und ausgewaschene, lösliche Bestandteile (Monomere, Additive) potenziell eine Schadwirkung entfalten [52]. MP als Vektor von sorbierten Schadstoffen wurde häufig untersucht [53, 54, 55], ist aber zumindest für Meereslebewesen gegenüber anderen partikulären Vektoren vernachlässigbar [56].

Für die Identifikation von Quellen, Eintragspfaden und dem Verbleib von MP entlang der Gewässer müssen zahlreiche Mechanismen im Detail untersucht werden. Dazu gehören die Sedimentation [57] als auch der Partikeltransport und -rückhalt in der hyporheischen Zone, der für Partikel <100 μm besonders signifikant sein kann [58]. Außerdem müssen Alterung und Wechselwirkung der MP-Partikel mit natürlichem organischem Material (NOM) [59] ebenso berücksichtigt werden wie ihre mikrobielle Besiedelung und ihr Abbau [60].

Alle Untersuchungen erfordern eine auf die Fragestellung angepasste Analytik, um die MP-Partikel adäquat qualitativ zu beurteilen oder quantitativ zu bestimmen [9]. Dass sich partikuläre Substanzen nicht wie gelöste homogen im Wasser verteilen, und verschiedenen Einflussfaktoren ausgesetzt sind (Sedimentation, Aggregation, hydrophobe Wechselwirkungen, etc.), stellt den gesamten Analyseprozess vor große Herausforderungen [7]. Fragestellungen, beginnend bei einer repräsentativen Probenahme, über eventuell benötigte Probenvorbereitung mit Aufkonzentration [61] bis zur Herstellung stabiler Suspensionen [62], müssen berücksichtigt werden und hohen qualitativen Anforderungen genügen [40].

Die angewendeten Analysemethoden lassen sich in spektroskopische und thermoanalytische Verfahren unterteilen. *Mikroskopisch-spektroskopische Methoden* setzen meist FITR oder Raman Spektroskopie ein, um MP-Partikel zu identifizieren. Sie stellen einzelne MP-Partikel visuell dar und ermöglichen so auch die Beschreibung ihrer Form. Durch automatisierte Auswertealgorithmen wird zudem die Gesamtanzahl an MP-Partikel auf einem Filter bestimmt [63, 64, 65]. Dem gegenüber stehen *thermoanalytische Methoden*, bei denen die Probe pyrolysiert wird und anhand polymerspezifischer Zersetzungsprodukte verschiedene MP-Gehalte in einer Probe differenziert und quantifiziert werden können [7, 66]. Für ausgewählte Polymere (z. B. Polyethylenterephthalat, PET) wurden auch *nass-chemische Extraktionsmethoden* entwickelt, bei denen durch Aufschluss der Probe mit chemischer Depolymerisation MP-Partikel zurück in ihre löslichen Monomere überführt werden, welche sich dann flüssig-chromatographisch detektieren lassen [67].

Wie Elert et al. (2017)[9] im Vergleich der MP-Detektionsmethoden hervorheben, so schlussfolgert auch Primke et al. (2020)[68], dass die Forschungsfrage im Vorfeld geklärt werden muss. Die Ergebnisse der Methoden sind grundlegend komplementär und nur eingeschränkt vergleichbar [8], da sich Masse und Partikelanzahl exponentiell gegenläufig zueinander verhalten (vgl. Skalen in Abbildung 1.2).

In dieser Arbeit werden thermoanalytische Verfahren verwendet und ihr Einsatz zur Detektion von MP im Folgenden Abschnitt beschrieben.

1.2.2 Thermoanalytische Mikroplastikdetektion

Thermoanalysen (TA) zur Materialcharakterisierung sind in den Polymerwissenschaften, der Metallurgie und Geologie weit verbreitet [69, 70, 71]. Dabei handelt es sich um die „Analyse der Änderung einer Probeneigenschaft, wobei diese Änderung mit einer aufgezwungenen Temperaturänderung verknüpft ist“ (DIN 51005)[72]. Typischerweise hat die umgebende Atmosphäre einen starken Einfluss auf das Ergebnis der TA, weshalb diese (je nach Fragestellung) oft als inert eingestellt wird, um eine Pyrolyse der Probe zu erreichen (siehe Abschnitt 1.4). Ein klassischer Vertreter ist die Thermogravimetrische Analyse (TGA), bei der die Probenmasse als Funktion der Temperatur untersucht wird. Unter pyrolytischen Bedingungen entsteht dabei ein für die Probe charakteristisches Massenverlustprofil, das Aufschluss auf ein verändertes Degradationsverhalten durch Alterung oder veränderte Probenzusammensetzung geben kann. Dass dies bereits Informationen über den MP-Gehalt in einer Probe enthält, konnte David et al. (2019)[73] mit MP-gespikten Bodenproben zeigen.

Die für die MP-Detektion zum Einsatz kommenden Methoden gehen über den einfach TGA Ansatz hinaus, indem sie nicht die Probenmasse, sondern die entstehenden Zersetzungsgase analysieren [7, 66]. Laut des Review-Artikels von Peñalver et al. (2020)[74] wird in der Hälfte der Publikationen die Pyrolyse in einer TGA realisiert, an die eine Zersetzungsgasanalyse gekoppelt ist. Zur anderen Hälfte wird die Probe direkt über ein Pyrolysemodul an einem Gaschromatographie-Massenspektrometrie System (Py-GC/MS) aufgegeben. Reine TGA oder kalorische Methoden (z. B. Dynamische Differenz-Kalorimetrie, DSC) sind kaum vertreten, da in echten Umweltproben damit keine einwandfreie Identifikation der Polymere möglich ist.

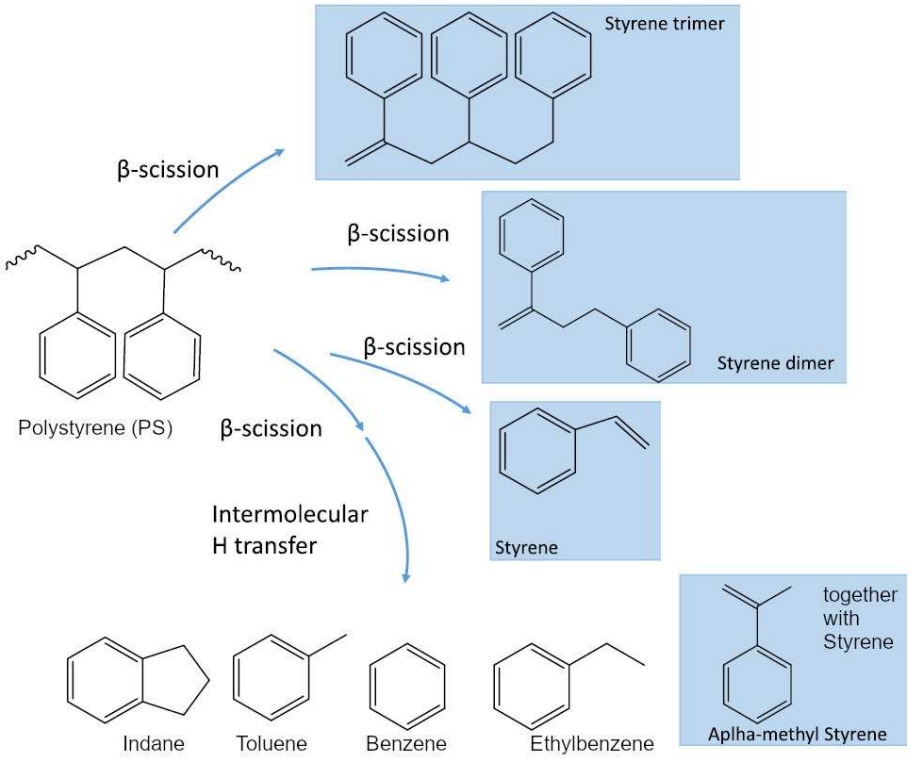

Abbildung 1.3: Spezifische Produkte der pyrolytischen Zersetzung von Polystyrol, in blauen Kästen, die zur Quantifizierung von MP-Gehalten genutzt werden können. Nach Yakovenko et al. (2020)[66].

Abbildung 1.3 zeigt exemplarisch Zersetzungsprodukte und -mechanismen (Abschnitt 1.4.1) von Polystyrol (PS), die für die Bestimmung von MP-Gehalten herangezogen werden können. Durch die Identifikation und eindeutige Zuordnung der Zersetzungsprodukte zu verschiedenen Polymeren können MP-Partikel in komplexen Umweltmatrizes differenziert und nachgewiesen werden [75]. Die Quantifizierung der MP-Gehalte ist durch eine externe Kalibrierung mit verschiedenen Mengen reiner Polymere oder, bei ausreichend vorhandener Probenmenge, durch Standardaddition realisierbar [76, 77]. Die Verwendung eines isotopenmarkierten internen Standards ist ebenfalls möglich und in Kombination mit der Standardaddition das analytisch sicherste Verfahren, um MP-Gehalte in unbekannten Umweltproben zu bestimmen.

Gegenüber Py-GC/MS Lösungen können mit TGA basierenden Methoden zur Zersetzungsgasanalyse größere Probenmengen analysiert werden. Das ist für die Aufgabe repräsentativer Mengen einer Umweltprobe vorteilhaft und erlaubt in vielen Fällen der Schwimm- und Schwebstoffanalyse eine Analytik ohne vorherige Probenvorbereitung zur Aufkonzentration der MP-Partikel [7]. Die verbreitetste Gerätekonfiguration zur MP-Analytik mit TGA ist die 2014 erstmals vorgestellte Thermische Extraktion- und Desorption Gaschromatographie-Massenspektrometrie (TED-GC/MS) [78]. Durch Weiterentwicklung und Automatisierung können damit die relevantesten Polymere in der Umwelt incl. Reifenabrieb binnen zwei Stunden in einer Probe bestimmt werden [76, 79]. Auf diesen Pyrolysetechniken lassen sich nun Monitoring-Programme aufsetzen, um Eintragspfade für MP genauer zu untersuchen und die MP-Frachten in den einzelnen Umweltkompartimenten zu bestimmen.

Der Betrieb eines TED-GC/MS Systems erfordert nach wie vor ein hohes Maß an Expertenwissen für die korrekte Durchführung und Auswertung der Ergebnisse. Andere auf TGA basierende Systeme werden daher ebenfalls für die Bestimmung von MP-Gehalten weiterentwickelt. Die flexiblen Möglichkeiten zur Kopplung für die Zersetzungsgasanalytik können zudem genutzt werden, um alternative Verfahren als ein GC/MS einzusetzen. Beispiele sind die Kopplung mit einem Fourier-Transform-Infrarotspektrometer (TGA-FTIR) [80] oder direkt mit einem Massenspektrometer (TGA-MS) [81]. Diese Verfahren arbeiten grundlegend anders, da die Zersetzungsgase für die Analytik nicht wie beim GC/MS gesammelt, sondern parallel zur Pyrolyse der Probe bei deren aktueller Temperatur analysiert werden. Dadurch sind diese Verfahren potenziell weniger empfindlich als die TED-GC/MS, eröffnen aber neben dem günstigeren Preis und der etablierten, robusteren Bauweise andere analytische Möglichkeiten, die auch im Rahmen dieser Arbeit evaluiert werden (Kapitel 2). Darüber hinaus gibt es weitere neue Systeme wie die TGA-FTIR-GC/MS, mit denen versucht wird die Vorteile verschiedener Zersetzungsgasanalysen zu kombinieren und für die MP-Detektion einzusetzen [82].

1.3 Aktivkohle für die Wasseraufbereitung

Verkohltes Holz und Knochen wurden bereits weit vor unserer Zeitrechnung zur Reinigung von Wasser eingesetzt. So empfahl Hippokrates von Kos das Filtern von schlecht riechendem und schmeckendem Wasser mit Holzkohle, um Krankheiten vorzubeugen [83]. Solch pyrolysiertes Material erfährt heute unter dem Namen „Biochar“ eine Renaissance als günstiges Adsorbens zur Wasseraufbereitung. Dabei handelt es sich um eine Vorstufe zur Aktivkohle, für die das Ausgangsmaterial nach der pyrolytischen Karbonisierung zusätzlich aktiviert wird (Abschnitt 1.3.2). Erst dadurch entwickeln sich die Materialeigenschaften (Abschnitt 1.3.3) sowie die mikroporöse Struktur, die zu vielfach verbesserten Adsorptionseigenschaften (Abschnitt 1.3.4) führen.

Als Erfinder der Aktivkohle gilt *Raphael von Ostrejko*, der ab 1900 in mehreren Patenten die Grundlagen der noch heute angewendeten thermischen und chemischen Aktivierung festhielt [1, 84]. Diese Klasse der Kohlenstoffmaterialien wurde in den letzten 100 Jahren vielfältig weiterentwickelt und für Anwendungen in der Lebensmittelindustrie, für die Gasadsorption bis hin zur Elektrochemie angepasst [85]. Mit den Befunden zu Mikroverunreinigungen in den Wasserkreisläufen finden Aktivkohleprodukte in den letzten Jahrzehnten auch zunehmende Verwendung in der kommunalen Wasserversorgung und Abwasserbehandlung.

1.3.1 Einsatz in Wasserwerken und auf Kläranlagen

Bei der Trinkwasseraufbereitung wird Aktivkohle hauptsächlich als granulierte Aktivkohle (GAK) in Festbettfiltern, die über mehrere Jahre laufen, eingesetzt [5]. Besonders bei der Verwendung von Rohwasser aus Flüssen und einer Desinfektion ist so eine nachgeschaltete Adsorptionsstufe als zusätzliche Barriere empfehlenswert [86]. Auf GAK-Filter wird typischerweise feststoffarmes Wasser aufgegeben, weshalb sie selten rückgespült werden müssen. Sind ausreichend Sauerstoff und Nährstoffe im Wasser vorhanden, können GAK-Filter als biologisch aktive Aktivkohlefilter (BAK-Filter) betreiben werden, wodurch auch nach Filterdurchbruch noch eine konstante Entfernung organischen Materials stattfindet [11, 87]. Das spezifische Durchbruchverhalten organischer Spurenstoffe kann daher von Adsorptions- und biologischen Transformationsprozessen abhängen und ist in vielen Fällen nicht prognostizierbar [88, 89]. Wegen der relativ niedrigen Spurenstoffkonzentrationen stellt ihr unkontrollierter Durchbruch im Rahmen der gesundheitlichen Orientierungswerte noch keine ausgewiesene Gefahr für die Trinkwasserqualität dar.

GAK wird mit fortschreitender Filterlaufzeit immer stärker beladen und nimmt ca. 10-20 % an Masse zu. Diese Beladung kann durch thermische Regeneration wieder entfernt und die Adsorptionskapazität teilweise wieder hergestellt werden. Zur Bemessung der Adsorptionskapazität wird mit dem Herstellung meist eine Iodzahl vereinbart (siehe Abschnitt 1.3.4), die das Regenerat aufweisen muss und ggf. durch Verschneidung mit frischer Aktivkohle sicherzustellen ist. Verglichen mit der Herstellung frischer Aktivkohle ist die Regeneration ökologisch sinnvoll, aber dennoch energetisch aufwendig [90]. Daher gibt es Bestrebungen, die in den Wasserwerken nur gering beladene GAK anders weiter zu verwerten, indem sie aufgemahlen und als PAK innerhalb des Wasserwerks in einem früheren Prozessschritt [91] oder auch extern in Kläranlagen weiterverwendet wird [92]. Bei solchen Verfahren muss das eingesetzte Produkt gut kontrolliert werden, um sicherzustellen, dass die Spurenstoffe im anderen Wasser nicht von der beladenen Aktivkohle desorbieren [91].

Bei der Abwasserbehandlung kommt neben GAK auch Pulveraktivkohle (PAK) zum Einsatz, die in bestehende Klärbecken oder in eigens dafür konzipierten Kontaktreaktoren dosiert wird [93]. PAK muss im Anschluss mittels Flockungsfiltration aus dem Wasser abgetrennt werden, wird dadurch aber auch innerhalb der Kläranlage rezirkuliert und ihre Adsorptionskapazität weiter ausgeschöpft. Die Kombination einer Aktivkohlestufe mit vorgeschalteter Ozonierung ist ebenfalls möglich, wodurch sich Synergieeffekte aus Entfernung von Transformationsprodukten als auch reduzierter Konkurrenzadsorption positiv auf die Spurenstoffentfernung auswirken können [94, 95]. Ebenso lässt sich Aktivkohle mit Membrananlagen gewinnbringend kombinieren, da Membranfouling reduziert werden kann und im Falle von PAK die Flockungsfiltration nur noch zur Phosphatfällung nötig ist [96, 97, 98]. Rizzo et al. (2019)[99] bewerten PAK-Verfahren als konsolodierte und derzeit aus Sicht der Kosteneffizienz als zu empfehlende Technologie. Die Deutsche Vereinigung für Wasserwirtschaft, Abwasser und Abfall e. V. (DWA) trägt mit der Herausgabe eines Themenbands zum Aktivkohleeinsatz auf kommunalen Kläranlagen sowie dem Entwurf des Regelwerks DWA-M 285 ebenfalls zu einer Konsolidierung der Verfahren bei [100, 101].

Die Konzentrationen von gelöstem organischem Material (DOM) und Spurenstoffen in Abwasser sind im Vergleich zur Trinkwasseraufbereitung deutlich höher (vgl. Abschnitt 1.1). Dadurch ist ihre Entfernung aus den Wasserkreisläufen an der Barriere Kläranlage am effizientesten zu realisieren [5]. In der Schweiz sind bereits 2016 gesetzliche Vorgaben in Kraft getreten, die den Ausbau von Kläranlagen erfordern, der bis spätestens 2040 abgeschlossen sein soll [102, 103]. Dies geschieht durch die Vorgabe eines Mindestentfernungsgrads von 80 % für ausgewählte Mikroverunreinigungen und wird über 9 CHF pro Einwohner und Jahr finanziert. Trotz eines zusätzlichen Energiebedarfs von 5-30 % für die Erweiterung von Kläranlagen um eine „4. Reinigungsstufe“ rechnet man in Deutschland mit Zusatzkosten von 0,05–0,19 € m^{-3} behandeltem Abwasser, was einer jährlichen Zusatzbelastung von 5-25 € pro Einwohner entspricht [33, 104, 105]. Durch den Ausbau der 230 größten Kläranlagen in Deutschland (> 100.000 Einwohnergleichwerte, Größenklasse 5) würden 50 % der anfallenden Abwassermenge einer erweiterten Abwasserbehandlung unterzogen und die Spurenstofffracht in die Gewässer deutlich reduziert [6]. Aktuell wird bei Trockenwetter auf 30 Anlagen eine erweiterte Abwasserbehandlung zur Spurenstoffelimination im Vollstrom betrieben [106]. Wie in Abbildung 1.4 dargestellt, befinden sich etwa 60 Anlagen in Planung oder Bau, wobei es sich mehrheitlich noch um Kläranlagen mittlerer Größe handelt. Der Bestand in Deutschland wurde größtenteils durch lokale Förderprogramme in den Ländern Baden-Württemberg und Nordrhein-Westfalen zum Schutz sensibler Gewässer und Trinkwasserressourcen finanziert. Mit den Ergebnissen zur „Spurenstoffstrategie des Bundes“ ist in naher Zukunft auf ein vereinheitlichtes Finanzierungskonzept zu hoffen [33].

Im Vergleich zur konventionellen biologischen Abwasserbehandlung bei der Mikroverunreinigungen in Summe zu weniger als 50 % zurückgehalten werden, lässt sich diese durch Einführung einer Aktivkohle- oder Ozonbehandlung im Idealfall auf über 95 % steigern [107]. Auch wenn eine solche beträchtlich gesteigerte Ablaufqualität keine kurzfristige Wirkung auf Zebrabärblinge zeigt [107], ließen sich am Beispiel der Schussen in Baden-Württemberg signifikant positive Effekte auf die Lebensgemeinschaften im Flussökosystem nach dem Ausbau von Kläranlagen nachweisen [108].

Wegen des zu erwartenden Bedarfs an Betriebsmitteln (Aktivkohle, Elektrizität, etc.) darf nicht nur die Entfernung der Mikroverunreinigungen berücksichtigt werden. Ökobilanzen legen neben

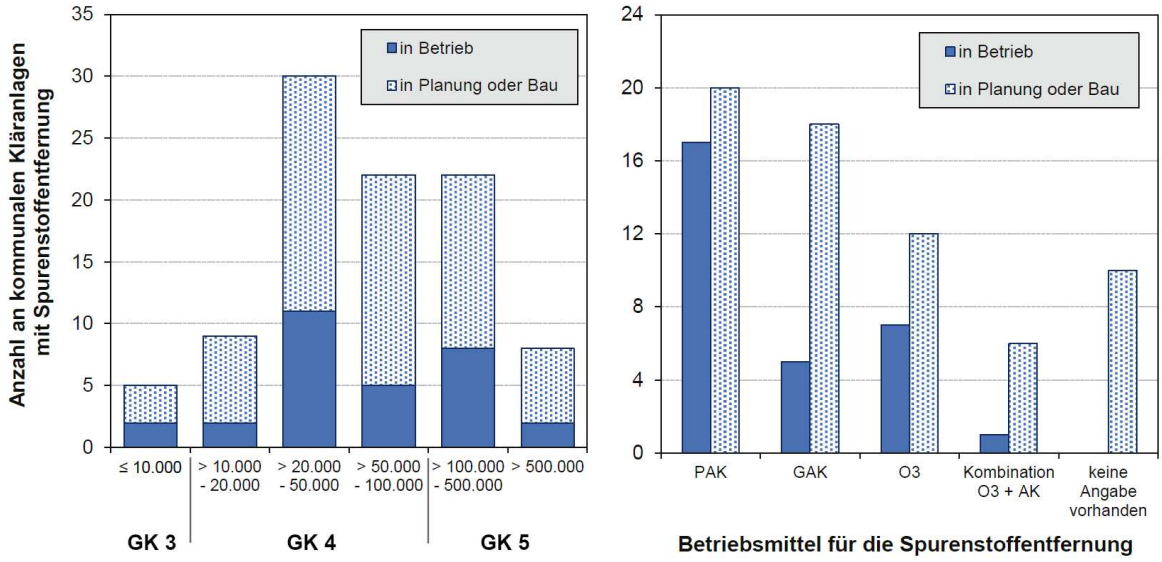

Abbildung 1.4: Kläranlagen mit Spurenstoffelimination in Deutschland, Planung und Betrieb, links: Größenklassen (GK) und Einwohnergleichwerte, rechts: Verfahren. Stand: August 2020, nach Metzger et al. (2020)[106].

der Regeneration von GAK auch den Wechsel zu Aktivkohle auf Basis lokaler, nachwachsender Rohstoffe nahe [5]. Die Effekte sind so eindeutig, dass ein ggf. erhöhter AK Bedarf, wegen schlechterer Adsorptionseigenschaften das Gesamtergebnis nicht signifikant verändert [109]. Dass der Ausbau einer Kläranlage mit einer Aktivkohlestufe nicht automatisch das 80 % Entfernungsziel der Schweiz erreicht, zeigten Guillossou et al. (2019)[110]. Die schon für GAK-Filter in der Trinkwasseraufbereitung angesprochene Schwierigkeit das Durchbruchverhalten einiger Spurenstoffe zu prognostizieren gilt besonders auch für die Prognose der Entfernungsleistung in Abwasser. Diese für ein Aktivkohleprodukt zu bestimmen erfordert Laborexperimente mit dem zu reinigenden Wasser, um die Wechselwirkungen mit Wassermatrix und den Spurenstoffen realitätsnah abzubilden [12, 111, 112, 113, 114].

Vielversprechende Ansätze zeigen, dass Entfernungsprognosen durch Simulation der Konkurrenzadsorption und einer detaillierten Charakterisierung des DOM möglich sind [115, 116, 117], heben aber zugleich hervor, dass dies mit etablierten und auf Kläranlagen verfügbaren Bestimmungsmethoden wie gelöstem organischem Kohlenstoff (DOC), UV-Absorption bei 254 nm (UVA_{254}) oder der Iodzahl nicht möglich ist [118]. Dennoch kann die Prozessüberwachung einer erweiterten Abwasserbehandlung mittels UVA_{254} erfolgen, da die Abnahme der aromatischen DOM Fraktion mit der Summe der meist aromatischen Spurenstoffe korreliert [101, 118]. Es kommt aber hinzu, dass verschiedene Aktivkohleprodukte und deren Chargen deutlich unterschiedliche Material- und damit verbundene Adsorptionseigenschaften aufweisen können [113]. Für Kläranlagenbetreibende gibt es aktuell keine Möglichkeit das Betriebsmittel Aktivkohle bei einer Lieferung schnell und aussagekräftig zu kontrollieren [119]. Dieser Zustand kann mittelfristig zu einer Verschlechterung der Reinigungsleistung einer Kläranlage führen, wie es sich bei anderen Betriebsmitteln wie Fäll- und Flockungshilfsmitteln zeigte [120]. Somit stellt die Auswahl bzw. die Abstimmung eines Aktivkohleprodukts auf das zu behandelnde Wasser als auch dessen regelmäßige Qualitätskontrolle eine aufwendige Herausforderung dar, für die es mit Bezug zur Spurenstoffentfernung noch keine zufriedenstellende Lösung gibt.

Dieser Problematik der Aktivkohlecharakterisierung für die Anwendung zur Wasseraufbereitung wird unter anderem in Kapitel 3 dieser Arbeit nachgegangen. Im Folgenden werden zunächst die Herstellungsprozesse für Aktivkohle beschrieben und danach auf die resultierenden Material- und Adsorptionseigenschaften eingegangen.

1.3.2 Aktivkohleherstellung

Der Markt für Aktivkohle ist in den letzten 30 Jahren kontinuierlich gewachsen. Betrug die weltweite Jahresproduktion 1993 noch 350 kt, waren es 2002 bereits 750 kt und 2019 2300 kt, was einer Verdopplung aller 10 Jahre nahekommt [83, 121]. Als Ausgangsmaterial für die Aktivkohleherstellung eignen sich besonders Pflanzenteile mit hohem Lignocellulose-Anteil oder fossiles organisches Material (Kohle), welches schon einem Karbonisierungsprozess unterlag [83]. Beispiele sind Holz(späne), Kokosnussschalen, Avocado-, Oliven- oder andere Fruchtkerne sowie weitere Abfälle aus der Pflanzenverarbeitung oder Papierindustrie [122]. Generell können auch organische Abfälle wie Klärschlamm, Fisch- oder Geflügelreste verwendet werden [123, 124, 125]. Wegen der hohen und teils günstigen Verfügbarkeit sind Braun- und Steinkohlen ebenfalls weitverbreitete Rohstoffe, aus denen sich qualitativ hochwertige Aktivkohlen herstellen lassen.

Die Produkteigenschaften sind eng mit dem Ausgangsmaterial und den Prozessparametern der Herstellung verknüpft [126]. Die entscheidenden Herstellungsprozesse nennen sich Karbonisierung und Aktivierung und müssen für jedes Ausgangsmaterial individuell angepasst werden, um den besten Kompromiss zwischen Materialausbeute, Porosität und Aschegehalt zu erhalten. Man unterscheidet zudem zwischen *thermischen* (physikalischen) und *chemischen* Verfahren [83, 122].

Bei thermischen Verfahren sind Karbonisierung und Aktivierung zwei getrennte, nacheinander ablaufende Prozesse, die sich separat steuern lassen. Die Karbonisierung wird durch eine thermische Behandlung zwischen 700-900 °C unter inerter Atmosphäre erreicht. Dieser Pyrolyseprozess entfernt flüchtige Bestandteile mit Sauerstoff- und Wasserstoffatomen, es bildet sich ein fester Pyrolyserückstand mit hohem Kohlenstoffanteil, Aromatizität und Porosität (siehe auch Abschnitt 1.4). Die Aktivierung ist eine erneute Hitzebehandlung unter leicht oxidativen Bedingungen bei 800-1000 °C. Dieser Vergasungsprozess mit Kohlenstoffdioxid, Wasserdampf oder eine Kombination aus beidem erweitert bereits vorhandene Mikroporen im Pyrolyserückstand und führt so zur Ausbildung des ausgeprägten Porennetzwerks in der Aktivkohle.

Bei chemischen Verfahren laufen Karbonisierung und Aktivierung unter inerter Atmosphäre gleichzeitig bei Temperaturen zwischen 400-800 °C ab. Dafür wird das Ausgangsmaterial zuvor mit dehydrierenden Chemikalien im Massenverhältnis 1:1 oder höher imprägniert. Häufig verwendete Aktivierungsmittel sind Phosphorsäure, Zinkchlorid oder Kaliumhydroxid, die dazu beitragen, dass die Entfernung der flüchtigen Bestandteile mit der Porositätsentwicklung gleichzeitig stattfinden können. Jedes Aktivierungsmittel hat eigene Mechanismen, mit denen es auf diese Prozesse einwirkt, bis seine löslichen Rückstände im Anschluss aus der Aktivkohle ausgewaschen werden [83]. Aktivierungsmittel, Massenverhältnis, Temperatur und Heizrate sind die Prozessparameter, über die sich die Materialeigenschaften des Aktivkohleprodukts über weite Bereiche steuern lassen.

Bezogen auf das Ausgangsmaterial hat dessen chemische Grundstruktur Einfluss auf die resultierende Aktivkohle, als auch seine anorganischen Bestandteile, welche katalytisch wirken können. So wird die ausgeprägte Mikroporosität und Härte von Aktivkohlen aus Kokosnussschalen auf den hohen Kaliumgehalt in ihrer Anorganik zurückgeführt [83]. Während das thermische

Verfahren mit Wasserdampf-Aktivierung das am weitesten verbreitete ist, werden mittlerweile 60 % aller Aktivkohlen auf Lignocellulose Basis chemisch mit Phosphorsäure aktiviert [122].

1.3.3 Materialeigenschaften

Die Eigenschaften eines Materials beschreiben seine Funktion und die Reaktion auf einwirkende Kräfte. Im Folgenden werden ausgewählte physikochemischen Eigenschaften von Aktivkohle behandelt, die vermutlich mit den Adsorptionseigenschaften in wässriger Lösung eng verbunden sind. Verfahrenstechnisch relevante Eigenschaften wie Härte, Schüttdichte und Korngrößen als auch Parameter zum sicheren Einsatz für den menschlichen Gebrauch wie wasserextrahierbare Substanzen oder Zinkgehalt werden daher nicht berücksichtigt [127]. Im Anschluss werden in Abschnitt 1.3.4 typische Adsorptionseigenschaften vorgestellt, mit denen Aktivkohlen anwendungsnah für die Wasseraufbereitung charakterisiert werden. Die Verknüpfung zwischen Material- und Adsorptionseigenschaften von Aktivkohle über ein Modell konnte bisher noch nicht in valide Adsorptionsprognosen umgesetzt werden.

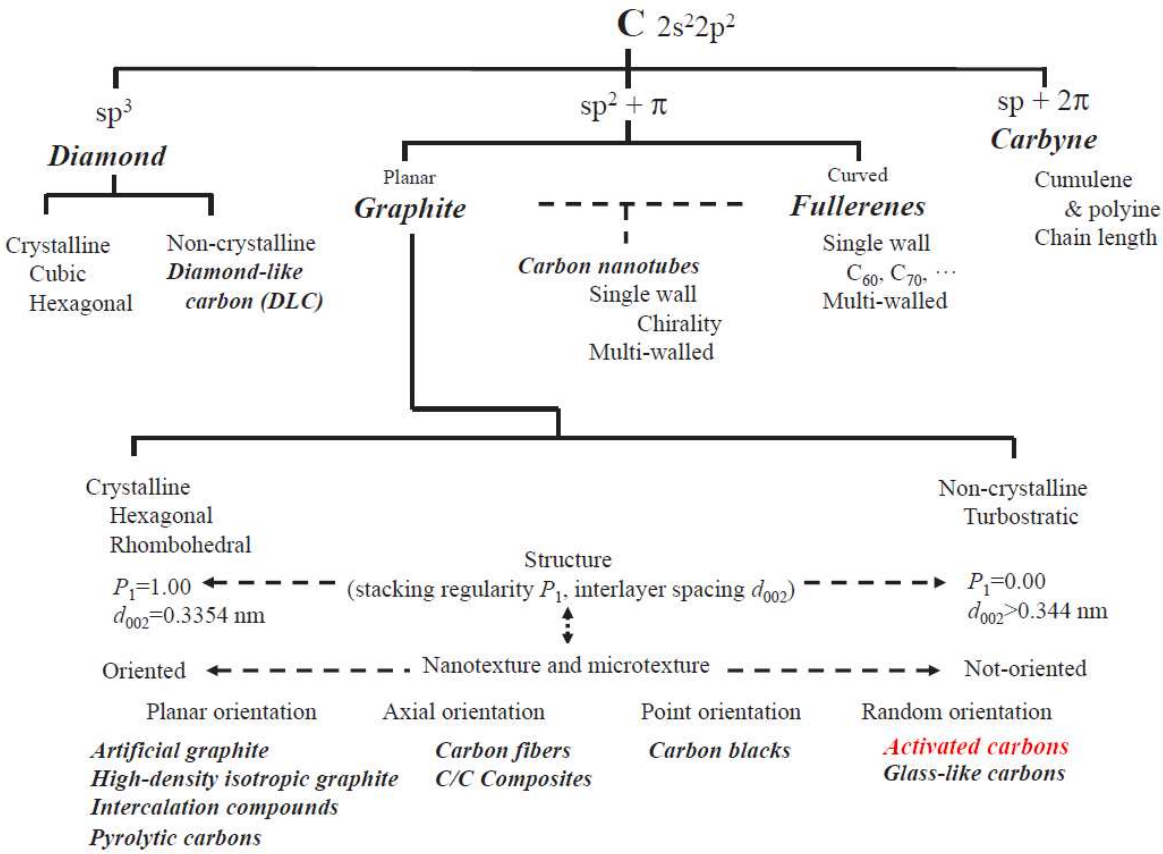

Abbildung 1.5: Klassifizierung der Kohlenstoffmodifikationen ausgehend von ihren Bindungsstrukturen. Nach Inagaki et al. (2016)[128].

Abbildung 1.5 zeigt die Einordnung von Aktivkohlen (activated carbons) in die Klassifizierung der Kohlenstoffmaterialien. Durch die sp^2 hybridisierte Bindung gehört Aktivkohle zur umfangreichen Graphit-Familie [128]. Ihre Struktur gilt als nicht kristallin, auch wenn mikro-kristallines Graphit zusammen mit turbostratisch angeordneten Graphenschichten ihre Kohlenstoffgrundstruktur bestimmen. Die Mikrostrukturen haben keine gemeinsame räumliche Ausrichtung, sondern sind isotrop angeordnet, wodurch Mikroporosität und damit verbunden eine

große innere Oberfläche entstehen. Zwei mögliche Modelle der schwammartigen Porenstruktur mit turbostratischen Graphenschichten sind in Abbildung 1.6 dargestellt. Wegen der hohen Unordnung ist es sehr schwierig die Struktur zu beschreiben und analytisch zu erfassen. Röntgenbeugungs (XRD) und -streuungsexperimente als auch Transmissionselektronenmikroskopie (TEM) geben Hinweise auf die mikro-kristallinen Graphitstrukturen, können aber ohne Porenmodell keine Aussage über das Porennetzwerk und seine Kenngrößen treffen [129].

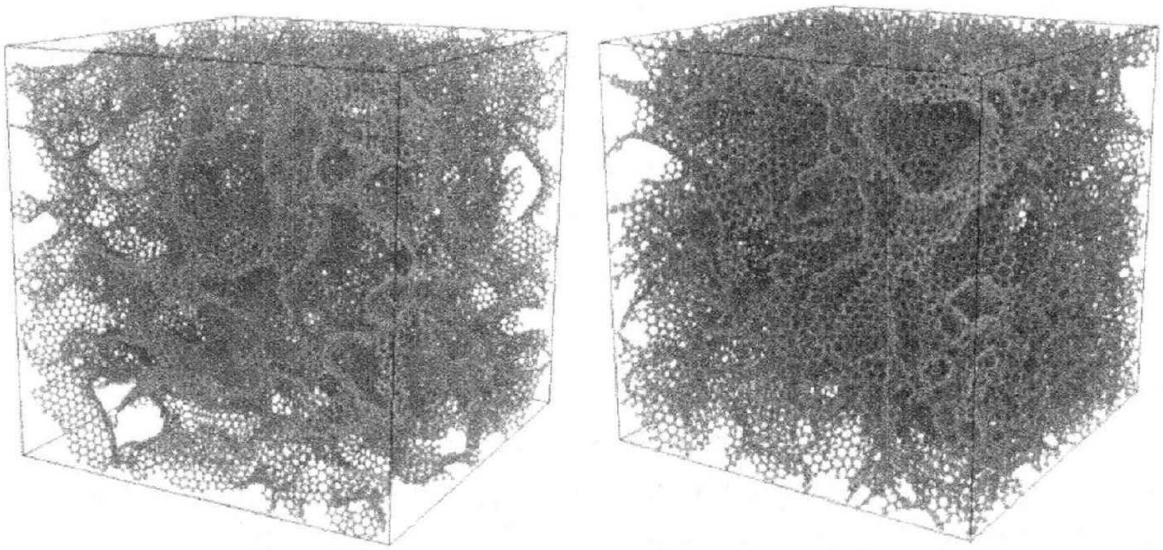

Abbildung 1.6: Simulierte Modelle zweier Aktivkohle-Mikrostrukturen mit 1530 $m^2\,g^{-1}$ (links) und 2180 $m^2\,g^{-1}$ (rechts) spezifischer innerer Oberfläche. Nach Yang et al. (2018)[130].

Für die physikalische Charakterisierung porösen Materials wird bevorzugt die Gasadsorption inerter Moleküle wie Stickstoff oder Argon bei deren Siedetemperaturen eingesetzt. Die resultierenden Adsorptions- und Desorptionsisothermen geben Aufschluss über das Vorhandensein verschiedener Porengrößen von Mikro-, Meso- und Makroporen. Über die adsorbierte Gasmenge kann das Porenvolumen bestimmt und damit die Porosität beschrieben werden. Kenngrößen wie die spezifische innere Oberfläche und der Anteil an Mikroporen lassen sich außerdem berechnen. Die weiterführende Interpretation der Daten auf Basis von Porenmodellen ist mit größerer Unsicherheit verbunden, worauf in Appendix B näher eingegangen wird. Die ausgeprägte Porosität der Aktivkohle gilt als entscheidende Eigenschaft für ihre bemerkenswerte Adsorptionskapazität und -leistung.

Neben der Kohlenstoffgrundstruktur weist die chemische Zusammensetzung von Aktivkohlen noch weitere Elemente auf. Sauerstoff, Stickstoff, Schwefel und Phosphor sind als Heteroatome an den Kanten und an Defektstellen von Graphit und Graphenschichten lokalisiert und bilden dort funktionelle Gruppen, die in Aktivkohle oft auch *aktive Zentren* genannt werden. Sauerstoff ist davon das am meisten vertretene Element und zugleich am schwierigsten quantitativ zu bestimmen, es wird meist als Differenz zu 100 % aus den zuvor genannten Elementen und dem Aschegehalt abgeschätzt. Funktionelle Oberflächengruppen tragen besonders in wässrigen Lösungen zur großen Zahl möglicher Adsorptionsmechanismen wie elektrostatischen Wechselwirkungen, Wasserstoffbrückenbindungen oder Elektronen-Donator-Akzeptor Mechanismen bei [131]. Neben direkten Wechselwirkungen mit Adsorptivmolekülen beeinflussen sie über mesomere und induktive Effekte die π-Orbitale der Graphenschichten und beeinflussen so auch die Stärke der dispersiven

Wechselwirkungen über London-Van-der-Waals-Kräfte [132, 133]. Der Einfluss der chemischen Beschaffenheit der inneren Aktivkohleoberfläche wurde schon mit verschiedenen Modellsubstanzen nachgewiesen und ist vermutlich eine entscheidende Eigenschaft für die Prognose spezifischer Adsorptionseigenschaften in Wasser.

Durch die natürlichen organischen Ausgangsmaterialien sind auch Metalle, quantifiziert durch den Aschegehalt, in der Aktivkohle vorhanden. Bei der Herstellung werden diese nicht entfernt, sondern durch den pyrolytischen Massenverlust und Abbrand während der Aktivierung relativ zur Gesamtmasse aufkonzentriert. Außerdem werden sie, wenn nicht schon geschehen, durch die hohen Temperaturen in anorganische mineralische Phasen umgewandelt. Diese tragen nicht zur Porosität bei und durch ihre relativ hohe Dichte verschlechtern sie alle anderen auf die Masse bezogenen Eigenschaften (g^{-1}). Für die Adsorptionskapazität gegenüber organischen Spurenstoffen werden diese Einschlüsse oder Verunreinigungen daher als nachteilig betrachtet. Dennoch können sie chemisch wechselwirken und die Sorptionskapazität für Fluorid-Ionen oder gelöste anorganische Elemente positiv beeinflussen.

In Kapitel 3 werden zahlreiche Aktivkohlen auf die genannten Materialeigenschaften hin charakterisiert, um ein umfassendes Bild über die Spannweiten der Eigenschaften zu gewinnen.

1.3.4 Adsorptionseigenschaften

Wie gut eine Aktivkohle gelöste Substanzen aus dem Wasser adsorbiert, beschreiben die Adsorptionseigenschaften. Sie werden oft als maximale Adsorptionskapazität für einen Stoff angegeben oder im Gleichgewichtszustand als Adsorptionsisothermen dargestellt. Aber auch Desorptionsgleichgewichte sowie die Kinetik gehören dazu und können in Einstoffsystemen bis hin zu komplexen Konkurrenz-Adsorptionssystemen in realem Wasser untersucht werden. Letzteres ist das typische Vorgehen für die Auswahl eines Aktivkohleprodukts in Wasserwerken und Kläranlagen. Es ist experimentell und analytisch aufwendig, liefert aber die verlässlichsten Aussagen über die angestrebte Wirkung von Aktivkohle auf das zu behandelnde Wasser [12].

Standardisierte Verfahren wie die Bestimmung der Iodzahl [127] und der Nitrobenzolzahl [134] sollen den Vergleich verschiedener Aktivkohlen ermöglichen. Sie repräsentieren grob die spezifische innere Oberfläche bzw. die Adsorption gut entfernbarer Substanzen und können schnell durch einen Batch-Ansatz mit einer definierten Lösung bestimmt werden. Es gibt weitere ähnlich bestimmte Kennzahlen wie die Melassezahl oder die Diatrizoatzahl [135], welche Fragestellungen zu größeren bzw. polaren und schlechter adsorbierbaren Molekülen adressieren.

Keine der Kennzahlen kann jedoch die hohe Komplexität an Adsorptionsmechanismen bei der Sorption organischer Spurenstoffe ausreichend abbilden, dass eine Prognose für reales Wasser möglich wäre [118]. Der starke Einfluss konzentrationsabhängiger Wechselwirkungen durch Konkurrenz zwischen Spurenstoffen und DOM um Sorptionsplätze an Aktivkohle spiegelt sich bereits in den Formen der Adsorptionsisothermen wider, die in realem Wasser nur in wenigen Fällen noch als Freundlich-Isotherme [136] beschreibbar sind. Einfache Surrogate können demnach nicht als Grundlage für Prognosemodelle zur Adsorption organischer Spurenstoffe dienen, sondern müssen mechanistisch an den Materialeigenschaften der Aktivkohle und der Zusammensetzung der Wassermatrix ansetzen. In Kapitel 3 werden daher die Materialeigenschaften von kommerziell verfügbaren Aktivkohlen im Detail bestimmt und in Kapitel 4 die Aufklärung spezifischer Adsorptionsplätze auf verschiedenen Aktivkohlen untersucht.

1.4 Pyrolyse organischen Materials

Pyrolyse ist die Spaltung chemischer Bindungen allein durch thermische Energie [137]. Das schließt Wechselwirkungen wie Oxidation oder Reduktion mit der umgebenden Atmosphäre aus, weshalb diese auch als inert bezeichnet wird. Der Begriff pyrolytische Zersetzung einer Feststoffprobe wird meist mit Blick auf die entstehenden flüssigen oder gasförmigen Produkte verwendet. Steht der feste Pyrolyserückstand als Produkt im Vordergrund, werden wie in Abschnitt 1.3.2 häufiger die Begriffe Karbonisierung oder Verkokung verwendet, obwohl es sich um die selben Pyrolyseprozesse handelt [83].

1.4.1 Pyrolyseprozesse

Die thermische Spaltung einer kovalenten Bindung ist eng mit ihrer Bindungsenergie verknüpft und bildet freie Radikale, die daraufhin die Pyrolysemechanismen bestimmen. „Die Kette bricht am schwächsten Glied“ beschreibt das Prinzip des initialen Schritts zutreffend (Tabelle 1.1). So

Tabelle 1.1: Bindungsenergie von Kohlenstoff-Einfachbindungen sortiert nach ihrem Betrag [138].

Bindung	Bindungsenergie in $kJ\,mol^{-1}$
C – H	416
C – O	358
C – C	331-358
C – Cl	327
C – N	305
C – S	289
C – P	264

bricht in Kohlenwasserstoffen die C–H Bindung zuletzt und die Bindung zu anderen Heteroatomen noch vor der C–C Bindung, bzw. bei niedrigeren Temperaturen. Solch homolytische Spaltungen erzeugen endständig radikalische Spezies, die wieder stabilisiert werden müssen. Ist es am Ende eines potenziellen Reaktionsweges jedoch nicht möglich stabile Produkte zu bilden, kommt es im ersten Schritt auch nicht zum Bindungsbruch. Die Pyrolyseprodukte werden also basierend auf dem initialen Bindungsbruch und der Stabilität der Radikale gebildet.

Bei der Degradation langer Kohlenstoffketten (z. B. Polyethylen (PE), Polypropylen (PP)) findet durch die vielen gleichwertigen C–C Bindungen eine *zufällige Kettenspaltung* statt. Ein häufiger Mechanismus zur Stabilisierung der primären freien Radikale ist der radikalische Angriff auf eine C–H Gruppe. Dadurch wird das freie Radikal mit einem Wasserstoffatom abgesättigt und in der angegriffenen Kohlenwasserstoffkette bleibt ein sekundäres Radikal zurück. Daraufhin wird dieses durch *β-Spaltung* der Kette stabilisiert, indem ein ungesättigtes Fragment ($-CH{=}CH_2$) sowie wieder ein endständig radikalisches Fragment ($\bullet CH_2{-}CH_2{-}$) entstehen. Infolge dessen werden bei der pyrolytischen Zersetzung von PE alle Oligomere entsprechend der Alkan-Reihe (zufällige Spaltung) als auch die korrespondierenden Alkene und Diene (β-Spaltung) gebildet. Bei der Degradation von PP entsteht durch die Methyl-Seitengruppe nur jedes dritte Alkan-Alken-Alkadien Triplet [137]. Außerdem entsteht beim Bindungsbruch sofort ein besser stabilisiertes sekundäres Radikal, als bei PE, weshalb PP bei niedrigerer Temperatur degradiert.

Ein völlig anderes Bild an Zersetzungsprodukten entsteht aus Polyvinylchlorid (PVC) durch den Pyrolysemechanismus der *Seitengruppenabspaltung*. Entsprechend Tabelle 1.1 bricht die C–Cl Bindung vor dem Polymerrückgrat (Backbone) und das Chlor-Radikal sättigt sofort mit dem angrenzenden Wasserstoff zu HCl ab. Zurück bleibt eine vinylisch ungesättigte Kohlenwasserstoffkette (–CH=CH–CH=CH–), aus der in den nächsten Zersetzungsschritten aromatische Produkte wie Benzen, Toluen und Naphthalen gebildet werden, die auf den ersten Blick nichts mehr mit der Ausgangsstruktur gemein haben.

Anders beim Mechanismus der *Depolymerisierung*, bei dem das Polymer zurück in seine Monomere degradiert. Ein Beispiel dafür ist Polymethylmethacrylat (PMMA), bei dem sich im Fall eines Copolymers, sogar das Verhältnis der Monomere aus der Synthese im Zersetzungsgas wiederfindet [137].

Die Stabilisierung der Radikale wird in vielen Fällen durch *Wasserstoff-Umlagerung* (intra- und intermolekular) erreicht. Wie dies in der chemischen Struktur der Probe möglich ist, entscheidet über die Ausbildung der gasförmigen Zersetzungsprodukte als Monomere, Oligomere oder als ganz andere Molekülstrukturen (vgl. Abbildung 1.3). Hinzu kommt der Einfluss der Pyrolysetemperatur sowie der Kinetik, die abhängig von Heizrate und Masse des Materials bzw. der Probe unterschiedliche Reaktionspfade priorisieren. So können die oben beschriebenen primären Pyrolyseprodukte miteinander in der Gasphase reagieren oder gecrackt werden und weniger spezifische sekundäre Produkte bilden [83].

Mit Blick auf Aktivkohlen und ihre Herstellung aus organischem Material (Abschnitt 1.3.2), sind die Pyrolysemechanismen sehr komplex. Die Zersetzung von Polysacchariden in Hölzern beginnt beispielsweise bei ca. 250 °C und es entstehen gasförmige Pyrolyseprodukte wie H_2O, CO_2, CH_3OH, HCOOH und CH_3COOH, die zusammen 60 % des pyrolytischen Massenverlustes erklären [139, 140]. Bis ca. 500 °C dominieren die primären und in ihrer Zusammensetzung materialspezifischen Produkte [83]. Um 600 °C werden zunehmend sekundäre Pyrolyseprodukte wie Wasserstoff und Methan freigesetzt [141], die zusammen mit Ruß ab 1000 °C alleinig in der Gasphase vorliegen. Bei hohen Heizraten wird der Ruß zusätzlich auf dem Pyrolyserückstand abgeschieden, was zum Verblocken von Poren und einer veränderten Oberflächenbeschaffenheit führt [83]. Diese aus den Pyrolyse- bzw. Karbonisierungsprozessen resultierenden Materialeigenschaften können durch leicht veränderte Pyrolysebedingungen signifikant unterschiedlich ausfallen [140, 142]. Generell begünstigen niedrige Heizraten das Ausbilden von harten Kohlen mit hohem Mikroporenanteil, wohingegen hohe Heizraten für eine ausgewogenere Porenstruktur mit Meso- und Makroporen sorgen [83].

Abhängig vom Ausgangsmaterial entstehen auch unterschiedliche Klassen der Kohlenstoffmaterialien (vgl. Abbildung 1.5). Marsh und Griffiths [143] haben mit Abbildung 1.7 die Veränderung der Kohlenstoffstruktur auf dem Weg zum thermodynamisch bevorzugten Graphit während der Pyrolyse anschaulich dargestellt. Aktivkohle als nicht-graphitisierbares Material kommt über die Bildung mikro-graphitischer Strukturen aber nicht hinaus, sondern verharrt im hoch-porösen Zustand auch noch bei 3000 °C [144]. Das Vorhandensein tertiärer Radikale deutet auf Defektstellen im Kohlenstoffgitter hin [129] und deutet darauf hin, dass es keine weiteren Reaktionswege zu ihrer Stabilisierung oder Eliminierung unter pyrolytischen Bedingungen gibt. Während der Aktivierung werden diese Defekte mit Sauerstoff abgesättigt und es bilden sich auf der inneren Oberfläche funktionelle Gruppen. Diese Sauerstofffunktionalitäten können

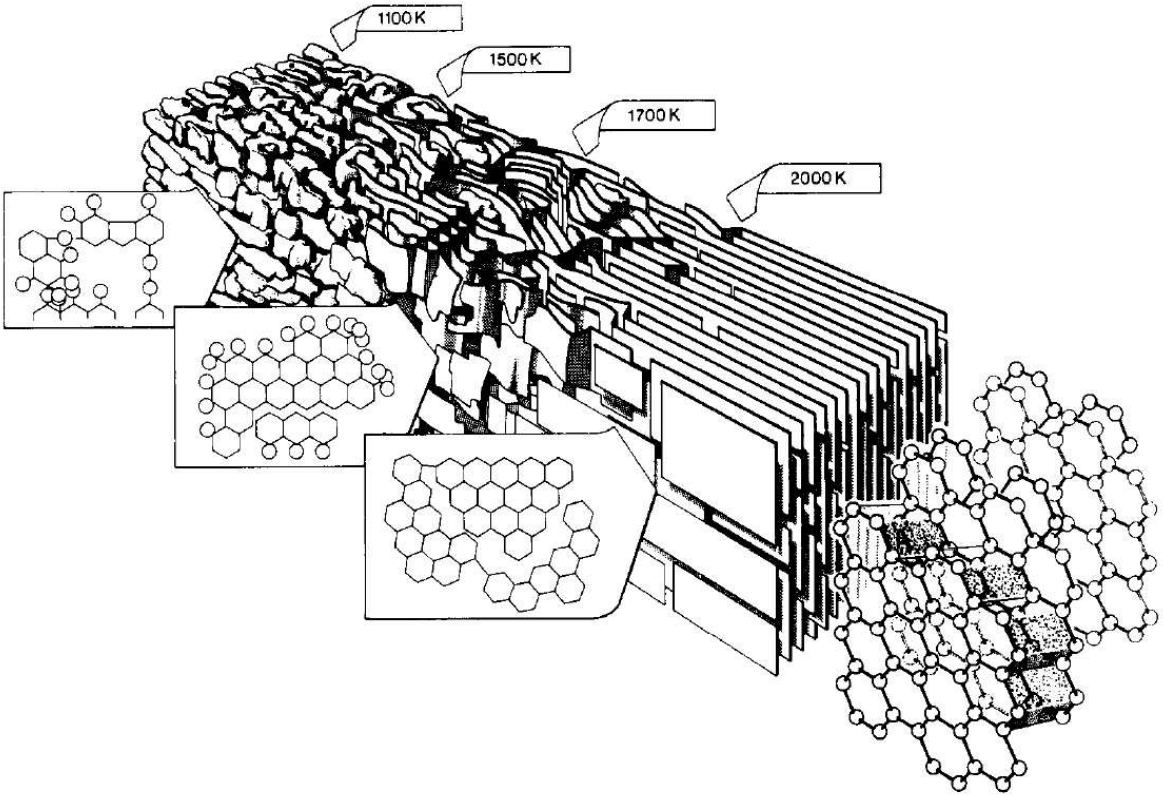

Abbildung 1.7: Pyrolyse von graphitisierendem Kohlenstoff. Aus Marsh (1991)[143]

bei einer erneuten Pyrolyse bis zu 1000 °C entsprechend ihrer Bindungsstärke wieder aus der Kohlenstoffstruktur entfernt werden. Die temperaturabhängige Abspaltung von H_2O, CO_2 und CO lässt sich für die analytische Bestimmung der funktionellen Gruppen nutzen und wird „temperature programmed desorption“ (TPD) genannt [145, 146]. In Kapitel 3 wird diese Methode zur Charakterisierung von Aktivkohlen angewendet und ist in Appendix A ausführlich beschrieben.

1.4.2 Pyrolyse als analytische Methode

In Abgrenzung zur thermischen Analyse genügt es nicht, eine Probe bei verschiedenen Temperaturen zu untersuchen (z. B. Bestimmung der Glasübergangstemperatur mittels DSC), sondern die Probe muss auch eine pyrolytische Zersetzung erfahren. Wampler (2007)[137] vergleicht den Pyrolyseprozess mit der Fragmentierung in einem Massenspektrometer. Sind die Parameter der eingetragenen thermischen Energie (Temperatur, Heizrate, Zeit) und die Probenmenge gleich, so entsteht aus der Analysenprobe immer wieder die selbe Verteilung an stabilen Fragmentmolekülen. Diese grundlegenden Mechanismen der Pyrolyseprozesse können für analytische Fragestellungen genutzt werden (vgl. Mikroplastikdetektion, Abschnitt 1.2.2).

Für reproduzierbare und aussagekräftige Analysenergebnisse müssen Sekundärreaktionen in der Gasphase vermieden werden. Moderne Analysegeräte realisieren das durch einen kontinuierlichen Spülgasstrom, der die Zersetzungsprodukte von der Probe abtransportiert, verdünnt und gleichzeitig die inerte Atmosphäre sicherstellt. Die exakte Temperaturkontrolle der Probe und des Ofenraums sind bei thermischen Analysen ebenfalls wichtig, weshalb normalerweise nur geringe Probenmengen (bei Reinsubstanzen < 1 mg) analysiert werden. Für die Repräsentativität einer Umweltprobe oder für die Untersuchung funktioneller Gruppen von Aktivkohle ist eine

größere Probenmasse vorteilhaft. Bei der Methodenentwicklung ist daher zu beachten, dass Sekundärreaktionen minimiert bleiben und kein zu großer Temperaturgradient innerhalb des Probenmaterials entsteht.

Die Pyrolyse einer Probe kann aus verschiedenen Perspektiven untersucht werden. Mittels TGA kann der temperaturabhängige Massenverlust direkt verfolgt werden oder mittels Py-GC/MS die Identifikation der Zersetzungsgase im Vordergrund stehen. Bei GC/MS Methoden werden die Zersetzungsgase zunächst gesammelt (Kryofalle oder Festphase) und verlieren dadurch den direkten Bezug zur Temperatur ihrer pyrolytischen Entstehung, werden so aber aufkonzentriert und nach chromatographischer Trennung leichter identifiziert. Erst durch die Kopplung einer TGA mit der Zersetzungsgasanalyse erschließt sich die vollständige Informationstiefe aus quantitativem Massenverlust der Probe und qualitativen Zersetzungsgasinformationen. Die Verwendung verschiedener Gasanalytik (spektroskopisch oder massenspektrometrisch) erlaubt ebenfalls komplementäre Ansätze für die Identifikation. Bei der TED-GC/MS werden die TGA-Informationen zwar erhoben, die Verknüpfung der Freisetzungstemperaturen mit den Zersetzungsgasen bleibt aber auf das Temperaturfenster der Gassammlung beschränkt. Bei kontinuierlicher Zersetzungsgasanalyse mittels FTIR oder MS lassen sich gasspezifische Freisetzungsraten erfassen, die direkt mit dem Massenverlustprofil der TGA korrespondieren.

Neben den beschriebenen grundlegenden Prinzipien, Gemeinsamkeiten und Unterschieden gibt es eine vielfältige Schar an Gerätekonfigurationen. Diese reichen vom Typen der TGA mit horizontaler oder vertikaler Anordnung von ein oder zwei Waagenarmen, erlaubtem Probenvolumen sowie paralleler Differenz-Thermoanalyse (DTA) über die Realisierung der Kopplung als beheiztes Rohr, Kapillare oder integrierte Überschalllösung [147], bis zur ggf. chromatographischen Trennung und Detektion mit Labor- oder Prozessanalysegeräten. Besonders von der Kopplung hängt das Analyseergebnis ab, da an ihr entschieden wird, ob große oder polare Moleküle den Detektor erreichen oder nicht [148].

Der Vielfalt an Geräten und Einflussfaktoren steht der große Nutzen der analytischen Pyrolyse gegenüber. So kann anhand der Pyrolyseprodukte die Ausgangsstruktur rekonstruiert und Zersetzungsmechanismen bspw. für die Flammschutzforschung abgeleitet werden [70]. Ebenso lassen sich Kinetikparameter wie Aktivierungsenergie und Frequenzfaktor bestimmen sowie die Reaktionsordnungen von Pyrolyseprozessen modellieren [149, 150, 151]. Das thermische Verhalten mineralischer Phasen und die Wechselwirkung von Alkali- und Erdalkalimetallen auf die thermische Zersetzung organischen Materials können ebenso charakterisiert werden wie biologische Makromoleküle und Mikroorganismen [137, 152]. Die Anwendungen reichen zudem bis in die Forensik sowie in die Lack- und Papierindustrie. Mit der Quantifizierung von Pulveraktivkohle in Klärbecken und Ablauf wurde die pyrolytische Analytik bereits vereinzelt für Fragestellungen in der Abwasserbehandlung eingesetzt [10, 153]. Außerdem wurden kürzlich erste Ergebnisse zur Zersetzung polyfluorierter Alkylsubstanzen (PFAS) bei der Regeneration von GAK publiziert und diskutiert [154, 155].

1.5 Zielstellung

Die Hochleistungsanalytik zur Bestimmung von Wasserinhaltsstoffen in geringsten Konzentrationen wurde in den letzten Jahren kontinuierlich weiterentwickelt. Zwei prominente Richtungen sind dabei die Erfassung hoch polarer Kontaminanten und das Screening nach einer großen Anzahl unbekannter Substanzen. Mit der Thematisierung von Kunststoffen in der Umwelt kam Mikroplastik als ungelöste, partikuläre Kontaminante zum Spektrum der Mikroverunreinigungen in Wasser hinzu. Für deren Bestimmung waren neue Herangehensweisen von Probenahme bis Analytik erforderlich, um die abfiltrierbaren Stoffe einer Wasserprobe repräsentativ und eingehend analysieren zu können.

Ein Ansatz ist die pyrolytische Zersetzung der gesamten Feststoffprobe, welche durch deren chemische Eigenschaften bestimmt ist und diese im Umkehrschluss charakterisiert. Analytische Verfahren mit Zersetzungsgasanalyse haben auf diese Weise erstmals breite Anwendung auf eine Umweltfragestellung gefunden. Anhand temperaturspezifischer Massenverlustprofile und der Charakterisierung der dabei entstehenden Zersetzungsgase ergeben sich mehrdimensionale Analysedaten, die auch kleinste Unterschiede in Feststoffproben aufdecken können. Potenziell ist es zudem möglich, aus Zersetzungstemperaturen, Massenverluststufen und der Kenntnis der Pyrolyseprodukte Zersetzungsmechanismen abzuleiten.

Durch diese Arbeit soll die analytische Pyrolyse mit ihrer relativ hohen Informationsdichte auf weitere aktuelle Fragestellungen zu Wasserqualität und Wasseraufbereitung angewendet und neue Forschungsfelder erschlossen werden. So werden zum einen verschiedene thermoanalytische Verfahren mit unterschiedlichem apparativem Aufbau verglichen und auf ihre Validität zur Bestimmung von Mikroplastik untersucht. Zum anderen soll Aktivkohle, die ebenfalls fest und partikulär vorliegt, aber zum Rückhalt gelöster Mikroverunreinigungen eingesetzt wird, thermoanalytisch charakterisiert werden. Eine Idee besteht darin, substanzspezifische Wechselwirkungen zwischen Spurenstoff und Aktivkohleoberfläche mit ihren heterogenen Sorptionsplätzen anhand der thermischen Zersetzung von Adsorbatsystemen aufzuklären.

1.5.1 Forschungsfragen und Struktur der Arbeit

- Sind einfachere apparative Aufbauten wie TGA-FTIR und TGA-MS im Vergleich zu TED-GC/MS in der Lage, Mikroplastikgehalte in einer Schwebstoffmatrix aus Oberflächenwasser zu bestimmen? Welche Einschränkungen oder auch Vorteile und neue Möglichkeiten implizieren diese Methoden für die Mikroplastikbestimmung? (Kapitel 2)

- Kann Thermogravimetrie und die Zersetzungsgasanalyse mittels Infrarotspektroskopie (TGA-FTIR) gewinnbringend für die Materialcharakterisierung von Aktivkohlen eingesetzt werden? Welchen Informationsgehalt liefern sie und ist die quantitative Bestimmung funktioneller Oberflächengruppen möglich? (Kapitel 3)

- Wie lassen sich Modell-Adsorbatsysteme aus einem Spurenstoff (Carbamazepin) und Aktivkohle durch TGA-FTIR und TED-GC/MS charakterisieren? Unterscheiden sich die Zersetzungsmechanismen des adsorbierten Carbamazepins auf verschiedenen Aktivkohlen? Sind Adsorptionsplätze oder Adsorptionszustände auf der Aktivkohle damit differenzierbar? (Kapitel 4)

2

Evaluation of thermoanalytical methods equipped with evolved gas analysis for the detection of microplastic in environmental samples

Caroline Goedecke[1], Daniel Dittmann[1], Paul Eisentraut, Yosri Wiesner, Bernhard Schartel, Patrick Klack, and Ulrike Braun

1: These authors have contributed equally to this work.

This chapter was published in the *Journal of Analytical and Applied Pyrolysis* in 2020 [156].

Abstract

Microplastic particles are currently detected in almost all environmental compartments. The results of detection vary widely, as a multitude of very different methods are used with very different requirements for analytical validity.

In this work four thermoanalytical methods are compared and their advantages and limitations are discussed. One of them is thermal extraction-desorption gas chromatography mass spectrometry (TED-GC/MS), an analysis method for microplastic detection that has become established in recent years. In addition, thermogravimetric analysis coupled with Fourier-transform infrared spectroscopy (TGA-FTIR) and mass spectrometry (TGA-MS) were applied, two methods that are less common in this field but are still used in other research areas. Finally, microscale combustion calorimeter (MCC) was applied, a method not yet used for microplastic detection.

The presented results are taken from a recently published interlaboratory comparison test by Becker et al. (2020)[157]. Here a reference material consisting of suspended matter and specified added polymer masses was examined, and only the results of the recoveries were presented. In

the present paper, however, the results for the individual polymers are discussed in detail and individual perspectives for all instruments are shown.

It was found that TED-GC/MS is the most suitable method for samples with unknown matrix and unknown, variable kinds and contents of microplastic. TGA-FTIR is a robust method for samples with known matrix and with defined kinds of microplastic. TGA-MS may offer a solution for the detection of PVC particles in the future. MCC can be used as a very fast and simple screening method for the identification of a potential microplastic load of standard polymers in unknown samples.

2.1 Introduction

Since the introduction of thermoplastic as industrial products, their use in such sectors as packaging, the automotive industry, and construction has increased constantly, amounting to a value of 65 million tons in Europe in 2017 [158]. Although proper waste management is supposed to include correct disposal and recycling as well, plastic is often leaked to the environment unintentionally. When thermoplastic products or materials are exposed to complex conditions, such as UV radiation, oxidation, hydrolysis, microbial degradation, higher temperatures and mechanical stress, they can fragment into smaller particles. This process is due to the degradation or scission of polymeric chains and can be observed macroscopically as embrittlement of the material [159]. Such small particles 1–1,000 μm in size are called microplastic [36]. They are observed almost everywhere in the environment and the risks or effects these particles present are still unclear. It is for example estimated that amounts of 108.9 ± 40.1 tons of macroplastic and 14.7 ± 9.0 tons of microplastic are ending up in Swiss fresh waters each year [46]. The amount of plastic waste flowing from rivers into global oceans, which serve as a final sink, is estimated at 1.15 to 2.41 million tons per year [160]. There are only few data available on the fate of plastic in terrestrial ecosystems, which could be anywhere from 4 to 23 times higher than in aquatic ecosystems [161]. The contribution of air, or better transport through air, is obvious, but its effects are still not understood and have yet to be quantified [50, 48].

Since there are no standardized or harmonized methods for the analysis of microplastic, a wide variety of different methods is applied. The application of different analytical tools with specific advantages and disadvantages is not only confusing for newcomers, but also for users from practical application (monitoring laboratories, regulatory authorities) and for stakeholders involved with this work (politicians, environmental organizations). When in peer reviewed articles analytical tools or results are presented often the scientific applicability of a single analytical tool is in the focus. Little attention is paid to the evaluation of the different methods in terms of their practical application, e. g. the time spent per measurement, possible complications through contamination, the need for user knowledge, as well as the complexity of the information obtained and the potential suitability of a given method for specific applications.

In most cases, spectroscopic methods are used for the analysis of microplastic particles, such as mid-infrared or Raman spectroscopy [162]. These methods allow the unambiguous identification of polymers in environmental samples by their specific absorption spectra. If the spectroscopic methods are linked with an imaging technique, additional information about the size, shape and number of particles is obtained. Automated data processing and correlation

to reference spectra or classification in characteristic clusters accelerate the evaluation of the data [64, 63]. But the greatest limitation of these methods is that complex and time-consuming sample preparation is needed in practice. Using such spectroscopic measurements yields particle numbers as the result.

Thermoanalytical methods like pyrolysis gas chromatography coupled with mass spectrometry (Py-GC/MS) or thermal extraction-desorption gas chromatography mass spectrometry (TED-GC/MS) can be used for the determination of mass fractions. These methods are already in use for the analysis of microplastic in complex environmental samples with a minimum of sample preparation [8, 76, 79]. However, interpreting the complex information those measurements contain still requires a high level of expertise.

But there are also simpler, less complex thermoanalytical methods. The coupling of thermogravimetry (TGA) with evolved gas analysis, e. g. Fourier-transform infrared spectroscopy (FTIR) or mass spectrometry (MS), is well established in research fields of polymer characterization such as processing stability and fire retardancy. Such analytical tools have been commercially available for decades. However, such methods have been used only sporadically in the field of environmental analysis. TGA-FTIR and TGA-MS have been used for the characterization and assessment of the volatile thermal degradation products of wood waste, refuse-derived fuel, waste plastic and waste tires [163, 164] as well as for the characterization of activated sludge interacting with activated carbon [10]. In the recent past, these methods have also been used to quantify microplastic. Yu et al. (2019)[80] proposed TGA-FTIR for the characterization and quantification of microplastic in mussels, seawater and soil. The polymers polyvinyl chloride (PVC), polyamide (PA) and polystyrene (PS) can be quantified by their method, but the detection of polypropylene (PP), polyethylene (PE) and polyethylene terephthalate (PET) was not possible. David et al. (2018)[81] successfully used TGA-MS for the direct quantitative analysis of PET in soil samples spiked with microplastic recyclate from PET bottles. Two reviews about application of thermoanalytical techniques can be found in literature [165, 66].

All of the existing thermoanalytical methods discussed above are based on structural information about the polymer-specific decomposition products. This is also meaningful because the chemical structure of a synthetic polymer is different from the chemical structure of the organic environmental matrix. However, these two components differ in terms of other characteristics as well, for instance, in their heat of combustion. In the area of waste management and fire retardancy the high heat of combustion or fire load of most common plastics like PE, PP or PS is well known. This is because those polymers pyrolyze completely into volatile hydrocarbons. Afterwards these gaseous pyrolysis products can be totally combusted into carbon dioxide and water. This thorough exothermic oxidation provides a maximum of heat release. In contrast to this, the environmental matrix pyrolyzes into volatiles, char and ash. Their volatile decomposition produces particular hetero-functionalities, including esters, ethers, hydroxyl groups, and amides. In consequence, the heat released by those components is clearly lower. The thermal analytical tool most suitable for measuring the heat released is called a microscale combustion calorimeter (MCC) and is well known from fire retardancy research [166, 167]. The functionality, application and the existing limitations of the method are presented and discussed as a potential new screening method for the analysis of microplastic in environmental samples. Very promising is that a single

measurement using this method takes only 10–20 min and allows very simple evaluation of the data collected.

The aim of this paper is to compare TED-GC/MS with the more common, well established thermoanalytical methods TGA-FTIR and TGA-MS for the analysis of microplastic in environmental samples, and also with the promising alternative method MCC. The comparison is made on a defined sample of polymers in a suspended matter matrix prepared for an interlaboratory test, which was recently published by Becker et al. (2020)[157]. Figure 2.1 and Table 2.1 show the results of the interlaboratory test samples of the individual polymers. The best results for PE and PP were achieved with TED-GC/MS. PS was detected with acceptable results using TED-GC/MS and TGA-FTIR. Only TED-GC/MS determined PET within an acceptable range. The lowest standard deviation was achieved by TGA-FTIR, and the highest observed for TGA-MS, which also exhibited the worst accuracy. In contrast to Becker's paper [157], this paper is more about the advantages and disadvantages of the individual methods and will highlight the possible application of the methods TGA-FTIR and TGA-MS, and also evaluate a new thermoanalytical method, MCC. In addition, the determination of PVC in environmental samples which cannot be detected by TED-GC/MS yet will be demonstrated as successful with TGA-MS.

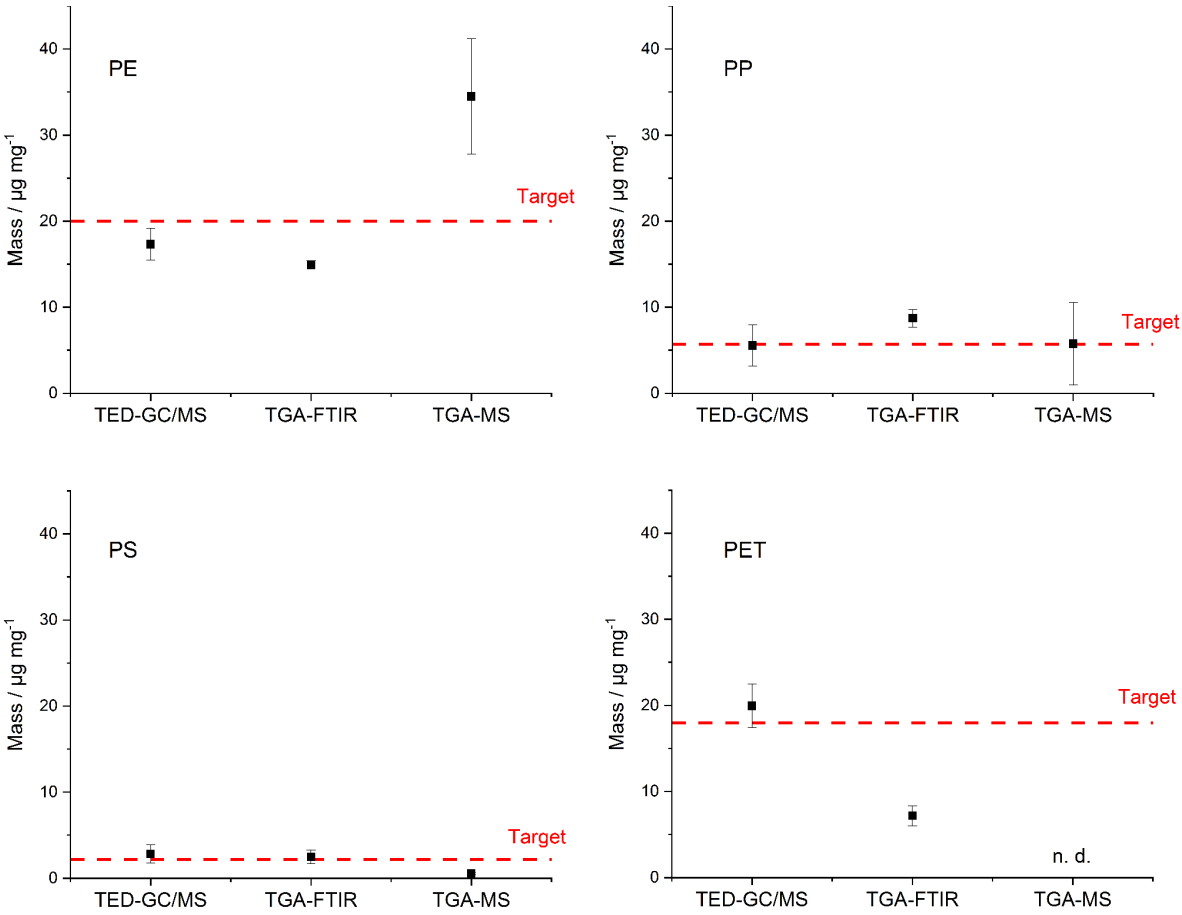

Figure 2.1: Results of the interlaboratory test samples for the investigated polymers PE, PP, PS and PET by the three TGA methods; n.d.: not detectable.

Table 2.1: Target values and results of the interlaboratory test samples using the three TGA methods in $\mu g\,mg^{-1}$; n.d.: not detectable.

Polymers	Target	TED-GC/MS	TGA-FTIR	TGA-MS
PE	20.00	17.33 ± 1.83	14.92 ± 0.48	34.51 ± 6.71
PP	5.70	5.56 ± 2.41	8.72 ± 1.02	5.78 ± 4.78
PS	2.20	2.84 ± 1.05	2.48 ± 0.81	0.54 ± 0.16
PET	18.00	19.95 ± 2.55	7.19 ± 1.17	n. d.

2.2 Materials and methods

2.2.1 Material

The interlaboratory test materials used to compare the methods were: suspended matter without polymers and suspended matter spiked with the polymers PE, PP, PS and PET. The ultrahigh-molecular-weight polyethylene PE was received from Celanese Corporation. The polymers PP, PS and PET were kindly provided as granules by PlasticEurope and their partners. The granules were cryo milled using a sieve mill (ultra-centrifugal mill ZM 200, Retsch, Haan, Germany) equipped with a ring sieve of 1 mm trapezoid holes. The polymeric materials contain a minimum of additives and are standard qualities for food packaging. The suspended matter was taken from the upper Danube River, sampled by a sedimentation box. The preparation of and detailed information on the interlaboratory test material are elaborated in Becker et al. (2020)[157].

The PVC powder (average particle size, D_{50} = 156 μm) was received from Vestolit (Marl, Germany). The other PVCs were basic commodities. We used two hard PVC materials which hereafter are called bar 1 and bar 2 (practical application: construction object, drainage pipe) and one soft PVC (PVC tube for medical applications). The matrices used for the PVC method development of TGA-MS were obtained from the Environmental Specimen Bank (Umweltbundesamt, Berlin, Germany. These matrices (suspended matter, sediments, plant material, soil, different kind of fish and honey) are not presented in detail here, because they only represent selected, representative matrices from different environmental media (aquatic, terrestrial and biological samples).

2.2.2 TED-GC/MS

Thermal extraction-desorption gas chromatography mass spectrometry (TED-GC/MS) is a two-step analytical approach. First, the sample is pyrolyzed under a gentle flow of nitrogen using a thermobalance (TGA2, Mettler Toledo, Columbus, USA) and the decomposition products are collected through a solid phase extraction (SorbStar, Mercury Instruments GmbH, Karlsfeld, Germany). Afterwards, the samples are desorbed and analyzed using a thermal desorption unit of a GC/MS system (TDU and CIS4, Gerstel, Mülheim an der Ruhr, Germany; gas chromatograph 7890B + mass spectrometer 5977B, Agilent, Palo Alto, USA). The qualification and quantification of the polymers in the environmental sample are based on specific decomposition products. Further information on the method and parameters are reported in the publications by Eisentraut et al. (2018)[76] and Duemichen et al. (2019)[79].

For the TED-GC/MS measurements, 150 μL aluminum oxide crucibles were used, with 15 mg of the interlaboratory test material with polymers and 20 mg of the interlaboratory test material without polymers. A heating rate of 10 K min^{-1} was applied. The decomposition products were collected between 25 and 600 °C for both sample types. For the quality control of the measurement, deuterated polystyrene was used as an internal standard (d5PS: fully deuterated aromatic ring, Polymer Source, Dorval, Canada). The interlaboratory test materials with and without polymers were each measured six times. Using the interlaboratory test material without polymers as matrix, an external calibration was recorded for the quantification. This spiking was realized using a micro balance with a reading accuracy of 5 μg. 15 mg of matrix material each were spiked with a constant amount of deuterated PS and with defined amounts of PE (0.04, 0.09, 0.17, 0.33, 0.40, 0.49 mg as particles), PP (0.05, 0.11, 0.16, 0.19, 0.24, 0.31 mg as particles), PS (0.01, 0.02, 0.03, 0.04, 0.05, 0.06 mg as solution in toluene) and PET (0.04, 0.14, 0.17, 0.27, 0.31, 0.21 mg as particles) at six mass content levels. In practice, this was done by first dosing and carefully detect the particles masses of the polymers and then adding the matrix.

Results of a preceding blank measurement and of the pure matrix were included in the calibration curve as the zero level.

2.2.3 TGA-FTIR

The TGA-FTIR measurements were performed using a TGA/DSC3+ thermobalance (Mettler Toledo, Columbus, USA) coupled with an FTIR spectrometer (Nicolet iS50 Advanced FT-IR, Thermo Fisher Scientific, Waltham, USA) equipped with a gas measuring cell (260 °C). The transfer line used (inner diameter: 1 mm) was maintained at 250 °C. The FTIR measurements were performed over a range of 4000–400 cm^{-1} with a resolution of 4 cm^{-1} and a scan rate of 16 scans per spectrum.

20 mg of the interlaboratory test material with and without polymers were measured six times each using 150 μL aluminum oxide crucibles. Heating rates of 10 K min^{-1} were applied and a nitrogen flow of 30 ml min^{-1} passes through the TGA and FTIR system. External calibration with about 0.5 and 2 mg of the pure polymers was used to calibrate the measurements. This is not enough for a basic validation of the method, but it is sufficient for the assessment of the method on the question.

Data from the evolved gas analyses were examined by creating release rates. This means that selected absorption bands or regions of the spectra were integrated, and their changes plotted over time or temperature, respectively. The software OMNIC 9 (Thermo Fisher Scientific, Waltham, USA) was used.

2.2.4 TGA-MS

The TGA-MS measurements were performed using a thermobalance (STA7200, Hitachi High-Tech Analytical Science, Oxford, UK) connected with a mass spectrometer (GSD 320 Thermostar TM, Pfeiffer-Vacuum, Asslar, Germany) by a coupling device (280 °C, REDshift, San Giorgio in Bosco, Italy).

The samples were weighed into a 65 μL aluminum oxide crucible (about 20 mg for the polymers in matrix or the pure matrix) and pyrolyzed in the TGA at a heating rate of 10 K min^{-1} under

a flow of nitrogen of about 200 mL min^{-1}. During measurement, part of the decomposition products were passed via a heated transfer capillary (deactivated fused silica tubing, outer diameter: 0.22 mm, inner diameter: 0.15 mm, maintained at 280 °C, split of 1:200) and the coupling into the inlet (150 °C) of the mass spectrometer. The mass spectrometer was operated in electron ionization (EI) mode at 70 eV. The measurements were performed in the single ion mode. Each of the interlaboratory test materials with and without polymers was measured six times. An external one-point calibration with about 1 mg of the pure polymers was used to calibrate the measurements. In this case, no major efforts were made to validate the method because the result of the TGA-MS measurements was not satisfactory for other reasons. However, this is explained in the results section.

Data from the evolved gas analyses were examined by creating mass traces. This means that the change in selected mass fragments is plotted over time or temperature, respectively. The PVC experiments were performed in 25 μL aluminum oxide crucibles containing about 5 mg of the PVC samples or 10 mg of matrix spiked with PVC.

2.2.5 MCC

The MCC measurements were performed using a FAA Microcalorimeter (Fire Testing Technology, East Grinstead, UK) in accordance with ASTM D 7309 [168]. Samples of 5.00 $\pm$ 0.05 mg were measured. The pyrolyzer temperature ranged from 150 to 800 °C at a heating rate of 1 K s^{-1}, and the combustor was set to a temperature of 900 °C. MCC takes advantage of the oxygen consumption method, with 1 g of consumed oxygen equating 13.1 $\pm$ 0.7 kJ of heat production [169]. The MCC measurements were not evaluated in the usual way, by determining heat release capacity and the total heat release per sample mass, but instead by determining the heat release in the typical decomposition range of the pure hydrocarbon polymers, such as PP, PE and PS. Thus, environmental matrices deliver heat release rate (HRR) curves rather like a background consisting of very broad and flat humps over temperature, whereas polymers become visible in sharp HRR peaks in temperature ranges well defined by their decomposition.

2.3 Results and discussion

For pyrolysis a thermobalance is used in TED-GC/MS, TGA-FTIR and TGA-MS. Figure 2.2 shows exemplary TGA measurements of the interlaboratory test materials as they were obtained by all presented methods. The graph consists of the sample's relative mass loss (TG) and the mass loss rate (DTG) to facilitate visual interpretation. The trend of the TG curves is similar up to 400 °C (mass loss approx. 10%). Between 400 and 500 °C, the degradation of the polymers takes place, which is recognizable by two peaks in the DTG curves. Overall, up to 600 °C, a pyrolytic mass loss of about 12% can be observed for the interlaboratory test material without polymers, and 16% for the sample with polymers. Therefore, for all TGA methods the mass loss of $\sim$4% can be taken as an indicator for the maximum polymer content in the sample. This maximum value should not be exceeded even if the polymer content in the sample is evaluated by evolved gas analysis. Additionally, the homogeneity of the analyzed samples can be assessed. The reproducible curve pattern of plotted curves indicates that a sample of 20 mg is in first approximation homogeneous.

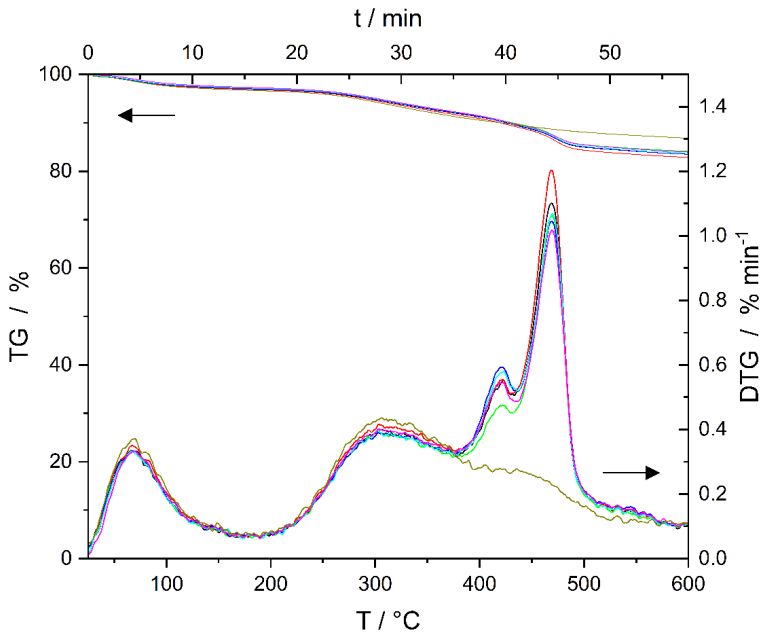

Figure 2.2: Thermogravimetry results of six measurements of the interlaboratory test material with polymers, and one measurement without polymers for comparison. Left axis: relative sample mass as TG curves; Right axis: corresponding DTG curves (first deviation of TG curves).

2.3.1 TED-GC/MS: The most powerful method

With TED-GC/MS, the polymers PE, PP, PS and PET are clearly identified by their specific decomposition products, which are well known [169]. Using gas chromatography, the resulting decomposition products of each polymer are separated and individually detected. This allows the identification of the decomposition products using the NIST database. An overview of the qualifiers and quantifiers used is presented in Table 2.2. More detailed information on the used marker substances has been published by Duemichen et al. (2017)[75]. All evaluated decomposition product peaks areas were normalized for the peak area of the monomeric decomposition product of the internal standard deuterated PS. A preceding analytical blank measurement was considered.

Table 2.2: List of qualifier and quantifier substances used for the PE, PP, PS and PET detection by TED-GC/MS.

Polymer	Qualifier	Quantifier
PE	1,12-tridecadiene 1,13-tetradecadiene 1,14-pentadecadiene 1,15-hexadecadiene	1,11-dodecadiene
PP	2,4-dimethylhept-1-ene 2,4,6-trimethylnon-1-ene (isomer 1) 2,4,6-trimethylnon-1-ene (isomer 2) 2,4,6,8-tetramethylundec-1-ene (isomer 2) 2,4,6,8-tetramethylundec-1-ene (isomer 3)	2,4,6,8-tetramethylundec-1-ene (isomer 1)
PS	2,4-diphenyl-1-butene 2,4,6-triphenyl-1-hexen	styrene
PET	vinyl benzoate benzoic acid	ethyl benzoate

The best results for the determination of PE and PP were achieved with TED-GC/MS. PET was determined with satisfactory results solely by this method. The determination of PS was also successful. The standard deviations were low (see Figure 2.1 and Table 2.1). These results of TED-GC/MS measurements confirm that this is the method most suitable for microplastic detection in unknown samples (matrix, kind of polymer und content) with a minimum of evaluation expense, but it does require user knowledge for technical handling. However, this will become clearer in the following parts of the work.

2.3.2 TGA-FTIR: A very robust routine method

For the evaluation of TGA-FTIR, measurements of the pure polymers were carried out first. Characteristic bands were selected for all four polymers (Figure 2.3). An overview of those characteristic vibrations is given in Table 2.3. More detailed information about evolved gas analyses of the investigated polymers can be found in works published by Braun and Schartel [170, 171, 172].

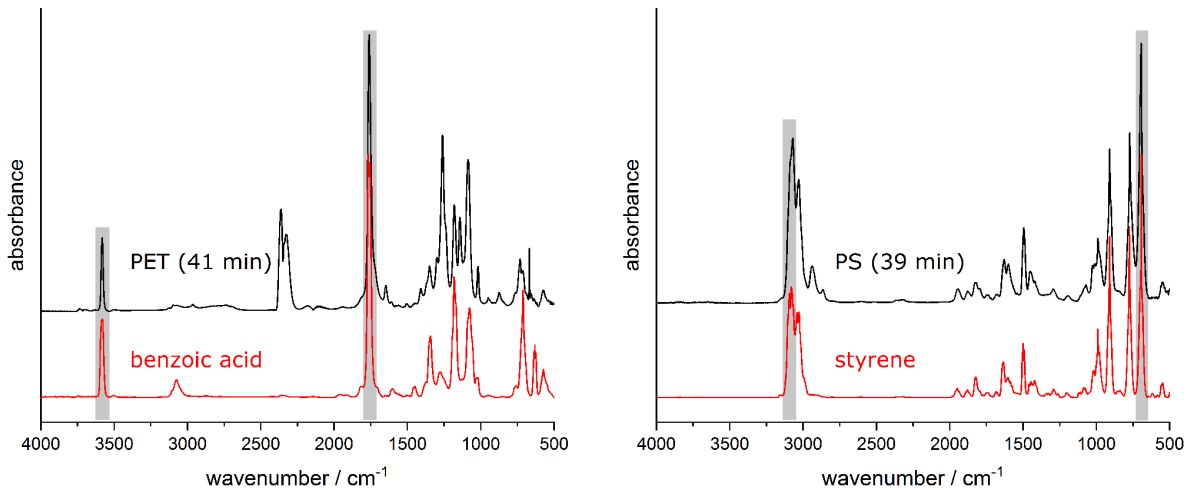

Figure 2.3: Gas phase IR spectra of the decomposition gases of PET and PS and the reference spectra of benzoic acid and styrene.

Table 2.3: Selected wave numbers for the detection of the polymers PE, PP, PS and PET using TGA-FTIR.

Polymer	Characteristic band	Description
PE + PP	$2990-2945\,cm^{-1}$	CH_3 groups
	$2885-2801\,cm^{-1}$	CH_2 groups
PS	$700-695\,cm^{-1}$	Mono substituted ring
	$3128-3052\,cm^{-1}$	C–H at aromatic rings
PET	$3582\,cm^{-1}$	O–H of free carboxylic acid
	$1826-1704\,cm^{-1}$	C=O of free carboxylic acid

The C=O stretching vibration band (1826–1707 cm^{-1}) was used for the quantification of PET; in addition, the O–H stretching vibration (3582 cm^{-1}) qualifies the characteristic decomposition product benzoic acid. For PS, the vibration band of the C–H resulting from plane deformation of the monosubstituted ring system (700–695 cm^{-1}) was used for quantification, and the vinylic bound C–H stretching vibration (3128–3052 cm^{-1}) was used to qualify the characteristic styrene.

These two bands (one for quantification, one for verification) were selected for each kind of polymer to ensure unambiguous identification of the polymers in complex matrices, since the bands individually might not be specific.

For the TGA-FTIR measurements of interlaboratory test samples with polymers, the decomposition products of PET and PS, benzoic acid and styrene, respectively, are clearly identified by gas phase FTIR. To determine the masses of PS and PET with TGA-FTIR, the release rates of the previously selected vibrational bands (Table 2.3) were integrated. The bands of these specific decomposition products of PS do not overlap with the signals of the environmental matrix. For PET, a small, interfering signal from the environmental matrix without polymer was observed; therefore, the integrated signal of the interlaboratory test material without polymers was then subtracted.

For PE and PP (see Figure 2.4, left), the intense symmetric C–H stretching vibration of CH_2 (2885–2801 cm^{-1}) as well as the symmetric C-H stretching vibration of CH_3 bands (2990–2945 cm^{-1}) in the aliphatic decomposition products interfere with each other, and the degradation of the two polymers occurs at the same temperatures. However, the measurements

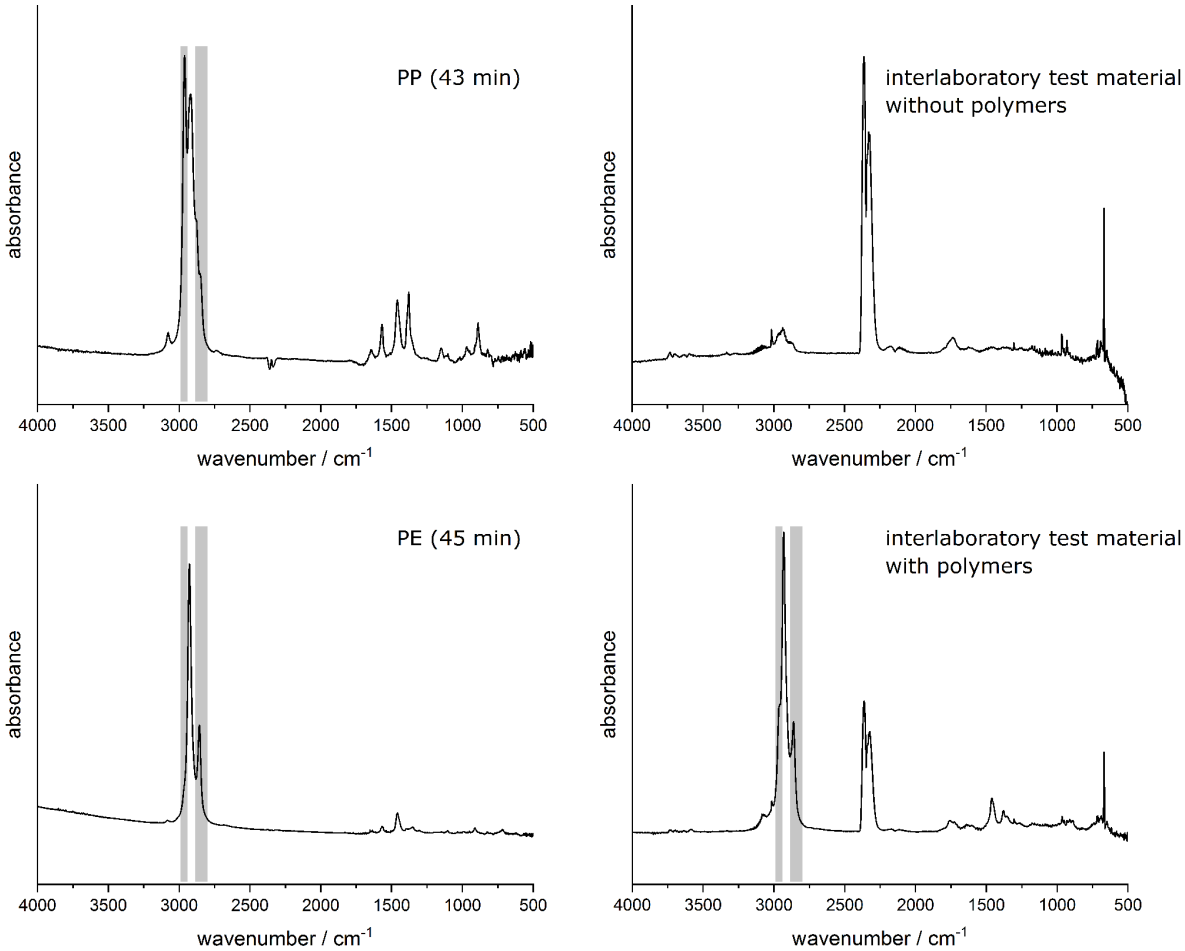

Figure 2.4: Gas phase IR spectra of the decomposition gases of polypropylene (PP), polyethylene (PE) and the interlaboratory test materials with and without polymers

of the pure polymers showed that the relative share of the band intensities differ in CH_2 and CH_3. This physical fact should be used to analyze the polymer mix in matrix to quantify both PE and PP in the samples. Unfortunately, the environmental matrix alone also shows low intensities

of CH_2 and CH_3 vibrations (wavelength range 3000–2800 cm^{-1}), which may be caused by e. g. content of humic substances.

Figure 2.5 provides examples for TGA data (2.5a) corresponding with the release rates for PE and PP (2.5c) and for PS (2.5e). For quantification, related release rates were integrated. While the results were used directly for PET and PS, further calculations are required for PE and PP since they are not distinguished by individual bands. This was done as follows.

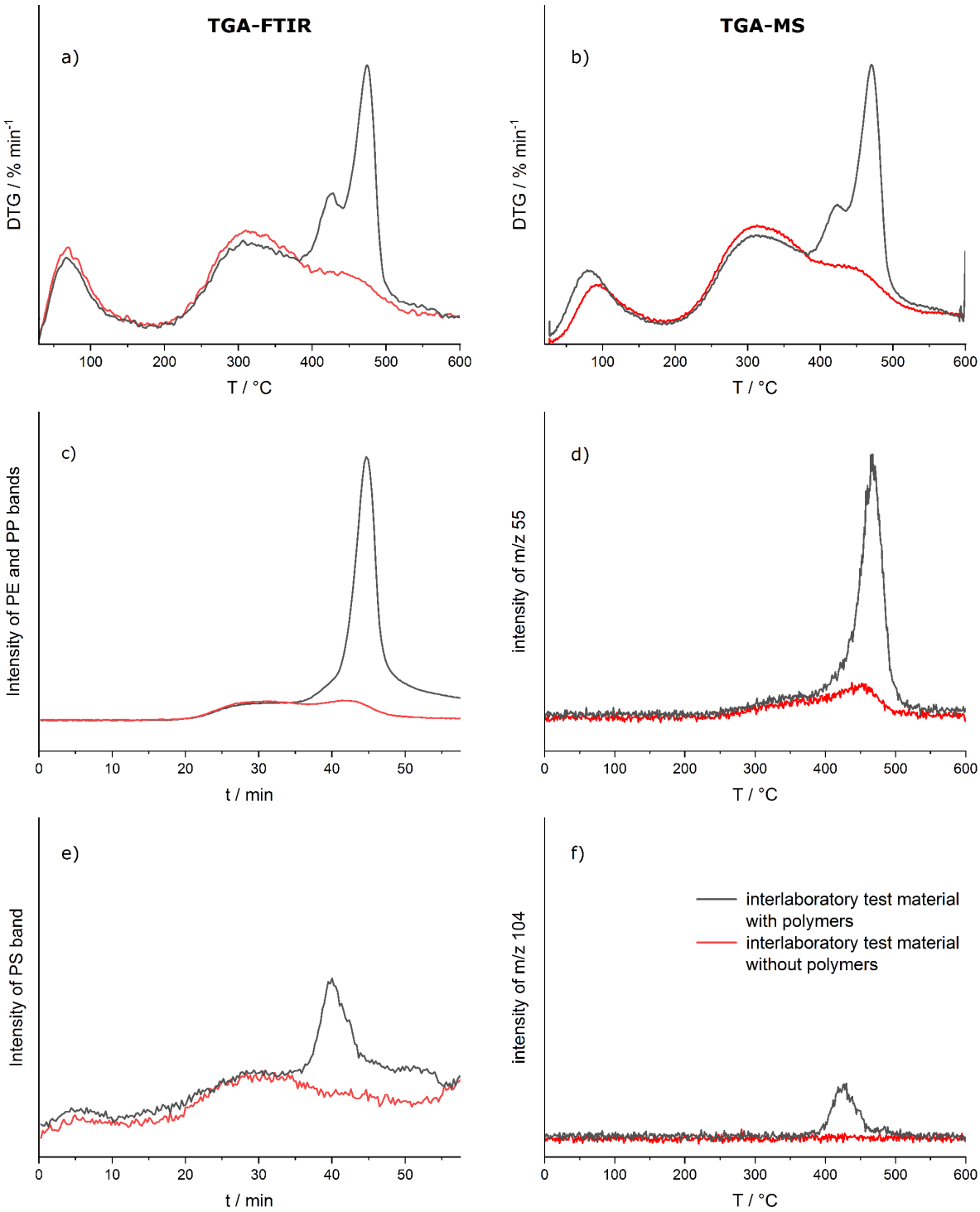

Figure 2.5: Gas phase IR spectra of the decomposition gases of polypropylene (PP), polyethylene (PE) and the interlaboratory test materials with and without polymers.

The proportion of PE or PP in the interlaboratory test material was calculated based on the ratio of the CH_3/CH_2 areas of the pure polymers. In a second step, the mass, as the sum of PE and PP (see Figure 2.5c), was determined by the external calibrations with the known ratio. Then the ratio was used to determine the masses of the individual polymers PE and PP in the sample. The results show that the sum of PE and PP was determined very well with 23.6 μg mg^{-1} (target: 25.7 μg mg^{-1}), while the proportion of the individual polymer was underestimated for PE with 14.9 μg mg^{-1} (target: 20 μg mg^{-1}) and overestimated for PP with 8.7 μg mg^{-1} (target: 5.7 μg mg^{-1}). These deviations may be due to scattering effects leading to spectroscopic base line shifts for pure PE and PP (Figure 2.4, left). However, no baseline shift was observed for the measurements of the interlaboratory test materials (Figure 2.4, right).

In sum, the TGA-FTIR measurements achieved the lowest standard deviations and show the smallest deviations from the target value after TED-GC/MS (see Figure 2.1). This simple, cost-efficient and a fully automated combination of devices is one of the routine methods in the field of polymer chemistry. The coupling between the thermobalance and the FTIR is realized via a heated transfer line with an inner diameter of 1 mm, which means that the risk of clogging and the cleaning effort are very low. The complete system can be heated out with synthetic air or even pure oxygen, and possible organic contamination will be easily oxidized.

The qualification and quantification of the polymers with TGA-FTIR may be restricted by knowledge of the pure matrix, since the selected IR bands may not allow unambiguous identification of the polymers in unknown environmental matrices.

2.3.3 TGA-MS: A possible alternative for detection of PVC

First, specific mass fragments representing the individual polymers were identified from the decomposition gases of the pure polymers. An overview of the detected mass to charge ratios is given in Table 2.4.

PS was identified and quantified in the interlaboratory test materials without further difficulties by the mass traces of the m/z ratios shown in Table 2.4. However, the measurements by TGA-MS led to an underestimation of the polystyrene. By means of TED-GC/MS and TGA-FTIR, PS values were determined that were significantly closer to the target value (see Figure 2.1 and Table 2.1).

The detected masses for PE and PP are almost identical. Only the aliphatic ratios of m/z 84 were found for PE, in contrast to m/z 72 for PP. In addition, some mass to charge ratios are more dominant for PP than for PE (m/z 55, 56, 57, 68, 69, 70, 71), while some signals (m/z 54) are almost equally intense in PE and PP.

The masses selected for PET (m/z 90, 105, 154) were not detected even in the pure polymer. This was due to the different setup of the TGA-MS coupling compared to David et al. (2018)[81]. The decomposition products are passed from the TGA to the MS through a heated transfer capillary (diameter: 150 μm). Due to the diameter of the capillary, a cut-off occurs for fragments with m/z above approx. 110. In addition, the degradation of PET results in a mixture of monomeric terephthalic acid and vinyl ester oligomers in a first stage, and the loss of low molecular weight and volatile substances in a second stage [173]. Since the sublimation point of terephthalic acid is at 402 °C, it can resublimate during the transition through the transfer capillary (T = 280 °C). The resublimation of terephthalic acid can lead to clogging of the transfer

Table 2.4: Selected m/z ratios for the detection of the polymers PE, PP and PS with TGA-MS.

Polymer	m/z	Description (possible mol peak)
PE	54	C_4H_6
	55	C_4H_7
	56	C_4H_8
	57	C_4H_9
	68	C_5H_8
	69	C_5H_9
	70	C_5H_{10}
	71	C_5H_{11}
	84	C_6H_{12} (hexene)
PP	54	C_4H_6
	55	C_4H_7
	56	C_4H_8
	57	C_4H_9
	68	C_5H_8
	69	C_5H_9
	70	C_5H_{10}
	71	C_5H_{11}
	72	C_5H_{12} (2-methyl-butane)
PS	77	C_6H_5
	78	C_6H_6 (benzene)
	92	C_7H_8
	103	C_8H_7
	104	C_8H_8 (styrene)
	118	C_9H_{10} (a-methylstyrene)

capillary. Therefore, the identification of PET is not possible with the present TGA-MS device. The effect of a blocked transfer capillary due to condensation effects or further reactions in the capillary has been discussed by Duemichen et al. (2014)[78].

Figures 2.5d and 2.5f show examples of the mass traces of m/z 55 (2.5d) and m/z 104 (2.5f) in the interlaboratory test material with and without polymers. The major part of the signal is caused by the polymers, since the traces are much more intense in the measurements with polymers. In addition, the signal reaches its maximum during the degradation temperatures of the pure polymers PE and PP, as can be seen in the DTG curve (2.5b), which already indicates relatively large amounts of these materials.

To quantify the polymers PE, PP and PS, the mass traces of the characteristic m/z ratios were integrated, and the blank values determined in the measurement of the interlaboratory test material without polymers were subtracted where necessary (see Figure 2.5). PE and PP cannot be distinguished based on the m/z ratios, since the distinguishing masses (m/z 72, 84) in the pure polymers had low intensities and were not detected in the interlaboratory test materials. Since PP and PE cannot be separated by specific m/z ratios or decomposition temperatures, quantification was achieved using the mass traces of the m/z ratios 54 and 55. m/z 54 was observed in the pure substances in both polymers in approx. equal intensities, while the release of m/z 55 was more intense in PP. The different release intensities of the mass fragments are needed to distinguish between PE and PP. Since both polymers contribute to the measured peak

areas for the release of m/z 54 ($a_{54,PE}$ and $a_{54,PP}$ as response factor or area per mass pure polymer, respectively) and m/z 55 ($a_{55,PE}$ and $a_{55,PP}$ as response factor or area per mass pure polymer, respectively), the following set of linear equations can be assumed for the resulting peak areas:

$$a_{54,sample} = a_{54,PE} \cdot m_{PE} + a_{54,PP} \cdot m_{PP} \tag{2.1}$$

$$a_{55,sample} = a_{55,PE} \cdot m_{PE} + a_{55,PP} \cdot m_{PP} \tag{2.2}$$

Unravel the equations 2.1 and 2.2 to the mass of PE (m_{PE}), then put both equations on a par and unravel to the mass of PP (m_{PP}) results in:

$$m_{PP} = \frac{a_{54,PE} \cdot a_{55,sample} - a_{55,PE} \cdot a_{54,sample}}{a_{54,PE} \cdot a_{55,PP} - a_{55,PE} \cdot a_{54,PP}} \tag{2.3}$$

To determine the mass of PE (m_{PE}), analogous to this 2.1 and 2.2 are unraveled to the mass of PP (m_{PP}) and the two formulas are equated, resulting in:

$$m_{PE} = \frac{a_{54,PP} \cdot a_{55,sample} - a_{55,PP} \cdot a_{54,sample}}{a_{54,PP} \cdot a_{55,PE} - a_{55,PP} \cdot a_{54,PE}} \tag{2.4}$$

The response factors are known from the measurements of pure PE and pure PP. Accordingly, PE and PP were distinguished and quantified in the interlaboratory test material with polymers using TGA-MS, even though the mass fragmentation patterns of the unseparated decomposition products were very similar. In addition, a 50:50 mixture of the two polymers was prepared and measured. This measurement confirmed the theoretical approach described above.

The TGA-MS measurements show the largest standard deviations in terms of PE and PP. This was because fewer measurements were analyzed, since only three of the six determinations were suitable for use. In the other three measurements, clogging of the capillary (probably related due to terephthalic acid formation, but also other molecules larger than 150 g mol^{-1}) resulted in strongly reduced MS signals of all masses. The m/z ratios for the determination of PE and PP are non-specific and may also be found in aliphatic matrix constituents like fatty acids, proteins or waxes. In addition, Figure 2.1 shows that the mass of PP determined by TGA-MS are very close to the target value, but PE and PS are clearly over- or underestimated, respectively. Even though TGA-MS is also a cost-efficient and a fully automated combination of devices, TGA-FTIR is more advantageous in practical use. In contrast to TGA-FTIR, the complete TGA-MS system cannot be heated out with air or oxygen. The MS is sensitive to oxygen; therefore, a limiting factor is the clogging of the capillary connecting the TGA to the MS.

Although TGA-MS does not appear to be a worthwhile alternative for microplastic analysis compared to TED-GC/MS and TGA-FTIR, we were able to identify a real advantage of using TGA-MS. TED-GC/MS allows the detection of PE, PP, PS and PET, but so far PVC is the only one of the mass-relevant polymers that cannot be detected. TGA-FTIR and TGA-MS should be suitable methods to detect PVC in environmental samples. PVC decomposes in two decomposition stages. According to the literature [174], hydrochloric acid and benzene are evolved as main products in the first decomposition process. In the second decomposition process mainly saturated and unsaturated aliphatic compounds are formed. Using the TED-GC/MS, hydrochloric acid is not detectable, benzene from PVC is not, without further measures, distinguishable from

benzene evolved by PET, PS or other sources and for the aliphatic compounds during the second step no specific markers were identified.

Hydrochloric acid is known to be analyzed sensitively by TGA-FTIR. However, ammonia released from environmental samples can react with hydrochloric acid to yield ammonium chloride, which may precipitate and interfering with quantification. Benzene shows a low sensitivity in infrared spectroscopy, because the only intense signal overlaps with the CO2 signal between 680 and 665 cm^{-1}. Therefore, TGA-FTIR is unsuitable for the analysis of PVC in environmental samples.

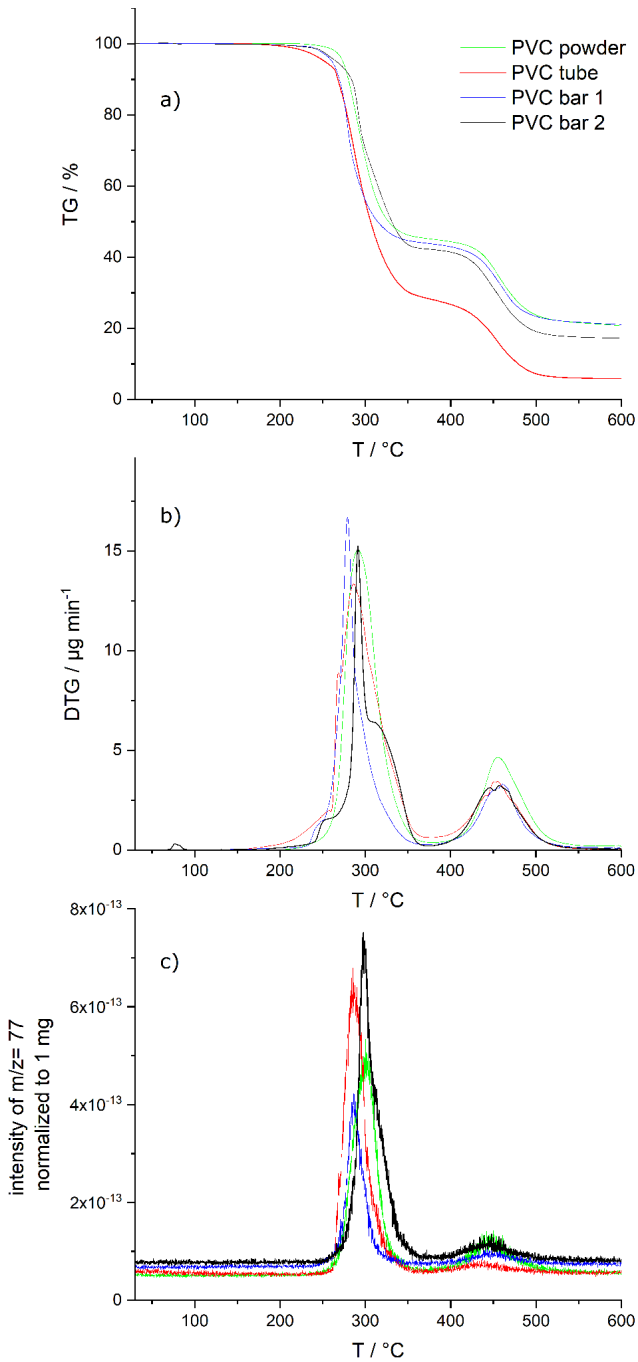

Figure 2.6: Results of the TGA-MS measurements of different PVCs; a) relative sample mass as TG curves; b) corresponding DTG curves (first deviation of TG curves), c) m/z 77 plotted over temperature.

Using TGA-MS, the decomposition product benzene can be detected with a high sensitivity. Benzene is also formed during the decomposition of PS and PET. However, it can be clearly attributed to PVC due to the decomposition temperature (400 °C for PS and 280 °C for PVC) and continuous evolved gas analysis, which is not provided by TED-GC/MS.

In order to identify specific m/z ratios by which PVC can be clearly detected, various types of PVC were measured with the TGA-MS. The TGA curves and the associated DTG profiles are shown in Figure 2.6. The TG curves show a decomposition process at approx. 280 °C and another at approx. 450 °C for all PVC samples. The three hard PVC samples showed a mass residue of approx. 21%, and the soft PVC sample (PVC tube) of approx. 6%. At the beginning of the first decomposition process of the soft PVC, an additional mass loss process occurs, which is probably attributable to plasticizers. The TG curve of the second PVC bar shows an additional decomposition process at the end of the first stage, which is probably caused by additives. No chlorinated decomposition products were detected, but m/z 77 of benzene was clearly recognized (Figure 2.6c).

A suspended matter matrix was spiked with PVC to assess the specificity of the decomposition products, determined during the measurements of the pure PVC samples. Benzene was the only degradation product that was detected. Figure 2.7 shows the intensity of benzene (m/z 77) over the temperature, normalized to the sample mass. At the first decomposition stage of the PVC, a signal with m/z 77 can clearly be seen, which also has a higher intensity when the amount of PVC is increased.

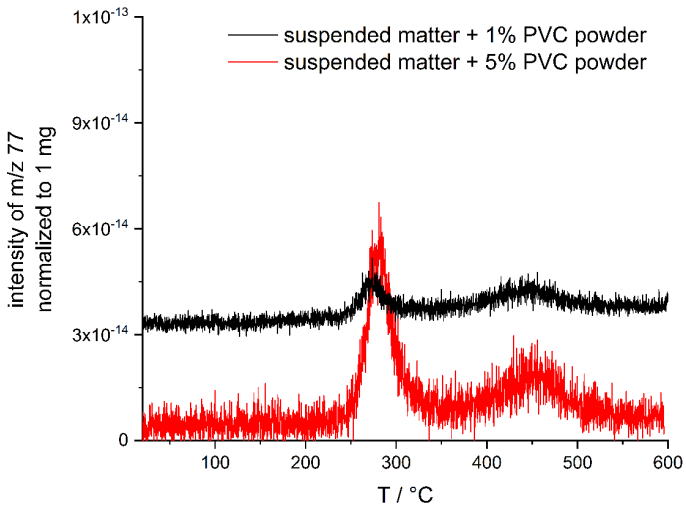

Figure 2.7: Results of the TGA-MS measurements of suspended matter spiked with 1% and 5% of PVC, respectively; m/z 77 is plotted over temperature.

Subsequently, a couple of matrices (suspended matter, sediments, plant material, soil, different kind of fish, honey) were screened with the TGA-MS to rule out that benzene was produced during the pyrolysis of natural substances. None of these matrices showed any release of benzene that might interfere with the detection of PVC.

Although TGA-MS showed the poorest performance in the interlaboratory comparison test compared to TED-GC/MS and TGA-FTIR, the identification of benzene as decomposition product marker for PVC is promising for the use of TGA-MS.

2.3.4 MCC: A possible alternative thermoanalytical screening tool?

In the interlaboratory comparison test by Becker et al. (2020)[157], further, less known methods where used. One of them was MCC. While evolved gas analysis with MS and FTIR uses structure related information on the polymeric decomposition products, MCC can use another polymer specific property: the formation of pyrolysis products with a very high effective heat of combustion.

This method determines the heat release rate (HRR) and total heat release (THR) per sample mass of a milligram sample based on the oxygen consumption method. A milligram sample is pyrolyzed in inert atmosphere flow under constant heating rates of typically $1\,\mathrm{K\,s^{-1}}$. Thus, the method corresponds closely with TGA measurements at high heating rates and can be classified as a thermoanalytical method. The formed decomposition gases are oxidized in a locally separated oven at 900 °C that adds an oxygen flow. The oxygen consumption is used to calculate the heat release rate versus the pyrolysis temperature. For hydrocarbon polymers like PE, PP, and PS, THR values of 38.8–41.6 $\mathrm{kJ\,g^{-1}}$ can be observed, whereas the value of PET is distinctly lower (15.3 $\mathrm{kJ\,g^{-1}}$) [166]. As the THR of environmental matrices is typically below $1\,\mathrm{kJ\,g^{-1}}$, and the heat release is rather evenly spread over the entire temperature range, the polymer content in the sample can be estimated in the temperature range of polymer decomposition. Here we used an estimated value of $40\,\mathrm{kJ\,g^{-1}}$ to evaluate the polymer combustion of polymers, consisting of mainly polyolefins and $31.13\,\mathrm{kJ\,g^{-1}}$, as the target mixture of PE, PP, PS and PET was known.

Because of the limited sample mass load of 5 mg in the current equipment, the measurements were repeated 5 times for the matrix and 10 times for the interlaboratory test material with polymers (Figure 2.8). The HRR curve of the environmental matrix is characterized by the expected very low HRR spread in broad humps over the whole temperature range of the measurement. Only a minor fraction of the mass is released; the effective heat of combustion of the volatiles is low. The HRR was always in the same order of magnitude as the background that is usually subtracted in the standard evaluation. All HRR curves of the interlaboratory test material with polymers show a clear peak around 475 °C with variations in the formation of a main HRR peak at 450 and 525 °C, with a distinctive shoulder between 400 and 450 °C. Related to the analysis sample, this indicates a clear inhomogeneity of the added polymers in the samples. However, the shoulder is assumed to relate to the PS and PET content in the sample, and the main peak to PE and PP. To integrate the HRR of the polymers, a line shift of about $5\,\mathrm{W\,g^{-1}}$ was done and a zero line correction performed (point 1: 150 °C and point 2: 800 °C). The integration of the peak, assuming an effective heat of combustion of $40\,\mathrm{kJ\,g^{-1}}$ and subtracting the matrix by a straight line between 370 and 550 °C before integration, yielded $35.0 \pm 7.6\,\mu\mathrm{g\,mg^{-1}}$; subtracting the matrix and additionally using the averaged heat of combustion for the target mixture yielded 45.0 ± 9.8 μg mg-1. The target value of all polymers in the interlaboratory test material is $45.9\,\mu\mathrm{g\,mg^{-1}}$, hence the result of MCC investigation is promising.

Because a single analysis takes only 10–20 min and the evaluation of data is very simple, applying MCC is promising for a fast screening method to detect the fulfillment of a critical limit value. However, the commercial MCCs available were obviously not designed to determine the content of polymer in a matrix. The current setup of MCC defines the limits for determining polymer content. Simultaneous determination of the mass loss rate would enable the data to be evaluated based on the real effective heats of combustion of different plastics instead of an estimated averaged value, increasing accuracy and selectivity. Reducing the heat release rate and

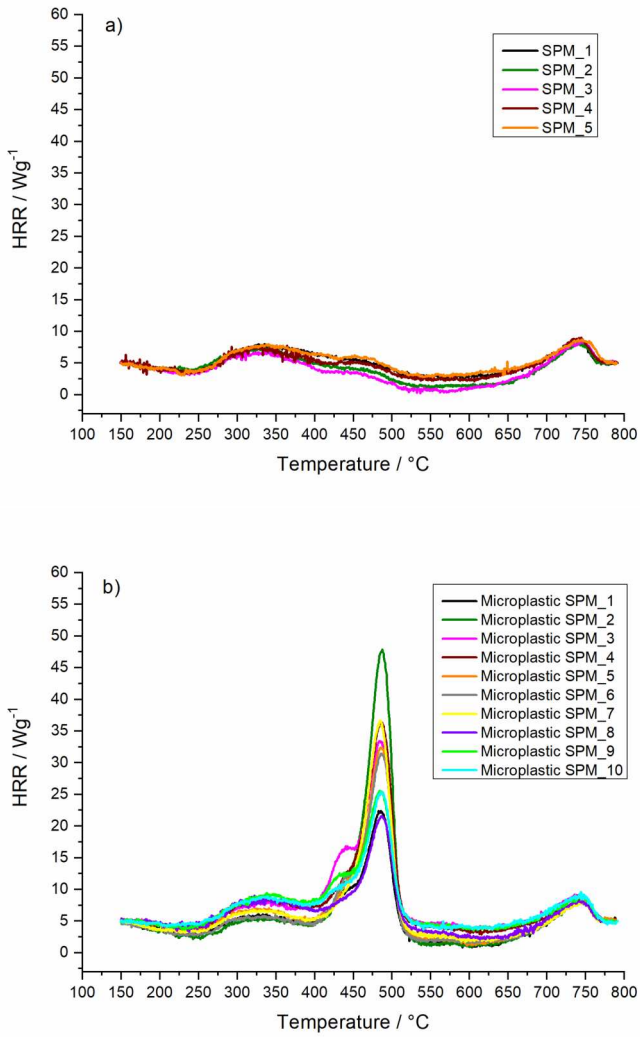

Figure 2.8: MCC results, heat release versus temperature, of a) the suspended matter matrix (SPM) and b) the suspended matter spiked with PE/PP/PS/PET mixture (Microplastic SPM) .

increasing the mass of the investigated specimen would deliver more representative results, and also reduce the number of measurements needed.

2.4 Conclusion

For the first time, the three thermoanalytical methods TED-GC/MS, TGA-MS and TGA-FTIR were systematically investigated and discussed for their ability to detect microplastic in environmental samples. A new method, MCC, was also applied. For the comparison of the methods, an interlaboratory test material was used without and with defined, added polymer masses of PE, PP, PS and PET. All polymers were used in unaged form; however, due to the detection of the bulk property of polymers in those thermoanalytical methods, the partial aging of the polymers, which is observed in real samples, will not affect the results significantly [75].

A summary is given about the advantages and limitation of the different tools in Table 2.5.

The TED-GC/MS is the only method that allows the unambiguous identification of specific decomposition products for the tested polymers PE, PP, PS and PET. In general TED-GC/MS

Table 2.5: Overview of the advantages and limitation of the different methods.

	Advantages	Limitation	Suitable method for ...
TED-GC/MS	• Almost matrix independent • Clear differentiation between various polymers	• Complex method — high user knowledge needed • Detection of PVC currently not possible	... unknown matrix samples with unknown variable kinds of microplastic and content
TGA-FTIR	• Less technically complex method • Easy to clean against organic contamination	• Matrix contribution to the signal needed (background value) • Differentiation between PE and PP only by calculation	... known matrix samples with defined kinds of microplastic
TGA-MS	• Less technically complex method • Detection of PVC is possible	• Matrix contribution to the signal needed (background value) • Differentiation between PE and PP only by calculation • No detection of marker compounds with molecular mass >150 g mol^{-1} (PET)	... detection of PVC
MCC	• Very fast measurement	• Matrix contribution to the signal needed (background value) • No differentiation between different polymers: only PE, PP, PS contribute significantly to the signal • Limited to only 5 mg of sample mass	... very fast and simple screening campaigns for the identification of a potential microplastic load of standard polymers in unknown samples

is independent of the matrix composition and can determine microplastic load without knowledge of the matrix composition. However, it is a complex trace analysis that requires extensive user knowledge, and it is sensitive to contamination, for example, when the sample contains large amounts of plastic contents. In addition, the analysis of PVC is not possible with this method, because for this polymer no specific markers are yet known. But in the framework of the comparison of methods in the present work, TED-GC/MS is the only solution for samples with unknown matrix and unknown, variable kinds and amounts of microplastic content.

TGA-FTIR and TGA-MS are technically simpler, since a transfer line or capillary, respectively, links the TGA directly with the evolved gas analysis. However, the unambiguous evaluation of the occurring vibration bands or m/z ratios is not possible if the matrix composition of the sample is not known. Here the matrix's contribution to the signals must always be considered or known. In practice this means that a background value is needed. Both TGA-FTIR and TGA-MS allow differentiation between PE and PP by using a model calculation. TGA-MS does not allow the analysis of PET, because no specific marker can pass the capillary due to its high molecular weight. In addition, the deviations from the target value for the quantification of PS were also greater for TGA-MS than for TGA-FTIR. A major advantage of TGA-FTIR is that it can be cleaned simply by running heat through it when organic residues contaminate the device. Based on the investigations carried out in this paper, TGA-FTIR would be preferable for analysis of

microplastic as a simpler technique for screening samples with well-known or constant matrix composition. Hence, TGA-FTIR is suitable for samples with known matrix composition and with defined kinds of microplastic.

But TGA-MS showed a high potential to detect PVC. Benzene evolved at 280 °C was therefore used as a marker molecule with m/z 77. TED-GC/MS and TGA-FTIR do not have this potential.

MCC, as it is established in the ASTM standard [168], does not effectively differentiate between the different polymers. Sensitivity increases by up to a factor of 10 with decreasing char yield and increasing effective heat of combustion. Nevertheless, the principle of the method is very promising as a fast screening method to detect the main standard polymers like PE, PP, PS that are found in the environment, and it shows clear development potential. Hence, MCC as a fast analysis tool is suitable for the first identification of a potential microplastic load of standard polymers in unknown samples.

Data Statement

The generated data are available on request from the corresponding author.

Acknowledgements

The authors thank Roland Becker and Korinna Altmann from BAM for providing the test samples. Authors are indebted to Environmental Specimen Bank of the German Environment Agency (UBA) for the providing the suspended organic matter.

Author Contributions

CG, DD, PE and UB planned the study and designed the experiments. CG and DD carried out the TGA-FTIR and TGA-MS experiments and interpreted the results. PE performed and interpreted the TED-GC/MS measurements. BS and PK carried out and interpreted the MCC measurements. YW was significantly involved in evaluating the TGA-MS data. CG and DD wrote the initial draft. All authors contributed to the final manuscript.

3

Characterization of activated carbon products for water treatment including extended analysis of oxygen-containing functional groups

Daniel Dittmann, Leon Saal, Frederik Zietzschmann, Maike Mai, Korinna Altmann, Dominik Al-Sabbagh, Pia Schumann, Aki Sebastian Ruhl, Martin Jekel, and Ulrike Braun

This chapter was submitted to *Water Research X*.

Abstract

Water treatment with activated carbon (AC) is an established method for the removal of organic micropollutants and natural organic matter. However, it is not yet possible to predict the removal of individual pollutants. An appropriate material characterization, matching adsorption processes in water, might be the missing piece in the puzzle. To this end, this study examined 25 different commercially available ACs to evaluate their material properties. Frequently reported analyses, including N_2 adsorption/desorption, CHNS(O), point of zero charge (PZC) analysis, and X-ray photoelectron spectroscopy (XPS) were conducted on a selected subset of powdered ACs. Inorganic elements examined using X-ray fluorescence (XRF) and X-ray diffraction spectroscopy (XRD) revealed that relative elemental contents were distinctive to the individual AC's raw material and activation procedure. This study also is the first to use thermogravimetric analysis (TGA) coupled to Fourier-transform infrared spectroscopy (FTIR) to conduct quantitative analyses of functional surface oxygen groups (SOGs: carboxylic acid, anhydride, lactone, phenol, carbonyl, and pyrone groups) on such a large number of ACs. We found that SOG contents covered a wide individual range and depended on the raw material of the AC. Surface chemistry might therefore provide an indication of the suitability of a particular AC for a variety of target substances in different target waters. Furthermore, the comparably economical TGA provides a surrogate for

the PZC, the oxygen and carbon content, as well as mass loss profiles that depict the AC's chemistry. TGA may therefore be able to help practitioners to control AC use in waterworks or wastewater treatment plants.

3.1 Introduction

Adsorption onto activated carbon (AC) is a widespread process for the remediation of contaminated groundwater and soil, or for flue gas treatment [175, 144]. Waterworks and municipal wastewater plants facilities apply ACs to cope with increasing concentrations of organic micropollutants (OMPs) in water cycles [88, 99, 110]. However, removal efficiencies in water are still not predictable today because of the large number of relatively complex interactions between the adsorbent, OMPs, and the water matrix [131, 132, 114]. In addition, the highly inconsistent material properties of ACs — even among batches of a product — play a fundamental role in process variabilities and OMP removals. Hence, ACs are not constantly homogeneous treatment substances, and thus their characteristics have to be controlled.

One key property for overall adsorption capacity of AC is a well-developed pore network (porosity) and hence a large internal surface area. These physical properties arise from AC production processes, specifically carbonization and activation at elevated temperatures of up to 1000 °C [122]. Carbon materials that withstand these temperatures and concurrently develop porosity can become activated carbon classified by isotropic (i.e. not oriented) and non-crystalline structures [128]. These carbon materials are called non-graphitizing carbons, since their elemental composition (characterized by high carbon and low hydrogen content or high carbon and high oxygen content) prevents them from becoming crystalline graphite. Many organic raw materials (fossil/regenerative) fulfill these requirements as AC precursors [176, 83]. As a result, the raw materials (e. g. coal, plants, crops, sewage sludge) used in thermal or chemical production procedures have become increasingly diverse, with a variety of process parameters [177, 109, 178, 179].

Due to these variations, typical characterizations of ACs solely according to a few selected physical properties (e. g. internal surface area or porosity) fall short of the mark, since the chemical properties of ACs also contribute to adsorption [180, 181, 132, 182]. Despite valuable characterizations of individual ACs employing various sophisticated analytical methods [128, 183, 184, 185, 186], plant operators lack an applicable integration of such analytical information. To facilitate the prediction of a given AC's performance, the overall goal of this study is to provide alternative, affordable, fast, and thus practically useful insights into the relevant material properties of commercially available ACs.

Thermogravimetric analysis (TGA) is a comparably inexpensive, quick, and robust method that provides a couple of parameters simultaneously and can be deployed on site for AC quality control. TGA is already being applied at mining sites to characterize seam and coal quality as so-called proximate analysis [187]. The proximate parameters moisture, volatile matter, fixed carbon and ash may imply different and more specific characteristics for ACs. In addition, TGA can be used to quantify powdered AC (PAC) in suspension or sludge [10].

This paper focuses attention on the surface chemistry of ACs, and especially their oxygen-containing functional groups (surface oxygen groups, SOGs), which affect the adsorption of organic

molecules in water [188, 189]. It has been reported that phenol groups of AC can chemically react with amide moieties of OMP molecules [181], and that carbonyl groups influence the adsorption of estradiol [190]. However, the quantification of SOGs is rarely applied to commercially available ACs. To fill this gap, we adapted the temperature-programmed decomposition (TPD) methodology [145] using TGA coupled to Fourier-transform infrared spectroscopy (TGA-FTIR) [191]. Not only can the thermal decomposition of a sample provide bulk information, but in the case of activated carbon TGA-FTIR can also be used to draw conclusions about the surface chemistry. This study therefore used various analytical methods to examine and compare 25 different AC products. For a subset of PACs made from different raw materials and production methods, we employed four common methods of analysis —- N_2 adsorption/desorption, CHNS analysis, point of zero charge (PZC) analysis, and X-ray photoelectron spectroscopy (XPS) In addition, less commonly utilized methods of analysis, such as particle-size determination and X-ray diffraction spectroscopy (XRD), were conducted. All ACs were characterized according to their inorganic elemental composition using X-ray fluorescence spectroscopy (XRF).

This study aims to (i) examine the results of frequently applied analyses concerning physical and chemical material properties of eight PACs and compare them; (ii) investigate organic and inorganic elemental compositions and crystalline phases; (iii) assess TGA for its informational value for ACs and surrogate potential with interrelating parameters; and (iv) quantify and systemize SOGs on ACs depending on their raw materials. Finally, this work is intended to fill in one piece of the puzzle of OMP removal using AC.

3.2 Materials and methods

Specific handling of the samples is provided in the Supplementary Information (SI) in the Appendix A, including particle-size determination and discussions on the applicability of certain parameters.

3.2.1 Activated carbons

Table 3.1 lists the eight PACs that underwent all analytical methods conducted. A list of all 25 AC products with batch numbers and milled specimen analyzed using XRF and TGA-FTIR is provided in Table A1 (SI, Appendix A).

Table 3.1: Powdered activated carbons that were extensively investigated and the abbreviations used in the following text and figures. 5000 P-f was not analyzed using XPS and XRD due to the limited sample mass.

Name	Manufacturer	Raw material	Activation	Abbreviation
HK 950	Carbon Service & Consulting	Wood charcoal	Phosphoric acid	HK
HKP 1050	Carbon Service & Consulting	Wood charcoal	Phosphoric acid	HKP
CCP 90D	Donau Carbon	Coconut shell	Steam	CCP
SAE Super	Cabot (Norit)	Mixture, Lot 3868836	Unknown	SAE
5000 P-f	Jacobi Carbons	Lignite	Unknown	P-f
AZ 1050	Carbon Service & Consulting	Bituminous coal	Unknown	AZ
PS-WP 235	Chemviron	Bituminous coal	Unknown	PS
CC 401	Chemviron	Hard coal (reactivate)	Unknown	CC

3.2.2 Physical characterization

3.2.2.1 Surface area and porosity analyses

N_2 gas adsorption and desorption at 77 K was carried out with an Autosorb-1-MP (Quantachrome Instruments, USA) in duplicate using sample weights of 20 to 50 mg. Prior to the measurements, the samples were out-gassed at 378 K under a vacuum of 1 Pa until the pressure rise was below 1.33 Pa min^{-1}. Fifty acquisition points in a relative pressure range of 0.010 to 0.995 were recorded. We used software versions of Autosorb for Windows 1.25 and AS1Win 2.11 to analyze the isotherm data and to extract information about porosity, surface area, and area of micropore surface and external surface. Detailed information is provided in SI (Appendix A).

3.2.3 Chemical characterization

3.2.3.1 Carbon, hydrogen, nitrogen, and sulfur (CHNS) analyses

CHNS analysis was conducted using a Thermo FlashEA 1112 Organic Elemental Analyzer with data evaluated using Eager 300 software (Thermo Scientific, USA). We placed defined amounts of 1 mg PAC into a silver capsule that was automatically deployed in a combustion chamber (990 °C) under an excess oxygen atmosphere, with subsequent catalysis of the evolved gases by tungsten trioxide, and nitrous oxide reduction using copper granules. This resulted in the final analyte gases CO_2, H_2O, N_2, SO_2, detected by zone chromatography with a heat conductivity detector, and a built-in flame photometric detector for SO_2.

It is possible to estimate the oxygen mass content (w_O) of a sample by the difference-to-100% method calculating the difference of the sum of the mass contents of C, H, N, and S, and the ash content on the one hand and the total mass on the other ($w_O = 100\% - w_{CHNS} - w_{Ash}$).

3.2.3.2 pH at the point of zero charge (PZC)

The PZC was determined using a pH drift method [192], in line with recent literature [193, 114]. In short, 50 mg of each PAC was placed in flasks containing 150 mL of a 0.01 M NaCl solution, with pH adjusted prior to use (3, 4, . . . , 11). After 23 h equilibrium time, the resulting pH values were measured and plotted against the initial pH values. The PZC was determined by interpolating between the two adjacent data points whose linear connection intersected with the bisector. Extrapolation was used for SAE whose PZC exceeded 11, since pH = 11 was the highest initial pH applied.

3.2.3.3 X-ray photoelectron spectroscopy (XPS)

X-ray photoelectron spectroscopy (XPS) was performed using a SAGE 100 device (Specs, Germany). Aluminum Kα radiation (1486.6 eV) was used to excite the photoelectrons at 20 mA and 10 kV under an ultra-high vacuum ($< 3{\cdot}10^{-7}$ mbar). The angle between the anode and the analyzer was 54.9°; the analyzer was adjusted to 18° to the surface normal. The area of the sample that was analyzed measured 3x1 mm. The measurements were performed in constant analyzer energy (CAE) mode with pass energy of 20 mA. The samples were analyzed in small aluminum cups 10 mm in diameter. At least two replicates were measured before calculating

mean values for the element contents. The spectra were analyzed using Specslab and fitted using CasaXPS. The C–C bond was used for standardization with a binding energy of 285 eV. Peak fitting was performed for C–O, C=O, O–C=O, and carbonate in accordance with Desimoni et al. (1990)[194] and Durán-Valle (2012)[183]. Additional information can be found in SI (Appendix A).

3.2.3.4 X-ray fluorescence spectroscopy (XRF)

Energy-dispersive X-ray fluorescence spectroscopy (XRF) was performed on a Spectro XEPOS III using X-LabPro 5.1/TurboQuant software (Spectro Analytical Instruments, Germany) on sample masses of at least 1 g. The XRF cell (inner diameter: 24 mm) was covered with a 4 μm Mylar film. The TurboQuant method applies the fundamental parameters method for the semi-quantitative analysis of elements ranging from aluminum to uranium. Additional details about the method is provided in SI (Appendix A); further information about the equipment can be found in Dittmann et al. (2020)[195].

3.2.3.5 X-ray diffraction (XRD)

XRD analysis was performed using a D8 ADVANCE (Bruker AXS, Germany) using Cu-Kα radiation with a LYNXEYE XE-T detector. Diffraction was recorded at 40 kV and 40 mA in a range of $5.0° \leq 2\theta \leq 80°$. The data were obtained using Bragg-Brentano geometry with a step size of 0.02° and an acquisition time of 0.5 s per step. We analyzed diffractograms using the DIFFRAC.EVA software (V5.2, Bruker AXS, Germany) and the ICDD database PDF-2 (release 2016 RDB) to identify crystalline structures above 1 μm in size.

3.2.3.6 Thermogravimetric analysis (TGA)

For temperature-controlled decomposition of the samples, a thermobalance TGA/DSC 3+ from Mettler Toledo (USA) with a purge gas flow of 50 mL min^{-1} was used (see SI in Appendix A for details). The continuous TGA data obtained as mass loss or TG curve were further differentiated according to measurement time, which yielded mass loss rates or a DTG curve. Specific mass losses were normalized to dry sample mass (145 °C) and consist of pyrolytic mass loss up to 600 °C (ML_{600}) and up to 1000 °C (ML_{1000}) in a nitrogen atmosphere and of subsequent mass loss by oxidation ($ML_{ox.}$) in synthetic air. The mass residue after oxidation is the ash content of the sample.

3.2.3.7 Thermogravimetry coupled to Fourier-transform infrared spectroscopy (TGA-FTIR)

To determine the so-called surface oxygen groups (SOGs) and the oxygen content of the samples, we coupled the TGA to a Fourier-transform infrared spectrometer to conduct continuous evolved gas analysis. We used a Nicolet iS50 with a DTGS detector as well as a TG-IR module consisting of a heated transfer line (250 °C) and IR cell (260 °C) from Thermo Fisher Scientific (USA). TGA-FTIR measurements were conducted in triplicate in a nitrogen atmosphere up to 1000 °C. FTIR spectra were analyzed for H_2O, CO_2, CO, and CH_4 to derive gas-specific release rates

(OMNIC 9.7.39 software). H_2O, CO_2, and CO were quantified using previous calibration with calcium oxalate monohydrate (purity 99.9985%, Alfan Aesar, USA).

According to temperature-programmed decomposition (TPD) methodology, individual SOGs in carbon materials decompose to H_2O, CO_2, or CO in certain temperature ranges [145]. These ranges overlap, but can be distinguished by deconvolution by fitting Gaussian curves. After reviewing the literature and analyzing the ACs, we adapted a TPD method for the TGA-FTIR setup. A Python package for the quantification of SOGs by TGA-FTIR has been developed that includes a robustness test of the fitting [191]. Variation of the initial parameters to certain extents provides mean values with standard deviations as uncertainty. See SI (Appendix A) for details.

3.2.4 Principal component analysis

Principal component analysis (PCA) was applied to the XRF and TGA-FTIR (SOGs) results, using a Python script with the PCA class and normalize function from the scikit-learn package (v. 0.23.2) [196].

3.3 Results and discussion

3.3.1 Characterization of (surface) morphology

The internal morphology of AC adsorbents is usually determined by pore volume, BET-surface (specific surface area, SSA), and pore size distribution (PSD). These parameters are derived from gas adsorption/desorption isotherms typically determined using N_2 at the boiling point. However, since the informational value of this basic data may be overlooked, Figure 3.1 illustrates the isotherm shapes for the PACs HK, CCP, and P-f as examples.

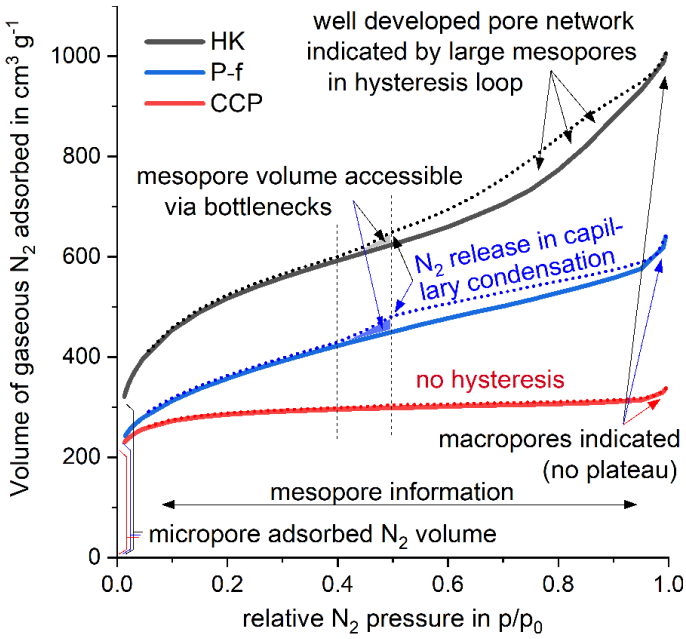

Figure 3.1: N_2 adsorption (solid lines) and desorption (dotted lines) isotherms shown for three of the eight PACs. Isotherms for all PACs are provided in Figures B1 and B2 (SI, Appendix B).

At low p/p_0 (pressure relative to the atmosphere), nitrogen commences condensation in micropores (< 2 nm). The first acquisition points in equilibrium are therefore far above the coordinate origin, since ACs exhibit remarkable micropore-sized pore volumes. However, the following acquisition points imply characteristic information about the mesopore network that may be not present at all (CCP) or very well developed (HK). Macropores (> 50 nm) cannot be examined, but they are indicated by the increasing slope close to a p/p_0 of 1. The isotherms obtained during desorption may show a hysteresis loop to the adsorption isotherm (HK and P-f) if multiple pore sizes in the pore network retain condensed nitrogen. Large mesopores in the HK are not completely filled by condensed N_2, and therefore they intensify hysteresis at high p/p_0 ratios [197]. Hysteresis ends in general at a p/p_0 of 0.4, releasing N_2 from mesopores blocked by capillary condensation in smaller pores as bottlenecks. This effect is more pronounced the more evenly distributed the mesopores are (P-f). The PACs under examination are mesoporous carbons with several pore sizes and with a remarkable share of micropores, except for CCP, which is a microporous carbon with narrow mesopores. Further classification informed by the IUPAC technical report by Thommes et al. (2015)[198] can be found in the SI (Appendix B).

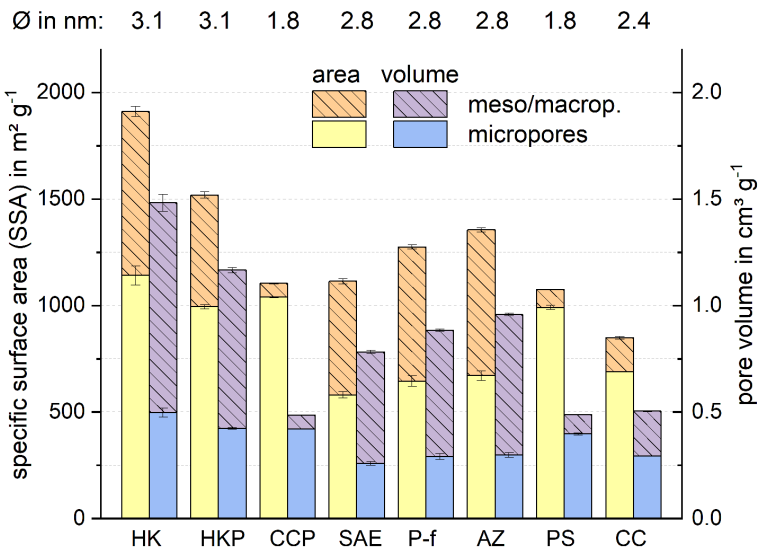

Figure 3.2: Specific surface area (SSA) and total pore volume of the eight PACs with respective shares of mesopores, macropores, and micropores, with average pore diameters (4 V/A) on top.

Quantitative values for total pore volume and SSA with respective shares of micropores, mesopores, and macropores for the eight PACs are shown in Figure 3.2. The specific micropore surface area does not correlate with the overall SSA (cf. HKP and CCP), and the variations in SSA and total pore volume are less pronounced with respect to micropores. In accordance with the N_2 adsorption/desorption isotherms (Figure 3.1), more differences can be seen in the proportions of the mesopores. These absolute distinctions are not reflected in the average pore diameter (Figure 3.2, top), because this is calculated by the ratio of total pore volume to SSA and multiplying by a factor of 4. The parameter called "hydraulic" or "4 V/A" average pore diameter therefore assumes a cylindrical pore geometry, and does not represent a feature of the PSD, but rather is related to the share of micropores. Since the pore network of an AC is more complex, this parameter should be used carefully. A comment on ACs and PSDs based on density function theories is given in SI (Appendix B).

In conclusion, N_2 adsorption/desorption isotherms are well suited for the qualitative comparison of AC products regarding their (meso-)pore network, which is crucial with respect to the adsorption of large molecules from dissolved organic matter and to adsorption kinetics. SSA and total pore volume with respective micropore and mesopore proportions provide valuable quantitative information on an AC product's porosity and its potential adsorption capacity for adsorptive molecules. However, these physical morphology characteristics are not sufficient for estimating the adsorption of specific molecules, apart from their steric access to the pores [180, 181, 132]; nor for obtaining information about the raw material of the AC product at hand. The chemical composition may reveal more insights, such as carbon content for dispersive interaction, oxygen content for hydrogen bonding, or even inorganic elements for ion binding.

3.3.2 Analysis of chemical composition

Common tools for the quantification of elements that comprise the carbon structure include CHNS analysis by thermal oxidation of the sample, as well as XPS or ash determination to estimate the oxygen content. The mass content of carbon in the eight PACs ranges between 75% and 92%, as listed in Table 3.2. The hydrogen contents of approx. 2% in the chemically activated PACs (HK and HKP) is a magnitude above that of the others. Nitrogen and sulfur, with a maximum content of 0.22% and 0.35% (CC), respectively, were not detected in all samples.

Table 3.2: Elemental composition of carbon, hydrogen, nitrogen, sulfur, and oxygen and the point of zero charge (PZC) for the eight PACs.

	Analysis	unit	**HK**	**HKP**	**CCP**	**SAE**	**P-f**	**AZ**	**PS**	**CC**
C	CHNS	wt.%	80.5 ± 0.8	75.0 ± 0.0	90.3 ± 2.4	79.0 ± 0.6	79.5 ± 1.3	84.7 ± 0.8	92.2 ± 1.2	83.4 ± 1.9
C	XPS	wt.%	81.4	73.5	76.3	72.7	n.d.	78.5	89.1	89.0
H	CHNS	wt.%	2.16 ± 0.20	2.06 ± 0.30	0.28 ± 0.15	0.14 ± 0.09	0.17 ± 0.10	0.35 ± 0.29	0.45 ± 0.07	0.21 ± 0.11
N	CHNS	wt.%	0.08 ± 0.01	0.22 ± 0.01	-	-	0.04 ± 0.01	0.04 ± 0.01	0.10 ± 0.02	0.22 ± 0.02
S	CHNS	wt.%	-	-	-	0.16 ± 0.06	-	0.11 ± 0.03	-	0.35 ± 0.04
O	$100\% - w_{CHNS} - w_{Ash}$	wt.%	13.6	16.1	5.3	4.6	7.4	6.7	3.7	3.0
O	XPS	wt.%	14.2	19.3	11.3	12.7	n.d.	9.7	10.9	11.0
PZC	pH drift	pH	3.3	2.8	9.1	11.4	7.3	8.4	9.5	9.7

The oxygen content significantly differs when calculated using the difference-to-100% method or X-ray photoelectron spectroscopy (XPS), as the oxygen content is not covered by the CHNS analysis (Table 3.2). Furthermore, XPS has frequently been used to determine surface oxygen groups (SOGs), since it can distinguish C–O, C=O, and O–C=O bonds. With regard to the high surface sensitivity of XPS (outer particle surface) and the enhanced oxidation found, XPS results are probably not representative of the total SOGs (see SI in Appendix B for details).

The point of zero charge (PZC) is an important parameter for the adsorption of ionic or ionizable molecules [131]. Table 3.2 shows that it ranges from a very low pH 2.8 for the chemically activated PACs to neutral and alkaline pH values. Delocalized π-electrons of basal planes of the ACs' carbon structures accept H^+ somewhat, and therefore provide large non-heteroatomic Lewis base sites [199]. As the oxygen content increases (or SOGs), the PZC decreases due to acidic functional groups as well as due to inductive and mesomeric effects that reduce the π-electron density [200]. However, the oxygen content obtained in this study did not correlate with the PZC.

The inorganic elemental composition is primarily composed of Al, Si, P, S, K, Ca, and Fe, whose relative proportions are not related to the ash content (Figure 3.3). Sodium and magnesium cannot be detected by X-ray fluorescence spectroscopy (XRF). The mass of residual ash is probably determined by burn-off mass losses during production and, to a lesser extent, by the ash content of the raw material.

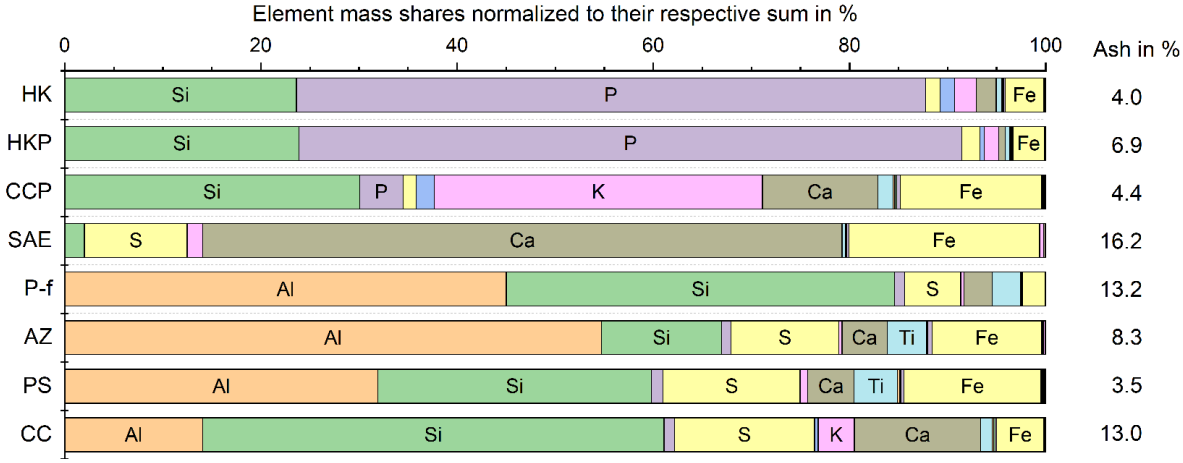

Figure 3.3: Elemental composition of the eight PACs relative to total (inorganic) elements obtained by X-ray fluorescence spectroscopy (XRF). Elements with a relative proportion of more than 3% are annotated. Ash content of the PACs is listed on the right to support quantitative estimations, since these elements (including sulfur to a certain extent) remain in the ash residue.

Similarity in the relative elemental composition was observed for both wood charcoals HK and HKP with a comparably high phosphorous content, which is typical for ACs that have been chemically activated with phosphoric acid [201]. Potassium is distinctive in the coconut shell-based CCP, and probably stems from the characteristic potash residue in thermally treated plant-based materials. The SAE contained large amounts of calcium present as calcite ($Ca(CO)_3$) and lime (CaO), which might contribute to the high PZC of this PAC. Transmission electron microscopy images of an Aquasorb 5000 GAC shown in the SI (Figures B14 and B15 in Appendix B) confirmed mineral impurities also in the nanoscale. Silicon dioxide was identified in all PACs, except for CCP and SAE, by X-ray diffraction (XRD, diffractograms are provided in the SI, Figures B7-B13 in Appendix B). Reflexes of graphite were observed in the PACs made of bituminous or hard coal. Advanced coalification of these raw materials might explain the existence of comparably large graphite crystals. However, graphite microcrystals are expected in each AC because ACs consist of disordered but highly condensed carbon molecules such as graphene sheets and graphite (cf. SI, Figures B16 and B17 in Appendix B). Large crystalline phases are detrimental to adsorption capacity, since these structures do not contribute to porosity, but to weight. However, adsorption mechanisms are probably not significantly influenced by crystalline phases.

We conducted principal component analysis (PCA) to evaluate the inorganic elemental composition (that had been determined using XRF) of 35 samples. PCA reduces the number of dimensions or elements, respectively, by aggregating them into principal components (PCs) according to their largest variances, thus emphasizing differences in the compositions. The results shown in Figure 3.4 clearly indicate several clusters of similar inorganic elemental compositions. The two clusters on the left-hand side mainly include ACs made of hard coal, lignite, or bituminous coal. These clusters separate due to the large aluminum content in the lignite

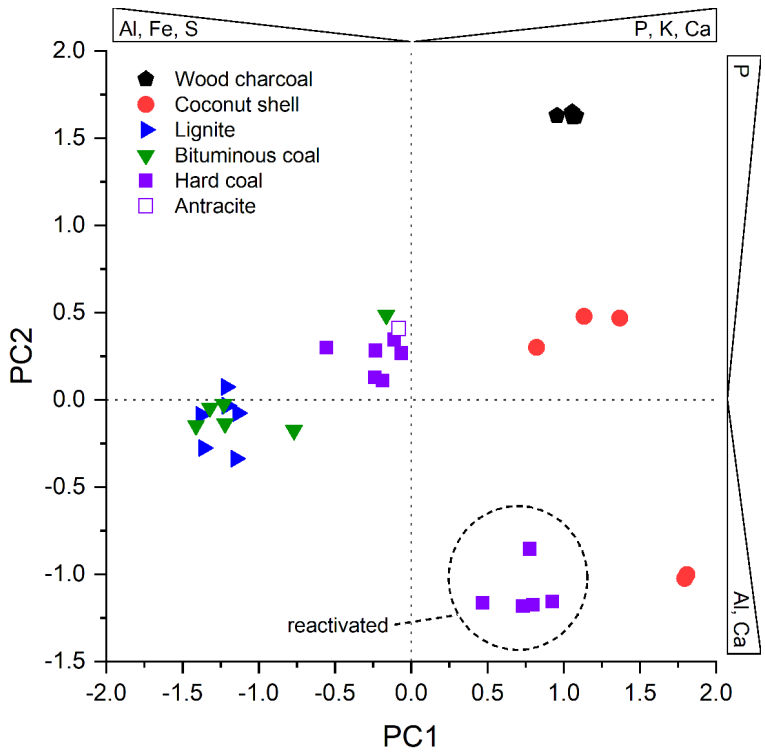

Figure 3.4: Score plot of the principal component analysis (PCA) with points representing 34 ACs (GACs and PACs) and anthracite, analyzed by X-ray fluorescence spectroscopy (XRF). Elements contributing the most to principal components (PC) 1 and 2 are indicated at the top and on the right-hand side, specific contributions (loadings) are provided in the SI (Figure B18, Appendix B).

samples (cf. Figure 3.3). AC products made of bituminous coal are found in both clusters, probably due to different qualities. Sub-bituminous coal has lignite characteristics and bituminous coal is comparable to hard coal. ACs at the bottom of the score plot, e. g. reactivated GACs from hard coal, revealed an increased relative calcium content. Chemically activated AC products made of wood charcoal cluster at the top due to their high phosphorous mass shares. The ACs made of coconut shell exhibited a separate cluster due to their potassium content. However, some of these samples also had a high calcium contents, which is why they were also separated from the primary coconut shell cluster.

In conclusion, the relative elemental composition of inorganic elements clearly represents the AC products' raw materials and activation procedures. These findings may help to classify unknown AC products. The PCA is published along with the experimental raw data [202], and can be expanded to include additional samples. Furthermore, the crucial oxygen content does not appear to be conclusively determined by the difference-to-100% method or by XPS, nor do the SOGs appear to be conclusive. It therefore made more sense to use the alternative methods of TGA and TGA-FTIR to characterize the bulk AC particles.

3.3.3 Analysis of oxygen and carbon content

AC samples primarily release CO_2, CO, and, if present, H_2O during pyrolysis, due to the decomposition of SOGs. The the pyrolytic mass loss up to 1000 °C (ML_{1000}) was therefore found to correlate very well ($R^2 = 0.994$) with the oxygen mass content determined by TGA-FTIR (Figure 3.5).

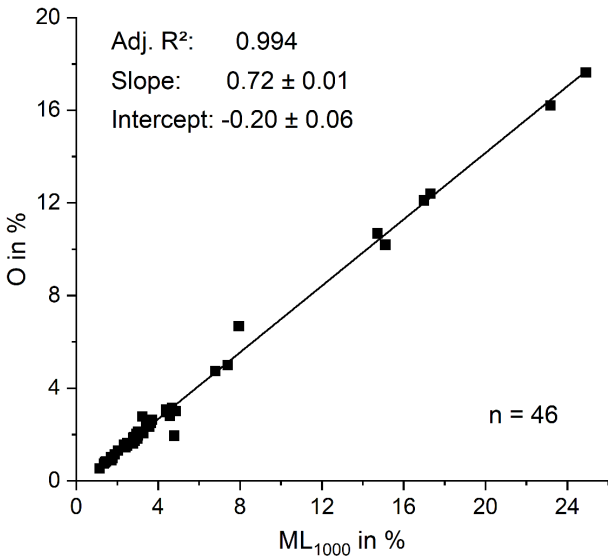

Figure 3.5: Linear correlation of the pyrolytic mass loss up to 1000 °C (ML_{1000}) and the oxygen mass content determined by TGA-FTIR.

This means that ML_{1000} is a good surrogate parameter for the oxygen content of ACs using the factor 0.72 (slope). It should be noted that the six chemically activated ACs made of wood charcoal obtained the highest values by far for ML_{1000} (and ML_{600}) or oxygen, respectively. In contrast, the majority of samples had an oxygen mass content below 3% (Figure 3.5). The effect that grinding GAC has on oxygen content is provided and discussed in the SI (Appendix B, Section B.4.2).

Additional correlations can be drawn with the properties determined for the eight PACs (Figure 3.6). Mass loss during oxidation ($ML_{ox.}$) was correlated to the carbon content by $R^2 = 0.952$ (Figure 3.6a). It is important to note that $ML_{ox.}$ is caused by the elements carbon and hydrogen, and that carbon is also a part of ML_{1000} released as CO_2 and CO. Proximate analysis therefore applies the term "fixed carbon" for the oxidative mass loss after pyrolysis. The ratio of ML_{1000} to $ML_{ox.}$ can function as a surrogate for the O/C ratio, which indicates the hydrophilic character of an AC, due again to a very close correlation ($R^2 = 0.982$, Figure 3.6b). Acidic functional groups (carboxylic acid, anhydride, and lactone groups) of the SOGs decompose into CO and CO_2 at lower temperatures. The pyrolytic mass loss up to 600 °C (ML_{600}) was therefore found to correlate with the point of zero charge (PZC) by $R^2 = 0.954$ (Figure 3.6c).

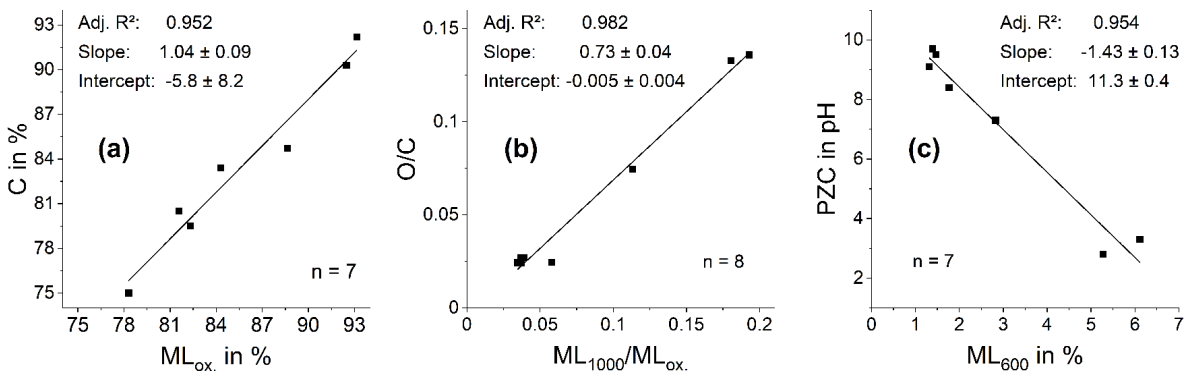

Figure 3.6: Linear correlations of (a) the oxidative mass loss and the carbon mass content determined by CHNS analysis, (b) the O/C ratio and the respective ratio of the surrogates, and (c) the pyrolytic mass loss up to 600 °C (ML_{600}) and the point of zero charge (PZC).

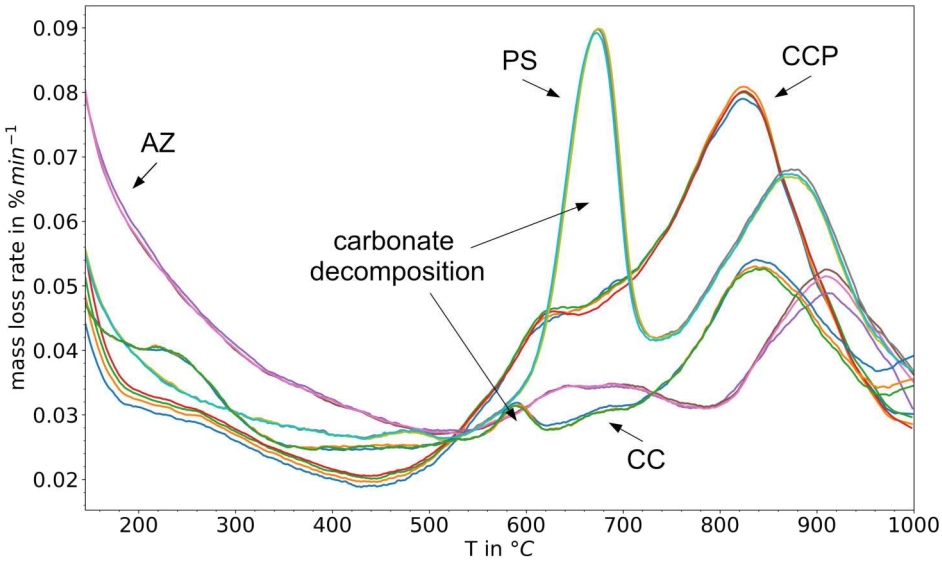

Figure 3.7: Mass loss profiles (DTG curves) of CCP, AZ, PS, and CC in multiple determinations. DTG curves for HK, HKP, SAE, and P-f are provided in the SI (Figure B21, Appendix B).

The PAC SAE was omitted from correlations with C and PZC, because the high calcite content distorts the results. DTG curves indicate the decomposition of carbonates between 600 and 700 °C as a distinctive peak (Figure 3.7, PS). For example, for SAE, this peak represents a mass loss of 4.9% (Figure B21, SI in Appendix B); if this is attributed to the release of CO_2 from the decomposition of calcite ($CaCO_3$) into calcium oxide (CaO), the calculated result should be 11.2% calcite (4.5% calcium) in the sample and 6.3% CaO in the ash. Furthermore, these values could be used to clarify the carbon and oxygen content as well as the PZC in advance, such as via SAE.

In conclusion, standalone TGA analyses are adequate for representing AC properties and for providing mass loss profiles (DTG curves) of pyrolysis. The latter not only indicates calcite or carbonate impurities, but also depicts the product-specific chemistry via the decomposition of SOGs released as CO_2 and CO.

3.3.4 Analysis of oxygen-containing functional groups

We used TGA-FTIR to determine the CO_2 and CO release rates, which in turn allowed us to determine specific SOGs by deconvolution. Of the 48 samples analyzed, only two could not be properly fitted (including SAE; relative squared error of the fit $> 0.4\%$). This might be related to high ash and calcium content affecting the thermal decomposition at lower temperatures [152]. Figure 3.8 shows examples of deconvolutions of the release rates of CC. Carboxylic acids and carboxylic anhydrides decompose below 600 °C. Both groups are acidic and of special interest with regard to the adsorption of polar or charged substances (cf. ML_{600} in Section 3.3.3). The example includes a sharp CO_2 peak at about 600 °C, which can be attributed to the decomposition of carbonates (cf. Figure 3.7). This peak was fitted by an additional “unassigned-CO2" peak, and is therefore not attributed to SOG. However, if there is more CO_2 that has evolved from carbonates, this may not be intercepted by a Gaussian-shaped “unassigned-CO2" peak. In such cases, the deconvolution was only evaluated up to 600 °C.

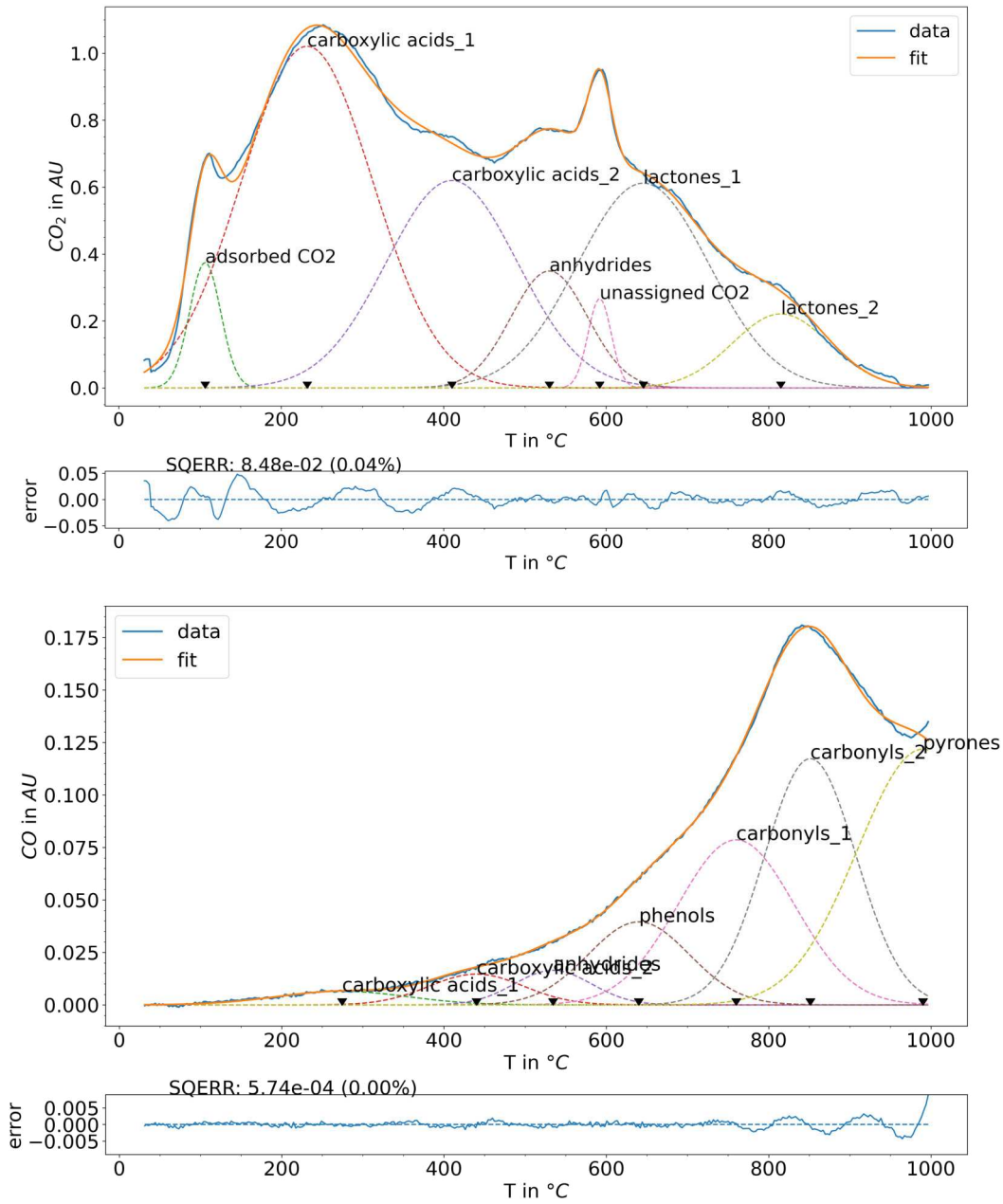

Figure 3.8: Deconvolution of CO_2 (top) and CO (below) release rates of CC with deviations (errors) between recorded data and resulting fit from the deconvolution with Gaussian peaks.

Furthermore, the evaluation must be limited to 600 °C if methane evolves above this temperature. Methane evolution indicates carbonization reactions, and the CO_2 and CO released cannot be fully assigned to SOGs. All chemically activated ACs released methane, probably due to the comparably low activation temperature that restricts carbonization reactions during production.

In summary, six SOGs were obtained for 34 samples, two SOGs (carboxylic acids and anhydrides) were determined for 12 samples, and two samples had to be excluded. Furthermore, the evolution of CO at very high temperatures was disturbed by inevitable oxidation reactions (for details, see Section A.6.3 in the SI, Appendix A). The quantity of pyrone groups is therefore overestimated, but their fit was reproducible, nevertheless. TGA-FTIR results with evolved gas

profiles and deconvolution figures of all samples are provided with the experimental raw data [202].

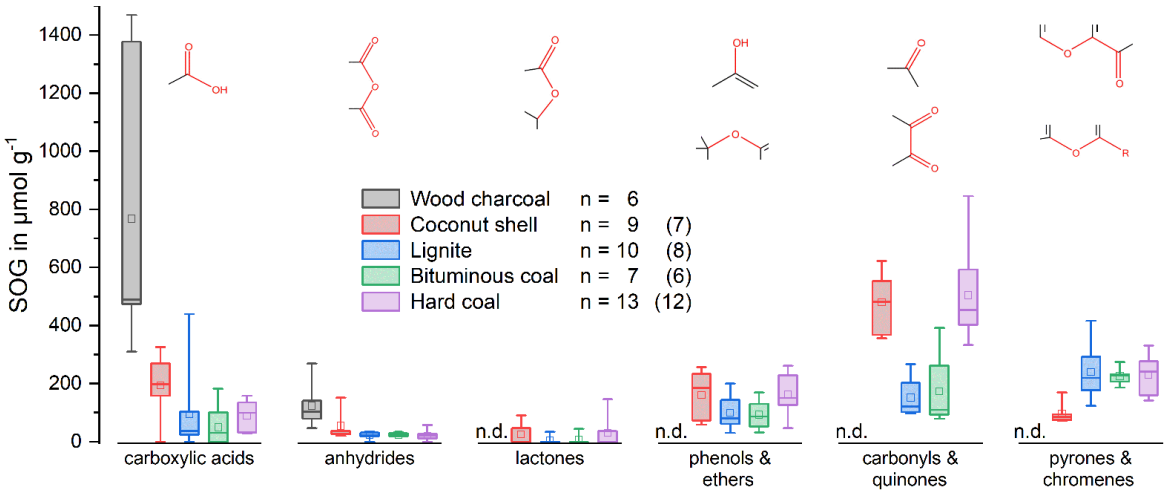

Figure 3.9: Box plots grouped by SOGs and sub-grouped by the raw material of ACs with whiskers representing the span; boxes include 50% of the results; means are given as squares and medians as horizontal bars. The number of measurements (n) is given for carboxylic acids and anhydrides in each subgroup; the number in parentheses refers to the remaining SOGs.

The raw material is expected to affect the nature of the chemistry, in terms of the absolute SOG composition as well as the relative SOG composition in a sample. The SOG quantities of the ACs presented as box plots in Figure 3.9 are therefore grouped according to the respective raw materials. High levels of a wide range of carboxylic acids were found for AC products made of wood charcoal (chemically activated with phosphoric acid). This observation corresponds with a high oxygen content and the low PZC of HK and HKP. It is likely that their chemical activation leads to the high content of acidic SOGs. Furthermore, high quantities of carbonyl groups were found, while a low content of anhydrides and lactone groups was determined. ACs made from coconut shell show a comparably high content of carboxylic acid groups compared to AC products from fossil precursors. ACs made from hard coal and their reactivates exhibit higher amounts of carbonyl and pyrone groups. ACs from lignite and bituminous coal and their reactivates contain fewer carbonyl groups and more pyrone groups than carbonyl groups. For hard coal and coconut shell, it is the other way around. These findings are also supported by two PCAs provided in the SI (Figures B31-B34, Appendix B).

In conclusion, the chemistry of AC products depends to some extent on the raw material, and can be quantified using a TGA-FTIR setup. Different SOGs probably influence the adsorption of specific target compounds, and therefore offer the opportunity to select AC products based on their surface chemistry. However, the impact of the SOG contents on OMP elimination in real water still requires clarification.

3.4 Conclusion

This study compared and characterized a large number of activated carbon products (ACs) using different analytical methods; here we draw the following conclusions.

- ACs showed large variations in their physical and chemical properties, probably due to different raw materials and activation procedures, both of which affect porosity development, elemental composition, and the surface chemistry of the product.
- The elemental composition of inorganic impurities was shown to be closely related to the raw material and the activation process of the AC, which allows for the classification of unknown samples.
- Thermogravimetric analysis (TGA) provides surrogate information on the point of zero charge (ML_{600}), the oxygen content (ML_{1000}), the carbon content ($ML_{ox.}$) and the derived O/C ratio. Derivative thermogravimetry (DTG) curves provide a chemical fingerprint of an AC. The oxygen content of an AC sample is more conclusively represented by its pyrolytic mass loss up to 1000 °C (ML_{1000}) than by estimation from CHNS analysis using ash content or by XPS analysis.
- Six types of oxygen-containing functional groups (SOGs) occur in different levels and contribute to significant differences among AC products. Chemically activated wood charcoals exhibit great quantities of carboxylic acids, whereas coconut shell and hard coal-based ACs are dominated by carbonyl groups; AC products made from lignite or bituminous coal imply lower SOG levels, mostly represented by carbonyl and pyrone groups.
- Generating appropriate material characterizations of ACs may fill in a missing piece of the puzzle when predicting organic micropollutant removals by AC, and will become even more crucial with increasing amounts of renewable products from diverse precursors, such as biochars, waste-derived carbons, and other lignocellulosic or carbonaceous materials.

Looking ahead, preliminary results show that systematic correlations between the AC properties examined here and individual OMP removals in real water depend on specific molecule moieties.

Data Availability

The obtained raw data and processed data is provided in a zenodo repository [202] and considered for publication in *Data in Brief*.

Acknowledgements

We would like to thank Frank Milczewski and Kay Matzdorf for conducting the TGA-FTIR measurements and Jutta Jakobs for performing the PZC determinations. We acknowledge Thomas Lucke, Michael Hermann, Geert Aschermann, Alexander Sperlich, and Daniel Sauter for providing activated carbon samples. Furthermore, we thank Carsten Prinz for his advice, valuable discussions about N_2 adsorption/desorption, and calculation of PSDs using QSDFT kernels, as well as Lars Eitzen for his advice on particle-size distributions. Lukas Wander must be acknowledged for discussing PCA approaches and providing Python code samples. We would like to thank Teresa Gehrs and Matt Rees of LinguaConnect for clear English revisions and the proofreading service of the Technical University of Berlin for financial support. Parts of the study

were supported by the Federal Ministry of Education and Research (BMBF) through the projects ASKURIS (contract 02WRS1278A), TestTools (02WRS1368A) and PROTECT (02WRS1495E).

Author contributions

D.D. and F.Z. compiled the set of samples. M.M. conducted the N_2 adsorptions/desorption experiments and interpreted the results. F.Z. accounts for CHNS ans PZC analyses and evaluated the data. K.A. conducted the XPS measurements and processed the peak fitting. K.A., L.S., and D.D. discussed and interpreted the XPS results. D.D. conducted the XRF measurements, including PCA evaluation. D.A. conducted the XRD measurements and interpreted the results. D.D. and L.S. carried out the TGA-FTIR experiments, developed the python package and evaluated the data. D.D., F.Z., M.J., A.S.R., and U.B. discussed the study comprehensively. D.D. wrote the original manuscript, which all authors reviewed and revised.

4

Specific adsorption sites and conditions derived by thermal decomposition of activated carbons and adsorbed carbamazepine

Daniel Dittmann, Paul Eisentraut, Caroline Goedecke, Yosri Wiesner, Martin Jekel, Aki Sebastian Ruhl, and Ulrike Braun

This chapter was published in *Scientific Reports* in 2020 [195].

Abstract

The adsorption of organic micropollutants onto activated carbon is a favourable solution for the treatment of drinking water and wastewater. However, these adsorption processes are not sufficiently understood to allow for the appropriate prediction of removal processes. In this study, thermogravimetric analysis, alongside evolved gas analysis, is proposed for the characterisation of micropollutants adsorbed on activated carbon. Varying amounts of carbamazepine were adsorbed onto three different activated carbons, which were subsequently dried, and their thermal decomposition mechanisms examined. The discovery of 55 different pyrolysis products allowed differentiations to be made between specific adsorption sites and conditions. However, the same adsorption mechanisms were found for all samples, which were enhanced by inorganic constituents and oxygen containing surface groups. Furthermore, increasing the loadings led to the evolution of more hydrated decomposition products, whilst parts of the carbamazepine molecules were also integrated into the carbon structure. It was also found that the chemical composition, especially the degree of dehydration of the activated carbon, plays an important role in the adsorption of carbamazepine. Hence, it is thought that the adsorption sites may have a higher adsorption energy for specific adsorbates, when the activated carbon can then potentially increase its degree of graphitisation.

4.1 Introduction

Increasing amounts of pharmaceuticals enter the water bodies and are detected all over the world [203, 21, 19]. Many of them are persistent and may accumulate within water cycles [24, 204, 205]. These organic micropollutants already show adverse effects in aquatic ecosystems despite their comparably low concentrations [206, 207, 208]. Therefore, technical measures are introduced as advanced wastewater treatment [209]. One of the favoured techniques is the removal by adsorption onto activated carbon [210, 211].

Activated carbon has been used in water purification for more than hundred years. In modern times, we face more ecological and economical challenges that require the accurate prediction of removal efficiencies prior to the upgrade of wastewater treatment plants. Hence, several approaches have been applied to gain fast and efficient predictions through laboratory experiments and the optimization of operating parameters through data driven modeling [12, 135, 212, 213]. The removal of the target substances has been shown to be strongly influenced by the composition of the waters and that of the activated carbons used in the removal [214, 113].

The underlying adsorption processes have been extensively described in theory and investigated experimentally [215, 131]. However, adsorption in the liquid phase has been proven to be much more complicated than adsorption in gas phases, especially in complex water matrices that are governed by the presence of dissolved organic matter, the ionic strength and the pH value [216, 114, 132]. Hence, both the adsorbate solution and the adsorbent, are mutually influenced. Moreover, activated carbon has a highly heterogeneous pore structure, easily observed by the shape of the adsorption isotherms obtained that are relatively consistent with Freundlich's model [175, 144]. Consequently, there are various adsorption sites that can act as reactive centres with specific adsorption energies/affinities, meaning that this can become an obstacle when trying to investigate different adsorption sites individually. To unravel the underlying mechanisms, researchers have varied solution parameters and modified the carbon surfaces, forming black-box approaches that have not provided sufficient information that is needed for the detailed prediction of adsorption in complex water matrices.

In this study, an approach for the characterisation of micropollutants adsorbed on activated carbons, rather than the analysis of changes in the solution, is proposed. Direct analyses of the inner surfaces of activated carbons are unfeasible, due to the complex adsorption processes and the low concentration of the adsorbates on the adsorbents that predominantly consist of carbon. Therefore, pyrolytic decomposition is applied to the solid sample, upon which the sample's mass loss is recorded by thermogravimetric analysis (TGA) and the decomposition gases are examined by evolved gas analysis.

As adsorbate model systems, three commercially available powdered activated carbons with differing properties were loaded with varying amounts of carbamazepine. Carbamazepine was selected due to its persistence and abundance in the aquatic environments, in remarkable concentrations, and as it is considered as an anthropogenic wastewater tracer [217, 205]. Furthermore, it adsorbs very well onto activated carbon, even under competitive conditions, and which has been shown extensively in literature for adsorption studies [12, 114, 214, 218, 113, 181, 219] and also in soil and sediment science [220, 221]. Additionally, transformation products of carbamazepine were extensively studied by electrochemical and ozone oxidation,

photodegradation and metabolic pathways in water, soil and humans [222, 16, 223, 224, 225, 226, 227]. Nielsen et al. (2014) conducted thermogravimetry studies coupled with mass spectrometry (TGA-MS) on very similar systems of carbamazepine and two activated carbons. They were able to observe the extensive surface reactions and transformation of carbamazepine during adsorption but could not identify the decomposition products [181].

To elucidate the underlying mechanisms at work, this study utilises evolved gas analyses through Fourier-transform infrared spectroscopy (TGA-FTIR) to identify the release of small molecules (e. g. H_2O, CO_2 or NH_3), and thermal extraction, combined with thermal desorption gas chromatography and mass spectrometry (TED-GC/MS) to detect larger molecules present in trace concentrations [79]. This can allow for the derivation of thermal decomposition mechanisms and deduce adsorption conditions. Furthermore, specific adsorption sites for the different activated carbons may be accessible by the investigation of thermal decomposition products. This will expand adsorption theories and facilitate the development of models for more accurate predictions.

4.2 Materials and methods

4.2.1 Carbamazepine

Carbamazepine (Sigma Aldrich, Germany) was purchased as a certified reference material with a purity of 99.9%. Working solutions of carbamazepine were prepared by dissolving appropriate amounts of the substance in ultra-pure water to reach target concentrations of 1, 5 and 20 mg L^{-1}.

4.2.2 Activated carbons

The powdered activated carbons SAE Super (Norit/Cabot, USA), HK 950 (Carbon Service & Consulting, Germany) and CCP 90D (Donau Carbon, Germany) were used as adsorbates. Table 4.1 provides detailed material characteristics. Results for the unloaded activated carbons were determined with samples treated like the loaded (see below) but with ultra-pure water instead of carbamazepine working solution.

X-ray fluorescence spectroscopy

For the characterisation of the inorganic constituents of the activated carbons, the samples were measured using energy-dispersive X-ray fluorescence spectroscopy. The measurements were performed on a Spectro XEPOS III with the software X-LabPro 5.1/TurboQuant (Spectro Analytical Instruments, Germany). The instrument was equipped with 50-W Pd end-window X-ray tube, three polarisation and secondary targets (highly oriented pyrolytic graphite crystal for exciting the elements Al to Cl, K to V, Al_2O_3 polarisation target for exciting the elements Zr to Ba and Mo, secondary target for exciting the K-lines of Cr to Y and L-lines of Ta to U) and silicon drift detector. For the measurements, at least 1 g of the powdered activated carbons was placed in an XRF cell (inner diameter of 24 mm) that was covered with 4 μm Mylar film. For semi-quantitative analyses of inorganic constituents in the samples, the fundamental parameters method was applied, which is integrated in the TurboQuant method. For quantitative results (Table 4.1) the relative amounts were calculated based on the ash content assuming Al as Al_2O_3, Si as SiO_2, P as P_2O_5, S as SO_3, K as K_2O, Ca as CaO, Ti as TiO_2 and Fe as Fe_2O_3.

4.2.3 Loading of the activated carbons with carbamazepine

For the adsorption experiments 100 mg of the individual activated carbons were weighed into a 1 L glass bottle and 950 mL of the carbamazepine working solution, with concentrations of 1, 5 or 20 mg L^{-1}, were added. 50 mL of the working solutions were kept to determine the initial carbamazepine concentration using UV/vis or LC-MS/MS. The samples were stirred at room temperature for a contact time of 80 min. Afterwards the activated carbons were filtered using cellulose nitrate membrane filters (0.45 μm). 50 mL of the filtrate were used to determine the final carbamazepine concentration in the solution. The loaded activated carbons on the filters were dried in a desiccator overnight. Prior to TGA measurements, the dry samples were detached from the filters.

Determination of the loadings

To calculate the carbamazepine loading on the activated carbon the initial and remaining concentrations of the analyte in the aqueous solution were determined by UV/vis spectroscopy and liquid chromatography coupled to tandem mass spectrometry (LC-MS/MS). The UV/vis measurements were performed without dilution on a Lambda 12 (PerkinElmer, USA), equipped with a 10 mm Suprasil quartz cuvette (Hellma, Germany) at a wavelength of 284 nm.

Additionally, the LC-MS/MS system TSQ Vantage triple quadrupole mass spectrometer (Thermo Scientific, USA) was used. The chromatographic separation was achieved using a XSelect HSS T3 column (2.1 x 50 mm, 2.5 μm particle size, Waters, USA) with a flow rate of 0.5 mL min^{-1}. For carbamazepine the mass to charge ratios (m/z) 194.1 and 179.1 were analysed and quantified via the internal standard consisting of deuterated carbamazepine (D8). Details about the chromatographic method and the applied parameters for the mass spectrometric detection are published elsewhere [12].

Microscopic and spectroscopic characterisation

For additional characterisation diffuse reflectance infrared Fourier-transform spectroscopy (DRIFTS) and scanning electron microscopy (SEM) was applied on loaded and unloaded activated carbon samples. The results are provided in the supplementary information (SI, Appendix C) and confirm adsorption on the inner surface of the activated carbons without altering the particle morphology.

4.2.4 Thermogravimetric analyses

The thermogravimetric measurements were conducted with the thermobalances TGA/DSC 3+ and TGA 2 (Mettler Toledo, USA) in 150 μL alumina crucibles from 25-600 °C with a heating rate of 10 °C min^{-1}. Sample masses of approximately 20 mg for SAE Super and CCP 90D systems were analysed. Due to the low bulk density, only 15 mg of systems with HK 950 were used (this does not alter the DTG profiles and DTG_{max} temperatures, Figure C1). An inert purge gas flow of 50 mL min^{-1} nitrogen (5.0) ensured pyrolytic conditions. Air buoyancy correction were applied by subtracting an empty crucible measurement or automatic compensation by TGA 2. Plotted

DTG data (1 s resolution) in Figures 4.1&4.2 are smoothed by Savitzky-Golay with polynomial order of 2 and 59 points of window.

Determination of decomposition kinetics

Ramp kinetics were conducted with the thermobalance STA-7200 (Hitachi, Japan) in 90 μL alumina crucibles with 5 mg sample mass. A nitrogen purge gas flow of 200 mL min^{-1} is applied for this type of balance. Heating rates of 1, 2, 5 and 10 °C min^{-1} were assessed and evaluated by Friedman's model free differential isoconversion method using the software NETZSCH Thermokinetics 3.1 (NETZSCH, Germany). Previously, TGA results were subtracted by the mass losses of the corresponding unloaded activated carbon to assess the decomposition stages of carbamazepine solely.

4.2.5 Evolved gas analyses

Analyses of the evolved decomposition gases during pyrolysis were performed by direct coupling with a Fourier-transform infrared spectrometer or by TED-GC/MS.

Fourier-transform infrared spectroscopy

TGA-FTIR was achieved by coupling the TGA/DSC 3+ with Nicolet iS50 (Thermo Fisher Scientific, USA) by heated transfer line (250 °C) and IR cell (260 °C). 16 scans per spectrum were collected with 4 cm^{-1} resolution in the range of 4000-400 cm^{-1} using the DTGS detector. Spectra identification and release rates evaluation were performed in the software OMNIC 9.7.39 with the database Nicolet FT-IR Vapor Phase Spectral Library (Thermo Fisher Scientific, USA).

Thermal extraction-desorption gas chromatography mass spectrometry (TED-GC/MS)

TED-GC/MS was conducted with the TGA 2 for the thermal extraction. The decomposition products of the sample were transferred by the nitrogen purge gas flow to a coupling device (Gerstel and BAM, Germany) and trapped on a polydimethylsiloxane solid phase SorbStar (Mercury Instruments, Germany). The use of the solid phase implies selectivity towards the decomposition products, therefore, (polar) substances may pass and will not be detected. The Multi-PurposeSampler MPS (Gerstel, Germany) allows to insert the solid phase at defined temperature ranges during the TGA run. For the measurements presented in this study, the decomposition products were collected between 300 and 600 °C. For sample HK+CBZ-5, an additional sampling step between 25 and 300 °C was performed previously. For the desorption process the loaded solid phase was transported by the autosampler to the thermal desorption gas chromatograph 7890 GC System with mass spectrometer 5977B MSD (Agilent Technologies, USA). The detailed conditions of the GC/MS measurements and further information on the TED-GC/MS can be found elsewhere [79, 76]. In this study no internal standard was applied and no quantification was carried out. Peak areas were divided by the sample mass of the respective sample pyrolysed in TGA, only the arising peak areas greater than 10^5 were taken into account. Due to this selection numbering of the substances is not continuously in the text, but all proposed substances are reported in the supplementary information (Appendix C).

4.3 Results

4.3.1 Characterisation of the activated carbons

Properties of the investigated powdered activated carbons HK 950, CCP 90D and SAE Super are listed in Table 4.1. The activated carbons are based on charcoal, coconut husk and a mixture containing lignite, respectively and therefore show large differences. The manufacturers specify similar BET surface areas, but elemental analyses show strong contrasts in the degree of dehydration (cf. C/H ratios). The ash contents also differ, representing the presence of inorganic impurities that are dominated by calcium and iron in the SAE Super. In contrast, phosphorus is dominating in the HK 950, indicating chemical activation with phosphoric acid [201]. Potassium is dominant in the CCP 90D, which is typcial for virgin activated carbons based on coconut husk. Furthermore, the presence of a high sulphur content in the SAE Super is clearly evident and may originate from the lignite portion. Thermal activation can be assumed for the SAE Super and the CCP 90D.

Table 4.1: Characteristics of the three powdered activated carbons as supplied by the manufacturers [5], ratios of carbon to hydrogen (C/H ratio) by elemental analyses (unpublished data), ash contents at 900 °C and the molar mass fraction of elements determined by XRF (uncertainty of measurement is negligible for the rounded values).

	unit	SAE Super	HK 950	CCP 90D
Manufacturer		Norit / Cabot	Carbon Service & Consulting	Donau Carbon
Raw material [5]		mixture	charcoal	coconut husk
BET surface area [5]	$m^2\,g^{-1}$	1050-1150	>950	1000-1100
C/H ratio		790	37	300
Ash content		9%	4%	4%
Si	$\mu mol\,g^{-1}$	57	160	220
P	$\mu mol\,g^{-1}$	1	180	14
S	$\mu mol\,g^{-1}$	210	8	7
K	$\mu mol\,g^{-1}$	54	19	310
Ca	$\mu mol\,g^{-1}$	1900	15	92
Ti	$\mu mol\,g^{-1}$	14	3	9
Fe	$\mu mol\,g^{-1}$	370	20	79

4.3.2 Characterisation of the thermal decomposition processes

The following sample nomenclature is utilised, where the short names of the activated carbons is used, + carbamazepine (CBZ) if adsorbed with its corresponding mass fraction on a percentage base. Table 4.2 lists the created adsorbate systems with the thermogravimetric results. Figure 4.1 shows the decomposition behaviours during TGA of the investigated samples. TGA graphs depict decreasing relative sample mass as thermogravimetry curve (TG) and its mass loss rate (first derivation of TG) as derivative thermogravimetry (DTG) profile as a function of temperature or measurement time, respectively. Figure 4.1a shows the thermal decomposition of pure carbamazepine within a single stage. The systems with the activated carbons (Figures 4.1b to 4.1d) decompose differently and show more complex DTG profiles. The two noticeable decomposition stages can be attributed to carbamazepine in the adsorbed state.

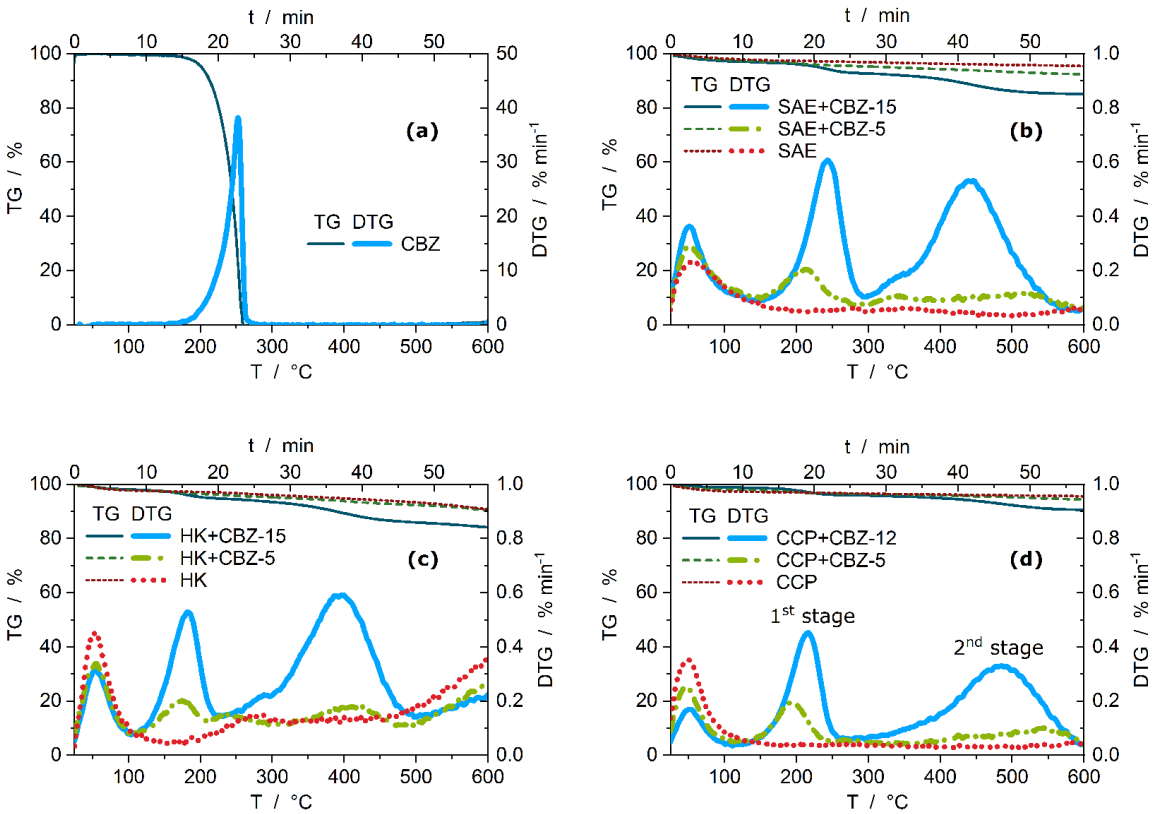

Figure 4.1: TGA decomposition graphs showing relative sample masses (TG) and mass loss rates (DTG) of (a) pure carbamazepine and (b) SAE Super, (c) HK 950 and (d) CCP 90D containing none, middle and high mass fractions of carbamazepine.

The mass loss up to 130 °C is governed by the vaporisation of adsorbed water. These amounts may change with varying ambient humidity and, therefore, the given values in Table 4.2, as well as all calculations, are based on values normalised to that of the dry sample masses after the vaporisation stage. Pyrolysis of the unloaded activated carbons (red dotted lines in Figure 4.1b to 4.1d) shows specific DTG profiles. These may be interpreted as baselines for each activated carbon and represent functional groups and oxygen containing surface complexes released from the adsorbent [228].

Two additional mass loss stages occur during pyrolysis of the loaded activated carbons compared to that of the unloaded adsorbents. The temperatures at which carbamazepine decomposes are observed. The 1st decomposition stage of carbamazepine, adsorbed on HK 950 and CCP 90D, begin at lower temperatures (130 °C and 160 °C, respectively) than that of the decomposition of pure carbamazepine (180 °C) or in the SAE Super systems. The 2nd decomposition stage takes place between 300 and 600 °C. At these temperatures pure carbamazepine is already decomposed completely.

In Figure 4.2a (and Table C1 in Appendix C) the thermal decomposition of the systems with the highest carbamazepine loadings are compared. No systematic shift in the decomposition temperature is observed to be dependent upon the activated carbon. The 1st and the 2nd mass loss stages shift independently to higher or lower temperatures.

There is no complete pyrolytic release of adsorbed carbamazepine. For SAE+CBZ-1, 74% of the initial carbamazepine mass is retained and represents 0.74% of mass fraction in the sample.

Table 4.2: Sample code, mass fractions (w_{CBZ}) and molar mass fraction of carbamazepine are given for the created adsorbate systems. Followed by thermogravimetric results with mean values of the mass loss for the 1st & 2nd stage and their share on w_{CBZ}. Uncertainties are given as standard deviation, in cases of n=2 it represents the range of the duplicate determination.

sample	w_{CBZ}	CBZ in μmol g^{-1}	1st mass loss stage in %	2nd mass loss stage in %	Share of 1st stage on w_{CBZ} in %	Share of 2nd stage on w_{CBZ} in %	n
SAE+CBZ-15	0.150	630	3.8±0.2	7.1±0.4	20±2	38±3	7
SAE+CBZ-5	0.045	190	1.8±0.2	2.7±0.1	21±4	30±5	4
SAE+CBZ-1	0.010	42	0.9±0.0	1.5±0.0	15±9	11±9	3
SAE	0	0	0.8±0.0	1.4±0.1	-	-	5
HK+CBZ-15	0.150	630	3.2±0.2	9.3±0.1	15±1	41±2	2
HK+CBZ-5	0.045	190	1.6±0.1	4.2±0.1	16±4	23±4	4
HK	0	0	0.9±0.1	3.1±0.1	-	-	4
CCP+CBZ-12	0.124	525	2.7±0.1	5.6±0.1	16±1	35±2	3
CCP+CBZ-5	0.045	190	1.4±0.1	2.1±0.1	15±4	19±4	4
CCP	0	0	0.7±0.2	1.3±0.1	-	-	4

For SAE+CBZ-15, only 42% of the initial carbamazepine mass is retained but this represents 6.3% of mass fraction in the sample. These are remarkable amounts considering the complete decomposition of pure carbamazepine.

Furthermore, the 2nd stage's mass loss of adsorbed carbamazepine decreases disproportionally with carbamazepine mass fraction and may disappear at very low loadings. Therefore, the increasing retention of carbamazepine at low loadings indicates high adsorption energies for the favoured adsorption sites. On the other hand, the increasing mass fraction of retained carbamazepine at high loadings indicates inter-molecular interactions, e. g. pore filling. In conclusion, high-energy adsorption sites dominate the incomplete release of carbamazepine at low loadings while pore filling may cause the high retention at high loadings.

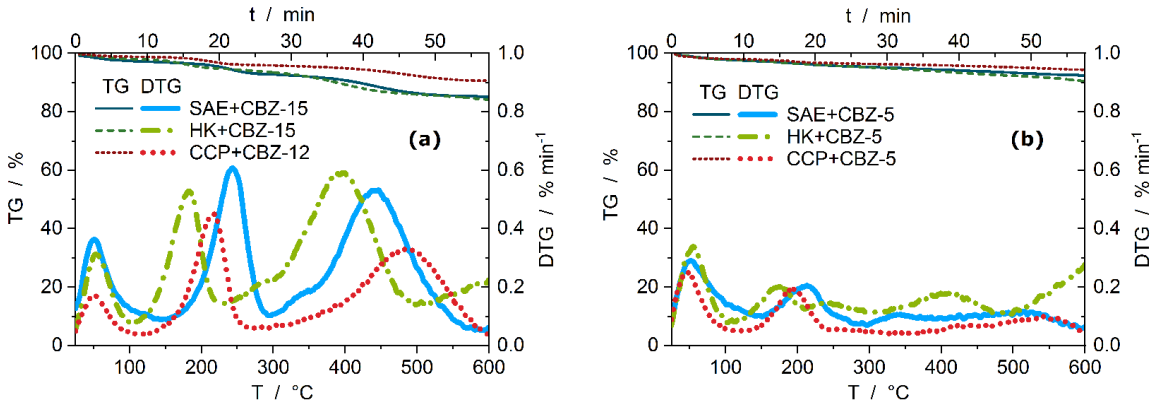

Figure 4.2: Comparisons of TGA decomposition graphs (from Figure 4.1) for the different loaded activated carbons; showing relative sample masses (TG) and mass loss rates (DTG) of (a) the systems with the highest carbamazepine loadings and (b) the systems with 4.5% mass fraction of carbamazepine.

4.3.3 Decomposition mechanism of the 1st mass loss stage

The main decomposition product evolved during the 1st decomposition stages is isocyanic acid, which was identified by TGA-FTIR (Figure 4.3). Isocyanic acid is a likely leaving group of carbamazepine. Furthermore, the elimination of isocyanic acid during the thermal decomposition of pure carbamazepine has been previously described by Pinto et al. (2014)[229]. CO_2 and NH_3

are released simultaneously as isocyanic acid may be hydrolysed. This secondary reaction is intensified on SAE Super and might be catalysed by its comparably high content of 9% inorganic compounds (containing Ca, Ti and Fe; see Table 4.1). A detailed description of this mechanism, and evidence for H_2O consumption, is given in the supplementary information (Figures C2&C3).

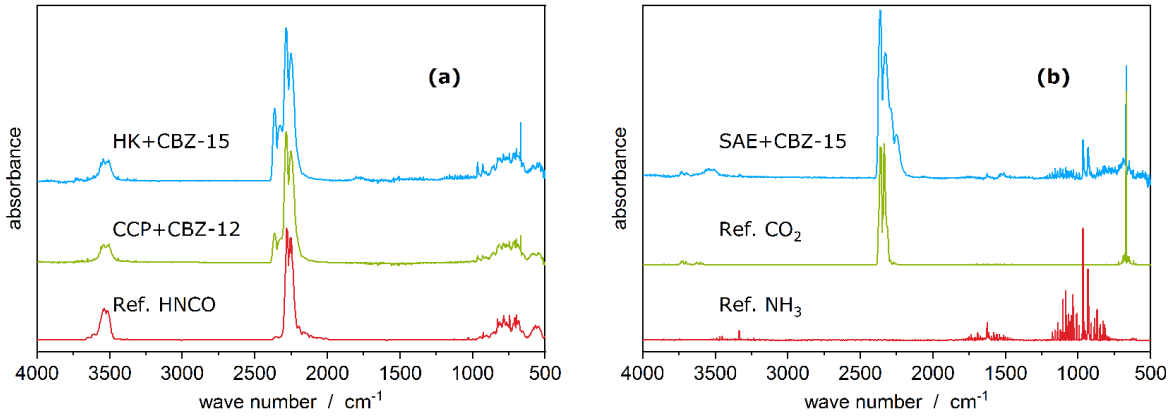

Figure 4.3: Infrared spectra of the gases evolving during the 1st decomposition stage. From top to bottom (blue – green – red): (a) spectra at 16.1 min and at 19.5 min as well as reference spectrum of isocyanic acid (HNCO); (b) spectrum at 22.3 min and reference spectra of carbon dioxide (CO_2) and ammonia (NH_3). The water spectrum was subtracted from the measured spectra.

We conducted experiments on decomposition kinetics for SAE+CBZ-15 and HK+CBZ-15, to investigate catalytic effects that may cause the observed temperature shift for the elimination of isocyanic acid in the 1st decomposition stages (Figure 4.2 and Table C1 in Appendix C). As a result, we determined activation energies of 92±2 kJ mol^{-1} for SAE+CBZ-15 and 92±3 kJ mol^{-1} for HK+CBZ-15 very close to 93±2 kJ mol^{-1} for pure carbamazepine (Table C2) [229]. In conclusion, no catalytic effects seem to be at play. There is no interaction between the amide group of carbamazepine and the activated carbon surface, as isocyanic acid is eliminated in the different systems without observed changes in the activation energy, in comparison to pure carbamazepine.

We assume, that the availability of hydrogen atoms in the activated carbons may affect eliminating isocyanic acid at lower temperatures. This hypothesis is supported by the fact that one hydrogen atom has to move from the amide group to the nitrogen atom of the dibenzazepine moiety (Figure 4.4). Furthermore, the order of the peak temperature in the DTG profiles of the 1st decomposition stages (Figure 4.2 and Table C1 in Appendix C) are in good agreement with the order of the C/H ratios of the activated carbons (HK – CCP – SAE, Table 4.1).

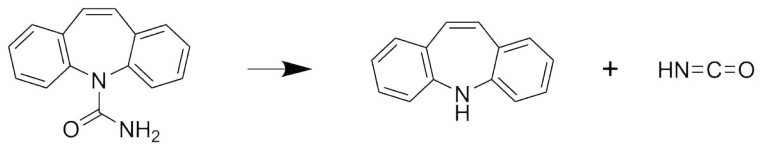

Figure 4.4: Elimination of isocyanic acid from the carbamazepine molecule with remaining dibenzazepine (60, numbering see supplementary information in Appendix C). This reaction occurs during the 1st decomposition stage of adsorbed carbamazepine and by thermal decomposition of pure carbamazepine. In the latter, both products evolve as gases. For adsorbed carbamazepine, only isocyanic acid is released while dibenzazepine remains on the activated carbon in the 1st stage independent of its loadings or type of adsorbent.

The known mass fraction of carbamazepine in the loaded activated carbons (w_{CBZ}) and the mass loss stages gained by TGA are provided in Table 4.2. The mass share of isocyanic acid in the carbamazepine molecule of 18.2% corresponds to the respective mass loss in the 1st decomposition stage, which are about 16 and 19% of w_{CBZ}.

In conclusion, the 1st decomposition stage of adsorbed carbamazepine on activated carbon arises out of the quantitative elimination of isocyanic acid and is observed to be independent of the carbamazepine loading (Figure 4.4).

4.3.4 Decomposition mechanisms of the 2nd mass loss stage

After the elimination of isocyanic acid in the 1st decomposition stage, dibenzazepine molecules should remain adsorbed on the activated carbon. The broad DTG peak of the 2nd mass loss stage (Figures 4.1&4.2) indicates a number of overlapping decomposition processes. Nielsen et al. (2014) conducted TGA-MS and assumed decomposition products in the 2nd mass loss stage with m/z higher than 100 [181]. We could confirm this from evolved gas analyses by TED-GC/MS, revealing 55 products (an overview with all proposed structures of decomposition products is presented in the supplementary information (Appendix C); initially 65 substances were observed, due to several reasons 10 were excluded). The evolved products may not completely originate from the carbamazepine molecule, as 6 substances contained oxygen, 5 sulphur and 27 contained no heteroatoms. However, these substances evolve solely or in increased amounts in systems with adsorbed carbamazepine. In contrast, pure carbamazepine releases mainly dibenzazepine (substance 60 in the SI in Appendix C, only numbers in brackets are given below) as detected by TED-GC/MS and Py-GC/MS [230]. Traces of acridine (54) and 10,11,-dihydro-5H-dibenzazepine (59) are observed, which are in in the first approximation related to a disproportionation reaction of (60). Pyrolysis and the evolution of decomposition products from the loaded activated carbons are driven by the chemical composition of the sample. For the heterogeneous activated carbon, this may be linked to reactive centres with varying adsorption energies for carbamazepine. These centres are called adsorption sites.

We assigned the decomposition products to nine groups (I-IX), based on their general molecular structure and release pattern in the investigated systems. Figure 4.5 shows selected proposed substances as representatives for each group and provides their relative releases (normalised to sample mass) from the unloaded activated carbons and the systems with 4.5% mass fraction of carbamazepine. Graphs of all 55 substances are provided in the supplementary information (Appendix C).

I. Tetradecane (39) and the group of *aliphatics* (decomposition products without aromatic moieties) are released predominantly from the HK+CBZ-5 system. They are not detected in the systems with CCP 90D. Figure 4.6a shows an increasing release of (39) with increasing carbamazepine mass fraction in SAE Super but the release of *aliphatics* is not present at low carbamazepine loadings.

II. Equally, the group of *strongly alkylated benzenes* (decomposition products consisting of a phenyl ring and a substitution with at least four carbon atoms) is progressively released with increased carbamazepine loading. Also, the lowest release occurs from CCP+CBZ-5.

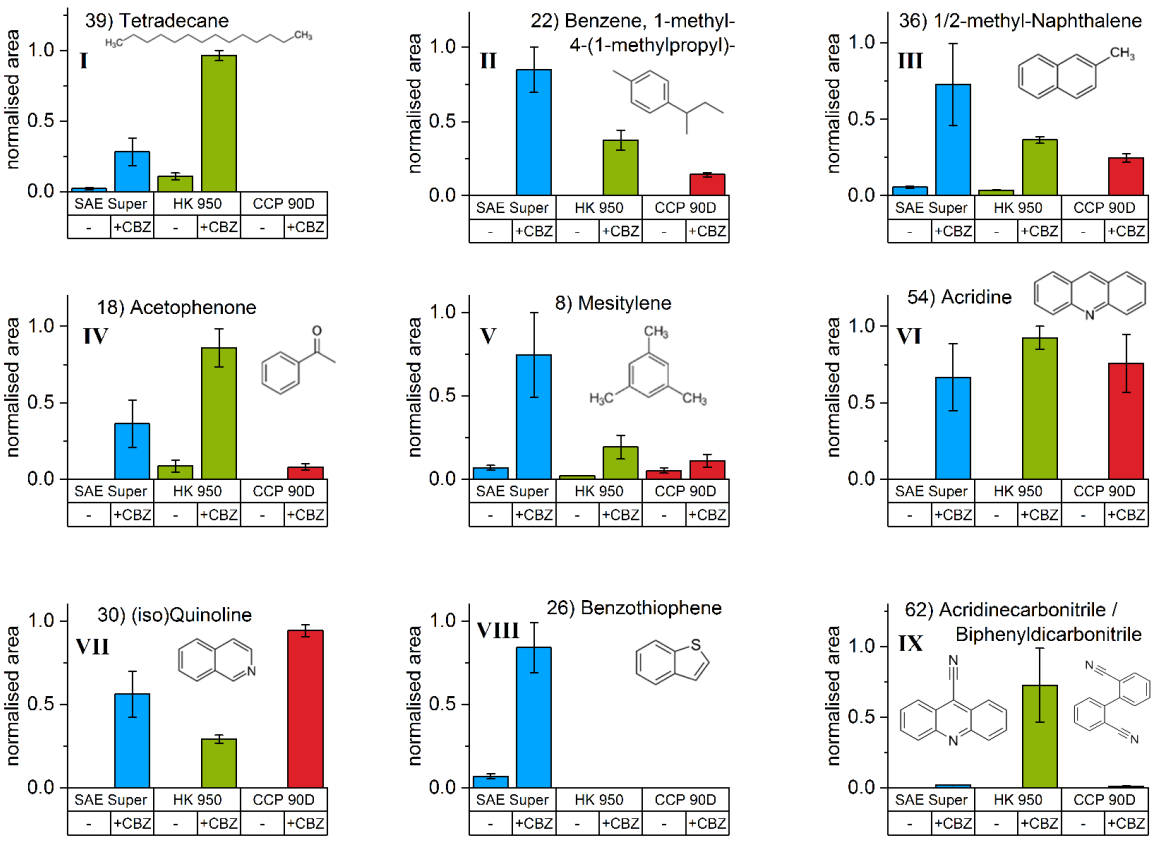

Figure 4.5: Relative comparison of selected evolved decomposition products of the unloaded and loaded activated carbons with 4.5% mass fraction of carbamazepine. Substances are representing the nine groups (I-IX) also shown in Figure 4.7. Values are normalised to sample mass and the maximum peak area of the single measurements. Error bars representing the range of the duplicate determination.

Like 1-methyl-4-(1-methylpropyl)-benzene (22), this group is not released from unloaded activated carbons but from all systems with adsorbed carbamazepine.

III. Methylnaphthalene (36) belongs to the group of *alkylated or bridged aromatics* (decomposition products consisting of more than one phenyl ring with substitutions) which is similar to the *strongly alkylated benzene* (II) group with regard to the release order of the three activated carbons.

IV. Substances in the group of *oxygen containing aromatics* (decomposition products consisting of aromatics with substitute oxygen), e. g. acetophenone (18), were released predominantly by HK+CBZ-5. This is in line with the comparably high amounts of oxygen containing surface complexes of HK 950, represented by its pyrolytic mass loss. Furthermore, benzaldehyde (9) was released even at low carbamazepine loadings on SAE Super (see SI, Appendix C) indicating specific surface reactions or adsorption sites.

V. *Slightly alkylated benzenes* (decomposition products consisting of phenyl ring and substitution having at most three carbon atoms) like Mesitylene (8) are found within all investigated systems.

VI. Acridine (54) gained, by far, the strongest intensities. Therefore, it is assumed to be a main decomposition product in the 2nd stage. It is assigned to the group of

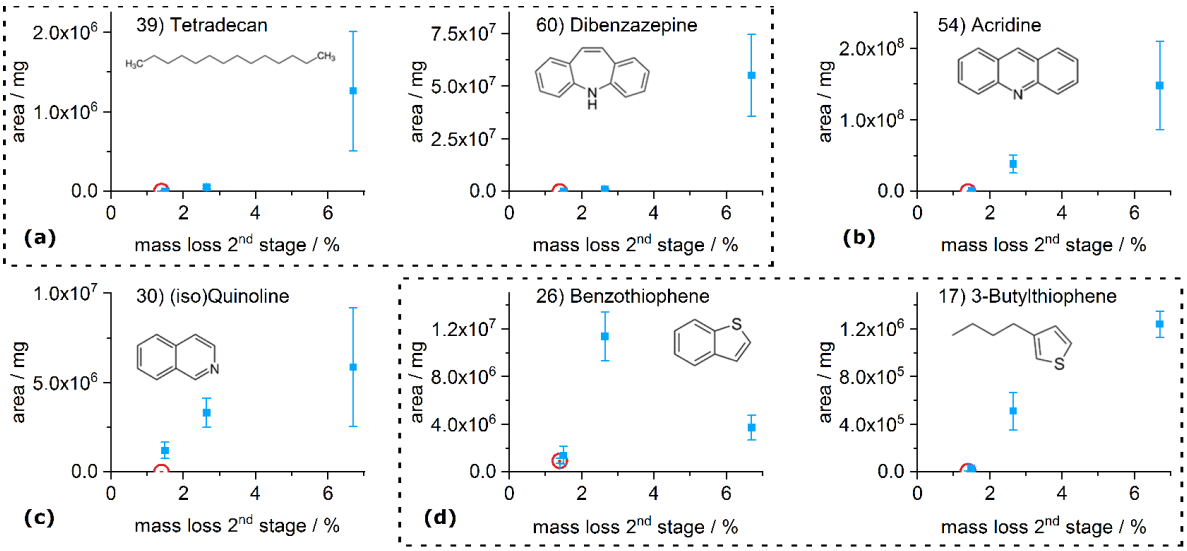

Figure 4.6: Selected evolved decomposition products of the unloaded SAE Super (red circle) and its systems with varying amounts of adsorbed carbamazepine, represented by the 2nd stage's mass loss. Types of release curves are shown for (a) starting at higher loadings, (b) continuously increasing, (c) limited at high loadings and (d) connected releases, due to hydration at high loadings. Values are normalised to sample mass. Error bars representing the range of the duplicate determination.

unsubstituted aromatics (aromatic decomposition products without substitutions) as well as dibenzazepine (60). All substances of this group are released in similar amounts from all three activated carbons. Figure 4.6b shows an increasing release of (54) with increasing carbamazepine mass fraction.

VII. Quinoline (30) is released from CCP+CBZ-5 in the largest quantities and represents the group of *unassigned, nitrogen containing* substances (decomposition products with differing release patterns, mostly containing nitrogen). This group is not released from unloaded activated carbons. Benzonitrile (11) and (30) are released even at low carbamazepine mass fractions in SAE Super (Figure 4.6c and SI in Appendix C).

VIII. Benzothiophene (26) is one of five *sulphur containing* decomposition products primarily released from the SAE Super systems, as this activated carbon contains the highest amount of sulphur (Table 4.1). Furthermore, Benzothiophene (26) shows a maximum with decreasing release after 4.5% mass fraction of carbamazepine whereas 3-butylthiophene (17) is observed to constantly increase (cf. Figure 4.6d). In total, the release of *sulphur containing* decomposition products reached a limitation at 4.5% mass fraction of carbamazepine. With regard to the available sulphur of 210 μmol g^{-1} in the SAE Super, it is close to the molar mass fraction of carbamazepine in SAE+CBZ-5 (cf. Tables 4.1&4.2).

IX. 9-Acridinecarbonitrile (62) is an outstanding and *specific* decomposition product containing two nitrogen atoms. It is released from all systems containing carbamazepine but predominantly by HK+CBZ-5. Additionally, TGA-FTIR revealed the release of hydrogen cyanide (Figure C4) solely from HK 950 that may facilitate the reaction of acridine (54) to (62). On the other hand at 180 °C water is also released from this system (Figure C3), which can transform carbamazepine to (62). Subsequently, (62) could release hydrogen cyanide during its thermal vaporisation.

Figure 4.7 shows the normalized peak areas and C/H ratios of all individual substances arranged in the nine groups. The dashed lines indicate the C/H ratio of dibenzazepine (60) to support differentiation whether the decomposition products become more or less hydrated during pyrolysis.

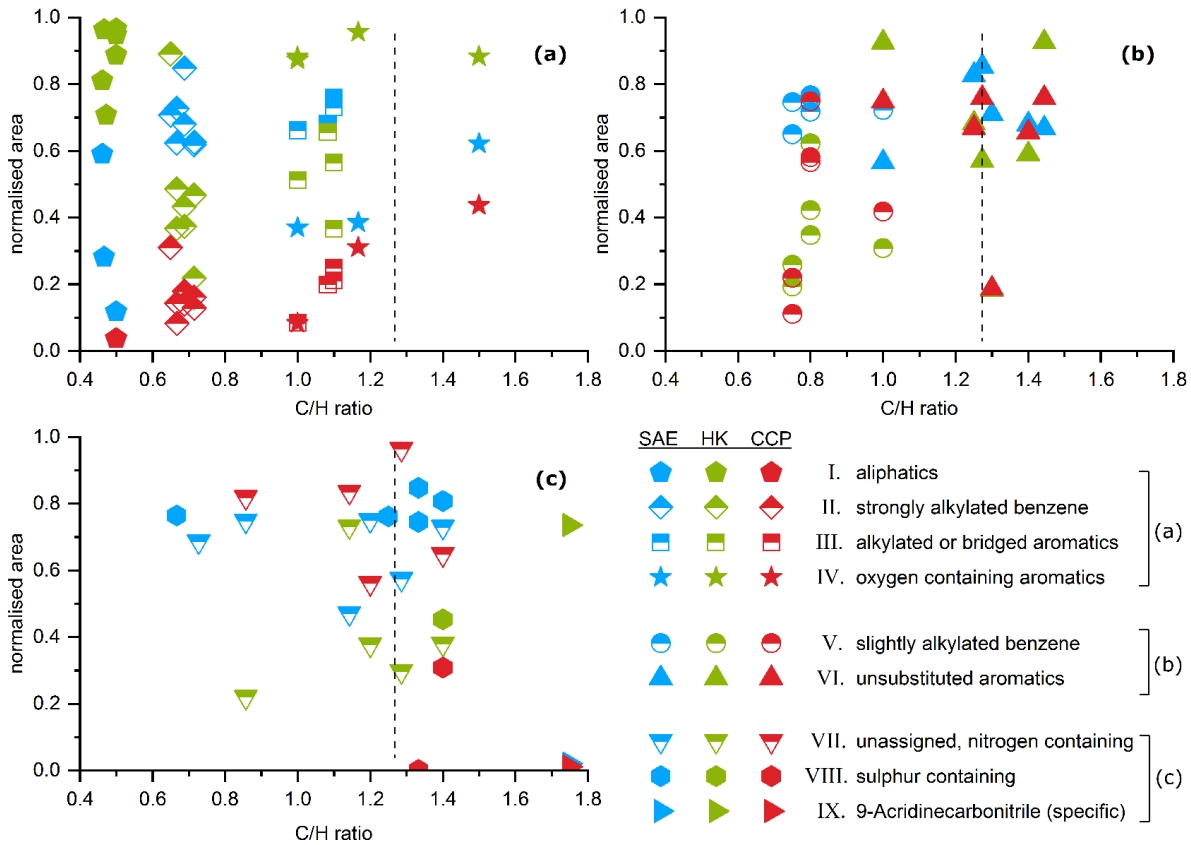

Figure 4.7: All decomposition products of the systems with 4.5% mass fraction of carbamazepine are plotted by their C/H ratios and normalised peak area, coloured for each activated carbon. Symbols represent the nine groups that are mapped in (a) good clustering by activated carbon, in (b) less distinctiveness and in (c) unassigned and specific released decomposition products. The dashed line indicates the C/H ratio of dibenzazepine (60).

The *aliphatics* (group I) have low C/H ratios or comparably high hydrogen contents, respectively (Figure 4.7a). Therefore, their release depends on receiving hydrogen atoms. The activated carbons have a much higher C/H ratio (Table 4.1) and are therefore considered as poor H sources. Thus, only carbamazepine can provide the hydrogen required for the observed evolution of hydrogen-rich substances. We attribute the release of *aliphatics* to pore filling and multi-layer formation since their low C/H ratios can only be obtained by inter-molecular reactions. Additionally, their releases evolve at high loadings and therefore decomposition products are not related to chemical properties of the activated carbons like hetero atoms or oxygen containing surface complexes. The group is clearly clustering by the type of activated carbon, showing a prevailing release of HK 950 after carbamazepine adsorption. This might be related to the pore structures supporting, or not supporting, pore filling and multi-layer formation. Also, the evolution of *strongly alkylated benzenes* (group II) depends on the availability of hydrogen provided by the adsorbed carbamazepine. However, clusters of the substances with low C/H ratio are observed in a different order to that seen for *aliphatics*, with respect to the activated carbon type. For *alkylated or bridged aromatics* (group III) and *oxygen containing aromatics* (group IV), a clear

differentiation of the activated carbons can be observed. These substances are much closer to the C/H ratio of dibenzazepine (60) and do not require the additional hydrogen atoms provided through inter-molecular reaction. Distinct adsorption sites may be associated to the evolution of *oxygen containing aromatics*. Interactions with the activated carbon surface, are also indicated, as oxygen is not present in the carbamazepine molecule.

Figure 4.7b shows the groups with non-distinctive clustering of the decomposition products such as *slightly alkylated benzenes* (group V) and *unsubstituted aromatics* (group VI). As they are found in all investigated systems, they can be said to originate from adsorption sites and conditions present in each activated carbon. These substances also indicate specific interactions with the activated carbon surface as their release curves do not increase linearly with increasing carbamazepine loadings, as it is shown for quinoline (30, group VII) in Figure 4.6c (cf. SI, Appendix C). There are two exceptions in group VI, acridine (54) shows a linear release curve (Figure 4.6b) and dibenzazepine (60) is only released at higher loadings. The intense release of acridine (54) already starts at low carbamazepine loadings and shows no limitation due to the availability of adsorption sites, which may be the most abundant and typical for activated carbons. In contrast, all other substances that are released at low loadings (9, 11, 25, 30, 53) show limitations or a maximum release at 4.5% mass fraction of carbamazepine. We suggest that this represents favoured adsorption sites, and these substances are assigned to the groups IV, VI and VII. In the case of no further increases in release beyond 4.5% mass fraction of carbamazepine, the adsorption conditions related to these decomposition products seem to be limited on the activated carbon surface.

Unassigned, nitrogen containing decomposition products (group VII) with a wide variety in C/H ratios are shown in Figure 4.7c. The graph also contains all *specifically* released substances (13, group IX and 62, group VII) including *sulphur containing* ones (group VIII), which prevail in the SAE Super systems. As shown in Figure 4.6d, there is a decrease in the evolution of benzothiophene (26) but an increase of 3-butylthiophene (17). The latter indicates the presence of pronounced hydration reactions with increasing carbamazepine loadings since it can be derived from (26) by hydration. These effects seem to be related to low C/H ratios of the evolved substances. It indicates increasing inter-molecular reactions at high carbamazepine loadings. This was already seen for the *aliphatics* (group I), which are only released when the amount of carbamazepine exceeds the mass fraction of 4.5%. This has also been observed for the *aliphatics* (group I), where the release only begins at 4.5% mass fraction of carbamazepine. These increasing release curves are similar to others from decomposition products occurring at high carbamazepine loadings, e. g. methyl-acridines (56, 58, 61) or iminodibenzyl (59). Furthermore, dibenzazepine (60) is only released at high loadings but is not hydrated. This may allow the differentiation between hydrated products generated by pore filling and (60), which may be evolved from multi-layers as it is released from pure carbamazepine.

In Figure 4.8, all observed decomposition products from the 2nd decomposition stage are arranged according to the examined features. There are specific decomposition products for SAE Super and HK 950 but none for CCP 90D, which has less distinctive properties. Furthermore, systems of CCP 90D do not release products dominating their substance group. The substances solely observed at high loadings from SAE+CBZ-15 are considered to originate from growing pore filling and multi-layer formation. However, the substances released, even at low loadings,

are emphasised and are mainly evolved from all adsorbate systems. Therefore, they represent favoured adsorption sites and the generally high affinity of carbamazepine to activated carbons.

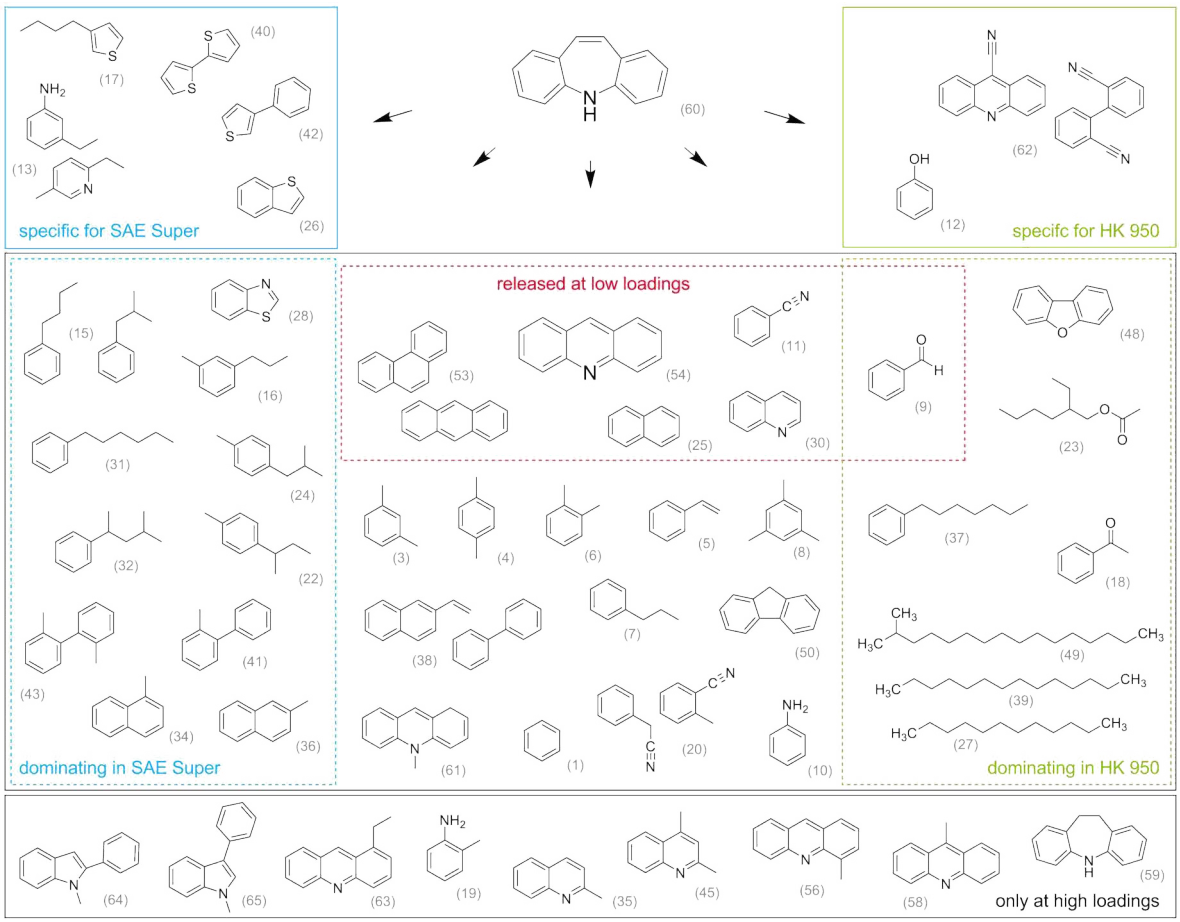

Figure 4.8: Proposed structures for substances released during the 2nd decomposition stage. Starting with dibenzazepine (60) ("iminostilbene") adsorbed on activated carbon strongly differing products are formed. Boxes support categorisation of substances which are *specific* for the activated carbons SAE Super or HK 950 as well as substances *dominating* in clustering groups (Figure 4.7a). The red dashed box emphasizes decomposition products which are released at low carbamazepine loadings. The gray box on the bottom indicates substances that were released only at high loadings investigated on the SAE Super.

4.4 Discussion

The three powdered activated carbons, studied with and without adsorbed carbamazepine, showed a variety of differences in thermal decomposition. However, it was observed that adsorbed carbamazepine decomposes in two stages on all activated carbon samples, within this study, showing that the adsorption mechanisms for carbamazepine is the same for the different activated carbons. In contrast, application of other adsorbents, such as mesoporous silicates with comparable amounts of adsorbed carbamazepine have been reported to decompose with only one stage. Furthermore, complete pyrolytic removal was achieved on these materials, indicating the presence of fewer complex mechanisms occurring in comparison to that occurring with activated carbon [231].

The quantitative release of isocyanic acid (Figure 4.4) in the 1st decomposition stage with all loaded activated carbons supports, indicating comparable adsorption mechanisms for all three adsorbents. Hence, the adsorption of carbamazepine on activated carbon is said to take place mainly at its dibenzazepine moiety. The temperature shift of the 1st decomposition stage can be explained by the differing availabilities of hydrogen atoms in the activated carbons (or hydrogen deficiencies), represented by the C/H ratio. The hydrogen content may be more important for thermal decomposition than for adsorption of carbamazepine in water.

To understand the adsorption process of carbamazepine, the 2nd decomposition stage reveals more information. It provides information on the specific properties of activated carbon, as well as the amount of adsorbed carbamazepine. 55 decomposition products were observed, by TED-GC/MS, during the pyrolytic decomposition of carbamazepine on activated carbon (Figure 4.8).

Highly hydrated substances, in the evolved gases, with comparably lower C/H ratios are *dominating* specific activated carbons but are *not released at low carbamazepine loadings*. Therefore, they are said to depend on the activated carbon properties such as pore structure or their degree of dehydration and may represent pore filling effects. In addition, dibenzazepine (60) and other decomposition products, that were observed *only at high loadings*, may represent multi-layer formation.

Sulphur or oxygen containing decomposition products indicate interactions of carbamazepine with heteroatoms or functional groups on the activated carbon surface, or with inorganic constituents. The latter may be Fe_xS_y that exchange to iron nitrates or cyanides and therefore, favour the presence of carbamazepine's nitrogen. The evolved substances are strongly associated with the activated carbon properties such as the amount of oxygen containing surface complexes or inorganic impurities, and hence, they may provide additional adsorption sites (cf. HK 950 and SAE Super).

The majority of decomposition products evolve from all three activated carbons despite the strongly differing adsorbent properties. This is in line with the similar TGA decomposition processes observed and the fact that carbamazepine is very well adsorbed on all activated carbons. Moreover, the substances *released at low loadings* (9,11,25,30,53,54) were observed with all three activated carbons. In conclusion, the favoured adsorption sites for carbamazepine are observed in all three activated carbons but present in differing amounts. Acridine (54) was the decomposition product with the most intense response during pyrolysis. This is also a well known transformation product of carbamazepine from electrochemical oxidation, photodegradation and metabolic pathways [222, 223, 224, 225, 226]. There are no comparable transformation products by ozonation [16].

Desorption studies in water indicate the release of intact carbamazepine molecules as well as desorption hystereses from activated carbons, graphene oxides and soils [232, 233, 221, 220]. For thermal desorption or decomposition, mass balances showed that dibenzazepine is partialy retained on the activated carbon support. Therefore, the decomposition products stem only from a fraction of the adsorbed carbamazepine. Moreover, there may be a high number of substances associated with the carbon structure of the activated carbon, rather than that of the carbamazepine molecule.

As a result, we can propose a hypothesis on these phenomena. During the formation of activated carbons as technical materials, hydrocarbons are dehydrated at 800-1000 °C and highly condensed aromatic systems arise (cf. C/H ratios). Subsequently, activated carbons are non-graphitic and non-graphitisable, meaning they will not reach the thermodynamically preferred state of graphite, even upon heating to 3000 °C [144]. However, activated carbon's highly disordered microstructure contains small graphite-like crystallites. Due to steric hindrance they are not able to become graphite within the carbon skeleton and there are no possible pathways for ongoing dehydration processes to proceed. An adsorbate could act as supporting structure donating hydrogen and could thus facilitate dehydration. In conclusion, adsorption sites of high adsorption energy, for carbamazepine, would represent regions in the activated carbon structure that have a strong dependence or high possibility to become more graphite-like. On the other hand, continual retention of carbamazepine mass fraction with increasing loadings are attributed to pore-filling effects.

In brief, adsorbates could support the closing of voids between graphite-like crystallites or reduce defects by squeezing out heteroatoms from the activated carbon. Therefore, strongly adsorbing molecules like carbamazepine are partially integrated in the activated carbon structure.

Future work is needed to verify the proposed hypothesis, keeping in mind the chemical composition of an activated carbon, especially the C/H ratio, in addition to pore structure and surface area. This will be a challenge for further investigations with more complex water matrices containing micropollutants. Other than this, the proposed approach could help in improving carbonaceous adsorbent materials, whilst providing further understanding in regeneration processes.

Data Availability

The datasets generated and analysed during the current study are available in the zenodo repository [234].

Acknowledgements

We thankfully acknowledge Frederik Zietzschmann for providing the activated carbons and the information about their characterisation, as well as Ute Kalbe, Jutta Jakobs and Christiane Weimann for very kindly XRF, LC-MS/MS and SEM measurements, respectively. We thank Glen J Smales for the very helpful proofreading. Last but not least we acknowledge support by the German Research Foundation and the Open Access Publication Fund of TU Berlin.

Author contributions

D.D., C.G., M.J., A.S.R. and U.B. planed the study and designed the experiments. D.D. conducted the experiments. All authors discussed the results. P.E. discovered the relationship of the activated carbon H content and elimination temperature of isocyanic acid. D.D. created all the figures. D.D. and C.G. wrote the original manuscript which all authors reviewed and revised.

5

Zusammenfassung und Schlussfolgerungen

Die Feststoffe in Wasserproben unterschiedlicher Herkunft müssen für aktuelle Fragestellungen eingehend charakterisiert werden, sei es für die Bestimmung von Mikroplastiksorten und -gehalten oder für die Charakterisierung frischer und beladener Aktivkohle. Dass thermoanalytische Verfahren mit Zersetzungsgasanalyse diese Fragestellungen unterstützen und darüber hinaus neue analytische Perspektiven für die Wasserqualität und Wasseraufbereitung bereithalten, wurde in den vorangegangenen Kapiteln gezeigt.

Thermoanalytische Detektion von Mikroplastik für spezifische Fragestellungen optimierbar
Am Beispiel der Detektion von Mikroplastik in einer Schwebstoffmatrix konnten die grundlegenden Pyrolysemechanismen gezeigt und deren analytische Zugänglichkeit über verschiedene apparative Zersetzungsgasanalysen demonstriert werden. Außerdem stellte sich der Mehrwert einer thermogravimetrischen Analyse (TGA) zur Pyrolyse der Probe heraus, der nicht nur in der Aufgabe einer größeren Probenmenge begründet ist. Die zusätzlich zur Zersetzungsgasanalyse bestimmten TGA-Massenverluste ermöglichen eine zusätzliche Kontrolle der bestimmten Polymergehalte und erlauben bei Mehrfachbestimmungen eine Homogenitätsprüfung der Probe. Das spezialisierte und häufig für die Mikroplastikdetektion eingesetzte TED-GC/MS System erwies sich für die Schwebstoffmatrix als einziges fähig, eine echte Identifikation der Polymere PE, PP, PS und PET zu leisten. Die einfacheren Systeme TGA-FTIR, TGA-MS und die für die Mikroplastikdetektion neu vorgestellte MCC sind jedoch durchaus in der Lage, Mikroplastikgehalte in *bekannter* Umweltmatrix zu quantifizieren. TGA-FTIR und MCC haben damit als erstaunlich robuste bzw. sehr schnelle Methode das Potenzial, in Monitoringprogrammen eingesetzt zu werden. Mit TGA-FTIR wurden die besten Wiederholgenauigkeiten (Präzision) erreicht, es zeigten sich aber Einschränkungen bei der Unterscheidung von PE und PP sowie bei der Bestimmung von PET. Die in diesem Fall weniger empfindliche TGA-MS eröffnet jedoch durch die Verbindung von Zersetzungstemperatur (TGA) und der Detektion des Zersetzungsprodukts Benzen (m/z 77) das Potenzial, PVC nachzuweisen. Durch Kapitel 2 wurde deutlich, dass bei der für thermoanalytische Verfahren etablierten Detektion von Mikroplastik Optimierungen entsprechend der Fragestellung möglich sind.

Thermoanalytische Aktivkohlecharakterisierung gewinnbringend und praxisnah einsetzbar
Herauszustellen ist die besondere Eignung der thermoanalytischen Verfahren für die Charakterisierung von Aktivkohle. Hier kommt zum Tragen, dass der Herstellungsprozess von Aktivkohle mit der Karbonisierung bereits eine Pyrolyse des Feststoffs darstellt. Die nachfolgende analytische Pyrolyse zeigt dadurch nur den chemischen Unterschied auf, der nach der Karbonisierung z. B. durch die Aktivierung entsteht. Für Aktivkohle ist das neben der Adsorption von Stickstoff und Wasser aus der Luft die Absättigung radikalischer Defektstellen in der Kohlenstoffstruktur durch Sauerstoff. Die dadurch entstehenden funktionellen Gruppen konnten mittels TGA-FTIR qualitativ und quantitativ für den Großteil der 25 untersuchten, kommerziell verfügbarer Aktivkohlen bestimmt werden. Chemisch aktivierte Aktivkohlen auf Holzkohlebasis wiesen die höchsten Gehalte und eine große Spannweite an Carboxylgruppen auf (310 - 1380 μmol g^{-1}). Aktivkohlen aus Kokosnussschalen und Steinkohlen hatten anteilig am meisten Carbonylgruppen (330 - 850 μmol g^{-1}). Aus Braunkohlen hergestellte Aktivkohlen enthielten generell die wenigsten funktionellen Gruppen, in denen am meisten Carbonyl- und Pyrongruppen vertreten waren (80 - 400 μmol g^{-1} bzw. 120 - 420 μmol g^{-1}). Aufgrund der pyrolytischen Vorgeschichte von Aktivkohle konnten zudem allein aus den TGA-Massenverlusten unter Pyrolyse und Oxidation Korrelationen mit dem Sauerstoff- und Kohlenstoffgehalt der Probe sowie ihrem Point-of-zero-charge hergestellt werden. Zusammen mit dem DTG-Profil der Pyrolyse bis 1000 °C, als *Fingerabdruck* der chemischen Zusammensetzung der Aktivkohle, könnte die TGA damit auch einen praktischen Nutzen für die Qualitätskontrolle in Wasserwerken und auf Kläranlagen mit Aktivkohlestufe erbringen.

Es wurde in Kapitel 3 gezeigt, dass TGA und TGA-FTIR auf verschiedenen Informationsniveaus die Charakterisierungsmethoden von Aktivkohle ergänzen können und wie stark die Eigenschaften zwischen verschiedenen Aktivkohleprodukten streuen (z. B. Sauerstoffgehalt von 0,5 % bis zu extremen 17,6 % in chemisch aktivierter Holzkohle). Es wurde zudem deutlich, dass die gewonnenen Informationen und die im großen Datensatz aufgedeckten Zusammenhänge nur mit Hilfe automatisierter und computergestützter Auswertealgorithmen möglich waren. Dazu zählen die Hauptkomponentenanalysen der relativen Zusammensetzung anorganischer Elemente sowie der funktionellen Gruppen. Es konnte gezeigt werden, dass die anorganische Elementzusammensetzung spezifisch für das Ausgangsmaterial und den Aktivierungsprozess ist. Mit Hilfe des entwickelten Python-Packages zur Auswertung von TGA-FTIR Messungen, wird eine reproduzierbare und wissenschaftlich bewertbare Bestimmung der sauerstoffhaltigen funktionellen Gruppen möglich [191]. Die gewonnenen Detailinformationen über das Auftreten funktioneller Gruppen in Abhängigkeit des Ausgangsmaterials und der Aktivierungsprozesse könnten zum Verständnis von Adsorptionsmechanismen in realem Wasser beitragen und uns einen Schritt näher an die Prognose von Entfernungsgraden bringen. Ein noch ausstehender Schritt ist nun die Materialeigenschaften der Aktivkohlen mit ihren Adsorptionseigenschaften in realem Wasser in Verbindung zu setzen.

Nachdem die analytische Pyrolyse in Kapitel 3 ihr Potenzial auch als reine TGA für praxisnahe Fragestellungen bewiesen hat, ist für grundlegendere Forschungsfragen die Kombination mehrerer komplementärer thermoanalytischer Methoden notwendig, um neue Ergebnisse aus den untersuchten Probensystemen fundiert zu interpretieren. In dieser Arbeit wurden daher die Adsorptionseigenschaften nicht vertieft betrachtet, sondern im letzten, 4. Kapitel das

Charakterisierungspotenzial für beladene Aktivkohle (Adsorbat-Systeme) untersucht. Dazu wurden drei deutlich unterschiedliche Pulveraktivkohlen ausgewählt und in Einstoffsystemen mit verschiedenen Mengen Carbamazepin beladen.

Grundlagenforschung zu Adsorptionszuständen und thermischen Regenerationsprozessen Die resultierenden Ergebnisse waren in vielfältiger Hinsicht bemerkenswert. So zeigte sich abermals der Nutzen der zahlreichen Möglichkeiten thermoanalytischer Verfahren. TGA, Zersetzungskinetik, TGA-FTIR und TED-GC/MS trugen alle zu wichtigen Einzelinformationen bei, um die Adsorbat-Systeme thermoanalytisch zu beschreiben. Verglichen mit der Materialcharakterisierung der unbeladenen Aktivkohlen, ist die Zersetzung des adsorbierten Carbamazepins im DTG-Profil gut von der Abspaltung der funktionellen Gruppen zu unterscheiden. Trotz starker Unterschiede zwischen den untersuchten Aktivkohlen zeigte das thermische Zersetzungsverhalten des sehr gut adsorbierbaren Carbamazepins zwei charakteristische Massenverluststufen, welche jedoch in den Temperaturen variierten. Carbamazepin kann thermisch nicht wieder vollständig von der Aktivkohle getrennt werden, es blieben indirekt proportional zur Beladung 42 % bis 74 % sorbiert. Im Gegensatz zu reinem Carbamazepin welches vollständig in Isocyansäure und Iminostilben zerfällt, konnten für die Adsorbat-Systeme 55 verschiedene Zersetzungsprodukte detektiert werden. Das Hauptzersetzungsprodukt Acridin wurde in allen Proben, auch bei geringer Carbamazepin-Beladung nachgewiesen. Die anderen Zersetzungsprodukte bildeten sich in Abhängigkeit des C/H-Verhältnisses als auch des Schwefelgehalts der Aktivkohlen. Diese Unterschiede zwischen den Adsorbat-Systemen unterschiedlicher Beladung sind möglicherweise auf verschiedene Adsorptionszustände des Carbamazepins auf den drei Aktivkohlen zurückzuführen. Es wurde geschlussfolgert, dass Sorptionsplätze und Adsorptionszustände auf Grundlage der Pyrolyseprozesse differenziert werden können.

Die Bildung der Zersetzungsprodukte, die durch intramolekulare Wasserstoffumlagerung oder durch Schwefel in der Molekülstruktur nicht von Carbamazepin abgeleitet werden konnten, deuten zudem auf eine starke Wechselwirkung zwischen Adsorptiv und Adsorbens hin. Die thermische Zersetzung adsorbierten Carbamazepins ist zusätzlich von intermolekularen Wasserstofftransfers bestimmt, die überwiegend von der ohnehin wasserstoffarmen Aktivkohle zu den Pyrolyseprodukten verlaufen, was sich an mehrheitlich niedrigeren C/H-Verhältnissen der Zersetzungsprodukte im Vergleich zu ihrem Ausgangsmolekül zeigt. Davon ausgehend wurde postuliert, dass die Pyrolyse von Aktivkohle-Adsorbaten, wie sie auch bei der thermischen Regeneration stattfindet, den Graphitisierungsgrad der Aktivkohle erhöht, da sich in der Gesamtbilanz ihr C/H-Verhältnis erhöhen muss. Aktivkohle an sich hätte damit nach der Regeneration einen thermodynamisch günstigeren Zustand erreicht als sie es noch vor der Beladung hatte. Aus dieser Perspektive könnten Adsorptivmoleküle für Sorptionsplätze bevorzugt werden, die durch die Adsorption potenziell die Aktivkohle ihrer thermodynamisch bevorzugten Kohlenstoffmodifikation des Graphits näherbringen.

Forschungsbedarf und Potenziale Aus den vorgestellten Einzelstudien lässt sich weiterführender Forschungsbedarf ableiten. Sie ergeben sich aus der neuen Perspektive, mit der durch thermoanalytische Verfahren wasserwirtschaftliche Fragestellungen bearbeitet werden können. Im Vordergrund steht sicherlich die Vereinigung der Ergebnisse mit den Adsorptionseigenschaften der Aktivkohlen, um Entfernungsgrade von Spurenstoffen zu prognostizieren. Aber auch die

mögliche Erhöhung des Graphitisierungsgrades und die starke Wechselwirkung in Adsorbaten bieten Forschungspotenziale, um die Adsorption an Aktivkohle besser zu verstehen und Mechanismen zu unterscheiden. Nicht zuletzt ist auch die Materialcharakterisierung von Aktivkohle noch kein abgeschlossenes Feld. So weisen beispielsweise chemisch aktivierte Aktivkohlen eine auffällig andere Porenstruktur auf, die möglicherweise durch Phosphor-Spezies im Kohlenstoffgerüst stabilisiert werden und durch OH-Gruppen auch die Oberflächenchemie im Vergleich zu anderen Aktivkohlen verändert. Mit Blick auf die Prognose von Spurenstoff-Entfernungsgraden lohnt es sich, diese detaillierter zu charakterisieren.

Die vorliegende Arbeit hat in den vorangegangenen Kapiteln gezeigt, dass thermoanalytische Methoden auf verschiedensten Ebenen gewinnbringend für aktuelle Fragen zu Wasserqualität und Wasseraufbereitung eingesetzt werden können. Im Kontext der Mikroverunreinigungen ist der Pool an pyrolytischen Methoden, die sich für eine *detektierende Fragestellung* in komplexen Umweltproben (Mikroplastikdetektion) als geeignet erwiesen haben vielversprechend und noch nicht ausgeschöpft. Außerdem können sie im Gebiet der Spurenstoffelimination mit Aktivkohle zu deren *Materialcharakterisierung* beitragen und leisten dort sowohl auf Anlagenebene für die Qualitätskontrolle als auch für Forschungsfragen bezüglich der Spurenstoffadsorption einen Beitrag mit der Differenzierung und Quantifizierung funktioneller Oberflächengruppen. Auf dem Weg zur Prognose von Entfernungsgraden für Spurenstoffe durch verschiedene Aktivkohlen ist eine vertiefende Untersuchung von *Adsorptionsplätzen und -zuständen* sowie von Prozessen während der Aktivkohleregeneration möglich und hält noch viel zu hebendes Potenzial bereit.

Literatur

[1] Harry Marsh, Edward A. Heintz und Francisco Rodríguez-Reinoso. *Introduction to Carbon Technologies*. Universidad de Alicante, 1997.

[2] DIN 2000. *DIN 2000:2017-02, Zentrale Trinkwasserversorgung — Leitsätze Für Anforderungen an Trinkwasser, Planung, Bau, Betrieb Und Instandhaltung Der Versorgungsanlagen*. 2017. DOI: 10.31030/2607901.

[3] UN. *Resolution Adopted by the General Assembly on 28 July 2010 — 64/292. The Human Right to Water and Sanitation*. 2010.

[4] UN. *Resolution Adopted by the General Assembly on 25 September 2015 — 70/1. Transforming Our World: The 2030 Agenda for Sustainable Development*. 2015.

[5] Martin Jekel, Nina Baur, Uta Böckelmann, Uwe Dünnbier, Alexander Eckhardt, Regina Gnirß, Tamara Grummt, Daniel Hummelt, Thomas Lucke, Felix Meinel, Ulf Miehe, Daniel Mutz, Stephan Pflugmacher Lima, Thorsten Reemtsma, Christian Remy, Linda Schlittenbauer, Wolfgang Schulz, Bettina Seiwert, Alexander Sperlich, Michael Stapf, Patricia van Zerball-Baar, Melanie Wenzel, Frederik Zietzschmann und Aki Sebastian Ruhl. *Anthropogene Spurenstoffe und Krankheitserreger im urbanen Wasserkreislauf - Bewertung, Barrieren und Risikokommunikation (ASKURIS)*. Universitätsverlag der TU Berlin, 2016. DOI: http://dx.doi.org/10.14279/depositonce-4979.

[6] M. Ahting, F. Brauer, A. Duffek und I. Ebert. *Empfehlungen Zur Reduzierung von Mikroverunreinigungen in Den Gewässern*. Hintergrund. Dessau-Roßlau: Umweltbundesamt, 2018.

[7] Ulrike Braun. *Statuspapier: Mikroplastik-Analytik — Probenahme, Probenaufbereitung Und Detektionsverfahren*. Techn. Ber. 2020, S. 65.

[8] Erik Hendrickson, Elizabeth C. Minor und Kathryn Schreiner. "Microplastic Abundance and Composition in Western Lake Superior As Determined via Microscopy, Pyr-GC/MS, and FTIR". In: *Environmental Science & Technology* 52.4 (2018), S. 1787–1796. DOI: 10.1021/acs.est.7b05829.

[9] Anna M. Elert, Roland Becker, Erik Duemichen, Paul Eisentraut, Jana Falkenhagen, Heinz Sturm und Ulrike Braun. "Comparison of Different Methods for MP Detection: What Can We Learn from Them, and Why Asking the Right Question before Measurements Matters?" In: *Environmental Pollution* 231 (2017), S. 1256–1264. DOI: 10.1016/j.envpol.2017.08.074.

[10] Daniel Dittmann, Ulrike Braun, Martin Jekel und Aki Sebastian Ruhl. "Quantification and Characterisation of Activated Carbon in Activated Sludge by Thermogravimetric and Evolved Gas Analyses". In: *Journal of Environmental Chemical Engineering* 6.2 (2018), S. 2222–2231. DOI: 10.1016/j.jece.2018.03.010.

[11] Daniel Dittmann, Thomas Lucke, Aki S. Ruhl, Rudi Winzenbacher, Martin Jekel und Ulrike Braun. "Untersuchungen zu biologischen, organischen und anorganischen Veränderungen granulierter Aktivkohlen während der Trinkwasseraufbereitung". In: *Vom Wasser* 118.2 (2020), S. 47–50.

[12] Frederik Zietzschmann, Stefan Dittmar, Lydia Splettstößer, Jonas Hunsicker, Daniel Dittmann, Felix Meinel, Annette Rößler, Steffen Metzger, Martin Jekel und Aki Sebastian Ruhl. "Fast Empirical Lab Method for Performance Projections of Large-Scale Powdered Activated Carbon Re-Circulation Plants". In: *Chemosphere* 215 (2019), S. 563–573. DOI: 10.1016/j.chemosphere.2018.10.055.

[13] Christian Abegglen und Hansruedi Siegrist. *Mikroverunreinigungen Aus Kommunalem Abwasser. Verfahren Zur Weitergehenden Elimination Auf Kläranlagen.* Umwelt-Wissen 1214. Bern: Bundesamt für Umwelt, 2012.

[14] Finnian Freeling, David Behringer, Felix Heydel, Marco Scheurer, Thomas A. Ternes und Karsten Nödler. "Trifluoroacetate in Precipitation: Deriving a Benchmark Data Set". In: *Environmental Science & Technology* 54.18 (2020), S. 11210–11219. DOI: 10.1021/acs.est.0c02910.

[15] Fatima El-Athman, Lorenz Adrian, Martin Jekel und Anke Putschew. "Deiodination in the Presence of Dehalococcoides Mccartyi Strain CBDB1: Comparison of the Native Enzyme and Co-Factor Vitamin B12". In: *Environmental Science and Pollution Research* 26.31 (2019), S. 32636–32644. DOI: 10.1007/s11356-019-06505-z.

[16] U. Hübner, B. Seiwert, T. Reemtsma und M. Jekel. "Ozonation Products of Carbamazepine and Their Removal from Secondary Effluents by Soil Aquifer Treatment – Indications from Column Experiments". In: *Water Research* 49 (2014), S. 34–43. DOI: 10.1016/j.watres.2013.11.016.

[17] Clara H. Jeong, Edward J. Machek, Morteza Shakeri, Stephen E. Duirk, Thomas A. Ternes, Susan D. Richardson, Elizabeth D. Wagner und Michael J. Plewa. "The Impact of Iodinated X-Ray Contrast Agents on Formation and Toxicity of Disinfection by-Products in Drinking Water". In: *Journal of Environmental Sciences*. Water Treatment and Disinfection By-Products 58 (2017), S. 173–182. DOI: 10.1016/j.jes.2017.03.032.

[18] Erica Donner, Tina Kosjek, Signe Qualmann, Kresten Ole Kusk, Ester Heath, D. Michael Revitt, Anna Ledin und Henrik Rasmus Andersen. "Ecotoxicity of Carbamazepine and Its UV Photolysis Transformation Products". In: *Science of The Total Environment* 443 (2013), S. 870–876. DOI: 10.1016/j.scitotenv.2012.11.059.

[19] Robert Loos, Raquel Carvalho, Diana C. António, Sara Comero, Giovanni Locoro, Simona Tavazzi, Bruno Paracchini, Michela Ghiani, Teresa Lettieri, Ludek Blaha, Barbora Jarosova, Stefan Voorspoels, Kelly Servaes, Peter Haglund, Jerker Fick, Richard H. Lindberg, David Schwesig und Bernd M. Gawlik. "EU-Wide Monitoring Survey on Emerging Polar Organic

Contaminants in Wastewater Treatment Plant Effluents". In: *Water Research* 47.17 (2013), S. 6475–6487. DOI: 10.1016/j.watres.2013.08.024.

[20] Hanwei Ren, Rikard Tröger, Lutz Ahrens, Karin Wiberg und Daqiang Yin. "Screening of Organic Micropollutants in Raw and Drinking Water in the Yangtze River Delta, China". In: *Environmental Sciences Europe* 32.1 (2020), S. 67. DOI: 10.1186/s12302-020-00342-5.

[21] Paul M. Bradley, Celeste A. Journey, Kristin M. Romanok, Larry B. Barber, Herbert T. Buxton, William T. Foreman, Edward T. Furlong, Susan T. Glassmeyer, Michelle L. Hladik, Luke R. Iwanowicz, Daniel K. Jones, Dana W. Kolpin, Kathryn M. Kuivila, Keith A. Loftin, Marc A. Mills, Michael T. Meyer, James L. Orlando, Timothy J. Reilly, Kelly L. Smalling und Daniel L. Villeneuve. "Expanded Target-Chemical Analysis Reveals Extensive Mixed-Organic-Contaminant Exposure in U.S. Streams". In: *Environmental Science & Technology* 51.9 (2017), S. 4792–4802. DOI: 10.1021/acs.est.7b00012.

[22] Rikard Tröger, Hanwei Ren, Daqiang Yin, Cristina Postigo, Phuoc Dan Nguyen, Christine Baduel, Oksana Golovko, Frederic Been, Hanna Joerss, Maria Rosa Boleda, Stefano Polesello, Marco Roncoroni, Sachi Taniyasu, Frank Menger, Lutz Ahrens, Foon Yin Lai und Karin Wiberg. "What's in the Water? – Target and Suspect Screening of Contaminants of Emerging Concern in Raw Water and Drinking Water from Europe and Asia". In: *Water Research* 198 (2021), S. 117099. DOI: 10.1016/j.watres.2021.117099.

[23] Marianne Stuart, Dan Lapworth, Emily Crane und Alwyn Hart. "Review of Risk from Potential Emerging Contaminants in UK Groundwater". In: *Science of The Total Environment* 416 (2012), S. 1–21. DOI: 10.1016/j.scitotenv.2011.11.072.

[24] Thorsten Reemtsma, Urs Berger, Hans Peter H. Arp, Hervé Gallard, Thomas P. Knepper, Michael Neumann, José Benito Quintana und Pim de Voogt. "Mind the Gap: Persistent and Mobile Organic Compounds—Water Contaminants That Slip Through". In: *Environmental Science & Technology* 50.19 (2016), S. 10308–10315. DOI: 10.1021/acs.est.6b03338.

[25] Frank Menger, Pablo Gago-Ferrero, Karin Wiberg und Lutz Ahrens. "Wide-Scope Screening of Polar Contaminants of Concern in Water: A Critical Review of Liquid Chromatography-High Resolution Mass Spectrometry-Based Strategies". In: *Trends in Environmental Analytical Chemistry* 28 (2020), e00102. DOI: 10.1016/j.teac.2020.e00102.

[26] Michael Neumann. "Vorschlag Für Kriterien Und Ein Bewertungskonzept Zur Identifizierung von Persistenten, Mobilen Und Toxischen (PMT-) Stoffen Zum Schutz Des Rohwassers Zur Trinkwassergewinnung Unter Der EU-Verordnung REACH". In: *Zbl. Geol. Paläont. Teil I* 1 (2017), S. 91–101.

[27] European Parliament and Council. *Regulation (EC) No 1907/2006 of the European Parliament and of the Council of 18 December 2006 Concerning the Registration, Evaluation, Authorisation and Restriction of Chemicals (REACH), Establishing a European Chemicals Agency, Amending Directive 1999/45/EC and Repealing Council Regulation (EEC) No 793/93 and Commission Regulation (EC) No 1488/94 as Well as Council Directive 76/769/EEC and Commission Directives 91/155/EEC, 93/67/EEC, 93/105/EC and 2000/21/EC*. 2007.

[28] European Parliament and Council. *Directive 2000/60/EC Establishing a Framework for the Community Action in the Field of Water Policy*. 2000.

[29] European Parliament and Council. *Directive 2008/105/EC of the European Parliament and of the Council of 16 December 2008 on Environmental Quality Standards in the Field of Water Policy, Amending and Subsequently Repealing Council Directives 82/176/EEC, 83/513/EEC, 84/156/EEC, 84/491/EEC, 86/280/EEC and Amending Directive 2000/60/EC of the European Parliament and of the Council*. 2008.

[30] European Parliament and Council. *Directive 2013/39/EU of the European Parliament and of the Council of 12 August 2013 Amending Directives 2000/60/EC and 2008/105/EC as Regards Priority Substances in the Field of Water Policy Text with EEA Relevance*. 2013.

[31] European Parliament and Council. *Commission Implementing Decision (EU) 2015/495 of 20 March 2015 Establishing a Watch List of Substances for Union-Wide Monitoring in the Field of Water Policy Pursuant to Directive 2008/105/EC (Notified under Document C(2015) 1756) Text with EEA Relevance*. 2015.

[32] UBA. "Bewertung Der Anwesenheit Teil- Oder Nicht Bewertbarer Stoffe Im Trinkwasser Aus Gesundheitlicher Sicht". In: *Bundesgesundheitsblatt - Gesundheitsforschung - Gesundheitsschutz* 46.3 (2003), S. 249–251. DOI: 10.1007/s00103-003-0576-7.

[33] T. Hillenbrand, F. Tettenborn und M. Bloser. *Ergebnispapier – Ergebnisse der Phase 2 des Stakeholder-Dialogs SSpurenstoffstrategie des Bundesßur Umsetzung von Maßnahmen für die Reduktion von Spurenstoffeinträgen in die Gewässer*. 2019.

[34] Carolin Völker, Johanna Kramm und Martin Wagner. "On the Creation of Risk: Framing of Microplastics Risks in Science and Media". In: *Global Challenges* 4.6 (2020), S. 1900010. DOI: 10.1002/gch2.201900010.

[35] Nanna B. Hartmann, Thorsten Hüffer, Richard C. Thompson, Martin Hassellöv, Anja Verschoor, Anders E. Daugaard, Sinja Rist, Therese Karlsson, Nicole Brennholt, Matthew Cole, Maria P. Herrling, Maren C. Hess, Natalia P. Ivleva, Amy L. Lusher und Martin Wagner. "Are We Speaking the Same Language? Recommendations for a Definition and Categorization Framework for Plastic Debris". In: *Environmental Science & Technology* (2019). DOI: 10.1021/acs.est.8b05297.

[36] ISO/TR 21960. *ISO/TR 21960:2020: Plastics — Environmental Aspects — State of Knowledge and Methodologies*. 2020.

[37] Committee for Risk Assessment (RAC) und Committee for Socio-economic Analysis (SEAC). *ECHA/RAC/RES-O-0000006790-71-01/F, ECHA/SEAC/RES-O-0000006901-74-01/F — Opinion of the Committee for Risk Assessment and Opinion of the Committee for Socio-Economic Analysison an Annex XV Dossier Proposing Restrictions of the Manufacture, Placing on the Market or Use of a Substance within the EU*. 2020.

[38] Anna Kukkola, Stefan Krause, Iseult Lynch, Gregory H. Sambrook Smith und Holly Nel. "Nano and Microplastic Interactions with Freshwater Biota – Current Knowledge, Challenges and Future Solutions". In: *Environment International* 152 (2021), S. 106504. DOI: 10.1016/j.envint.2021.106504.

[39] Stefan Krause, Viktor Baranov, Holly A. Nel, Jennifer D. Drummond, Anna Kukkola, Timothy Hoellein, Gregory H. Sambrook Smith, Joerg Lewandowski, Berta Bonet, Aaron I. Packman, Jon Sadler, Valentyna Inshyna, Steve Allen, Deonie Allen, Laurent Simon, Florian Mermillod-Blondin und Iseult Lynch. "Gathering at the Top? Environmental Controls of Microplastic Uptake and Biomagnification in Freshwater Food Webs". In: *Environmental Pollution* 268 (2021), S. 115750. DOI: 10.1016/j.envpol.2020.115750.

[40] Albert A. Koelmans, Nur Hazimah Mohamed Nor, Enya Hermsen, Merel Kooi, Svenja M. Mintenig und Jennifer De France. "Microplastics in Freshwaters and Drinking Water: Critical Review and Assessment of Data Quality". In: *Water Research* 155 (2019), S. 410–422. DOI: 10.1016/j.watres.2019.02.054.

[41] Merel Kooi und Albert A. Koelmans. "Simplifying Microplastic via Continuous Probability Distributions for Size, Shape, and Density". In: *Environmental Science & Technology Letters* 6.9 (2019), S. 551–557. DOI: 10.1021/acs.estlett.9b00379.

[42] M. Jekel. "Flockung (Flocculation)". In: *DVGW-Schriftenreihe Wasser, Kurs 6: Wasseraufbereitungstechnik Für Ingenieure*. Bd. 206. Bonn: Wirtschafts- und Verlagsges. Gas und Wasser mbH., 1987, S. 4.1–4.28.

[43] Stephan Wagner, Thorsten Hüffer, Philipp Klöckner, Maren Wehrhahn, Thilo Hofmann und Thorsten Reemtsma. "Tire Wear Particles in the Aquatic Environment - A Review on Generation, Analysis, Occurrence, Fate and Effects". In: *Water Research* 139 (2018), S. 83–100. DOI: 10.1016/j.watres.2018.03.051.

[44] Fionn Murphy, Ciaran Ewins, Frederic Carbonnier und Brian Quinn. "Wastewater Treatment Works (WwTW) as a Source of Microplastics in the Aquatic Environment". In: *Environmental Science & Technology* 50.11 (2016), S. 5800–5808. DOI: 10.1021/acs.est.5b05416.

[45] Fabio Corradini, Pablo Meza, Raúl Eguiluz, Francisco Casado, Esperanza Huerta-Lwanga und Violette Geissen. "Evidence of Microplastic Accumulation in Agricultural Soils from Sewage Sludge Disposal". In: *Science of The Total Environment* 671 (2019), S. 411–420. DOI: 10.1016/j.scitotenv.2019.03.368.

[46] Delphine Kawecki und Bernd Nowack. "Polymer-Specific Modeling of the Environmental Emissions of Seven Commodity Plastics As Macro- and Microplastics". In: *Environmental Science & Technology* 53.16 (2019), S. 9664–9676. DOI: 10.1021/acs.est.9b02900.

[47] Rachid Dris, Johnny Gasperi, Mohamed Saad, Cécile Mirande und Bruno Tassin. "Synthetic Fibers in Atmospheric Fallout: A Source of Microplastics in the Environment?" In: *Marine Pollution Bulletin* 104.1 (2016), S. 290–293. DOI: 10.1016/j.marpolbul.2016.01.006.

[48] Melanie Bergmann, Sophia Mützel, Sebastian Primpke, Mine B. Tekman, Jürg Trachsel und Gunnar Gerdts. "White and Wonderful? Microplastics Prevail in Snow from the Alps to the Arctic". In: *Science Advances* 5.8 (2019), eaax1157. DOI: 10.1126/sciadv.aax1157.

[49] Rosa Peñalver, Isabel Costa-Gómez, Natalia Arroyo-Manzanares, José María Moreno, Ignacio López-García, Stella Moreno-Grau und Manuel Hernández Córdoba. "Assessing the Level of Airborne Polystyrene Microplastics Using Thermogravimetry-Mass Spectrometry:

Results for an Agricultural Area". In: *Science of The Total Environment* 787 (2021), S. 147656. DOI: 10.1016/j.scitotenv.2021.147656.

[50] Alvise Vianello, Rasmus Lund Jensen, Li Liu und Jes Vollertsen. "Simulating Human Exposure to Indoor Airborne Microplastics Using a Breathing Thermal Manikin". In: *Scientific Reports* 9.1 (2019), S. 1–11. DOI: 10.1038/s41598-019-45054-w.

[51] Valerie Stock, Christoph Fahrenson, Andreas Thuenemann, Merve Hilal Dönmez, Linn Voss, Linda Böhmert, Albert Braeuning, Alfonso Lampen und Holger Sieg. "Impact of Artificial Digestion on the Sizes and Shapes of Microplastic Particles". In: *Food and Chemical Toxicology* 135 (2020), S. 111010. DOI: 10.1016/j.fct.2019.111010.

[52] James H. Bridson, Evamaria C. Gaugler, Dawn A. Smith, Grant L. Northcott und Sally Gaw. "Leaching and Extraction of Additives from Plastic Pollution to Inform Environmental Risk: A Multidisciplinary Review of Analytical Approaches". In: *Journal of Hazardous Materials* 414 (2021), S. 125571. DOI: 10.1016/j.jhazmat.2021.125571.

[53] Caroline Goedecke, Ulrike Mülow-Stollin, S. Hering, Janine Richter, Christian Piechotta, Andrea Paul und Ulrike Braun. "A First Pilot Study on the Sorption of Environmental Pollutants on Various Microplastic Materials". In: (2017).

[54] Axel Müller, Roland Becker, Ute Dorgerloh, Franz-Georg Simon und Ulrike Braun. "The Effect of Polymer Aging on the Uptake of Fuel Aromatics and Ethers by Microplastics". In: *Environmental Pollution* 240 (2018), S. 639–646. DOI: 10.1016/j.envpol.2018.04.127.

[55] Thorsten Hüffer, Anne-Katrin Weniger und Thilo Hofmann. "Sorption of Organic Compounds by Aged Polystyrene Microplastic Particles". In: *Environmental Pollution* 236 (2018), S. 218–225. DOI: 10.1016/j.envpol.2018.01.022.

[56] Albert A. Koelmans, Adil Bakir, G. Allen Burton und Colin R. Janssen. "Microplastic as a Vector for Chemicals in the Aquatic Environment: Critical Review and Model-Supported Reinterpretation of Empirical Studies". In: *Environmental Science & Technology* 50.7 (2016), S. 3315–3326. DOI: 10.1021/acs.est.5b06069.

[57] S. Dittmar, J. Pries, A. S. Ruhl und M. Jekel. "System zur Untersuchung der Sedimentation von Mikroplastik (10–300 μm)". In: *Vom Wasser* 119.2 (2021), S. 35–37. DOI: 10.1002/vomw.202100004.

[58] Jennifer D. Drummond, Holly A. Nel, Aaron I. Packman und Stefan Krause. "Significance of Hyporheic Exchange for Predicting Microplastic Fate in Rivers". In: *Environmental Science & Technology Letters* 7.10 (2020), S. 727–732. DOI: 10.1021/acs.estlett.0c00595.

[59] Wei Chen, Zhen-Yu Ouyang, Chen Qian und Han-Qing Yu. "Induced Structural Changes of Humic Acid by Exposure of Polystyrene Microplastics: A Spectroscopic Insight". In: *Environmental Pollution* 233 (2018), S. 1–7. DOI: 10.1016/j.envpol.2017.10.027.

[60] Ren Wei und Wolfgang Zimmermann. "Microbial Enzymes for the Recycling of Recalcitrant Petroleum-Based Plastics: How Far Are We?" In: *Microbial Biotechnology* 10.6 (2017), S. 1308–1322. DOI: 10.1111/1751-7915.12710.

[61] Gerrit Renner, Alexander Nellessen, Alexander Schwiers, Mike Wenzel, Torsten C. Schmidt und Jürgen Schram. "Hydrophobicity–Water/Air–Based Enrichment Cell for Microplastics Analysis within Environmental Samples: A Proof of Concept". In: *MethodsX* 7 (2020), S. 100732. DOI: 10.1016/j.mex.2019.11.006.

[62] Lars Eitzen, Aki Sebastian Ruhl und Martin Jekel. "Particle Size and Pre-Treatment Effects on Polystyrene Microplastic Settlement in Water: Implications for Environmental Behavior and Ecotoxicological Tests". In: *Water* 12.12 (2020), S. 3436. DOI: 10.3390/w12123436.

[63] Lukas Wander, Alvise Vianello, Jes Vollertsen, Frank Westad, Ulrike Braun und Andrea Paul. "Exploratory Analysis of Hyperspectral FTIR Data Obtained from Environmental Microplastics Samples". In: *Analytical Methods* 12.6 (2020), S. 781–791. DOI: 10.1039/C9AY02483B.

[64] Gerrit Renner, Alexander Nellessen, Alexander Schwiers, Mike Wenzel, Torsten C. Schmidt und Jürgen Schram. "Data Preprocessing & Evaluation Used in the Microplastics Identification Process: A Critical Review & Practical Guide". In: *TrAC Trends in Analytical Chemistry* 111 (2019), S. 229–238. DOI: 10.1016/j.trac.2018.12.004.

[65] Gerrit Renner, Torsten C. Schmidt und Jürgen Schram. "Automated Rapid & Intelligent Microplastics Mapping by FTIR Microscopy: A Python–Based Workflow". In: *MethodsX* 7 (2020), S. 100742. DOI: 10.1016/j.mex.2019.11.015.

[66] Nadiia Yakovenko, Aline Carvalho und Alexandra ter Halle. "Emerging Use Thermo-Analytical Method Coupled with Mass Spectrometry for the Quantification of Micro(Nano)Plastics in Environmental Samples". In: *TrAC Trends in Analytical Chemistry* 131 (2020), S. 115979. DOI: 10.1016/j.trac.2020.115979.

[67] Axel Müller, Caroline Goedecke, Paul Eisentraut, Christian Piechotta und Ulrike Braun. "Microplastic Analysis Using Chemical Extraction Followed by LC-UV Analysis: A Straightforward Approach to Determine PET Content in Environmental Samples". In: *Environmental Sciences Europe* 32.1 (2020), S. 85. DOI: 10.1186/s12302-020-00358-x.

[68] Sebastian Primpke, Marten Fischer, Claudia Lorenz, Gunnar Gerdts und Barbara M. Scholz-Böttcher. "Comparison of Pyrolysis Gas Chromatography/Mass Spectrometry and Hyperspectral FTIR Imaging Spectroscopy for the Analysis of Microplastics". In: *Analytical and Bioanalytical Chemistry* 412.30 (2020), S. 8283–8298. DOI: 10.1007/s00216-020-02979-w.

[69] Stefano Materazzi. "Thermogravimetry – Infrared Spectroscopy (TG-FTIR) Coupled Analysis". In: *Applied Spectroscopy Reviews* 32.4 (1997), S. 385–404. DOI: 10.1080/05704929708003320.

[70] Ulrike Braun, Aliaksandr I. Balabanovich, Bernhard Schartel, Uta Knoll, Johannes Artner, Michael Ciesielski, Manfred Döring, Raul Perez, Jan K. W. Sandler, Volker Altstädt, Thorsten Hoffmann und Doris Pospiech. "Influence of the Oxidation State of Phosphorus on the Decomposition and Fire Behaviour of Flame-Retarded Epoxy Resin Composites". In: *Polymer* 47.26 (2006), S. 8495–8508. DOI: 10.1016/j.polymer.2006.10.022.

[71] Mária Földvári. *Handbook of Thermogravimetric System of Minerals and Its Use in Geological Practice*. Occasional Papers of the Geological Institute of Hungary 213. Budapest: Geological Inst. of Hungary, 2011.

[72] DIN 51005. *DIN 51005:2005-08: Thermische Analyse (TA) — Begriffe*. 2005.

[73] Jan David, Helena Doležalová Weissmannová, Zacharias Steinmetz, Lucie Kabelíková, Michael Scott Demyan, Jana Šimečková, David Tokarski, Christian Siewert, Gabriele E. Schaumann und Jiří Kučerík. "Introducing a Soil Universal Model Method (SUMM) and Its Application for Qualitative and Quantitative Determination of Poly(Ethylene), Poly(Styrene), Poly(Vinyl Chloride) and Poly(Ethylene Terephthalate) Microplastics in a Model Soil". In: *Chemosphere* 225 (2019), S. 810–819. DOI: 10.1016/j.chemosphere.2019.03.078.

[74] Rosa Peñalver, Natalia Arroyo-Manzanares, Ignacio López-García und Manuel Hernández-Córdoba. "An Overview of Microplastics Characterization by Thermal Analysis". In: *Chemosphere* 242 (2020), S. 125170. DOI: 10.1016/j.chemosphere.2019.125170.

[75] Erik Duemichen, Paul Eisentraut, Claus Gerhard Bannick, Anne-Kathrin Barthel, Rainer Senz und Ulrike Braun. "Fast Identification of Microplastics in Complex Environmental Samples by a Thermal Degradation Method". In: *Chemosphere* 174 (2017), S. 572–584. DOI: 10.1016/j.chemosphere.2017.02.010.

[76] Paul Eisentraut, Erik Dümichen, Aki Sebastian Ruhl, Martin Jekel, Mirko Albrecht, Michael Gehde und Ulrike Braun. "Two Birds with One Stone—Fast and Simultaneous Analysis of Microplastics: Microparticles Derived from Thermoplastics and Tire Wear". In: *Environmental Science & Technology Letters* (2018). DOI: 10.1021/acs.estlett.8b00446.

[77] DIN 32633. *DIN 32633:2013-05: Chemische Analytik — Verfahren Der Standardaddition*. 2013.

[78] E. Duemichen, U. Braun, R. Senz, G. Fabian und H. Sturm. "Assessment of a New Method for the Analysis of Decomposition Gases of Polymers by a Combining Thermogravimetric Solid-Phase Extraction and Thermal Desorption Gas Chromatography Mass Spectrometry". In: *Journal of Chromatography A* 1354 (2014), S. 117–128. DOI: 10.1016/j.chroma.2014.05.057.

[79] E. Duemichen, P. Eisentraut, M. Celina und U. Braun. "Automated Thermal Extraction-Desorption Gas Chromatography Mass Spectrometry: A Multifunctional Tool for Comprehensive Characterization of Polymers and Their Degradation Products". In: *Journal of Chromatography A* 1592 (2019), S. 133–142. DOI: 10.1016/j.chroma.2019.01.033.

[80] Jianping Yu, Pingya Wang, Fengli Ni, James Cizdziel, Dongxu Wu, Qiaoling Zhao und Ying Zhou. "Characterization of Microplastics in Environment by Thermal Gravimetric Analysis Coupled with Fourier Transform Infrared Spectroscopy". In: *Marine Pollution Bulletin* 145 (2019), S. 153–160. DOI: 10.1016/j.marpolbul.2019.05.037.

[81] Jan David, Zacharias Steinmetz, Jiří Kučerík und Gabriele E. Schaumann. "Quantitative Analysis of Poly(Ethylene Terephthalate) Microplastics in Soil via Thermogravimetry–Mass Spectrometry". In: *Analytical Chemistry* 90.15 (2018), S. 8793–8799. DOI: 10.1021/acs.analchem.8b00355.

[82] Holly A. Nel, Andrew J. Chetwynd, Catherine A. Kelly, Christopher Stark, Eugenia Valsami-Jones, Stefan Krause und Iseult Lynch. "An Untargeted Thermogravimetric Analysis-Fourier Transform Infrared-Gas Chromatography-Mass Spectrometry Approach for Plastic Polymer Identification". In: *Environmental Science & Technology* (2021). DOI: 10.1021/acs.est.1c01085.

[83] J. A. Menéndez-Diaz und I. Martin-Gullón. "Types of Carbon Adsorbents and Their Production". In: *Activated Carbon Surfaces in Environmental Remediation*. Hrsg. von T. J. Bandosz. First. Bd. 7. New York [u.a.]: Elsevier, 2006, S. 1–47.

[84] Sontheimer, Frick, Fettig, Hörner, Hubele und Zimmer. *Activated Carbon for Water Treatment*. Second. Karlsruhe: DVWG-Forschungsstelle Engler-Bunte-Institut, 1988.

[85] Harry Marsh und Francisco Rodríguez Reinoso. *Activated Carbon*. Elsevier, 2006.

[86] D. M. Golea, P. Jarvis, B. Jefferson, G. Moore, S. Sutherland, S. A. Parsons und S. J. Judd. "Influence of Granular Activated Carbon Media Properties on Natural Organic Matter and Disinfection By-Product Precursor Removal from Drinking Water". In: *Water Research* 174 (2020), S. 115613. DOI: 10.1016/j.watres.2020.115613.

[87] Laura Piai, Marco Blokland, Albert van der Wal und Alette Langenhoff. "Biodegradation and Adsorption of Micropollutants by Biological Activated Carbon from a Drinking Water Production Plant". In: *Journal of Hazardous Materials* 388 (2020), S. 122028. DOI: 10.1016/j.jhazmat.2020.122028.

[88] Oksana Golovko, Luana de Brito Anton, Claudia Cascone, Lutz Ahrens, Elin Lavonen und Stephan J. Köhler. "Sorption Characteristics and Removal Efficiency of Organic Micropollutants in Drinking Water Using Granular Activated Carbon (GAC) in Pilot-Scale and Full-Scale Tests". In: *Water* 12.7 (2020), S. 2053. DOI: 10.3390/w12072053.

[89] Alexander Sperlich, Mareike Harder, Frederik Zietzschmann und Regina Gnirss. "Fate of Trace Organic Compounds in Granular Activated Carbon (GAC) Adsorbers for Drinking Water Treatment". In: *Water* 9.7 (2017), S. 479. DOI: 10.3390/w9070479.

[90] Martin Jekel, Johannes Altmann, Aki Sebastian Ruhl, Alexander Sperlich, Jana Schaller, Regina Gnirß, Ulf Miehe, Michael Stapf, Christian Remy und Daniel Mutz. *Integration der Spurenstoffentfernung in Technologieansätze der 4. Reinigungsstufe bei Klärwerken*. Universitätsverlag der TU Berlin, 2016. DOI: http://dx.doi.org/10.14279/depositonce-4942.

[91] Thomas Lucke, Tobias Bader, Wolfgang Schulz, Martin Jekel und Rudi Winzenbacher. "Bewertung gebrauchter Wasserwerksaktivkohlen mittels Non-Target-Screening im Hinblick auf eine brancheninterne Zweitverwertung". In: *gwf-Wasser|Abwasser* 3 (2019), S. 75–83.

[92] M. Lübken, P. Kosse, K. Clausen, B. Pehl, T. Bendt und M. Wichern. "Direct Dosage of Reactivated Carbon from Waterworks into the Activated Sludge Tank for Removal of Organic Micropollutants". In: *Water Science and Technology* 2017.2 (2018), S. 370–377. DOI: 10.2166/wst.2018.154.

[93] Judith Streicher, Aki Sebastian Ruhl, Regina Gnirß und Martin Jekel. "Where to Dose Powdered Activated Carbon in a Wastewater Treatment Plant for Organic Micro-Pollutant Removal". In: *Chemosphere* 156 (2016), S. 88–94. DOI: 10.1016/j.chemosphere.2016.04.123.

[94] Ronan Guillossou, Julien Le Roux, Stéphan Brosillon, Romain Mailler, Emmanuelle Vulliet, Catherine Morlay, Fabrice Nauleau, Vincent Rocher und Johnny Gaspéri. "Benefits of Ozonation before Activated Carbon Adsorption for the Removal of Organic Micropollutants from Wastewater Effluents". In: *Chemosphere* 245 (2020), S. 125530. DOI: 10.1016/j.chemosphere.2019.125530.

[95] F. Zietzschmann, R. -L. Mitchell und M. Jekel. "Impacts of Ozonation on the Competition between Organic Micro-Pollutants and Effluent Organic Matter in Powdered Activated Carbon Adsorption". In: *Water Research* 84 (2015), S. 153–160. DOI: 10.1016/j.watres.2015.07.031.

[96] Marina Gutiérrez, Vittoria Grillini, Dragana Mutavdžić Pavlović und Paola Verlicchi. "Activated Carbon Coupled with Advanced Biological Wastewater Treatment: A Review of the Enhancement in Micropollutant Removal". In: *Science of The Total Environment* 790 (2021), S. 148050. DOI: 10.1016/j.scitotenv.2021.148050.

[97] P. Schumann, J. A. Ordóñez Andrade, M. Jekel und A. S. Ruhl. "Packing Granular Activated Carbon into a Submerged Gravity-Driven Flat Sheet Membrane Module for Decentralized Water Treatment". In: *Journal of Water Process Engineering* 38 (2020), S. 101517. DOI: 10.1016/j.jwpe.2020.101517.

[98] Luong N. Nguyen, Faisal I. Hai, Long D. Nghiem, Jinguo Kang, William E. Price, Chul Park und Kazuo Yamamoto. "Enhancement of Removal of Trace Organic Contaminants by Powdered Activated Carbon Dosing into Membrane Bioreactors". In: *Journal of the Taiwan Institute of Chemical Engineers* 45.2 (2014), S. 571–578. DOI: 10.1016/j.jtice.2013.05.021.

[99] Luigi Rizzo, Sixto Malato, Demet Antakyali, Vasiliki G. Beretsou, Maja B. Dolic, Wolfgang Gernjak, Ester Heath, Ivana Ivancev-Tumbas, Popi Karaolia, Ana R. Lado Ribeiro, Giuseppe Mascolo, Christa S. McArdell, Heidemarie Schaar, Adrián M. T. Silva und Despo Fatta-Kassinos. "Consolidated vs New Advanced Treatment Methods for the Removal of Contaminants of Emerging Concern from Urban Wastewater". In: *Science of The Total Environment* 655 (2019), S. 986–1008. DOI: 10.1016/j.scitotenv.2018.11.265.

[100] DWA-M 285-2. *Spurenstoffentfernung auf kommunalen Kläranlagen — Teil 2: Einsatz von Aktivkohle — Verfahrensgrundsätze und Bemessung*. 2020.

[101] Steffen Metzger, Klaus Alt, Frank Benstöm, Norbert Biebersdorf, Marc Böhler, Catrin Bornemann, Christian Hiller, Klaus Jedele, Martin Jekel, Sven Lyko, Andreas Nahrstedt und Thomas Wintgens. *Aktivkohleeinsatz Auf Kommunalen Kläranlagen Zur Spuren-*

stoffentfernung - Verfahrensvarianten, Reinigungsleistung Und Betriebliche Aspekte -. DWA-Themen. Hennef: DWA, 2019.

[102] Damian Dominguez, Vinitha Diggelmann und Stefan Binggeli. *Elimination von Organischen Spurenstoffen Bei Abwasseranlagen. Finanzierung von Massnahmen*. Umwelt-Vollzug 1618. Bern: Bundesamt für Umwelt, 2016.

[103] Verband Schweizer Abwasser- und Gewässerschutzfachleute. *Micropoll - VSA Plattform: Verfahrenstechnik Mikroverunreinigungen*. https://www.micropoll.ch/aktuell/. 2021.

[104] Karin Lehmphul. *Organische Mikroverunreinigungen in Gewässern*. Umweltbundesamt, 2015.

[105] S Metzger, I. O. Tjoeng, A Rößler, Gert Schwentner und R Rölle. "Kosten Der Pulveraktivkohleanwendung Zur Spurenstoffelimination Am Beispiel Ausgeführter Und in Bau Befindlicher Anlagen". In: *KA Korrespondenz Abwasser, Abfall* 61.11 (2014), S. 1029–1037.

[106] Steffen Metzger, Matthias Barjenbruch, Silvio Beier, Ulf Miehe und Issa Nafo. "Statusbericht „Spurenstoffentfernung auf kommunalen Kläranlagen in Deutschland"". In: *Korrespondenz Abwasser, Abfall* 2020.10 (2020), S. 769–779. DOI: 10.3242/kae2020.10.002.

[107] Luisa F. Angeles, Rachel A. Mullen, Irvin J. Huang, Christopher Wilson, Wendell Khunjar, Howard I. Sirotkin, Anne E. McElroy und Diana S. Aga. "Assessing Pharmaceutical Removal and Reduction in Toxicity Provided by Advanced Wastewater Treatment Systems". In: *Environmental Science: Water Research & Technology* 6.1 (2019), S. 62–77. DOI: 10.1039/C9EW00559E.

[108] Rita Triebskorn, Ludek Blaha, Claudia Gallert, Sabrina Giebner, Harald Hetzenauer, Heinz-R. Köhler, Bertram Kuch, Frauke Lüddeke, Jörg Oehlmann, Katharina Peschke, Frank Sacher, Marco Scheurer, Simon Schwarz, Paul Thellmann, Karl Wurm und Sabrina Wilhelm. "Freshwater Ecosystems Profit from Activated Carbon-Based Wastewater Treatment across Various Levels of Biological Organisation in a Short Timeframe". In: *Environmental Sciences Europe* 31.1 (2019), S. 85. DOI: 10.1186/s12302-019-0267-0.

[109] Ben Joseph, Korbinian Kaetzl, Frank Hensgen, Bernhard Schäfer und Michael Wachendorf. "Sustainability Assessment of Activated Carbon from Residual Biomass Used for Micropollutant Removal at a Full-Scale Wastewater Treatment Plant". In: *Environmental Research Letters* 15.6 (2020), S. 064023. DOI: 10.1088/1748-9326/ab8330.

[110] Ronan Guillossou, Julien Le Roux, Romain Mailler, Emmanuelle Vulliet, Catherine Morlay, Fabrice Nauleau, Johnny Gasperi und Vincent Rocher. "Organic Micropollutants in a Large Wastewater Treatment Plant: What Are the Benefits of an Advanced Treatment by Activated Carbon Adsorption in Comparison to Conventional Treatment?" In: *Chemosphere* 218 (2019), S. 1050–1060. DOI: 10.1016/j.chemosphere.2018.11.182.

[111] Michael Cimbritz, Ellen Edefell, Elias Thörnqvist, Haitam El-taliawy, Maria Ekenberg, Cecilia Burzio, Oskar Modin, Frank Persson, Britt-Marie Wilén, Kai Bester und Per Falås. "PAC Dosing to an MBBR – Effects on Adsorption of Micropollutants, Nitrification and

Microbial Community". In: *Science of The Total Environment* 677 (2019), S. 571–579. DOI: 10.1016/j.scitotenv.2019.04.261.

[112] Jan Freihardt, Martin Jekel und Aki S. Ruhl. "Comparing Test Methods for Granular Activated Carbon for Organic Micropollutant Elimination". In: *Journal of Environmental Chemical Engineering* 5.3 (2017), S. 2542–2551. DOI: 10.1016/j.jece.2017.05.002.

[113] Aki S. Ruhl, Frederik Zietzschmann, Inga Hilbrandt, Felix Meinel, Johannes Altmann, Alexander Sperlich und Martin Jekel. "Targeted Testing of Activated Carbons for Advanced Wastewater Treatment". In: *Chemical Engineering Journal* 257 (2014), S. 184–190. DOI: 10.1016/j.cej.2014.07.069.

[114] Stefan Dittmar, Frederik Zietzschmann, Maike Mai, Eckhard Worch, Martin Jekel und Aki S. Ruhl. "Simulating Effluent Organic Matter Competition in Micropollutant Adsorption onto Activated Carbon Using a Surrogate Competitor". In: *Environmental Science & Technology* 52.14 (2018), S. 7859–7866. DOI: 10.1021/acs.est.8b01503.

[115] Qi Wang, Frederik Zietzschmann, Jianwei Yu, Roberta Hofman, Wei An, Min Yang und Luuk C. Rietveld. "Projecting Competition between 2-Methylisoborneol and Natural Organic Matter in Adsorption onto Activated Carbon from Ozonated Source Waters". In: *Water Research* 173 (2020), S. 115574. DOI: 10.1016/j.watres.2020.115574.

[116] Frederik Zietzschmann, Geert Aschermann und Martin Jekel. "Comparing and Modeling Organic Micro-Pollutant Adsorption onto Powdered Activated Carbon in Different Drinking Waters and WWTP Effluents". In: *Water Research* 102 (2016), S. 190–201. DOI: 10.1016/j.watres.2016.06.041.

[117] Frederik Zietzschmann, Eckhard Worch, Johannes Altmann, Aki Sebastian Ruhl, Alexander Sperlich, Felix Meinel und Martin Jekel. "Impact of EfOM Size on Competition in Activated Carbon Adsorption of Organic Micro-Pollutants from Treated Wastewater". In: *Water Research* 65 (2014), S. 297–306. DOI: 10.1016/j.watres.2014.07.043.

[118] Frederik Zietzschmann, Johannes Altmann, Aki Sebastian Ruhl, Uwe Dünnbier, Ingvild Dommisch, Alexander Sperlich, Felix Meinel und Martin Jekel. "Estimating Organic Micro-Pollutant Removal Potential of Activated Carbons Using UV Absorption and Carbon Characteristics". In: *Water Research* 56 (2014), S. 48–55. DOI: 10.1016/j.watres.2014.02.044.

[119] Annette Rößler und Aline Meier. "Praxiserfahrungen zum Einkauf und zur Qualitätskontrolle von Pulveraktivkohle bei der kommunalen Abwasserbehandlung". In: *Korrespondenz Abwasser, Abfall* 66.2 (2019), S. 125–132. DOI: 10.3242/kae2019.02.005.

[120] Ingrid Steinle-Silva. "Vertrauen Ist Gut, Doch Es Bleibt Die KontrolleQualitätskontrolle von Fäll- Und Flockungshilfsmitteln". In: *KA Betriebs-Info* 43.2 (2013), S. 2071–2076.

[121] IndexBox. *Previously Driven by the Growth of the Chemical Industry and Construction, the Global Activated Carbon Market to Struggle with the Pandemic*. https://www.globaltrademag.com/previously-driven-by-the-growth-of-the-chemical-industry-and-construction-the-global-activated-carbon-market-to-struggle-with-the-pandemic/. 2020.

[122] Virginia Hernández-Montoya, Josafat García-Servin und José Iván Bueno-López. "Thermal Treatments and Activation Procedures Used in the Preparation of Activated Carbons". In: *Lignocellulosic Precursors Used in the Synthesis of Activated Carbon - Characterization Techniques and Applications in the Wastewater Treatment*. 2012. DOI: 10.5772/39365.

[123] Lilja Nielsen, Pengfei Zhang und Teresa J. Bandosz. "Adsorption of Carbamazepine on Sludge/Fish Waste Derived Adsorbents: Effect of Surface Chemistry and Texture". In: *Chemical Engineering Journal* 267.Supplement C (2015), S. 170–181. DOI: 10.1016/j.cej.2014.12.113.

[124] Lilja Nielsen und Teresa J. Bandosz. "Analysis of the Competitive Adsorption of Pharmaceuticals on Waste Derived Materials". In: *Chemical Engineering Journal* 287.Supplement C (2016), S. 139–147. DOI: 10.1016/j.cej.2015.11.016.

[125] Isabel M. Lima, Andrew McAloon und Akwasi A. Boateng. "Activated Carbon from Broiler Litter: Process Description and Cost of Production". In: *Biomass and Bioenergy* 32.6 (2008), S. 568–572. DOI: 10.1016/j.biombioe.2007.11.008.

[126] Melanie Kah, Huichao Sun, Gabriel Sigmund, Thorsten Hüffer und Thilo Hofmann. "Pyrolysis of Waste Materials: Characterization and Prediction of Sorption Potential across a Wide Range of Mineral Contents and Pyrolysis Temperatures". In: *Bioresource Technology* 214 (2016), S. 225–233. DOI: 10.1016/j.biortech.2016.04.091.

[127] *DIN EN 12902:2004 — Produkte Zur Aufbereitung von Wasser Für Den Menschlichen Gebrauch — Anorganische Filterhilfs- Und Filtermaterialien — Prüfverfahren*. 2005. DOI: https://dx.doi.org/10.31030/9563882.

[128] Michio Inagaki und Feiyu Kang, Hrsg. *Materials Science and Engineering of Carbon*. Elsevier, 2016. DOI: 10.1016/C2014-0-03769-0.

[129] Jared Bourke, Merilyn Manley-Harris, Chihiro Fushimi, Kiyoshi Dowaki, Teppei Nunoura und Michael Jerry Antal. "Do All Carbonized Charcoals Have the Same Chemical Structure? 2. A Model of the Chemical Structure of Carbonized Charcoal". In: *Industrial & Engineering Chemistry Research* 46.18 (2007), S. 5954–5967. DOI: 10.1021/ie070415u.

[130] Po-Yu Yang, Shin-Pon Ju und Siou-Mei Huang. "Predicted Structural and Mechanical Properties of Activated Carbon by Molecular Simulation". In: *Computational Materials Science* 143 (2018), S. 43–54. DOI: 10.1016/j.commatsci.2017.10.051.

[131] Melanie Kah, Gabriel Sigmund, Feng Xiao und Thilo Hofmann. "Sorption of Ionizable and Ionic Organic Compounds to Biochar, Activated Carbon and Other Carbonaceous Materials". In: *Water Research* 124 (2017), S. 673–692. DOI: 10.1016/j.watres.2017.07.070.

[132] Carlos Moreno-Castilla. "Adsorption of Organic Molecules from Aqueous Solutions on Carbon Materials". In: *Carbon* 42.1 (2004), S. 83–94. DOI: 10.1016/j.carbon.2003.09.022.

[133] Stefan Leisering und Christoph A Schalley. *Tutorium Reaktivität und Synthese*. Berlin, Heidelberg: Springer Berlin Heidelberg, 2017. DOI: 10.1007/978-3-662-53852-4.

[134] DVGW. *Arbeitsblatt W 239: Entfernung Organischer Stoffe Bei Der Trinkwasseraufbereitung Durch Adsorption an Aktivkohle*. 2011.

[135] Lucas Landwehrkamp, Arman Kouchaki-Shalmani, Claudia Forner, Ralph Hobby, John Eduful und Christoph Wagner. "Development of Efficient Characterization Parameters for Activated Carbon Used in Drinking Water Treatment". In: *Journal of Water Supply: Research and Technology-Aqua* 64.6 (2015), S. 688–696. DOI: 10.2166/aqua.2015.157.

[136] Herbert Freundlich. "Über Die Adsorption in Lösungen". In: *Zeitschrift für Physikalische Chemie* 57U.1 (1906), S. 385–470. DOI: 10.1515/zpch-1907-5723.

[137] Thomas P. Wampler. *Applied Pyrolysis Handbook*. Second. Boca Raton: CRC Press Taylor & Francis Group, 2007.

[138] Nils Wiberg. *Lehrbuch der anorganischen Chemie [mit 188 Tabellen]*. 102., stark umgearb. und verb. Aufl. / von Nils Wiberg. Berlin [u.a.]: de Gruyter, 2007.

[139] William F. Degroot, Wei-Ping Pan, M. Dalilur Rahman und Geoffrey N. Richards. "First Chemical Events in Pyrolysis of Wood". In: *Journal of Analytical and Applied Pyrolysis* 13.3 (1988), S. 221–231. DOI: 10.1016/0165-2370(88)80024-X.

[140] Tao Kan, Vladimir Strezov und Tim J. Evans. "Lignocellulosic Biomass Pyrolysis: A Review of Product Properties and Effects of Pyrolysis Parameters". In: *Renewable and Sustainable Energy Reviews* 57 (2016), S. 1126–1140. DOI: 10.1016/j.rser.2015.12.185.

[141] Frederik Ossler, Louis J. Santodonato, Jeffrey M. Warren, Charles E. A. Finney, Jean-Christophe Bilheux, Rebecca A. Mills, Harley D. Skorpenske und Hassina Z. Bilheux. "In Situ Monitoring of Hydrogen Loss during Pyrolysis of Wood by Neutron Imaging". In: *Proceedings of the Combustion Institute* 37.2 (2019), S. 1273–1280. DOI: 10.1016/j.proci.2018.07.051.

[142] Tao Kan, Vladimir Strezov und Tim Evans. "Effect of the Heating Rate on the Thermochemical Behavior and Biofuel Properties of Sewage Sludge Pyrolysis". In: *Energy & Fuels* 30.3 (2016), S. 1564–1570. DOI: 10.1021/acs.energyfuels.5b02232.

[143] Harry Marsh. "A Tribute to Philip L. Walker". In: *Carbon* 29.6 (1991), S. 703–704. DOI: 10.1016/0008-6223(91)90004-3.

[144] Teresa J. Bandosz, Hrsg. *Activated Carbon Surfaces in Environmental Remediation*. First. Bd. 7. New York [u.a.]: Elsevier, 2006.

[145] J. L Figueiredo, M. F. R Pereira, M. M. A Freitas und J. J. M Órfão. "Modification of the Surface Chemistry of Activated Carbons". In: *Carbon* 37.9 (1999), S. 1379–1389. DOI: 10.1016/S0008-6223(98)00333-9.

[146] H. P Boehm. "Surface Oxides on Carbon and Their Analysis: A Critical Assessment". In: *Carbon*. Third International Conference on Carbon Black 40.2 (2002), S. 145–149. DOI: 10.1016/S0008-6223(01)00165-8.

[147] Gabriela Hotová und Václav Slovák. "Quantitative TG-MS Analysis of Evolved Gases during the Thermal Decomposition of Carbon Containing Solids". In: *Thermochimica Acta* 632 (2016), S. 23–28. DOI: 10.1016/j.tca.2016.03.012.

[148] Dominique Lörchner, Daniel Dittmann, Ulrike Braun, Lothar W. Kroh und Robert Köppen. "Investigation of Two Triazine-Based Heterocyclic Brominated Flame Retardants by Coupled Thermogravimetry-Fourier Transform Infrared Spectroscopy". In: *Journal of Analytical and Applied Pyrolysis* 141 (2019), S. 104635. DOI: 10.1016/j.jaap.2019.104635.

[149] Maren Erdmann, Volker Trappe, Heinz Sturm, Ulrike Braun und Erik Duemichen. "Cure Conversion of Structural Epoxies by Cure State Analysis and in Situ Cure Kinetics Using Nondestructive NIR Spectroscopy". In: *Thermochimica Acta* 650 (2017), S. 8–17. DOI: 10.1016/j.tca.2017.01.010.

[150] Sergey Vyazovkin. "Kissinger Method in Kinetics of Materials: Things to Beware and Be Aware Of". In: *Molecules* 25.12 (2020), S. 2813. DOI: 10.3390/molecules25122813.

[151] Sergey Vyazovkin. "Determining Preexponential Factor in Model-Free Kinetic Methods: How and Why?" In: *Molecules* 26.11 (2021), S. 3077. DOI: 10.3390/molecules26113077.

[152] Gábor Várhegyi, Michael Jerry Antal, Emma Jakab und Piroska Szabó. "Kinetic Modeling of Biomass Pyrolysis". In: *Journal of Analytical and Applied Pyrolysis* 42.1 (1997), S. 73–87. DOI: 10.1016/S0165-2370(96)00971-0.

[153] Therese Krahnstöver, Julia Plattner und Thomas Wintgens. "Quantitative Detection of Powdered Activated Carbon in Wastewater Treatment Plant Effluent by Thermogravimetric Analysis (TGA)". In: *Water Research* 101 (2016), S. 510–518. DOI: 10.1016/j.watres.2016.06.008.

[154] Feng Xiao, Pavankumar Challa Sasi, Bin Yao, Alena Kubátová, Svetlana A. Golovko, Mikhail Y. Golovko und Dana Soli. "Thermal Stability and Decomposition of Perfluoroalkyl Substances on Spent Granular Activated Carbon". In: *Environmental Science & Technology Letters* 7.5 (2020), S. 343–350. DOI: 10.1021/acs.estlett.0c00114.

[155] Frank-Dieter Kopinke und Lisa-Marie Frenzel. "Comment on "Thermal Stability and Decomposition of Perfluoroalkyl Substances on Spent Granular Activated Carbon"". In: *Environmental Science & Technology Letters* 8.4 (2021), S. 362–363. DOI: 10.1021/acs.estlett.0c00742.

[156] C. Goedecke, D. Dittmann, P. Eisentraut, Y. Wiesner, B. Schartel, P. Klack und U. Braun. "Evaluation of Thermoanalytical Methods Equipped with Evolved Gas Analysis for the Detection of Microplastic in Environmental Samples". In: *Journal of Analytical and Applied Pyrolysis* 152 (2020), S. 104961. DOI: 10.1016/j.jaap.2020.104961.

[157] Roland Becker, Korinna Altmann, Thomas Sommerfeld und Ulrike Braun. "Quantification of Microplastics in a Freshwater Suspended Organic Matter Using Different Thermoanalytical Methods – Outcome of an Interlaboratory Comparison". In: *Journal of Analytical and Applied Pyrolysis* (2020), S. 104829. DOI: 10.1016/j.jaap.2020.104829.

[158] PlasticsEurope. *Plastics – the Facts 2018: An Analysis of European Plasticsproduction, Demand and Waste Data*. 2018.

[159] Hans Zweifel, Ralph D. Maier, Michael Schiller und St E. Amos. *Plastics Additives Handbook*. Sixth. Cincinnati, Ohio: Hanser Publications, 2009.

[160] Laurent C. M. Lebreton, Joost van der Zwet, Jan-Willem Damsteeg, Boyan Slat, Anthony Andrady und Julia Reisser. "River Plastic Emissions to the World's Oceans". In: *Nature Communications* 8.1 (2017), S. 15611. DOI: 10.1038/ncomms15611.

[161] Alice A. Horton, Alexander Walton, David J. Spurgeon, Elma Lahive und Claus Svendsen. "Microplastics in Freshwater and Terrestrial Environments: Evaluating the Current Understanding to Identify the Knowledge Gaps and Future Research Priorities". In: *Science of The Total Environment* 586 (2017), S. 127–141. DOI: 10.1016/j.scitotenv.2017.01.190.

[162] Andrea Käppler, Dieter Fischer, Sonja Oberbeckmann, Gerald Schernewski, Matthias Labrenz, Klaus-Jochen Eichhorn und Brigitte Voit. "Analysis of Environmental Microplastics by Vibrational Microspectroscopy: FTIR, Raman or Both?" In: *Analytical and Bioanalytical Chemistry* 408.29 (2016), S. 8377–8391. DOI: 10.1007/s00216-016-9956-3.

[163] Surjit Singh, Chunfei Wu und Paul T. Williams. "Pyrolysis of Waste Materials Using TGA-MS and TGA-FTIR as Complementary Characterisation Techniques". In: *Journal of Analytical and Applied Pyrolysis* 94 (2012), S. 99–107. DOI: 10.1016/j.jaap.2011.11.011.

[164] Gamzenur Özsin und Ayşe Eren Pütün. "TGA/MS/FT-IR Study for Kinetic Evaluation and Evolved Gas Analysis of a Biomass/PVC Co-Pyrolysis Process". In: *Energy Conversion and Management* 182 (2019), S. 143–153. DOI: 10.1016/j.enconman.2018.12.060.

[165] Jacopo La Nasa, Greta Biale, Daniele Fabbri und Francesca Modugno. "A Review on Challenges and Developments of Analytical Pyrolysis and Other Thermoanalytical Techniques for the Quali-Quantitative Determination of Microplastics". In: *Journal of Analytical and Applied Pyrolysis* 149 (2020), S. 104841. DOI: 10.1016/j.jaap.2020.104841.

[166] Richard E Lyon und Richard N Walters. "Pyrolysis Combustion Flow Calorimetry". In: *Journal of Analytical and Applied Pyrolysis*. Practical Applications of Analytical Pyrolysis (Special Section) 71.1 (2004), S. 27–46. DOI: 10.1016/S0165-2370(03)00096-2.

[167] Bernhard Schartel, Kristin H. Pawlowski und Richard E. Lyon. "Pyrolysis Combustion Flow Calorimeter: A Tool to Assess Flame Retarded PC/ABS Materials?" In: *Thermochimica Acta* 462.1 (2007), S. 1–14. DOI: 10.1016/j.tca.2007.05.021.

[168] ASTM D7309-19a. *Standard Test Method for Determining Flammability Characteristics of Plastics and Other Solid Materials Using Microscale Combustion Calorimetry*. DOI: 10.1520/D7309-19A.

[169] Clayton Huggett. "Estimation of Rate of Heat Release by Means of Oxygen Consumption Measurements". In: *Fire and Materials* 4.2 (1980), S. 61–65. DOI: 10.1002/fam.810040202.

[170] Ulrike Braun, Paul Eisentraut, Sabine Fuchs und Peter Deglmann. "Sulphurous Additives for Polystyrene: Influencing Decomposition Behavior in the Condensed Phase". In: *Journal of Applied Polymer Science* 132.12 (2015). DOI: 10.1002/app.41665.

[171] Ulrike Braun und Bernhard Schartel. "Flame Retardancy Mechanisms of Aluminium Phosphinate in Combination with Melamine Cyanurate in Glass-Fibre-Reinforced Poly(1,4-Butylene Terephthalate)". In: *Macromolecular Materials and Engineering* 293.3 (2008), S. 206–217. DOI: 10.1002/mame.200700330.

[172] B. Schartel, U. Braun, U. Schwarz und S. Reinemann. "Fire Retardancy of Polypropylene/Flax Blends". In: *Polymer* 44.20 (2003), S. 6241–6250. DOI: 10.1016/S0032-3861(03)00692-X.

[173] S.A. Jenekhe, J.W. Lin und B. Sun. "Kinetics of the Thermal Degradation of Polyethylene Terephthalate". In: *Thermochimica Acta* 61.3 (1983), S. 287–299. DOI: 10.1016/0040-6031(83)80283-4.

[174] A. Marongiu, T. Faravelli, G. Bozzano, M. Dente und E. Ranzi. "Thermal Degradation of Poly(Vinyl Chloride)". In: *Journal of Analytical and Applied Pyrolysis* 70.2 (2003), S. 519–553. DOI: 10.1016/S0165-2370(03)00024-X.

[175] Eckhard Worch. *Adsorption Technology in Water Treatment, Fundamentals, Processes, and Modeling*. Berlin, Boston: De Gruyter, 2012. DOI: 10.1515/9783110240238.

[176] Erika Mészáros, Emma Jakab, Gábor Várhegyi, Jared Bourke, Merilyn Manley-Harris, Teppei Nunoura und Michael Jerry Antal. "Do All Carbonized Charcoals Have the Same Chemical Structure? 1. Implications of Thermogravimetry-Mass Spectrometry Measurements". In: *Industrial & Engineering Chemistry Research* 46.18 (2007), S. 5943–5953. DOI: 10.1021/ie0615842.

[177] Rui M. C. Viegas, Ana S. Mestre, Elsa Mesquita, Margarida Campinas, Marta A. Andrade, Ana P. Carvalho und Maria João Rosa. "Assessing the Applicability of a New Carob Waste-Derived Powdered Activated Carbon to Control Pharmaceutical Compounds in Wastewater Treatment". In: *Science of The Total Environment* 743 (2020), S. 140791. DOI: 10.1016/j.scitotenv.2020.140791.

[178] A. Alicia Peláez-Cid und M. M. Margarita Teutli-León. "Lignocellulosic Precursors Used in the Elaboration of Activated Carbon". In: *Lignocellulosic Precursors Used in the Synthesis of Activated Carbon - Characterization Techniques and Applications in the Wastewater Treatment*. 2012. DOI: 10.5772/39364.

[179] Suhas, P. J. M. Carrott und M. M. L. Ribeiro Carrott. "Lignin – from Natural Adsorbent to Activated Carbon: A Review". In: *Bioresource Technology* 98.12 (2007), S. 2301–2312. DOI: 10.1016/j.biortech.2006.08.008.

[180] Laura Piai, Jouke E. Dykstra, Mahesa G. Adishakti, Marco Blokland, Alette A. M. Langenhoff und Albert van der Wal. "Diffusion of Hydrophilic Organic Micropollutants in Granular Activated Carbon with Different Pore Sizes". In: *Water Research* 162 (2019), S. 518–527. DOI: 10.1016/j.watres.2019.06.012.

[181] Lilja Nielsen, Mark J. Biggs, William Skinner und Teresa J. Bandosz. "The Effects of Activated Carbon Surface Features on the Reactive Adsorption of Carbamazepine and Sulfamethoxazole". In: *Carbon* 80 (2014), S. 419–432. DOI: 10.1016/j.carbon.2014.08.081.

[182] Phillip Pendleton, Sophie Hua Wu und Alexander Badalyan. "Activated Carbon Oxygen Content Influence on Water and Surfactant Adsorption". In: *Journal of Colloid and Interface Science* 246.2 (2002), S. 235–240. DOI: 10.1006/jcis.2001.8052.

[183] Carlos J. Durán-Valle. "Techniques Employed in the Physicochemical Characterization of Activated Carbons". In: *Lignocellulosic Precursors Used in the Synthesis of Activated Carbon - Characterization Techniques and Applications in the Wastewater Treatment*. IntechOpen, 2012, S. 37–55. DOI: 10.5772/39366.

[184] Wan Mohd Ashri Wan Daud und Amir Hossein Houshamnd. "Textural Characteristics, Surface Chemistry and Oxidation of Activated Carbon". In: *Journal of Natural Gas Chemistry* 19.3 (2010), S. 267–279. DOI: 10.1016/S1003-9953(09)60066-9.

[185] Manuel Fernando R Pereira, Samanta F Soares, José J. M Órfão und José L Figueiredo. "Adsorption of Dyes on Activated Carbons: Influence of Surface Chemical Groups". In: *Carbon* 41.4 (2003), S. 811–821. DOI: 10.1016/S0008-6223(02)00406-2.

[186] Donald Rivin. "Surface Properties of Carbon". In: *Rubber Chemistry and Technology* 44.2 (1971), S. 307–343. DOI: 10.5254/1.3547370.

[187] James G. Speight. "Proximate Analysis". In: *Handbook of Coal Analysis*. John Wiley & Sons, Ltd, 2015. Kap. 5, S. 116–143. DOI: 10.1002/9781119037699.ch5.

[188] L. R. Radovic, I. F. Silva, J. I. Ume, J. A. Menéndez, C. A. Leon Y Leon und A. W. Scaroni. "An Experimental and Theoretical Study of the Adsorption of Aromatics Possessing Electron-Withdrawing and Electron-Donating Functional Groups by Chemically Modified Activated Carbons". In: *Carbon* 35.9 (1997), S. 1339–1348. DOI: 10.1016/S0008-6223(97)00072-9.

[189] Marcus Franz, Hassan A. Arafat und Neville G. Pinto. "Effect of Chemical Surface Heterogeneity on the Adsorption Mechanism of Dissolved Aromatics on Activated Carbon". In: *Carbon* 38.13 (2000), S. 1807–1819. DOI: 10.1016/S0008-6223(00)00012-9.

[190] Matteo Tagliavini, Peter Georg Weidler, Christian Njel, Julia Pohl, Dennis Richter, Bertram Böhringer und Andrea I. Schäfer. "Polymer-Based Spherical Activated Carbon – Ultrafiltration (UF-PBSAC) for the Adsorption of Steroid Hormones from Water: Material Characteristics and Process Configuration". In: *Water Research* 185 (2020), S. 116249. DOI: 10.1016/j.watres.2020.116249.

[191] Leon Saal und Daniel Dittmann. *TGA-FTIR-Hyphenation-Tool-Kit*. BAMResearch. 2021. DOI: 10.5281/zenodo.4917313.

[192] Günther Müller, C. J Radke und J. M Prausnitz. "Adsorption of Weak Organic Electrolytes from Dilute Aqueous Solution onto Activated Carbon. Part I. Single-Solute Systems". In: *Journal of Colloid and Interface Science* 103.2 (1985), S. 466–483. DOI: 10.1016/0021-9797(85)90123-7.

[193] J Rivera-Utrilla, I Bautista-Toledo, M A Ferro-García und C Moreno-Castilla. "Activated Carbon Surface Modifications by Adsorption of Bacteria and Their Effect on Aqueous Lead Adsorption". In: *Journal of Chemical Technology & Biotechnology* 76.12 (2001), S. 1209–1215. DOI: 10.1002/jctb.506.

[194] E. Desimoni, G. I. Casella, A. Morone und A. M. Salvi. "XPS Determination of Oxygen-Containing Functional Groups on Carbon-Fibre Surfaces and the Cleaning of These Surfaces". In: *Surface and Interface Analysis* 15.10 (1990), S. 627–634. DOI: 10.1002/sia.740151011.

[195] Daniel Dittmann, Paul Eisentraut, Caroline Goedecke, Yosri Wiesner, Martin Jekel, Aki Sebastian Ruhl und Ulrike Braun. "Specific Adsorption Sites and Conditions Derived by Thermal Decomposition of Activated Carbons and Adsorbed Carbamazepine". In: *Scientific Reports* 10.1 (2020), S. 6695. DOI: 10.1038/s41598-020-63481-y.

[196] Fabian Pedregosa, Gaël Varoquaux, Alexandre Gramfort, Vincent Michel, Bertrand Thirion, Olivier Grisel, Mathieu Blondel, Peter Prettenhofer, Ron Weiss, Vincent Dubourg, Jake Vanderplas, Alexandre Passos, David Cournapeau, Matthieu Brucher, Matthieu Perrot und Édouard Duchesnay. "Scikit-Learn: Machine Learning in Python". In: *Journal of Machine Learning Research* 12.85 (2011), S. 2825–2830.

[197] Yu-Chun Chiang, Pen-Chi Chiang und Chin-Pao Huang. "Effects of Pore Structure and Temperature on VOC Adsorption on Activated Carbon". In: *Carbon* 39.4 (2001), S. 523–534. DOI: 10.1016/S0008-6223(00)00161-5.

[198] Matthias Thommes, Katsumi Kaneko, Alexander V. Neimark, James P. Olivier, Francisco Rodriguez-Reinoso, Jean Rouquerol und Kenneth S.W. Sing. "Physisorption of Gases, with Special Reference to the Evaluation of Surface Area and Pore Size Distribution (IUPAC Technical Report)". In: *Pure and Applied Chemistry* 87.9-10 (2015), S. 1051–1069. DOI: 10.1515/pac-2014-1117.

[199] T. J. Bandosz und C. O. Ania. "Surface Chemistry of Activated Carbons and Its Characterization". In: *Activated Carbon Surfaces in Environmental Remediation*. Hrsg. von T. J. Bandosz. First. Bd. 7. New York [u.a.]: Elsevier, 2006, S. 159–229.

[200] Jin-Pei Deng, Wen-Hao Chen, Shou-Po Chiu, Chih-Hsun Lin und Bo-Cheng Wang. "Edge-Termination and Core-Modification Effects of Hexagonal Nanosheet Graphene". In: *Molecules* 19.2 (2014), S. 2361–2373. DOI: 10.3390/molecules19022361.

[201] Alexander M. Puziy, Olga I. Poddubnaya, Amelia Martínez-Alonso, Fabian Suárez-García und Juan M. D. Tascón. "Surface Chemistry of Phosphorus-Containing Carbons of Lignocellulosic Origin". In: *Carbon* 43.14 (2005), S. 2857–2868. DOI: 10.1016/j.carbon.2005.06.014.

[202] Daniel Dittmann, Leon Saal, Frederik Zietzschmann, Maike Mai und Dominik Al-Sabbagh. *Experimental Raw Data for "Characterization of Activated Carbon Products for Water Treatment Including Extended Analysis of Oxygen-Containing Functional Groups"*. 2021. DOI: 10.5281/zenodo.4923133.

[203] Sergi Sabater, Francesco Bregoli, Vicenç Acuña, Damià Barceló, Arturo Elosegi, Antoni Ginebreda, Rafael Marcé, Isabel Muñoz, Laia Sabater-Liesa und Verónica Ferreira. "Effects of Human-Driven Water Stress on River Ecosystems: A Meta-Analysis". In: *Scientific Reports* 8.1 (2018), S. 11462. DOI: 10.1038/s41598-018-29807-7.

[204] Amrita Pal, Yiliang He, Martin Jekel, Martin Reinhard und Karina Yew-Hoong Gin. "Emerging Contaminants of Public Health Significance as Water Quality Indicator Compounds in the Urban Water Cycle". In: *Environment International* 71 (2014), S. 46–62. DOI: 10.1016/j.envint.2014.05.025.

[205] Mark J. Benotti, Rebecca A. Trenholm, Brett J. Vanderford, Janie C. Holady, Benjamin D. Stanford und Shane A. Snyder. "Pharmaceuticals and Endocrine Disrupting Compounds in U.S. Drinking Water". In: *Environmental Science & Technology* 43.3 (2009), S. 597–603. DOI: 10.1021/es801845a.

[206] T. Brodin, J. Fick, M. Jonsson und J. Klaminder. "Dilute Concentrations of a Psychiatric Drug Alter Behavior of Fish from Natural Populations". In: *Science* 339.6121 (2013), S. 814–815. DOI: 10.1126/science.1226850.

[207] Alvine C. Mehinto, Elizabeth M. Hill und Charles R. Tyler. "Uptake and Biological Effects of Environmentally Relevant Concentrations of the Nonsteroidal Anti-Inflammatory Pharmaceutical Diclofenac in Rainbow Trout (Oncorhynchus Mykiss)". In: *Environmental Science & Technology* 44.6 (2010), S. 2176–2182. DOI: 10.1021/es903702m.

[208] Benoıt Ferrari, Nicklas Paxéus, Roberto Lo Giudice, Antonino Pollio und Jeanne Garric. "Ecotoxicological Impact of Pharmaceuticals Found in Treated Wastewaters: Study of Carbamazepine, Clofibric Acid, and Diclofenac". In: *Ecotoxicology and Environmental Safety* 55.3 (2003), S. 359–370. DOI: 10.1016/S0147-6513(02)00082-9.

[209] N. Bolong, A. F. Ismail, M. R. Salim und T. Matsuura. "A Review of the Effects of Emerging Contaminants in Wastewater and Options for Their Removal". In: *Desalination* 239.1 (2009), S. 229–246. DOI: 10.1016/j.desal.2008.03.020.

[210] I. Michael, L. Rizzo, C. S. McArdell, C. M. Manaia, C. Merlin, T. Schwartz, C. Dagot und D. Fatta-Kassinos. "Urban Wastewater Treatment Plants as Hotspots for the Release of Antibiotics in the Environment: A Review". In: *Water Research* 47.3 (2013), S. 957–995. DOI: 10.1016/j.watres.2012.11.027.

[211] M. Boehler, B. Zwickenpflug, J. Hollender, T. Ternes, A. Joss und H. Siegrist. "Removal of Micropollutants in Municipal Wastewater Treatment Plants by Powder-Activated Carbon". In: *Water Science and Technology* 66.10 (2012), S. 2115–2121. DOI: 10.2166/wst.2012.353.

[212] Rama Rao Karri, N. S. Jayakumar und J. N. Sahu. "Modelling of Fluidised-Bed Reactor by Differential Evolution Optimization for Phenol Removal Using Coconut Shells Based Activated Carbon". In: *Journal of Molecular Liquids* 231 (2017), S. 249–262. DOI: 10.1016/j.molliq.2017.02.003.

[213] Mohammad Hadi Dehghani, Rama Rao Karri, Zeinab Tafaroji Yeganeh, Amir Hossein Mahvi, Heshmatollah Nourmoradi, Mehdi Salari, Ahmad Zarei und Mika Sillanpää. "Statistical Modelling of Endocrine Disrupting Compounds Adsorption onto Activated Carbon Prepared from Wood Using CCD-RSM and DE Hybrid Evolutionary Optimization Framework: Comparison of Linear vs Non-Linear Isotherm and Kinetic Parameters". In: *Journal of Molecular Liquids* 302 (2020), S. 112526. DOI: 10.1016/j.molliq.2020.112526.

[214] Frank Benstoem, Andreas Nahrstedt, Marc Boehler, Gregor Knopp, David Montag, Hansruedi Siegrist und Johannes Pinnekamp. "Performance of Granular Activated Carbon to Remove Micropollutants from Municipal Wastewater—A Meta-Analysis of Pilot- and Large-Scale Studies". In: *Chemosphere* 185 (2017), S. 105–118. DOI: 10.1016/j.chemosphere.2017.06.118.

[215] Yanhong Zhang, Changqing Zhu, Fuqiang Liu, Yuan Yuan, Haide Wu und Aimin Li. "Effects of Ionic Strength on Removal of Toxic Pollutants from Aqueous Media with Multifarious Adsorbents: A Review". In: *Science of The Total Environment* 646 (2019), S. 265–279. DOI: 10.1016/j.scitotenv.2018.07.279.

[216] Geert Aschermann, Lino Neubert, Frederik Zietzschmann und Martin Jekel. "Impact of Different DOM Size Fractions on the Desorption of Organic Micropollutants from Activated Carbon". In: *Water Research* 161 (2019), S. 161–170. DOI: 10.1016/j.watres.2019.05.039.

[217] Martin Jekel, Wolfgang Dott, Axel Bergmann, Uwe Dünnbier, Regina Gnirß, Brigitte Haist-Gulde, Gerd Hamscher, Marion Letzel, Tobias Licha, Sven Lyko, Ulf Miehe, Frank Sacher, Marco Scheurer, Carsten K. Schmidt, Thorsten Reemtsma und Aki Sebastian Ruhl. "Selection of Organic Process and Source Indicator Substances for the Anthropogenically Influenced Water Cycle". In: *Chemosphere* 125 (2015), S. 155–167. DOI: 10.1016/j.chemosphere.2014.12.025.

[218] Jian Chen, Di Zhang, Huang Zhang, Saikat Ghosh und Bo Pan. "Fast and Slow Adsorption of Carbamazepine on Biochar as Affected by Carbon Structure and Mineral Composition". In: *Science of The Total Environment* 579 (2017), S. 598–605. DOI: 10.1016/j.scitotenv.2016.11.052.

[219] Nakorn Suriyanon, Patiparn Punyapalakul und Chawalit Ngamcharussrivichai. "Mechanistic Study of Diclofenac and Carbamazepine Adsorption on Functionalized Silica-Based Porous Materials". In: *Chemical Engineering Journal* 214 (2013), S. 208–218. DOI: 10.1016/j.cej.2012.10.052.

[220] Weihao Zhang, Yunjie Ding, Stephen A. Boyd, Brian J. Teppen und Hui Li. "Sorption and Desorption of Carbamazepine from Water by Smectite Clays". In: *Chemosphere* 81.7 (2010), S. 954–960. DOI: 10.1016/j.chemosphere.2010.07.053.

[221] Chi Wang, Hao Li, Shaohua Liao, Hao Zheng, Zhenyu Wang, Bo Pan und Baoshan Xing. "Coadsorption, Desorption Hysteresis and Sorption Thermodynamics of Sulfamethoxazole and Carbamazepine on Graphene Oxide and Graphite". In: *Carbon* 65 (2013), S. 243–251. DOI: 10.1016/j.carbon.2013.08.020.

[222] Bettina Seiwert, Naama Golan-Rozen, Cindy Weidauer, Christina Riemenschneider, Benny Chefetz, Yitzhak Hadar und Thorsten Reemtsma. "Electrochemistry Combined with LC–HRMS: Elucidating Transformation Products of the Recalcitrant Pharmaceutical Compound Carbamazepine Generated by the White-Rot Fungus Pleurotus Ostreatus". In: *Environmental Science & Technology* 49.20 (2015), S. 12342–12350. DOI: 10.1021/acs.est.5b02229.

[223] Tina Kosjek, Henrik R. Andersen, Boris Kompare, Anna Ledin und Ester Heath. "Fate of Carbamazepine during Water Treatment". In: *Environmental Science & Technology* 43.16 (2009), S. 6256–6261. DOI: 10.1021/es900070h.

[224] Hélène Breton, Marylène Cociglio, Françoise Bressolle, Hélène Peyriere, Jean Pierre Blayac und Dominique Hillaire-Buys. "Liquid Chromatography–Electrospray Mass Spectrometry Determination of Carbamazepine, Oxcarbazepine and Eight of Their Metabolites in Human Plasma". In: *Journal of Chromatography B* 828.1 (2005), S. 80–90. DOI: 10.1016/j.jchromb.2005.09.019.

[225] Elena Brezina, Carsten Prasse, Johannes Meyer, Harald Mückter und Thomas A. Ternes. "Investigation and Risk Evaluation of the Occurrence of Carbamazepine, Oxcarbazepine, Their Human Metabolites and Transformation Products in the Urban Water Cycle". In: *Environmental Pollution* 225 (2017), S. 261–269. DOI: 10.1016/j.envpol.2016.10.106.

[226] Juying Li, Laurel Dodgen, Qingfu Ye und Jay Gan. "Degradation Kinetics and Metabolites of Carbamazepine in Soil". In: *Environmental Science & Technology* 47.8 (2013), S. 3678–3684. DOI: 10.1021/es304944c.

[227] Anne König, Cindy Weidauer, Bettina Seiwert, Thorsten Reemtsma, Tina Unger und Martin Jekel. "Reductive Transformation of Carbamazepine by Abiotic and Biotic Processes". In: *Water Research* 101 (2016), S. 272–280. DOI: 10.1016/j.watres.2016.05.084.

[228] Gabriela Hotová und Václav Slovák. "Determination of the Surface Oxidation Degree of the Carbonaceous Materials by Quantitative TG-MS Analysis". In: *Analytical Chemistry* 89.3 (2017), S. 1710–1715. DOI: 10.1021/acs.analchem.6b03914.

[229] Mônia Aparecida Lemos Pinto, Beatriz Ambrozini, Ana Paula Garcia Ferreira und Éder Tadeu Gomes Cavalheiro. "Thermoanalytical Studies of Carbamazepine: Hydration/Dehydration, Thermal Decomposition, and Solid Phase Transitions". In: *Brazilian Journal of Pharmaceutical Sciences* 50.4 (2014), S. 877–884. DOI: 10.1590/S1984-82502014000400023.

[230] Lei Tian, Stéphane Bayen und Varoujan Yaylayan. "Thermal Degradation of Five Veterinary and Human Pharmaceuticals Using Pyrolysis-GC/MS". In: *Journal of Analytical and Applied Pyrolysis* 127 (2017), S. 120–125. DOI: 10.1016/j.jaap.2017.08.016.

[231] Valeria Ambrogi, Luana Perioli, Fabio Marmottini, Oriana Accorsi, Cinzia Pagano, Maurizio Ricci und Carlo Rossi. "Role of Mesoporous Silicates on Carbamazepine Dissolution Rate Enhancement". In: *Microporous and Mesoporous Materials* 113.1 (2008), S. 445–452. DOI: 10.1016/j.micromeso.2007.12.003.

[232] Geert Aschermann, Frederik Zietzschmann und Martin Jekel. "Influence of Dissolved Organic Matter and Activated Carbon Pore Characteristics on Organic Micropollutant Desorption". In: *Water Research* 133 (2018), S. 123–131. DOI: 10.1016/j.watres.2018.01.015.

[233] Nan Cai und Philip Larese-Casanova. "Sorption of Carbamazepine by Commercial Graphene Oxides: A Comparative Study with Granular Activated Carbon and Multiwalled Carbon Nanotubes". In: *Journal of Colloid and Interface Science* 426 (2014), S. 152–161. DOI: 10.1016/j.jcis.2014.03.038.

[234] Daniel Dittmann. *Experimental Raw Data for "Specific Adsorption Sites and Conditions Derived by Thermal Decomposition of Activated Carbons and Adsorbed Carbamazepine"*. 2020. DOI: 10.5281/zenodo.3716316.

[235] Stephen Brunauer, P. H. Emmett und Edward Teller. "Adsorption of Gases in Multimolecular Layers". In: *Journal of the American Chemical Society* 60.2 (1938), S. 309–319. DOI: 10.1021/ja01269a023.

[236] J. Rouquerol, P. Llewellyn und F. Rouquerol. "Is the Bet Equation Applicable to Microporous Adsorbents?" In: *Studies in Surface Science and Catalysis*. Bd. 160. Elsevier, 2007, S. 49–56. DOI: 10.1016/S0167-2991(07)80008-5.

[237] R. W. Magee. "Evaluation of the External Surface Area of Carbon Black by Nitrogen Adsorption". In: *Rubber Chemistry and Technology* 68.4 (1995), S. 590–600. DOI: 10.5254/1.3538760.

[238] Gabriela Hotová, Václav Slovák, Olívia S. G. P. Soares, José L. Figueiredo und Manuel F. R. Pereira. "Oxygen Surface Groups Analysis of Carbonaceous Samples Pyrolysed at Low Temperature". In: *Carbon* 134 (2018), S. 255–263. DOI: 10.1016/j.carbon.2018.03.067.

[239] Djamila Hourlier. "Thermal Decomposition of Calcium Oxalate: Beyond Appearances". In: *Journal of Thermal Analysis and Calorimetry* 136.6 (2019), S. 2221–2229. DOI: 10.1007/s10973-018-7888-1.

[240] DIN 32645. *DIN 32645:2008-11, Chemische Analytik — Nachweis-, Erfassungs- Und Bestimmungsgrenze Unter Wiederholbedingungen — Begriffe, Verfahren, Auswertung*. 2008. DOI: 10.31030/1465413.

[241] Harald Muckenhuber und Hinrich Grothe. "The Heterogeneous Reaction between Soot and NO2 at Elevated Temperature". In: *Carbon* 44.3 (2006), S. 546–559. DOI: 10.1016/j.carbon.2005.08.003.

[242] B. Marchon, J. Carrazza, H. Heinemann und G. A. Somorjai. "TPD and XPS Studies of O2, CO2, and H2O Adsorption on Clean Polycrystalline Graphite". In: *Carbon* 26.4 (1988), S. 507–514. DOI: 10.1016/0008-6223(88)90149-2.

[243] B. Marchon, W. T. Tysoe, J. Carrazza, H. Heinemann und G. A. Somorjai. "Reactive and Kinetic Properties of Carbon Monoxide and Carbon Dioxide on a Graphite Surface". In: *The Journal of Physical Chemistry* 92.20 (1988), S. 5744–5749. DOI: 10.1021/j100331a039.

[244] Yoshinobu Otake und Robert G. Jenkins. "Characterization of Oxygen-Containing Surface Complexes Created on a Microporous Carbon by Air and Nitric Acid Treatment". In: *Carbon* 31.1 (1993), S. 109–121. DOI: 10.1016/0008-6223(93)90163-5.

[245] Q-L. Zhuang, T. Kyotani und A. Tomita. "DRIFT and TK/TPD Analyses of Surface Oxygen Complexes Formed during Carbon Gasification". In: *Energy & Fuels* 8.3 (1994), S. 714–718. DOI: 10.1021/ef00045a028.

[246] U. Zielke, K. J. Hüttinger und W. P. Hoffman. "Surface-Oxidized Carbon Fibers: I. Surface Structure and Chemistry". In: *Carbon* 34.8 (1996), S. 983–998. DOI: 10.1016/0008-6223(96)00032-2.

[247] C. Moreno-Castilla, F. Carrasco-Marín und A. Mueden. "The Creation of Acid Carbon Surfaces by Treatment with (NH4)2S2O8". In: *Carbon* 35.10 (1997), S. 1619–1626. DOI: 10.1016/S0008-6223(97)00121-8.

[248] G. de la Puente, J. J. Pis, J. A. Menéndez und P. Grange. "Thermal Stability of Oxygenated Functions in Activated Carbons". In: *Journal of Analytical and Applied Pyrolysis* 43.2 (1997), S. 125–138. DOI: 10.1016/S0165-2370(97)00060-0.

[249] C. Moreno-castilla, F. Carrasco-marín, F. J. Maldonado-hódar und J. Rivera-utrilla. "Effects of Non-Oxidant and Oxidant Acid Treatments on the Surface Properties of an Activated Carbon with Very Low Ash Content". In: *Carbon* 36.1 (1998), S. 145–151. DOI: 10.1016/S0008-6223(97)00171-1.

[250] D. M. Nevskaia, A. Santianes, V. Muñoz und A. Guerrero-Ruız. "Interaction of Aqueous Solutions of Phenol with Commercial Activated Carbons: An Adsorption and Kinetic Study". In: *Carbon* 37.7 (1999), S. 1065–1074. DOI: 10.1016/S0008-6223(98)00301-7.

[251] S. Haydar, C. Moreno-Castilla, M. A. Ferro-Garcıa, F. Carrasco-Marın, J. Rivera-Utrilla, A. Perrard und J. P. Joly. "Regularities in the Temperature-Programmed Desorption Spectra of CO2 and CO from Activated Carbons". In: *Carbon* 38.9 (2000), S. 1297–1308. DOI: 10.1016/S0008-6223(99)00256-0.

[252] Issa I. Salame und Teresa J. Bandosz. "Surface Chemistry of Activated Carbons: Combining the Results of Temperature-Programmed Desorption, Boehm, and Potentiometric Titrations". In: *Journal of Colloid and Interface Science* 240.1 (2001), S. 252–258. DOI: 10.1006/jcis.2001.7596.

[253] Grzegorz S Szymański, Zbigniew Karpiński, Stanisław Biniak und Andrzej Światkowski. "The Effect of the Gradual Thermal Decomposition of Surface Oxygen Species on the Chemical and Catalytic Properties of Oxidized Activated Carbon". In: *Carbon* 40.14 (2002), S. 2627–2639. DOI: 10.1016/S0008-6223(02)00188-4.

[254] Purnakala V. Samant, Filomena Gonçalves, Maria Madalena A. Freitas, Manuel Fernando R. Pereira und José L. Figueiredo. "Surface Activation of a Polymer Based Carbon". In: *Carbon*. Carbon '03 Conference 42.7 (2004), S. 1321–1325. DOI: 10.1016/j.carbon.2004.01.034.

[255] José L. Figueiredo, Manuel F. R. Pereira, Maria M. A. Freitas und José J. M. Órfão. "Characterization of Active Sites on Carbon Catalysts". In: *Industrial & Engineering Chemistry Research* 46.12 (2007), S. 4110–4115. DOI: 10.1021/ie061071v.

[256] Jing-Hong Zhou, Zhi-Jun Sui, Jun Zhu, Ping Li, De Chen, Ying-Chun Dai und Wei-Kang Yuan. "Characterization of Surface Oxygen Complexes on Carbon Nanofibers by TPD, XPS and FT-IR". In: *Carbon* 45.4 (2007), S. 785–796. DOI: 10.1016/j.carbon.2006.11.019.

[257] Honória F. Gorgulho, João P. Mesquita, Filomena Gonçalves, Manuel Fernando R. Pereira und José L. Figueiredo. "Characterization of the Surface Chemistry of Carbon Materials by Potentiometric Titrations and Temperature-Programmed Desorption". In: *Carbon* 46.12 (2008), S. 1544–1555. DOI: 10.1016/j.carbon.2008.06.045.

[258] Sabine Kohl, Alfons Drochner und Herbert Vogel. "Quantification of Oxygen Surface Groups on Carbon Materials via Diffuse Reflectance FT-IR Spectroscopy and Temperature Programmed Desorption". In: *Catalysis Today*. Carbon for Catalysis: CarboCat-III Symposium, Berlin, Germany, 2008 150.1 (2010), S. 67–70. DOI: 10.1016/j.cattod.2009.05.016.

[259] François Gaillard, Amal El Hachimi, Claude Descorme, Michèle Besson, Jean-Pierre Joly, Elena M. Polyanskaya, Oxana P. Taran und Valentin N. Parmon. "Study of Oxygen Groups at a Porous Carbon Surface by a New Fast Intermittent Thermodesorption Technique". In: *Carbon* 49.6 (2011), S. 2062–2073. DOI: 10.1016/j.carbon.2011.01.036.

[260] Na Li, Xiaoliang Ma, Qingfang Zha, Kyungsoo Kim, Yongsheng Chen und Chunshan Song. "Maximizing the Number of Oxygen-Containing Functional Groups on Activated Carbon by Using Ammonium Persulfate and Improving the Temperature-Programmed Desorption Characterization of Carbon Surface Chemistry". In: *Carbon* 49.15 (2011), S. 5002–5013. DOI: 10.1016/j.carbon.2011.07.015.

[261] Patrice Brender, Roger Gadiou, Jean-Christophe Rietsch, Philippe Fioux, Joseph Dentzer, Arnaud Ponche und Cathie Vix-Guterl. "Characterization of Carbon Surface Chemistry by Combined Temperature Programmed Desorption with in Situ X-Ray Photoelectron Spectrometry and Temperature Programmed Desorption with Mass Spectrometry Analysis". In: *Analytical Chemistry* 84.5 (2012), S. 2147–2153. DOI: 10.1021/ac102244b.

[262] Sergio Morales-Torres, Tânia L. S. Silva, Luisa M. Pastrana-Martínez, Ana T. S. C. Brandão, José L. Figueiredo und Adrián M. T. Silva. "Modification of the Surface Chemistry of Single- and Multi-Walled Carbon Nanotubes by HNO3 and H2SO4 Hydrothermal Oxidation for Application in Direct Contact Membrane Distillation". In: *Physical Chemistry Chemical Physics* 16.24 (2014), S. 12237–12250. DOI: 10.1039/C4CP00615A.

[263] Jose F. Vivo-Vilches, Esther Bailón-García, Agustín F. Pérez-Cadenas, Francisco Carrasco-Marín und Francisco J. Maldonado-Hódar. "Tailoring the Surface Chemistry and Porosity of Activated Carbons: Evidence of Reorganization and Mobility of Oxygenated Surface Groups". In: *Carbon* 68 (2014), S. 520–530. DOI: 10.1016/j.carbon.2013.11.030.

[264] Klaus Friedel Ortega, Rosa Arrigo, Benjamin Frank, Robert Schlögl und Annette Trunschke. "Acid–Base Properties of N-Doped Carbon Nanotubes: A Combined Temperature-Programmed Desorption, X-Ray Photoelectron Spectroscopy, and 2-Propanol Reaction Investigation". In: *Chemistry of Materials* 28.19 (2016), S. 6826–6839. DOI: 10.1021/acs.chemmater.6b01594.

[265] M. Domingo-García, F. J. López Garzón und M. J. Pérez-Mendoza. "On the Characterization of Chemical Surface Groups of Carbon Materials". In: *Journal of Colloid and Interface Science* 248.1 (2002), S. 116–122. DOI: 10.1006/jcis.2001.8207.

[266] Leland McInnes, John Healy und Steve Astels. "Hdbscan: Hierarchical Density Based Clustering". In: *Journal of Open Source Software* 2.11 (2017), S. 205. DOI: 10.21105/joss.00205.

[267] Jan Schönherr, Johannes R. Buchheim, Peter Scholz und Philipp Adelhelm. "Boehm Titration Revisited (Part II): A Comparison of Boehm Titration with Other Analytical Techniques on the Quantification of Oxygen-Containing Surface Groups for a Variety of Carbon Materials". In: *C* 4.2 (2018), S. 22. DOI: 10.3390/c4020022.

[268] Teresa J. Bandosz, Mykola Seredych, Enrique Rodríguez-Castellón, Yongqiang Cheng, Luke L. Daemen und Anibal J. Ramírez-Cuesta. "Evidence for CO2 Reactive Adsorption on Nanoporous S- and N-Doped Carbon at Ambient Conditions". In: *Carbon* 96 (2016), S. 856–863. DOI: 10.1016/j.carbon.2015.10.007.

[269] Mirosław Kwiatkowski, Vanessa Fierro und Alain Celzard. "Confrontation of Various Adsorption Models for Assessing the Porous Structure of Activated Carbons". In: *Adsorption* 25.8 (2019), S. 1673–1682. DOI: 10.1007/s10450-019-00129-y.

[270] Jacek Jagiello und Jeffrey Kenvin. "Consistency of Carbon Nanopore Characteristics Derived from Adsorption of Simple Gases and 2D-NLDFT Models. Advantages of Using Adsorption Isotherms of Oxygen (O2) at 77 K". In: *Journal of Colloid and Interface Science* 542 (2019), S. 151–158. DOI: 10.1016/j.jcis.2019.01.116.

[271] Pascaline Pré, Guillaume Huchet, Dominique Jeulin, Jean-Noël Rouzaud, Mohamed Sennour und Alain Thorel. "A New Approach to Characterize the Nanostructure of Activated Carbons from Mathematical Morphology Applied to High Resolution Transmission Electron Microscopy Images". In: *Carbon* 52 (2013), S. 239–258. DOI: 10.1016/j.carbon.2012.09.026.

[272] N. J Welham, V Berbenni und P. G Chapman. "Increased Chemisorption onto Activated Carbon after Ball-Milling". In: *Carbon* 40.13 (2002), S. 2307–2315. DOI: 10.1016/S0008-6223(02)00123-9.

[273] John C. Crittenden, Parimi Sanjay Reddy, Harish Arora, John Trynoski, David W. Hand, David L. Perram und R. Scott Summers. "Predicting GAC Performance With Rapid Small-Scale Column Tests". In: *Journal - American Water Works Association* 83.1 (1991), S. 77–87. DOI: 10.1002/j.1551-8833.1991.tb07088.x.

[274] Pei-Zhe Cheng und Hsisheng Teng. "Electrochemical Responses from Surface Oxides Present on HNO3-Treated Carbons". In: *Carbon* 41.11 (2003), S. 2057–2063. DOI: 10.1016/S0008-6223(03)00212-4.

[275] Gerd Fischer, Janna Geith, Thomas M. Klapötke und Burkhard Krumm. "Synthesis, Properties and Dimerization Study of Isocyanic Acid". In: *Zeitschrift für Naturforschung B* 57.1 (2002), S. 19–24. DOI: 10.1515/znb-2002-0103.

Verzeichnisse

Abbildungen

1.1 Quellen und Eintragspfade von organischen Spurenstoffen 3
1.2 Gegenüberstellung von Größenspektren 5
1.3 Spezifische Produkte der pyrolytischen Zersetzung von Polystyrol 7
1.4 Kläranlagen mit Spurenstoffelimination in Deutschland 11
1.5 Spezifische Produkte der pyrolytischen Zersetzung von Polystyrol 13
1.6 Simulierte Modelle zweier Aktivkohle-Mikrostrukturen 14
1.7 Pyrolyse von graphitisierendem Kohlenstoff. Aus Marsh (1991)[143] 18

2.1 Results of the interlaboratory test samples 24
2.2 Thermogravimetry results of six measurements 28
2.3 Gas phase IR spectra of the decomposition gases of PET and PS 29
2.4 Gas phase IR spectra of the decomposition gases of PP and PE 30
2.5 Gas phase IR spectra of the decomposition gases of PP and PE 31
2.6 Results of the TGA-MS measurements of different PVCs 35
2.7 Results of the TGA-MS measurements of suspended matter spiked with PVC . . 36
2.8 MCC results of suspended matter spiked with PE/PP/PS/PET mixture 38

3.1 N_2 adsorption/desorption isotherms shown for three of the eight PACs 46
3.2 Specific surface area (SSA) and total pore volume of the eight PACs 47
3.3 Elemental composition of the eight PACs obtained by XRF 49
3.4 Score plot of the principal component analysis (PCA) of XRF analyses 50
3.5 Linear correlation of ML_{1000} and the oxygen mass content 51
3.6 Linear correlations of $ML_{ox.}$, ML_{600}, and ML_{1000} with C, PZC, and O 51
3.7 Mass loss profiles (DTG curves) of CCP, AZ, PS, and CC 52
3.8 Deconvolution of CO_2 and CO release rates of CC 53
3.9 Box plots grouped by SOGs and sub-grouped by the raw material of ACs 54

4.1 TGA decomposition graphs of carbamazepine, SAE Super, HK 950 and CCP 90D 63
4.2 Comparisons of TGA decomposition graphs for the loaded activated carbons . . 64
4.3 Infrared spectra of the gases evolving 65
4.4 Elimination of isocyanic acid from the carbamazepine molecule 65
4.5 Relative comparison of selected evolved decomposition products 67
4.6 Selected evolved decomposition products of SAE Super 68

4.7 All decomposition products of the systems with 4.5% mass fraction of carbamazepine 69
4.8 Proposed structures for substances released 71

A1 CO_2 release rate correction by an reference measurement of an empty crucible. . 120
A2 TGA of 4 mg calcium oxalate monohydrate. 120
A3 H_2O, CO and CO_2 release rates calcium oxalate monohydrate 121
A4 CO_2 calibration by linear regression. 122
A5 CO calibration by linear regression. 122
A6 H_2O calibration by linear regression. 123
A7 Calibration lines for CO_2, CO and H_2O by linear regression. 123
A8 TGA-FTIR measurement comprised of heating, cooling and heating 124

B1 Isotherms for N_2 adsorption/desorption, grouped 130
B2 Isotherms for N_2 adsorption/desorption, separated 131
B3 Pore size distribution of 5000 P-f based on NLDFT 132
B4 Pore size distribution of 5000 P-f based on QSDFT 133
B5 Particle-size distributions of the PACs 133
B6 Particle-size distributions of the powdered activated carbons 134
B7 XRD diffractogram of HK 950. 135
B8 XRD diffractogram of HKP 1050. 136
B9 XRD diffractogram of CCP 90D. 136
B10 XRD diffractogram of SAE Super. 136
B11 XRD diffractogram of AZ 1050. 137
B12 XRD diffractogram of PS WP 235. 137
B13 XRD diffractogram of CC 401. 137
B14 TEM image with inorganic impurities. 138
B15 TEM image with highlighted inorganic impurities. 139
B16 TEM image with highlighted graphitic structures. 140
B17 TEM image with graphitic structures. 141
B18 PCA (loadings) with row-wise normalized XRF data 142
B19 Parameters from TGA measurements shown in a tertiary plot 143
B20 Parameters from TGA shown in a tertiary plot 143
B21 Mass loss rate profiles (DTG) of HK, HKP, SAE and P-f 144
B22 Pyrolytic mass loss for 18 GACs and their milled representatives 145
B23 Surface chemistry results grouped by PACs. 146
B24 Surface chemistry results grouped by SOGs. 146
B25 Carboxylic acid SOG quantified for all ACs. 147
B26 Anhydride SOG quantified for all ACs. 148
B27 Lactone SOG quantified for all ACs. 149
B28 Phenol SOG quantified for all ACs. 150
B29 Carbonyl SOG quantified for all ACs. 151
B30 Pyrone SOG quantified for all ACs. 152
B31 PCA (scores) of not normalized SOG data 153
B32 PCA (loadings) with not normalized SOG data. 155

B33 PCA (scores) with row-wise normalized SOG data . . . 156
B34 PCA (loadings) with row-wise normalized SOG data . . . 157
B35 C1s peak (left) and O1s peak (right) of HK 950. . . . 159
B36 C1s peak of HK 950 with fittings according to Table B4. . . . 159
B37 C1s peak (left) and O1s peak (right) of HKP 1050. . . . 160
B38 C1s peak of HKP 1050 with fittings according to Table B5. . . . 160
B39 C1s peak (left) and O1s peak (right) of CCP 90D. . . . 161
B40 C1s peak of CCP 90D with fittings according to Table B6. . . . 161
B41 C1s peak of SAE Super. . . . 162
B42 C1s peak of SAE Super with fittings according to Table B7. . . . 162
B43 C1s peak (left) and O1s peak (right) of AZ 1050. . . . 163
B44 C1s peak of AZ 1050 with fittings according to Table B8. . . . 163
B45 C1s peak (left) and O1s peak (right) of PS WP 235. . . . 164
B46 C1s peak of PS WP 235 with fittings according to Table B9. . . . 164
B47 C1s peak (left) and O1s peak (right) of CC 401. . . . 165
B48 C1s peak of CC 401 with fittings according to Table B10. . . . 165

C1 TGA results for the SAE+CBZ-15 system with varying sample masses . . . 168
C2 Hydrolysis of isocyanic acid to carbon dioxide and ammonia. . . . 169
C3 TGA-FTIR release rates of carbon dioxide, water, isocyanic acid and ammonia . 170
C4 TGA-FTIR release rates of hydrogen cyanide from adsorbed carbamazepine . . . 171
C5 Benzene (1) . . . 172
C6 1,3-dimethyl-Benzene (3) . . . 172
C7 p-Xylene (4) . . . 173
C8 Styrene (5) . . . 173
C9 o-Xylene (6) . . . 173
C10 Propyl-Benzene (7) . . . 174
C11 Mesitylene (8) . . . 174
C12 Mesitylene (9) . . . 174
C13 Mesitylene (10) . . . 175
C14 Benzonitrile (11) . . . 175
C15 Phenol (12) . . . 175
C16 ethyl-methyl-Pyridine or m-Ethylanaline (13) . . . 176
C17 x-methyl-Alkane (14) . . . 176
C18 n-butyl-Benzene or (2-methylpropyl)-Benzene (15) . . . 176
C19 methyl-propyl-Benzene (16) . . . 177
C20 3-Butylthiophene (17) . . . 177
C21 Acetophenone (18) . . . 177
C22 Acetophenone (19) . . . 178
C23 Benzylnitrile or methyl-Benzonitril (20) . . . 178
C24 Benzene, 1-methyl-4-(1-methylpropyl)- (22) . . . 178
C25 Acetic acid, 2-ethylhexyl ester (23) . . . 179
C26 Benzene, 1-methyl-4-(2-methylpropyl)- (24) . . . 179
C27 Naphthalene (25) . . . 179

C28 Benzothiophene (26) . . . 180
C29 Dodecane (27) . . . 180
C30 Benzothiazole (28) . . . 180
C31 (iso)Quinoline (30) . . . 181
C32 Hexyl-Benzene (31) . . . 181
C33 Benzene, (1,3-dimethylbutyl)- (32) . . . 181
C34 x-methyl-Alkane (33) . . . 182
C35 methyl-Naphthalene (34) . . . 182
C36 methyl-Quinoline (35) . . . 182
C37 1- or 2-methyl-Naphthalene (36) . . . 183
C38 Heptyl-Benzene (37) . . . 183
C39 2-ethenyl-Naphthalene or Biphenyl (38) . . . 183
C40 Tetradecane (39) . . . 184
C41 Bithiophene (40) . . . 184
C42 methyl-Biphenyl (41) . . . 184
C43 3-phenyl-Thiophene (42) . . . 185
C44 2,2'-Dimethylbiphenyl (43) . . . 185
C45 dimethyl-Quinoline (45) . . . 185
C46 Dibenzofuran (48) . . . 186
C47 2-methyl-Hexadecane (49) . . . 186
C48 Fluorene (50) . . . 186
C49 Phenanthrene or Anthracene (53) . . . 187
C50 Acridine (54) . . . 187
C51 (4-)methyl-Acridine (56) . . . 187
C52 (9-)methyl-Acridine (58) . . . 188
C53 5H-Dibenzazepine, 10,11-dihydro- (59) . . . 188
C54 Dibenzazepine, "Iminostilbene" (60) . . . 188
C55 9-Acridinecarbonitrile or Biphenyldicarbonitrile (62) . . . 189
C56 Ethylacridine (63) . . . 189
C57 1-methyl-2-phenyl-Indole (64) . . . 189
C58 1-methyl-3-phenyl-Indole (65) . . . 190
C59 SEM images of HK 950 systems . . . 191
C60 SEM images of CCP 90D systems . . . 191
C61 DRIFT spectra of SAE Super and CCP 90D systems . . . 192
C62 DRIFT spectra of loaded and unloaded HK 950 systems . . . 192

Tabellen

1.1 Bindungsenergie von Kohlenstoff-Einfachbindungen sortiert nach ihrem Betrag [138]. 16

2.1 Target values and results of the interlaboratory test samples 25
2.2 List of qualifier and quantifier substances detection by TED-GC/MS 28
2.3 Selected wave numbers for the detection of the polymers using TGA-FTIR . . . 29
2.4 Selected m/z ratios for the detection of the polymers PE, PP and PS with TGA-MS. 33
2.5 Overview of the advantages and limitation of the different methods. 39

3.1 Activated carbon samples 43
3.2 Carbon, hydrogen, nitrogen, sulfur, and oxygen content and PZC for the eight PACs 48

4.1 Characteristics of the three powdered activated carbons 62
4.2 Sample code, mass fractions and thermogravimetric results 64

A1 Complete list of activated carbon samples 114
A2 Integration regions and baselines used for FTIR release rates 117
A3 Statistics of the linear calibration function for TGA-FTIR 118
A4 Assignment of CO_2, CO and H_2O to surface oxygen groups 119
A5 Literature about the temperature-programmed decomposition (TPD) methodology125

B1 Physical characteristics obtained for the eight PACs 128
B2 Chemical characteristics obtained for the eight PACs 129
B3 Elements determined by XPS 158
B4 Fitting of the C1s peak of HK 950, corresponding to Figure B36. 159
B5 Fitting of the C1s peak of HKP 1050, corresponding to Figure B38. 160
B6 Fitting of the C1s peak CCP 90D, corresponding to Figure B40. 161
B7 Fitting of the C1s peak of SAE Super, corresponding to Figure B42. 162
B8 Fitting of the C1s peak of AZ 1050, corresponding to Figure B44. 163
B9 Fitting of the C1s peak of PS WP 235, corresponding to Figure B46. 164
B10 Fitting of the C1s peak of CC 401, corresponding to Figure B48. 165

C1 TGA characteristics for the 1st & 2nd mass loss stage 168
C2 Kinetic parameters determined by ramp kinetic experiments 169

Abkürzungen

AC	Activated carbon
AK	Aktivkohle
approx.	approximately (circa)
AZ	AZ 1050, Pulveraktivkohle von CSC
BET	Brunauer–Emmett–Teller, Theorie zur SSA-Bestimmung
bzw.	beziehungsweise
C	Carbon (Kohlenstoff)
ca.	circa
CBZ	Carbamazepin
CC	CC 401, Pulveraktivkohle von Chemviron
CCP	CCP 90D, Pulveraktivkohle von Donau Carbon
CHNS	Analysemethode zur Bestimmung der Elementgehalte von C, H, N und S
CSC	Carbon Service & Consulting
DEET	Diethyltoluamid
DFT	Density Function Theory
DOC	Dissolved organic carbon (gelöster organischer Kohlenstoff)
DOM	Dissolved organic matter (gelöstes organisches Material)
DTA	Differenz-Thermoanalyse
DTG	Differenzierte Thermogravimetrie (1. Ableitung der TG Kurve)
DWA	Deutsche Vereinigung für Wasserwirtschaft, Abwasser und Abfall e.V.
ECHA	European Chemicals Agency (Europäische Chemikalienagentur)
EQSD	Environmental Quality Standard Directive (Umweltqualitätsnorm)
FTIR	Fourier-Transform-Infrarotspektrometer
GAC	Granular activated carbon
GAK	Granulierte Aktivkohle
GC/MS	Gaschromatographie-Massenspektrometrie
ggf.	gegebenen falls
GOW	Gesundheitlicher Orientierungswert
H	Hydrogen (Wasserstoff)
HK	HK 950, Pulveraktivkohle von CSC
HKP	HKP 1050, Pulveraktivkohle von CSC
HRR	Heat release rate
incl.	inklusive
IR	Infrarotspektroskopie
m/z	Masse zu Ladungsverhältnis
MCC	Microscale combustion calorimeter
ML_{600}	Pyrolytischer TGA Massenverlust bis 600 °C
ML_{1000}	Pyrolytischer TGA Massenverlust bis 1000 °C
$ML_{ox.}$	Oxidativer TGA Massenverlust bei 1000 °C
MP	Mikroplastik
MS	Massenspektrometrie

N	Nitrogen (Stickstoff)
NLDFT	Non-Linear Density Function Theory
NOM	Natural organic matter (natürliches organisches Material)
O	Oxygen (Sauerstoff)
OMP	Organic micro-pollutant
P	Phosphorous (Phoshphor)
P-f	5000 P-f, Pulveraktivkohle von Jacobi Carbons
PAC	Powdered activated carbon
PAK	Pulveraktivkohle
PCA	principal component analysis (Hauptkomponentenanalyse)
PE	Polyethylen
PET	Polyethylenterephthalat
PFAS	Polyfluorierte Alkylsubstanzen
PMMA	Polymethylmethacrylat
PP	Polypropylen
PS	Polystyrol
PS	PS-WP 235, Pulveraktivkohle von Chemviron
PSD	Pore size distribution
PVC	Polyvinylchlorid
Py-GC/MS	Pyrolyse-Gaschromatographie-Massenspektrometrie
PZC	Point of zero charge
QSDFT	Quenched Solid Density Function Theory
S	Sulfur (Schwefel)
SAE	SAE Super, Pulveraktivkohle von Cabot (Norit)
SI	Supplementary Information
SSA	Specific surface area
TA	Thermische Analyse oder Thermoanalyse
TCPP	Tris(2-chlorisopropyl)phosphat
TED-GC/MS	Thermische Extraktion- und Desorption Gaschromatographie-Massenspektrometrie
TEM	Transmissionselektronenmikroskop
TFA	Trifluoressigsäure
TG	Thermogravimetrie (Ergebnis der TGA, Probenmasse als Funktion der Temperatur)
TGA	Thermogravimetrische Analyse
TGA-FTIR	Thermogravimetrie-Fourier-Transform-Infrarotspektroskopie
TGA-FTIR-GC/MS	Thermogravimetrie-Fourier-Transform-Infrarotspektroskopie-Gaschromatographie-Massenspektrometrie
TGA-MS	Thermogravimetrie-Massenpektrometrie
THR	Total heat release
TPD	Temperature programmed decomposition (auch: desorption)
UVA_{254}	UV-Absorption bei 254 nm
vgl.	vergleiche

WFD	Water Framework Directive (Wasserrahmenrichtlinie)
XPS	X-ray photoelectron spectroscopy (Röntgenphotoelektronen-spektroskopie)
XRD	X-ray diffraction (Röntgenbeugung)
XRF	X-ray fluorescence spectroscopy (Röntgenfluoreszenz)
z. B.	zum Beispiel

A

Supplementary information (Methods) for "Characterization of activated carbon products for water treatment including extended analysis of oxygen-containing functional groups"

This appendix is part of chapter 3, provides details on materials and methods, and was submitted to *Water Research X* on June 29th, 2021.

This appendix contains

1 Complete set of activated carbon samples
2 Surface area and porosity analyses
3 Particle size determination
4 X-ray photoelectron spectroscopy (XPS)
5 X-ray fluorescence spectroscopy (XRF)
6 Thermogravimetry coupled to Fourier-transform infraredspectroscopy (TGA-FTIR)
7 Cluster analysis on PCA score plots
8 Other techniques

A.1 Complete set of activated carbon samples

TGA-FTIR and XRF analysis were conducted on the complete set of 55 individual samples listed in Table A1. The set is comprised of 25 different activated carbons, GAC or PAC, some of different batches or of the same batch being ground (milled) GAC to PAC. Additionally, anthracite coal was added for XRF analysis.

Table A1: Complete list of activated carbon samples, starting with the eight PAC that where extensively investigated in the original research paper.

name	manufacturer	raw material	type	batch
HK 950	CSC	Wood charcoal	PAC	
HKP 1050	CSC	Wood charcoal	PAC	
CCP 90D	Donau Carbon	Coconut shell	PAC	
SAE Super	Cabot (Norit)	Mixture	PAC	
5000 P-f	Jacobi Carbons	Lignite	PAC	
AZ 1050	CSC	Bituminous coal	PAC	
PS-WP 235	Chemviron	Bituminous coal	PAC	
CC 401	Chemviron	Hard coal (reactivate)	PAC	
Epibon A	Donau Carbon	Lignite	GAC	
Epibon A	Donau Carbon	Lignite	GAC	milled
HK 1200	CSC	Wood charcoal	GAC	
HK 1200	CSC	Wood charcoal	GAC	milled
Hydraffin CC	Donau Carbon	Coconut shell	GAC	
Hydraffin CC	Donau Carbon	Coconut shell	GAC	milled
AquaSorb MP23	Jacobi Carbons	Lignite	PAC	
AquaSorb 2000	Jacobi Carbons	Bituminous coal	GAC	
Carbopal AP	Donau Carbon	Lignite	PAC	
GAK-FM (OWA)			GAC	
AS 6300	Jacobi Carbons	Hard coal	GAC	A
AS 6300	Jacobi Carbons	Hard coal	GAC	A, milled
AS 6300	Jacobi Carbons	Hard coal	GAC	B
AS 6300	Jacobi Carbons	Hard coal	GAC	B, milled
HyA	Donau Carbon	Lignite	GAC	
HyA	Donau Carbon	Lignite	GAC	milled
Hydraffin CC	Donau Carbon	Coconut shell	GAC	
Hydraffin CC	Donau Carbon	Coconut shell	GAC	milled
HyCC plus	Donau Carbon	Coconut shell	GAC	
HyCC plus	Donau Carbon	Coconut shell	GAC	milled
Hydraffin XC 30	Donau Carbon	Hard coal	GAC	A
Hydraffin XC 30	Donau Carbon	Hard coal	GAC	A, milled
Hydraffin XC 30	Donau Carbon	Hard coal	GAC	B
Hydraffin XC 30	Donau Carbon	Hard coal	GAC	B, milled
HKP 1000	CSC	Wood charcoal	GAC	
HKP 1000	CSC	Wood charcoal	GAC	milled
HCK 1050	CSC	Coconut shell	GAC	
HCK 1050	CSC	Coconut shell	GAC	milled
HCR+ 1	CSC	Bituminous coal (reactivate)	GAC	A
HCR+ 1	CSC	Bituminous coal (reactivate)	GAC	A, milled
HCR+ 1	CSC	Bituminous coal (reactivate)	GAC	B
HCR+ 1	CSC	Bituminous coal (reactivate)	GAC	B, milled
AS 5000	Jacobi Carbons	Lignite	GAC	A

Table A1 continued from previous page

name	manufacturer	raw material	type	batch
AS 5000	Jacobi Carbons	Lignite	GAC	A, milled
AS 5000	Jacobi Carbons	Lignite	GAC	B
AS 5000	Jacobi Carbons	Lignite	GAC	B, milled
ROW 0.8 SUPRA	Cabot (Norit)	Hard coal (reactivate)	GAC	A
ROW 0.8 SUPRA	Cabot (Norit)	Hard coal (reactivate)	GAC	B
ROW 0.8 SUPRA	Cabot (Norit)	Hard coal (reactivate)	GAC	C
ROW 0.8 SUPRA	Cabot (Norit)	Hard coal (reactivate)	GAC	D
ROW 0.8 SUPRA	Cabot (Norit)	Hard coal (reactivate)	GAC	E
ROW 0.8 SUPRA	Cabot (Norit)	Hard coal (reactivate)	GAC	F
ROW 0.8 SUPRA	Cabot (Norit)	Hard coal (reactivate)	GAC	G
ROW 0.8 SUPRA	Cabot (Norit)	Hard coal (reactivate)	GAC	H
ROW 0.8 SUPRA	Cabot (Norit)	Hard coal (reactivate)	GAC	H, milled
CC PHO 8x30	Eurocarb	Coconut shell	GAC	
CC PHO 8x30	Eurocarb	Coconut shell	GAC	milled
Anthrazit		Anthracite	granular	

A.2 Surface area and porosity analyses

N_2 gas adsorption and desorption at 77 K was carried out with an Autosorb-1-MP (Quantachrome Instruments, USA) in duplicates using sample weights of 20 to 50 mg. Prior to the measurements the samples were out-gassed at 378 K under vacuum of 1 Pa until the pressure rise was below 1.33 Pa min^{-1}. The measurements were performed recording 50 acquisition points in a relative pressure range of 0.010 - 0.995 (29 points for adsorption branch, 22 points for desorption branch). In order to reduce void volume effects measurements were conducted using a glass rod inside the sample cell. Equilibration time was set to 2 min. The tolerance level was set to "0". That means for the pressure range $p/p_0 = 0.01 - 0.025$ a tolerance from $+3.0e{-}5$ to $-1.0e{-}5$, and for the range $p/p_0 = 0.025 - 1$ a tolerance from $+0.003$ to -0.001 was accepted.

For analysis of the isotherm data the software versions Autosorb for Windows 1.25 and AS1Win 2.11 were used to extract the information about porosity and surface as described below.

The specific surface area (SSA) was determined by using the equation by Brunauer et al. (1938)[235]. As this BET equation is not valid to microporous adsorbents the method was modified, as recommended by Rouquerol et al. (2007)[236] with a shifted pressure range to lower p/p_0 (best linear fit in the range of $0.01 \leq p/p_0 \leq 0.15$). Thus, the calculated SSA is not a "monolayer content" according to Brunauer et al. (1938)[235] but more a "BET strong retention capacity" or a useful representative of that.

Total pore volume was determined using the Gurvich rule at $p/p_0 = 0.95$. The average pore diameter was calculated from the ratio of total pore volume and SSA assuming a cylindrical pore geometry as 4V/SSA.

Micropore volume and external area were estimated based on the statistical thickness of the layer adsorbed by the t-plot method with a statistical layer thickness of carbon black = 0.088 $(p/p_0)^2 + 0.645\ (p/p_0) + 0.298$ [237]. Surface area corresponding to micropores was obtained from the difference between external area and SSA.

Pore size distribution (PSD) was determined by different built-in Non-Local Density Functional Theory (NLDFT) models and Quenched Solid Density Functional Theory (QSDFT) equilibrium

transition kernels from the Quantachrome DFT models library. All used kernels for adsorption of nitrogen at 77 K on carbon are based on models of typical pore geometries: slit pore, cylindrical pores, and a mixture slit/cylindrical pores. Exemplary PSDs and kernel designations are provided in the SI, Appendix B (Figures B3 and B4).

A.3 Particle size determination

The particle size distribution was determined as duplicates using a laser light extinction particle counter (type SVSS with HCB-LD optical sensor, PAMAS, Germany), equipped with a 100 μm pre-screen. 1 mg L^{-1} suspensions of each PAC were prepared in ultra-pure water in rinsed flasks (ultra-pure water, followed by washing with diluted HCl, followed by ultra-pure water), ultrasonicated, and left 24 h for full soaking, followed by measurement at a flow of 2.5 mL min^{-1} for 2-3 min (two duplicates directly after one another). 32 channels record size classes from 1 to 400 μm (width of channel 1-9: 1 μm, 10-14: 2 μm, 15-18: 5 μm, 19-24: 10 μm, 25-29: 50 μm). The software PMA (PAMAS, Germany) calculated the cumulative volume according to the detected particle sizes (assuming spherical shape), in combination with particle counts of defined particle size fractions. Additional information are published by Dittmar et al. (2018)[114].

A.4 X-ray photoelectron spectroscopy (XPS)

X-ray photoelectron spectroscopy (XPS) was performed on a SAGE 100 device (Specs, Germany). Aluminum Kα radiation (1486.6 eV) was used for excitation of the photoelectrons with 20 mA, and 10 kV under ultra-high vacuum ($< 3{\cdot}10^{-7}$ mbar). The angle between anode and analyzer was 54.9°, the analyzer was adjusted with 18° to the surface normal. The analyzed area of the sample was 3x1 mm. The measurements were performed in constant analyzer energy mode (CAE) with pass energy of 20 mA. The samples were analyzed in small aluminum cups with 10 mm in diameter. At least two replicates were measured before calculating mean values for the element contents. The spectra were analyzed by Specslab and fitted by CasaXPS. The C–C bond is used for standardization with a binding energy of 285 eV. Furthermore, peak fitting was performed for C–O, C=O, O–C=O, carbonate, **and the shake-up peak of aromatic structures** in accordance with Desimoni et al. (1990)[194] and Durán-Valle (2012)[183]. **The peaks assigned as carbonate and $\pi - \pi^*$ were attributed primarily to plasmon loss and shake-up features, respectively, rather than to surface characteristics.**

A.5 X-ray fluorescence spectroscopy (XRF)

Energy-dispersive X-ray fluorescence spectroscopy (XRF) was performed on a Spectro XEPOS III with the software X-LabPro 5.1/TurboQuant (Spectro Analytical Instruments, Germany). The XRF cell (inner diameter: 24 mm) was covered with a Mylar film (thickness: 4 μm). The TurboQuant method applies the fundamental parameters method for semi-quantitative analyses of the elements ranging from aluminium to uranium. **Masses of at least 1 g were analysed, except for HKP 1050 with 528 mg and 5000 P-f with 43 mg, due to limited sample mass. Experiments showed that these sample masses do not effect the semi-quantitative results.**

Additional details on the equipment and a way to obtain quantitative results are published in Dittmann et al. (2020)[195].

A.6 Thermogravimetry coupled to Fourier-transform infrared spectroscopy (TGA-FTIR)

For temperature controlled decomposition of the samples a thermobalance TGA/DSC 3+ from Mettler Toledo (USA) was used. Continuous evolved gas analysis was achieved by coupling to a Fourier-transform infrared spectrometer Nicolet iS50 with DTGS detector and TG-IR module, consisting of a heated transferline (250 °C) and IR cell (260 °C), from Thermo Fisher Scientific (USA). During TGA measurements IR spectra of the gaseous decomposition products were recorded for wave numbers 4000 – 400 cm^{-1} by 16 scans per spectrum with 4 cm^{-1} resolution.

Thermogravimetric analysis Two TGA methods were used as several parameters were determined by TGA-FTIR. Each measurement commences in a nitrogen atmosphere at 25 °C isotherm for 5 min, followed by a constant heating rate of 10 °C min^{-1} with a purge gas flow of 50 mL min^{-1}. The first method applied 20 mg sample mass in 150 μL aluminum oxide crucibles and switched the purge gas at 600 °C to synthetic air, heating further up to 900 °C. The second method applied 75 mg sample mass in 600 μL aluminum oxide crucibles and kept the nitrogen purge gas up to 1000 °C without changing the atmosphere. For both methods sample mass is recorded every second and subsequently subtracted by a reference measurement of an empty crucible. The obtained TGA data as mass loss- or TG curve was furthermore differentiated with respect to measurement time to yield the mass loss rates- or DTG curve.

Specific mass losses were normalized to dry sample mass (145 °C) and are comprised of pyrolytic mass loss up to 600 °C (ML_{600}) and up to 1000 °C (ML_{1000}) in nitrogen atmosphere and of subsequent mass loss by oxidation ($ML_{ox.}$) in synthetic air. The mass residue after oxidation is the ash content of the sample. $ML_{ox.}$ is calculated by subtracting ML_{1000} and ash of 100%.

Gas-specific release rates and quantification For the determination of oxygen-containing functional groups (surface oxygen groups, SOG) and the oxygen content of the samples, TGA-FTIR measurements up to 1000 °C were conducted as triplicates. The reference measurement with an empty crucible was performed every working day to correct TGA and FTIR data. FTIR spectra were analyzed for H_2O, CO_2, CO and CH_4 (Table A2) with respect to derive gas specific release rates (Software OMNIC 9.7.39).

Table A2: Integration regions and baselines used to derive gas specific release rates from the FTIR spectra collected during TGA.

gas	band region	baseline
H_2O	1346–1330 cm^{-1}	1346–1330 cm^{-1}
CO	2244–2143 cm^{-1}	2400–2143 cm^{-1}
CO_2	2400–2244 cm^{-1}	2400–2143 cm^{-1}
CH_4	3024–3001 cm^{-1}	3024–3001 cm^{-1}

H_2O, CO_2 and CO were quantified by previous calibration with calcium oxalate monohydrate (purity 99.9985%, Alfan Aesar, USA). Calibration features are given in Table A3 and additional details are provided in section A.6.2.

Table A3: Linear calibration functions and statistical values obtained by calcium oxalate monohydrate measurements. Corresponding linear regressions are provided in Figures A4-A7.

	slope in area mmol^{-1}	intercept in area	R^2	LOD in μmol	LOQ in μmol
CO_2	9144.38	24.03	0.99752	0.8	2.4
CO	435.43	-0.42	0.99883	0.6	1.7
H_2O	17.17	0.02	0.99942	0.4	1.3

By integration of the release rates of the quantified gases, the amount of evolved oxygen could be derived as sample's oxygen content. The oxygen of H_2O above the dry temperature (specimen dependent between 120 and 150 °C) was considered if a significant release occurred. Otherwise, uncertainty of the results increases, due to lower sensitivity of H_2O compared to CO_2 and CO.

Release rate deconvolution and associated parameters According to the temperature-programmed decomposition (TPD) methodology, individual SOGs in carbon materials decompose to H_2O, CO_2 or CO at certain temperature ranges. These ranges will overlap for activated carbon, but can be distinguished by deconvolution with the fitting of Gaussian curves. Based on a literature review and on the analysis of the activated carbons, a TPD method was adapted to our TGA-FTIR setup (see section A.6.4 for details). Table A4 lists the temperatures and gases used for the assignment to the SOGs. The deconvolution algorithm was allowed to adjust these temperatures by a tolerance of ± 30 °C. Additionally, the fitted Gaussian curves are limited to 95 °C for half width at half maximum (HWHM). The small but sharp "unassigned CO_2" peak evolving at 625 °C is thought to evolve from the decomposition of inorganic substances, e. g. carbonates. Therefore, this peak is limited to maximum HWHM of 30 °C and attributed with a slightly higher center tolerance of ± 35 °C. If the "unassigned CO_2" peak is used for the fitting, the next peak of lactones 1 additionally, is limited to minimum HWHM of 30 °C, to prevent mixing up the assignment.

Uncertainty and robustness testing Deconvolution applied to release rates imply several uncertainties and in general the risk of overfitting. To achieve reproducible results and reveal uncertainties, we developed a Python package for the evaluation of SOGs by TGA-FTIR or similar configurations [191]. A robustness testing is included that varies the initial temperatures in Table A4 and separately its tolerances by ± 10 °C. Furthermore, the initial values of the Gaussian curve parameters height and HWHM as well as their limits were varied by ± 30%. Therefore, for each SOG eleven results are obtained that represent the robustness of the fitting and hence, provide a mean value with standard deviation as uncertainty.

Table A4: Assignment of CO_2, CO and H_2O to surface oxygen groups released at certain temperatures (in °C). a: unassigned H_2O releases found from HK 950 and HKP 1050; b: unassigned CO_2 release found from CC 401; *: CO release predefined by quantity of the respective CO_2 release (by width and height of fitted Gauss curves)

	CO_2	CO	H_2O
adsorbed	95	-	90
unassigned 1	-	-	210[a]
unassigned 2	-	-	255[a]
carboxylic acids 1	245	255	-
carboxylic acids 2	380	410	-
anhydrides	500*	530*	-
unassigned CO2	625[b]	-	-
lactones 1	635	-	-
lactones 2	785	-	-
phenols	-	670	-
carbonyls 1	-	790	-
carbonyls 2	-	870	-
pyrones	-	960	-

A.6.1 FTIR release rate corrections

Release rates are created from FTIR gas phase spectra recorded during the TGA measurement. Right before the beginning of the measurement a background spectrum is collected that is subtracted from the following spectra. During the measurement time of 98 min the FTIR spectra may fluctuate and the respective release rates can show a noisy baseline. Therefore, the release rates were corrected by constant y-axis shifts. In a first step, the minimum of the release rate was set to zero and in a second step the release rate was subtracted by a gas specific threshold value to intercept the noise. In conclusion, integration of the noisy release rate in a temperature range without gas evolution will be zero and is not compromised from the noise.

Additionally, the release rate of CO_2 may imply strong periodic fluctuations, due to the high infrared sensitivity of this gas and an adsorption dryer flushing the FTIR device by air and regularly switching the adsorption columns. Therefore the CO_2 release rate obtained by the reference measurement with an empty crucible was used to especially correct the CO_2 release rates.

For this purpose, the reference measurement needs to be from the same day and was aligned to the period of the sample, before subtraction. The applied correction is exemplary shown in Figure A1. These corrections have been automated within the data evaluation by the Python package [191].

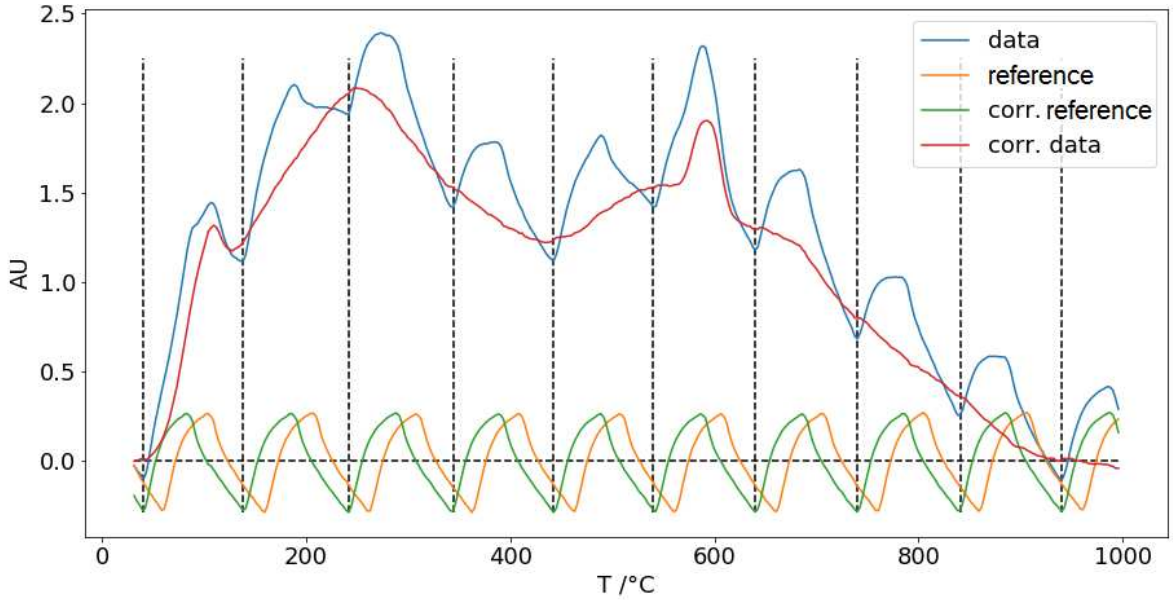

Figure A1: CO_2 release rate correction by an reference measurement of an empty crucible.

A.6.2 Calibration with Calcium oxalate monohydrate

Thermal decomposition of calcium oxalate monohydrate obtains three well separated decomposition steps as shown in Figure A2.

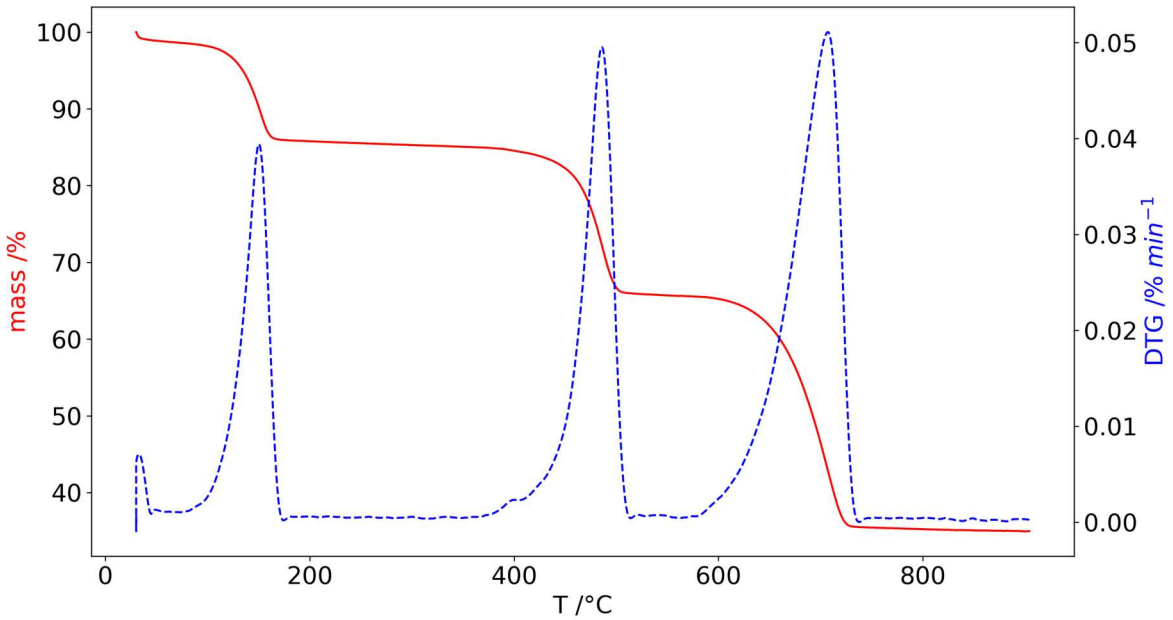

Figure A2: TGA of 4 mg calcium oxalate monohydrate.

They correspond to the release of H_2O, CO and CO_2, respectively and can be used to calibrate the release of these gases [238, 176]. Therefore, amounts of 1, 2, 3, and 4 mg of calcium oxalate monohydrate were determined in triplicates. However, in the second decomposition step small amounts of CO_2 are released concurrently with CO and vice versa in the third decomposition step (cf. Figure A3).

Different reasons for this effect are discussed in literature [239, 238]. We coped with it using an iterative calibration for CO_2 and CO, which assumes the partly oxidation of CO by residual

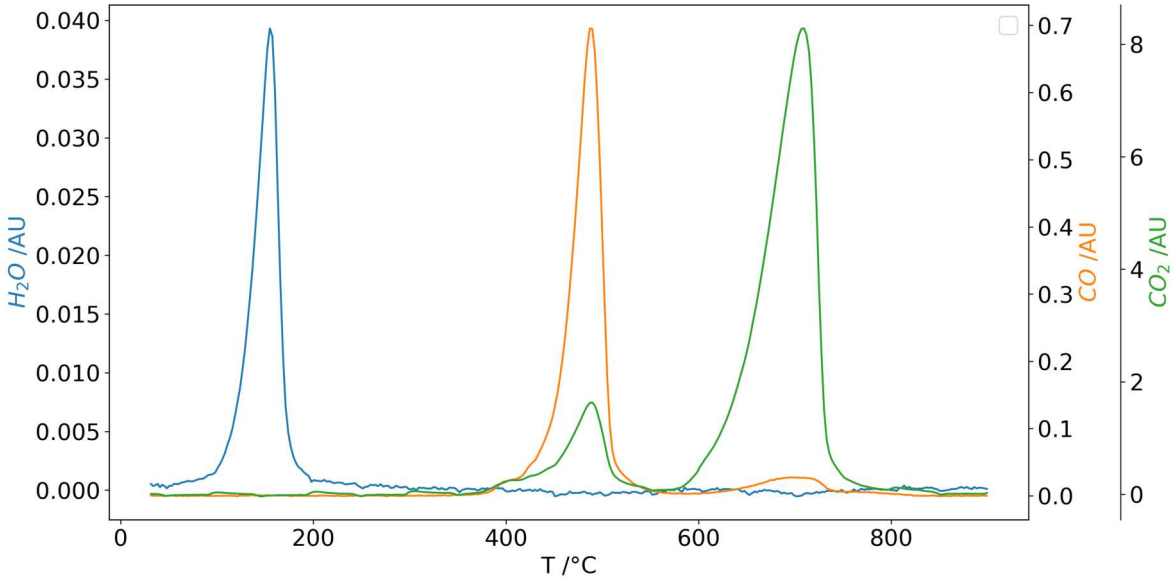

Figure A3: H_2O, CO and CO_2 release rates obtained by TGA-FTIR of 4 mg calcium oxalate monohydrate, corresponding with Figure A2.

oxygen in the purge gas. Therefore, the obtained calibration features from the first iteration were applied to quantify the gases and correct their amounts mutually, followed by the next iteration step until their amounts converged.

The finally obtained features of the linear calibration functions for CO_2, CO and H_2O were previously shown in Table A3. The corresponding linear regressions are provided in Figures A4-A6. Additionally, Figure A7 emphasizes the different sensitivities of the individual gases.

The limit of detection (LOD) and the limit of quantification (LOQ) were obtained according to DIN 32645 (2008)[240] with n = 12 samples, m = 1 repetitions per sample, $\alpha = \beta = 95\%$ and a relative reciprocal uncertainty of $k = 3$.

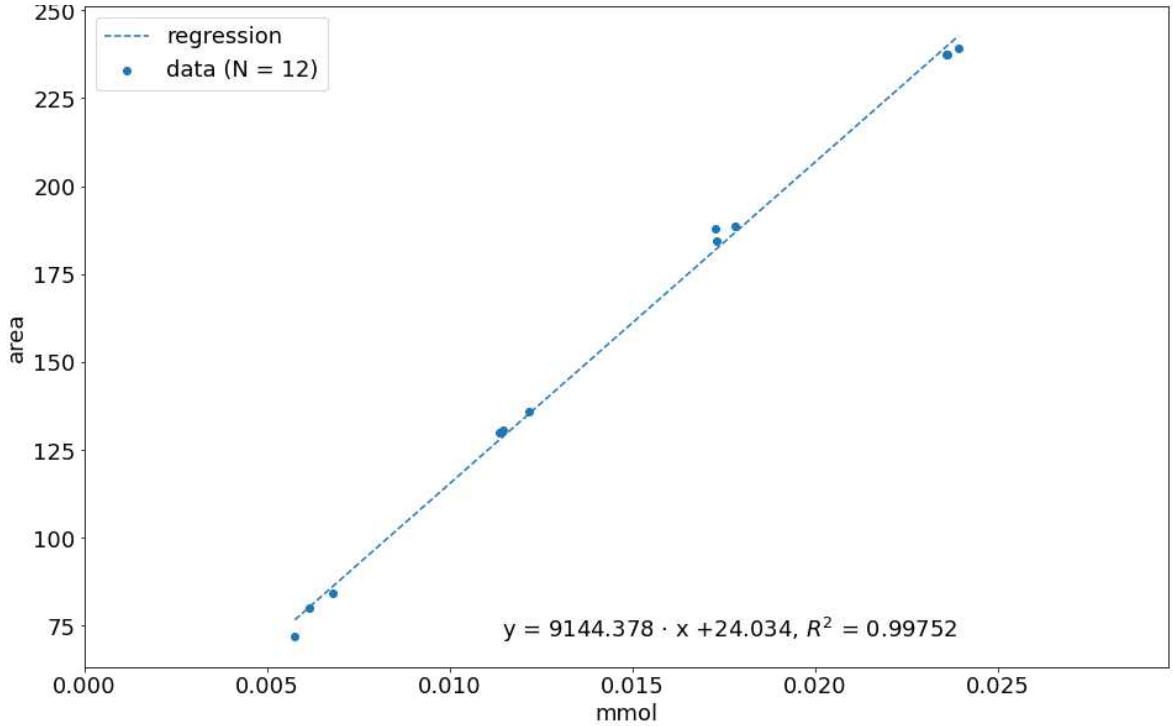

Figure A4: CO_2 calibration by linear regression.

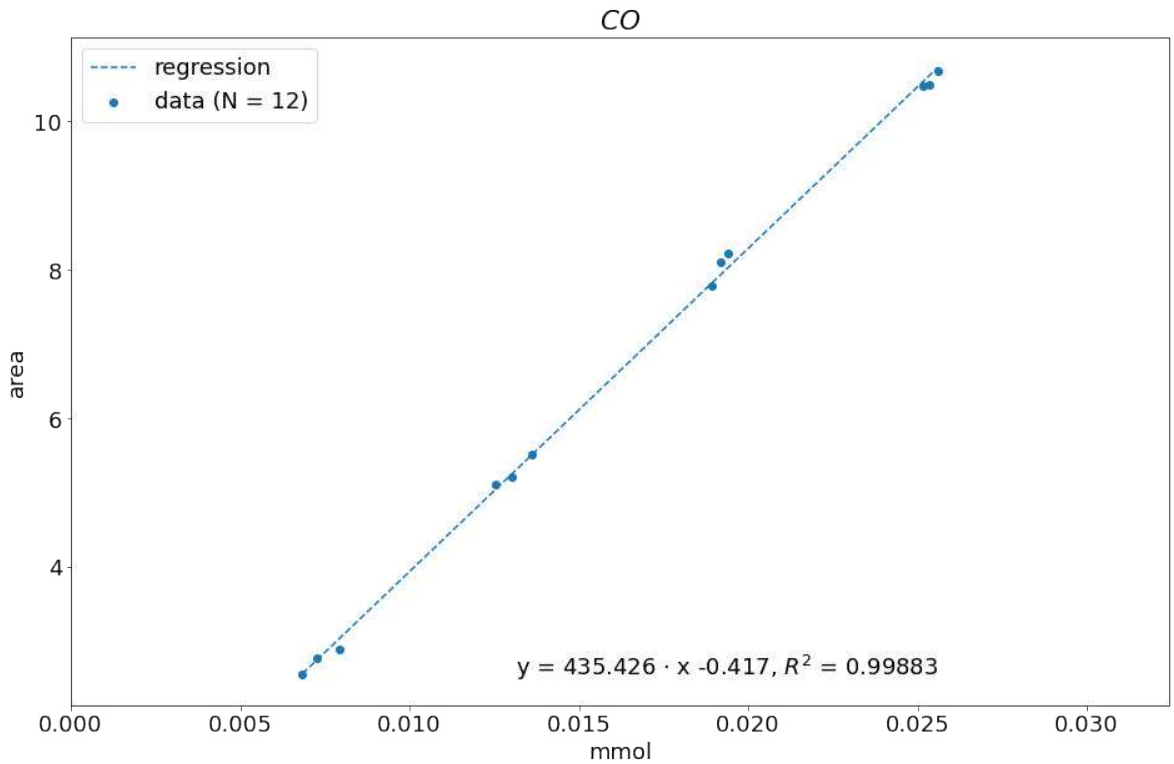

Figure A5: CO calibration by linear regression.

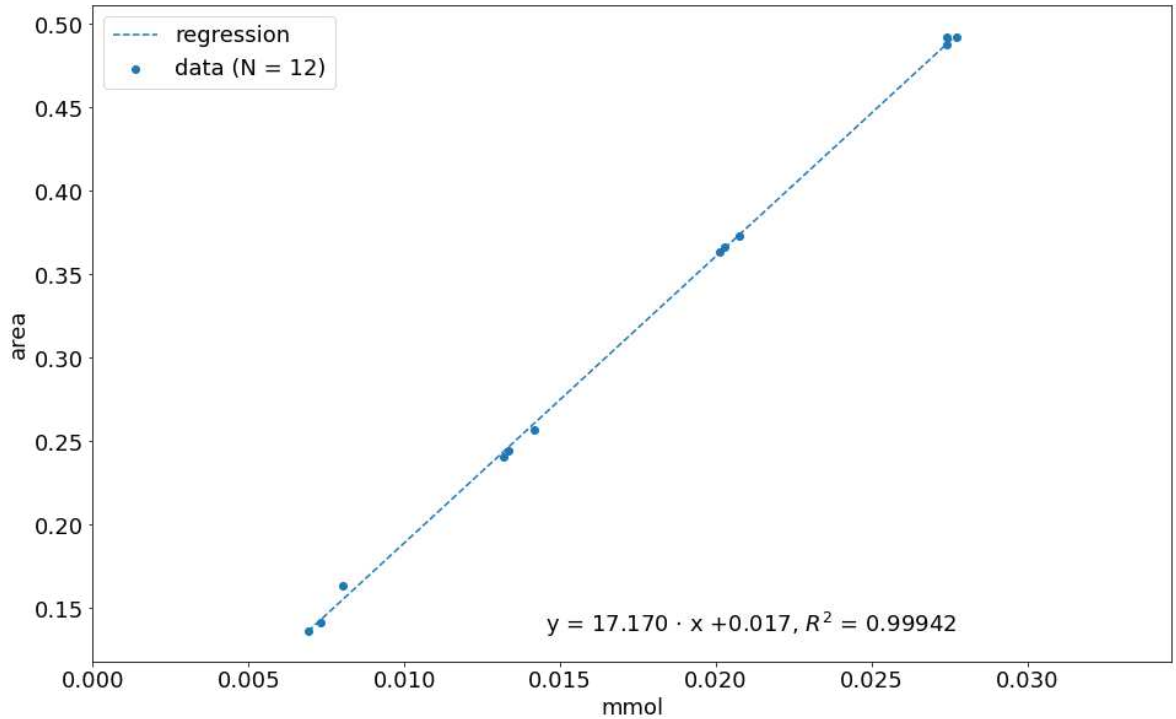

Figure A6: H_2O calibration by linear regression.

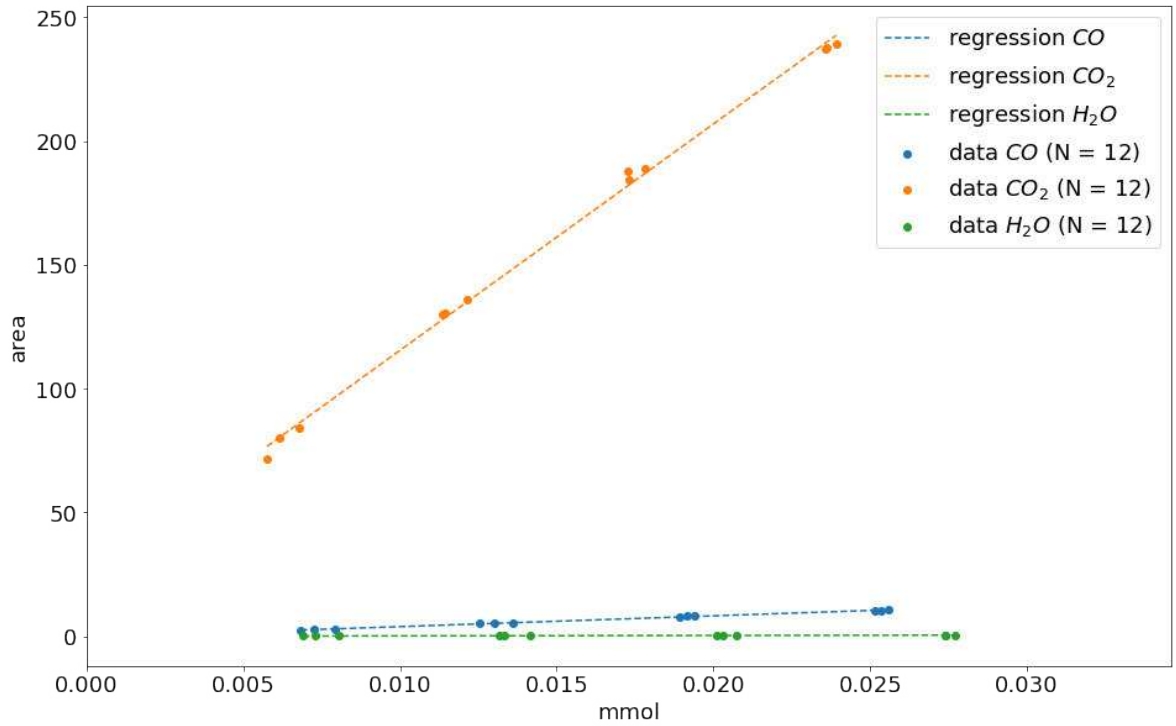

Figure A7: Calibration lines for CO_2, CO and H_2O by linear regression.

A.6.3 Check for secondary reactions

The appearance of secondary reactions concurrently with SOG decomposition was analyzed by the variation of the TGA heating rate (5, 10, 20 °C min^{-1}). If the amounts of evolved gases remain constant, the specific gas is not involved in secondary reactions [241]. This was the case for H_2O and CO_2, while the evolution of CO decreased with increasing heating rates. Residual oxygen in the purge gas as assumed in section A.6.2 is not conclusive since the CO_2 evolution did not change. Therefore, slight leakages of the TGA oven at very high temperatures may account for this effect by inevitable oxidation of the carbon structure by diffusive oxygen intrusion. This was confirmed by consecutive heating, cooling and heating as shown in Figure A8 as CO is again released during the second heating. Furthermore, at the end of the cooling step and at the beginning of the second heating a hysteresis is shown by the DTG curve that does not correspond to the analyzed gases. We suggest adsorption of N_2 (in micropores) to cause this observation.

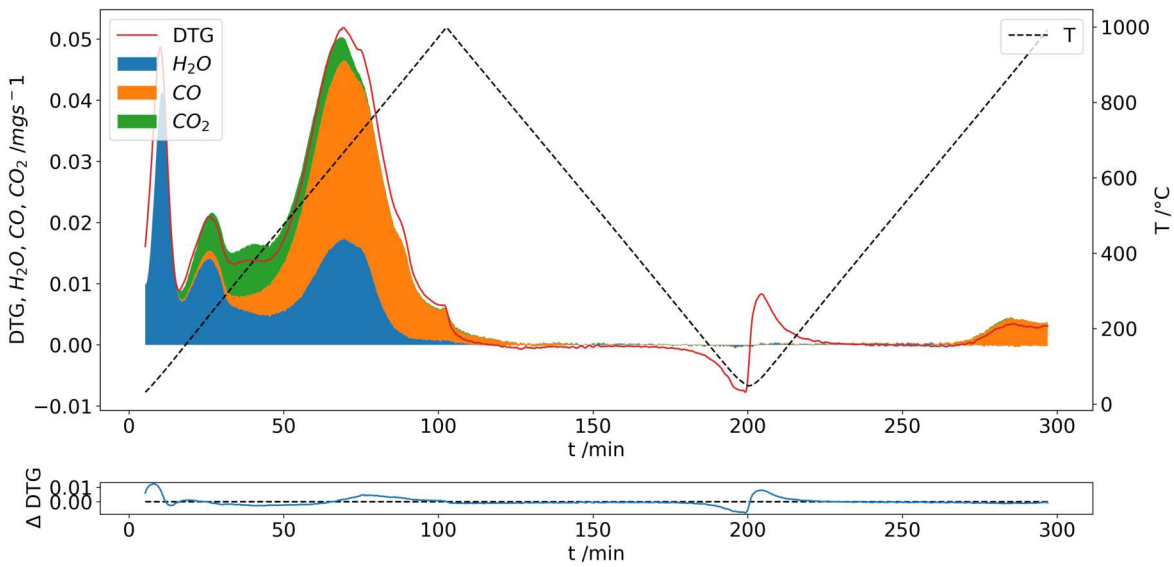

Figure A8: TGA-FTIR measurement comprised of heating, cooling and heating under nitrogen atmosphere of an HK 950 sample. DTG and the quantified release rates of H_2O, CO, and CO_2 are shown, their difference is indicated below.

A.6.4 Method development for the determination of oxygen-containing functional groups

Temperature-programmed decomposition (TPD) is an established methodology in carbon research. Therefore, the previously shown assignment of decomposition temperatures to SOGs (Table A4) was based on a literature review. The considered literature is listed in Table A5 with the reported temperature ranges.

Comparably wide temperature ranges account for differing desorption-energies of surface oxygen complexes as discussed by Moreno-castilla et al. (1998)[249] for olive stones and acid treatment. Effects like condensation reactions releasing H_2O as described by Domingo-García et al. (2002)[265] were not observed for our AC samples. However, only a few publications provide necessary parameters to perform the release rate deconvolution by Gaussian curves apart from the temperature-SOG assignments (temperature tolerance, HWHM and height limits).

Table A5: Literature about the temperature-programmed decomposition (TPD) methodology with used desorption (decomposition) temperature ranges for the different SOGs, sorted by year of publication.

desorption temperature in °C								
carboxylic	anhydrides	lactones	peroxides	phenols	carbonyls	ethers	pyrones	reference
		170 - 650			127 - 427, 727 - 927			[242]
		127 - 650			700 - 980			[243]
600	900							[244]
	627	627			700	700		[245]
200 - 400	350 - 500	350 - 400	550 - 600	600 - 700	800 - 900		1000	[246]
327	777	377 - 777			800 - 877			[247]
127 - 350		350 - 550		> 600		> 600		[248]
237 - 317	433 - 661, 700 - 980	433 - 661		700 - 980	700 - 980			[249]
100 - 400	547	667		632	807			[145]
247 - 287	407 - 447		587 - 617	627 - 657				[250]
127 - 327	327 - 677	327 - 677			150 - 527, 627			[251]
297 - 477								[252]
272 - 317	417 - 437	517, 667		567	277, 677			[253]
	600	719		645	775	645		[254]
375	625	625		625	625	625		[144]
237 - 447	527 - 627	627 - 727		667 - 717	817 - 877			[255]
260 - 300	440 - 480	600 - 740	500 - 540	550 - 590	770 - 810	640 - 680	910 - 950	[256]
257 - 419	457 - 583	607 - 694		659 - 737	783 - 890			[257]
100	150	350			400			[258]
275	425	620	520					[259]
245 - 325	480 - 500	616 - 755		635	760 - 878		1015	[260]
	500	500		500	700	500		[261]
247 - 392	647 - 688	647 - 688		663 - 724	826 - 905			[262]
278								[263]
275	435 - 460	650		735	920			[264]
200 - 500	450 - 650	450 - 700		600 - 750				[238]

Hence, these parameters were obtained by a systematic examination with regard to optimum and reasonable fit results for the analyzed ACs.

To assure reproducible results with transparent accounting for the aforementioned aspects, we developed the Python package "TGA-FTIR-hyphenation-tool-kit" [191].

A.7 Cluster analysis on PCA score plots

Cluster analysis was performed with the hdbscan package (v. 0.8.27) [266] to highlight clustering of data points in PCA score plots.

A.8 Other techniques

Titration techniques like Boehm-titration [146] were dismissed, since it may inchoate determine SOGs and bias by inorganic impurities that are anticipated to be present in commercially purchased activated carbons [267, 183, 252].

B

Supplementary information (Results) for "Characterization of activated carbon products for water treatment including extended analysis of oxygen-containing functional groups"

This appendix is part of chapter 3, and was submitted to *Water Research X* on June 29th, 2021. The following sections are corresponding to the *results and discussion* section of the original research paper (chapter 3) and describe the results more in detail and with additional plots.

This appendix contains

1 Details on results
2 Characterization of (surface) morphology
3 Analysis of elemental composition
4 Analysis of oxygen and carbon content
5 Analysis of oxygen-containing functional groups

B.1 Details on results

The Tables B1 and B2 list the obtained physical and chemical properties, respectively.

Table B1: Physical characteristics obtained for the eight powdered activated carbons (PACs), including manufacturer's specification. Columns divide PACs based on renewable raw material and fossil raw material, respectively.

	unit	**HK**	**HKP**	**CCP**	**SAE**	**P-f**	**AZ**	**PS**	**CC**
Manufacturer specification									
Raw material	-	Wood charcoal	Wood charcoal	Coconut shell	Mixture	Lignite	Bituminous coal	Bituminous coal	Hard coal (reactivate)
Specific surface area (SSA)	$m^2\,g^{-1}$	> 950	> 1050	1000 - 1100	1050 - 1150	1150	1050	910	> 900
Porisity and surface area									
N_2 Isotherm shape	-	Type I+IV(a)		Type I(b)		Type I+IV(a)		Type I(b)	Type I+IV(a)
N_2 Isotherm hysteresis	-	H3	H3	-	H4	H4	H4	H4	H4
Specific surface area (SSA)	$m^2\,g^{-1}$	1911 ± 24	1519 ± 14	1104 ± 2	1114 ± 13	1275 ± 9	1355 ± 10	1076 ± 1	849 ± 6
External area	$m^2\,g^{-1}$	770 ± 68	525 ± 4	66 ± 1	533 ± 3	629 ± 16	684 ± 13	84 ± 10	160 ± 4
Micropore area	$m^2\,g^{-1}$	1141 ± 44	994 ± 9	1039 ± 3	580 ± 15	645 ± 25	671 ± 23	991 ± 10	689 ± 2
Area's micropore share	%	60	65	94	52	51	50	92	81
Total pore volume	$cm^3\,g^{-1}$	1.48 ± 0.04	1.17 ± 0.01	0.49 ± 0.00	0.78 ± 0.01	0.88 ± 0.01	0.96 ± 0.01	0.49 ± 0.00	0.50 ± 0.00
Micropore volume	$cm^3\,g^{-1}$	0.50 ± 0.02	0.42 ± 0.00	0.42 ± 0.00	0.26 ± 0.01	0.29 ± 0.01	0.30 ± 0.01	0.40 ± 0.01	0.29 ± 0.00
Volume's micropore share	%	34	36	86	33	33	31	82	58
Average pore diameter	nm	3.1	3.1	1.8	2.8	2.8	2.8	1.8	2.4
Particle size									
D_{50}	μm	15.0 ± 0.3	20.0 ± 0.4	15.5 ± 1.3	25.8 ± 5.6	16.2 ± 0.2	28.0 ± 3.7	18.5 ± 1.0	14.8 ± 0.3
D_{10}	μm	5.5 ± 0.1	5.1 ± 0.1	3.7 ± 0.1	4.6 ± 0.3	4.4 ± 0.0	6.7 ± 0.7	4.4 ± 0.1	5.7 ± 0.1

Table B2: Chemical characteristics obtained for the eight powdered activated carbons (PACs). Inorganic elements are given as relative mass share of all elements determined by XRF semi-quantitatively. Columns divide PACs based on renewable raw material and fossil raw material, respectively. Detailed data of the XPS results are provided in section B.5.4 and Tables B3-B10.

	unit	**HK**	**HKP**	**CCP**	**SAE**	**P-f**	**AZ**	**PS**	**CC**
Raw material		Wood charcoal	Wood charcoal	Coconut shell	Mixture	Lignite	Bituminous coal	Bituminous coal	Hard coal (reactivate)
Thermogravimetric analysis									
moisture	wt.%	5.0 ± 2.4	9.2 ± 3.5	3.4 ± 1.3	2.7 ± 1.8	5.1 ± 2.5	4.3 ± 0.9	2.4 ± 0.9	2.5 ± 0.8
ML_{600}	wt.%	6.1 ± 0.1	5.3 ± 0.1	1.3 ± 0.1	2.0 ± 0.3	2.8 ± 0.5	1.8 ± 0.0	1.5 ± 0.1	1.4 ± 0.0
ML_{1000}	wt.%	14.7 ± 0.0	15.1 ± 0.0	3.4 ± 0.0	8.5 ± 0.0	4.8	3.3 ± 0.0	3.6 ± 0.0	2.9 ± 0.0
ML_{1000}/ML_{600}	-	2.4	2.8	2.6	4.3	1.7	1.8	2.4	2.1
$ML_{ox.}$	wt.%	81.6 ± 0.3	78.3 ± 0.1	92.5 ± 0.0	75.4 ± 0.2	82.3	88.6 ± 0.0	93.1 ± 0.0	84.3 ± 0.1
ash	wt.%	3.7 ± 0.3	6.6 ± 0.1	4.1	16.1 ± 0.2	12.9	8.1	3.2	12.8 ± 0.1
Elemental composition									
C	wt.%	80.5 ± 0.8	75.0 ± 0.0	90.3 ± 2.4	79.0 ± 0.6	79.5 ± 1.3	84.7 ± 0.8	92.2 ± 1.2	83.4 ± 1.9
H	wt.%	2.16 ± 0.20	2.06 ± 0.30	0.28 ± 0.15	0.14 ± 0.09	0.17 ± 0.10	0.35 ± 0.29	0.45 ± 0.07	0.21 ± 0.11
N	wt.%	0.08 ± 0.01	0.22 ± 0.01	0	0	0.04 ± 0.01	0.04 ± 0.01	0.10 ± 0.02	0.22 ± 0.02
S	wt.%	0	0	0	0.16 ± 0.06	0	0.11 ± 0.03	0	0.35 ± 0.04
O by TGA-FTIR	wt.%	10.68 ± 0.08	10.19 ± 0.07	2.45 ± 0.07	5.88 ± 0.04	1.95 ± 0.07	2.06 ± 0.06	2.5 ± 0.07	2.03 ± 0.06
molar H/C	-	0.322 ± 0.030	0.329 ± 0.048	0.038 ± 0.019	0.022 ± 0.014	0.025 ± 0.015	0.050 ± 0.041	0.058 ± 0.009	0.031 ± 0.017
molar O/C	-	0.100 ± 0.001	0.102 ± 0.001	0.020 ± 0.001	0.056 ± 0.001	0.018 ± 0.001	0.018 ± 0.001	0.020 ± 0.001	0.018 ± 0.001
Al	% (XRF)	0	0	0	0	45	55	32	14
Si	% (XRF)	24	24	30	2	40	12	28	45
P	% (XRF)	64	68	4	0	1	1	1	1
S	% (XRF)	2	2	1	10	6	11	14	13
Cl	% (XRF)	1	0	2	0	0	0	0	0
K	% (XRF)	2	1	34	2	0	0	1	4
Ca	% (XRF)	2	1	12	66	3	5	5	12
Ti	% (XRF)	1	0	2	0	3	4	4	1
Fe	% (XRF)	4	3	15	20	2	11	14	9
Σ XRF elements	%	100	100	100	100	100	100	100	100
Na by XPS	at.%			0.1	0.7				
Na and Mg by XRD	-				Mg				Na
Oxygen related information									
PZC	pH	3.3	2.8	9.1	11.4	7.3	8.4	9.5	9.7
CO_2 release	$\mu mol\,g^{-1}$	465 ± 22	453 ± 20	294 ± 20	911 ± 11	247 ± 21	306 ± 19	330 ± 19	298 ± 19
CO release	$\mu mol\,g^{-1}$	2889 ± 16	3001 ± 14	940 ± 15	1459 ± 8	723 ± 15	673 ± 14	903 ± 14	671 ± 13
CO/CO_2	-	6.2	6.6	3.2	1.6	2.9	2.2	2.7	2.3
Carboxylic acids	$\mu mol\,g^{-1}$	478 ± 87	310 ± 28	159 ± 17	n.d.	219 ± 12	182 ± 13	101 ± 11	140 ± 9
Anhydrides	$\mu mol\,g^{-1}$	104 ± 12	103 ± 13	23 ± 10	n.d.	31 ± 7	29 ± 2	33 ± 7	30 ± 11
Lactones	$\mu mol\,g^{-1}$	n.d.	n.d.	47 ± 15	n.d.	< LOD	44 ± 5	n.d.	< LOQ
Phenols, ether	$\mu mol\,g^{-1}$	n.d.	n.d.	234 ± 41	n.d.	193 ± 21	170 ± 30	n.d.	86 ± 29
Carbonyls, quinone	$\mu mol\,g^{-1}$	n.d.	n.d.	509 ± 128	n.d.	256 ± 52	262 ± 34	n.d.	375 ± 65
Pyrones, chromene	$\mu mol\,g^{-1}$	n.d.	n.d.	170 ± 28	n.d.	207 ± 22	187 ± 24	n.d.	159 ± 15
[C-C]	at.%	54.3	48.1	55.1	52.1	n.d.	51.2	56.0	53.0
[C-O] (phenol, ether, pyrone, chromene)	at.%	3.1	9.7	7.9	13.1	n.d.	11.6	8.4	11.7
[C=O] (carbonyls, quinone, pyrone)	at.%	18.4	14.0	10.0	10.6	n.d.	7.6	7.4	10.3
[O-C=O] (carboxylic acid, anhydrides, lactones)	at.%	1.6	6.2	11.8	1.5	n.d.	6.4	5.3	5.7

B.2 Characterization of (surface) morphology

B.2.1 Nitrogen adsorption/desorption isotherms

Obtained N_2 adsorption/desorption isotherms of the eight PACs are presented with commonly scaled y-axes in Figure B1 and individually in Figure B2. Recorded isotherms were classified by type and hysteresis according to the IUPAC technical report [198] that categorizes distinct pore network characteristics. All isotherms are comprised of characteristics of type I and type IV(a), which is typical for mesoporous carbons with several pore sizes and with a remarkable share of micropores. Hysteresis loops occur during desorption down to p/p_0 of 0.4 except for CCP 90D (Figure B1a), which shows a clear reversible type I(b) isotherm and therefore, is a pure microporous carbon with narrow mesopores. Very similar adsorption is observed for PS WP 235, but with H4 hysteresis, indicating capillary condensation in the mesopore network with micropore filling. The PACs in Figure B1b are made from bituminous coal, lignite and of a mixture and are comprised of isotherm This is typical for mesoporous carbons with several pore sizes but with a remarkable share of micropores, due to the N_2 volume adsorbed in the beginning of the isotherms. The chemically activated PACs of wood charcoal obtain isotherms that also have characteristics of type II (Figure B1c) and therefore, provide H3 hysteresis loops [197], which indicate large mesopores that cannot completely be filled by condensed N_2. Therefore, the pore network is well developed with respect to pore width expanding the whole mesopore size range. The qualitative shape of N_2 adsorption/desorption isotherms imply distinct information about the physical pore network characteristics and therefore, is perfectly suited to compare AC pore structures for adsorption processes regarding pore transport (kinetics) or the removal potential of large molecules from natural organic matter.

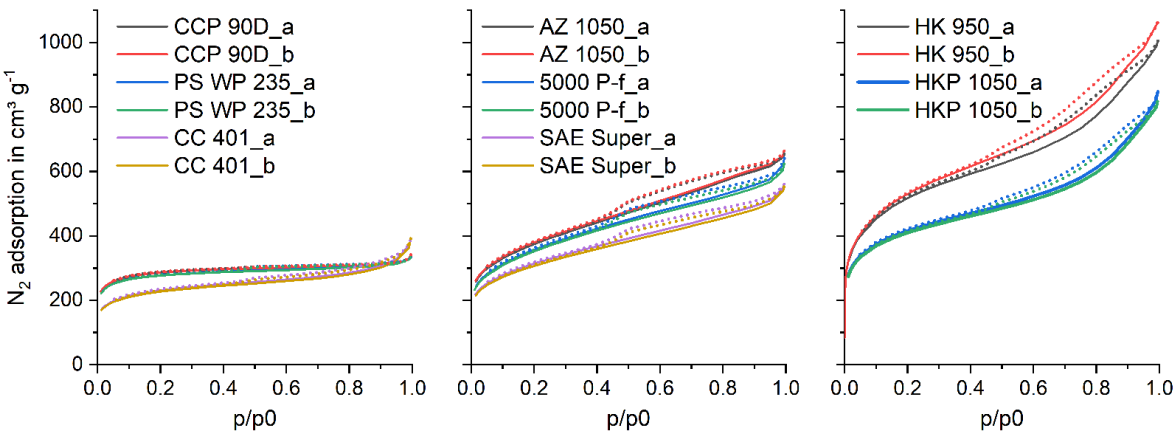

Figure B1: Isotherms for N_2 adsorption (solid lines) and desorption (dotted lines) for the eight activated carbons in duplicate determination.

The specific micropore surface area does not correspond with the overall SSA, but is linked to the shape types of the isotherms (Table B1). PACs of Types I(b) or hysteresis H3 obtain the highest specific micropore surface areas of about $1000\,m^2\,g^{-1}$, whereas the PACs assigned to type I+IV(a) and H4 are significantly below $700\,m^2\,g^{-1}$. This is also reflected by the average micropore diameter that ranges between 0.84-1.00 nm for the PS WP 235 and AZ 1050,

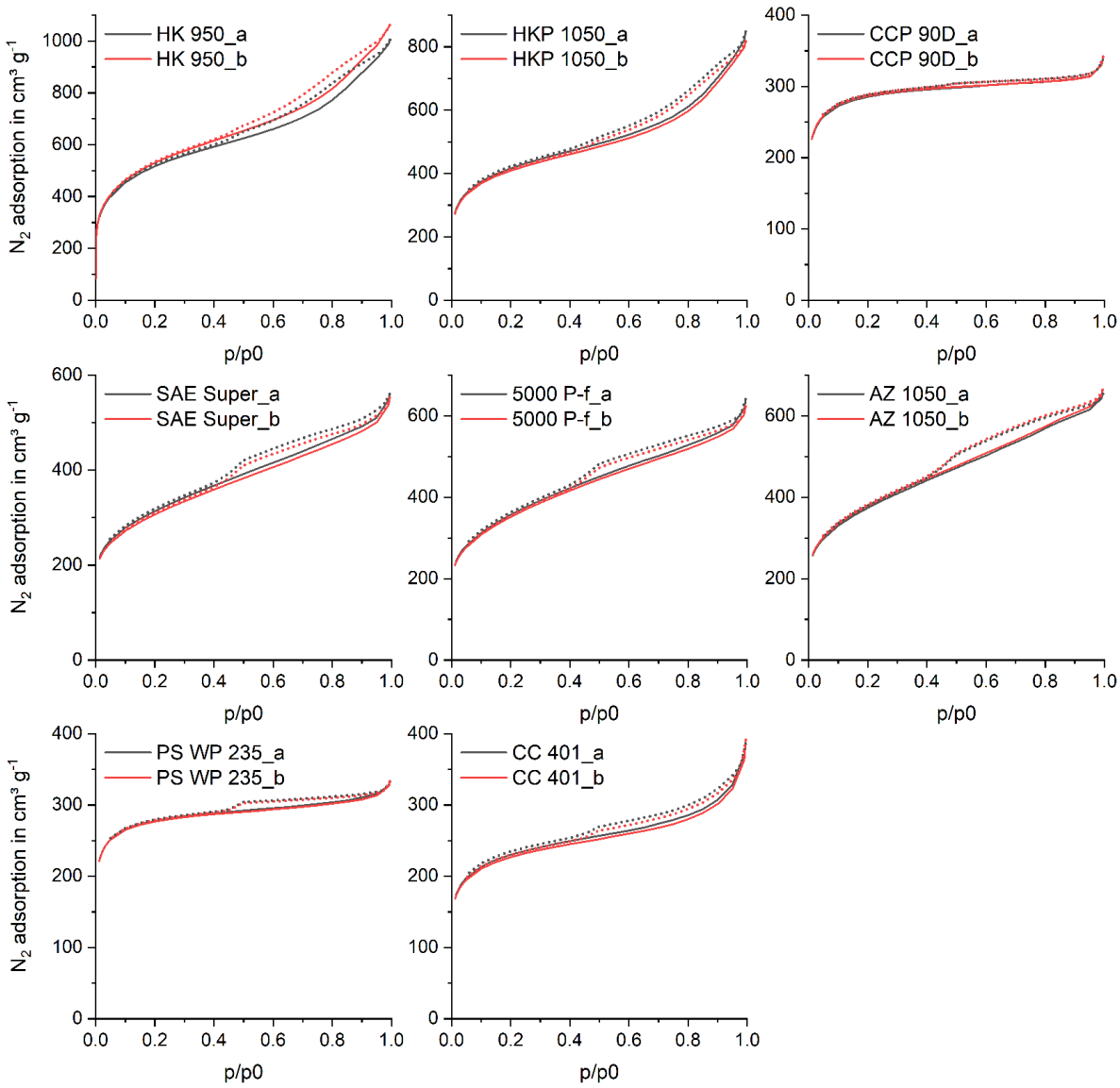

Figure B2: Isotherms for N_2 adsorption (solid lines) and desorption (dotted lines) for the eight activated carbons in duplicate determination.

respectively. In contrast, the average pore diameter ranges from 1.8-3.1 nm for PACs of type I(b) isotherms or H3 hysteresis, respectively.

With respect to the measurement methodology we want to add the following. The investigated PACs do not show an adsorption plateau, which would be typical for microporous materials. However, this indicates the presence of meso- and macropores or may be due to inter-granular condensation, if the sample contains very small particles. The last we would attribute to CC 401 that observed a relative steep gradient at the end of the isotherm and below, particle-size distribution will confirm this. Furthermore, we used p/p_0 of 0.95 for the determination of the total pore volume, rather than p/p_0 of 0.99 that may be used for isotherms possessing an adsorption plateau. Therefore, the determination of pore volumes comes with increased uncertainty. To determine reproducible N_2 adsorption/desorption isotherms, we want to highlight the importance of out-gas conditions (temperature and pressure) that should be specified for the method used.

From our point of view, it is not necessary to apply time-consuming micropore adsorption measurements with respect to OMP adsorption from water. On the one hand, target substances are of molecule sizes that are not accessible for primary micropores and as explained above, PSDs are not conclusive to distinguish certain pore widths. Furthermore, adsorbents used to study micropores like CO_2 are discussed to interact with nitrogen-containing moieties of ACs [268].

As a side note, the obtained specific surface area (SSA) for SAE Super is $1114 \pm 13\,m^2\,g^{-1}$ (Table B1). This is in good agreement with [115] that obtained a SSA of $1122\,m^2\,g^{-1}$ by Ar adsorption on the same PAC.

B.2.2 Pore size distributions

Pore size distributions (PSDs) characterize the pore network with micropores and mesopores based on density function theories (DFTs). DFTs rely on pore models, e. g. slit-shaped pores, the PSDs obtained significantly differ based on the pore model used [269]. The pore textures of AC products are formed by complex structures composed of graphite microcrystals and turbostratic graphene layers; however, these structures vary by AC based on its raw material and activation procedure [270, 271]. Therefore, DFT approaches are not suitable for the comparison of ACs indicated for water purification, since the values obtained would not be comparable. Exemplary PSDs are shown for the 5000 P-f_a measurement using the non-linear density function theory (NLDFT) and the quenched solid density function theory (QSDFT) each with three different kernels. Results for NLDFT are presented in Figure B3 and for QSDFT in Figure B4.

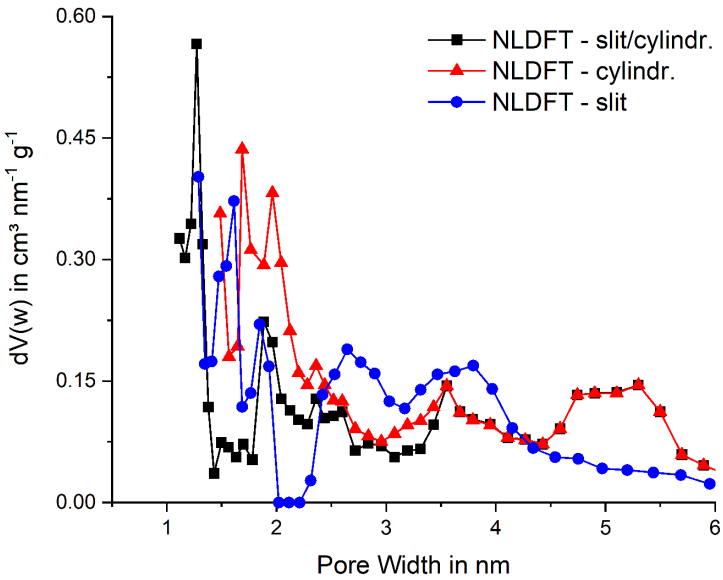

Figure B3: Pore size distribution of PAC 5000 P-f based on the non-linear density function theory (NLDFT), calculated with with different kernels.

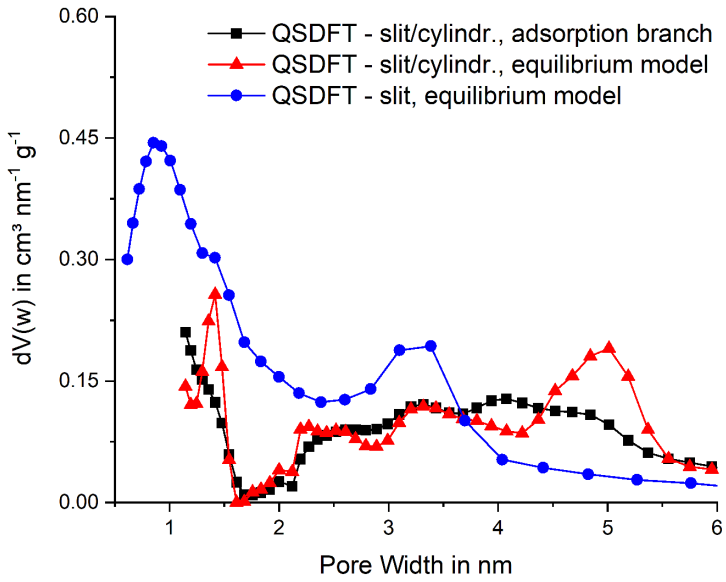

Figure B4: Pore size distribution of PAC 5000 P-f based on the quenched solid density function theory (QSDFT), calculated with with different kernels.

B.2.3 Particle-size distributions

Particle-size distributions are presented in Figure B5 and separated for each PAC in Figure B6 and show a wide range from 1-100 μm without dominating size classes.

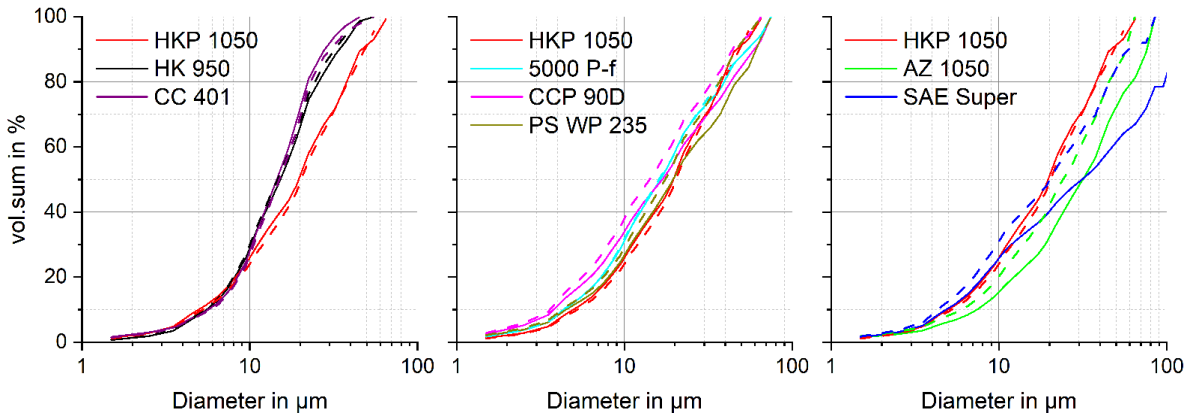

Figure B5: Particle-size distributions of the powdered activated carbons, as cumulative curves in duplicate determination visualized as solid and dashed lines of one color. HK 1050 is shown in each graph to enhance comparability.

Volume fractions divide in half at D_{50} values ranging from 14.8 to 28.0 μm (Table B1). Typical S-shaped cumulative curves were observed only for HK 950 and CC 401 that also have the smallest D_{50} values with 14.8 and 15.0 μm. This may hint to production processes with additional washing or sieving procedures, e. g. CC 401 is a powder obtained from reactivation of granular activated carbon (GAC). The largest amount of very small particles was found for CCP 90D with D_{10} of 3.7 μm, whereas for AZ 1050 and SAE Super a few large particles > 80 μm occurred. The particle size is relevant for the adsorption kinetic. Furthermore, in comparison with the identified crystalline structures by XRD (> 1 μm), mineral matter can be of significant size for the PAC particles.

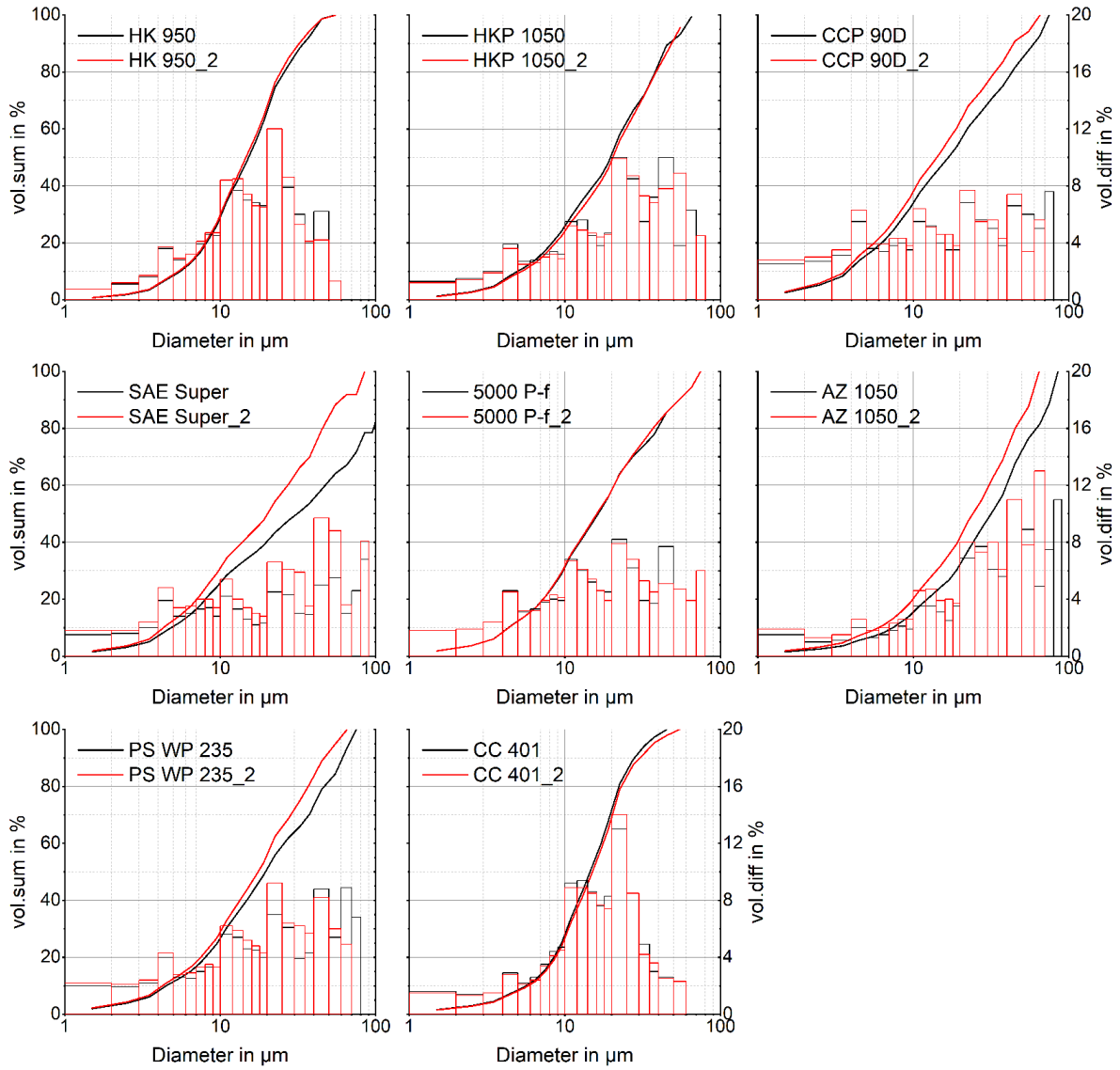

Figure B6: Particle-size distributions of the powdered activated carbons, as cumulative curves and histograms, in duplicate determination.

B.3 Analysis of elemental composition

B.3.1 CHNS results

The error for hydrogen determination is remarkable (Table B1). Standard deviation ranges from 9% (HK 950) to 82% (AZ-1050) for the hydrogen content. This also affects the molar H/C ratios, which obtain the same uncertainties.

B.3.2 X-ray diffraction (XRD)

Obtained diffractograms of the analyzed PACs are presented in Figures B7-B13, except for 5000 P-f that could not be analyzed due to limited sample mass.

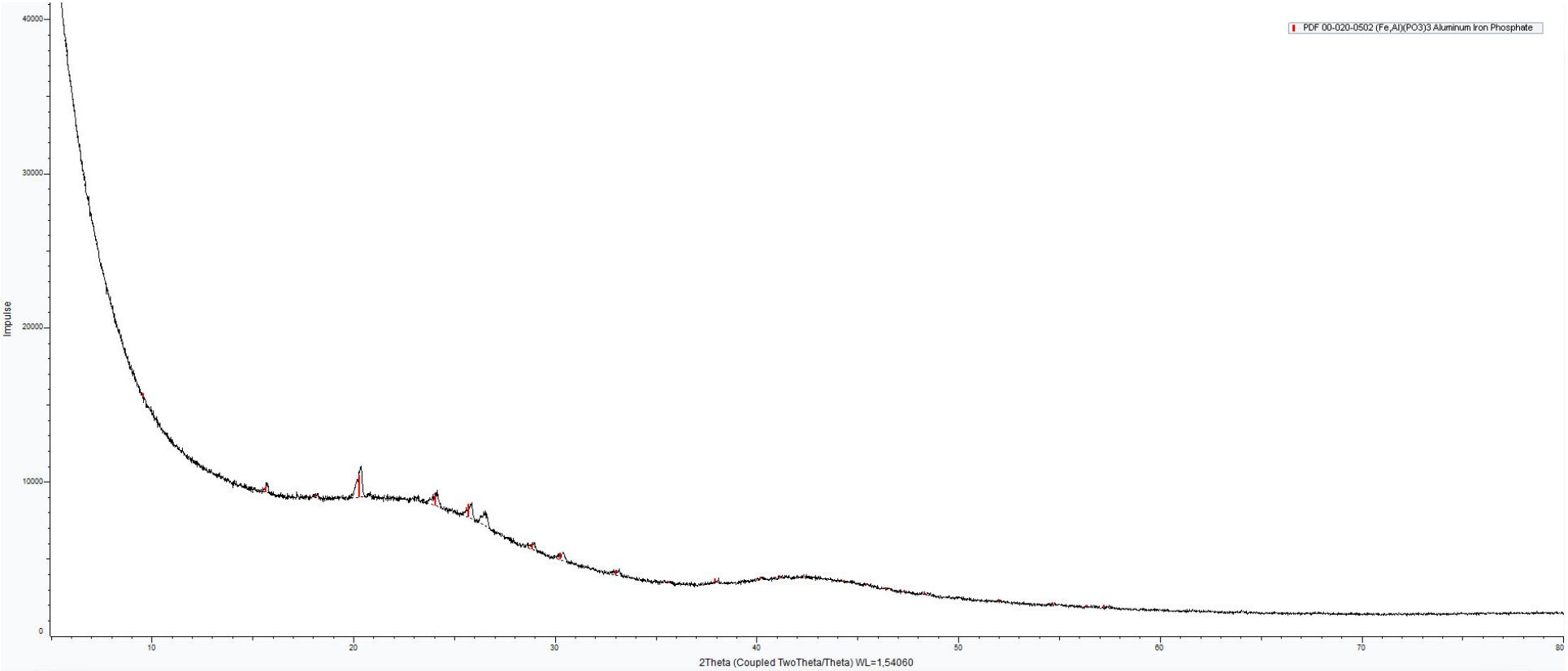

Figure B7: XRD diffractogram of HK 950.

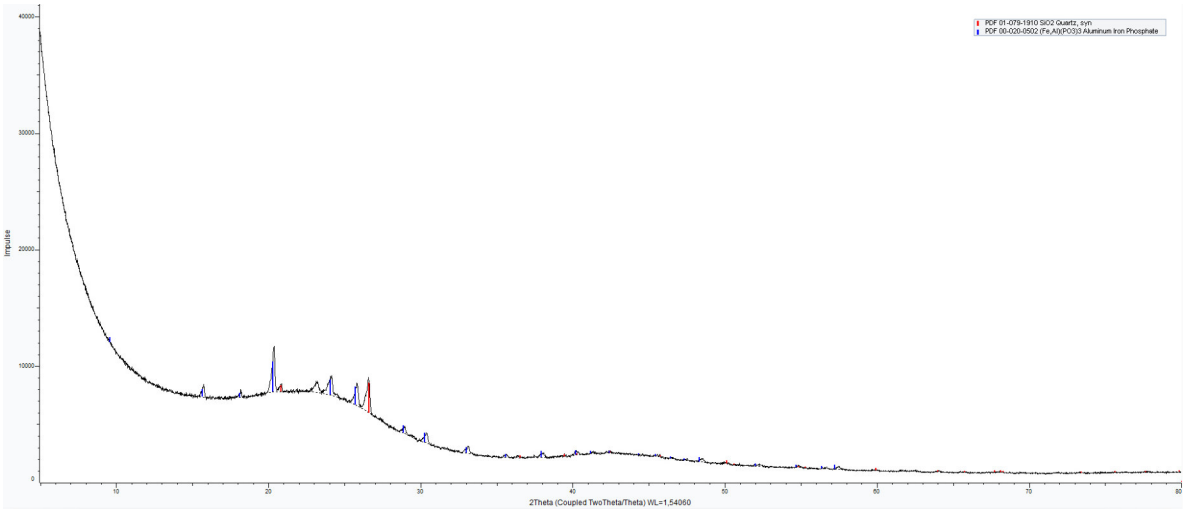

Figure B8: XRD diffractogram of HKP 1050.

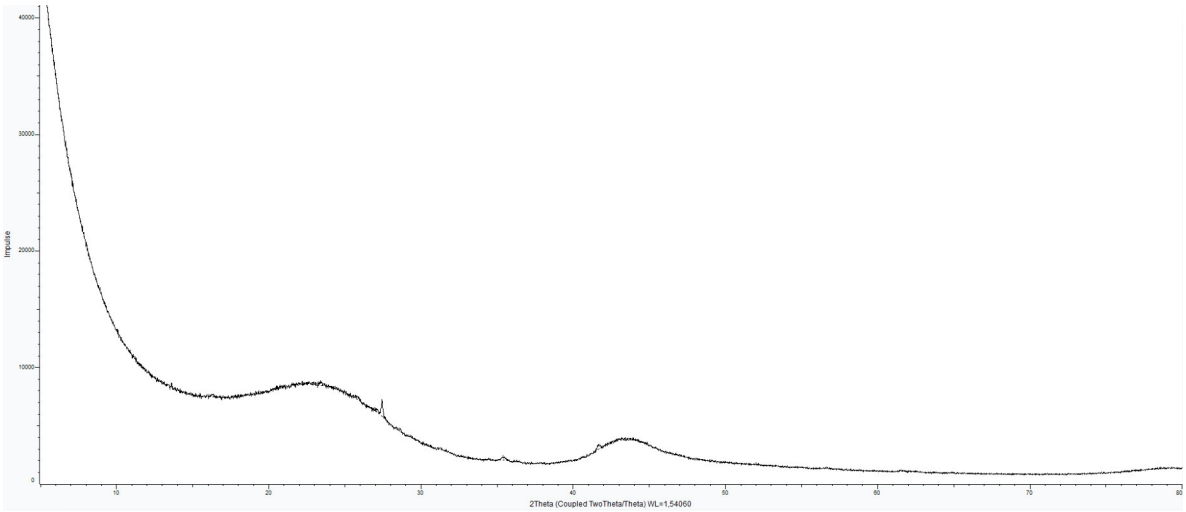

Figure B9: XRD diffractogram of CCP 90D.

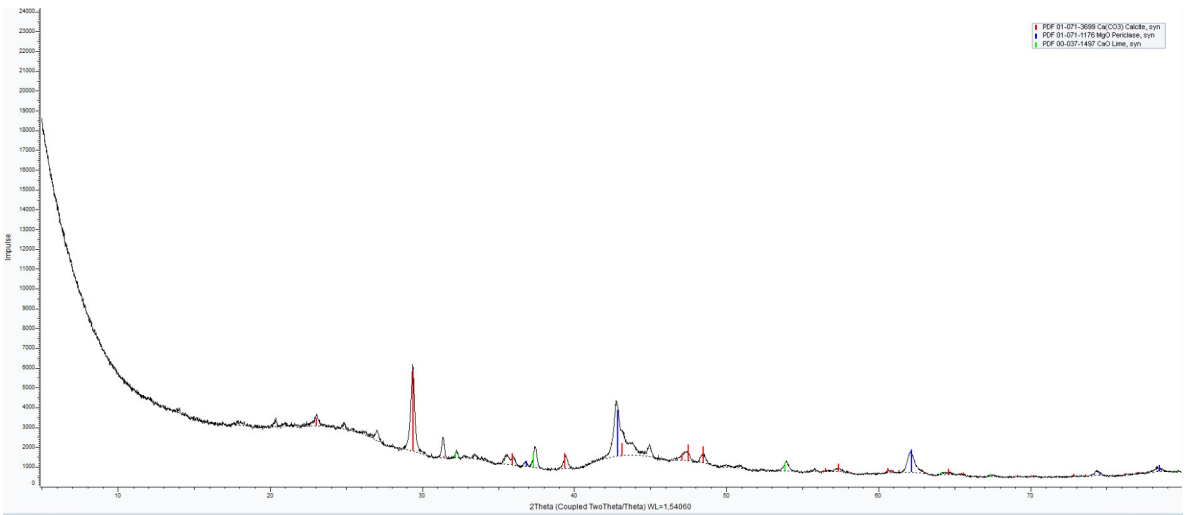

Figure B10: XRD diffractogram of SAE Super.

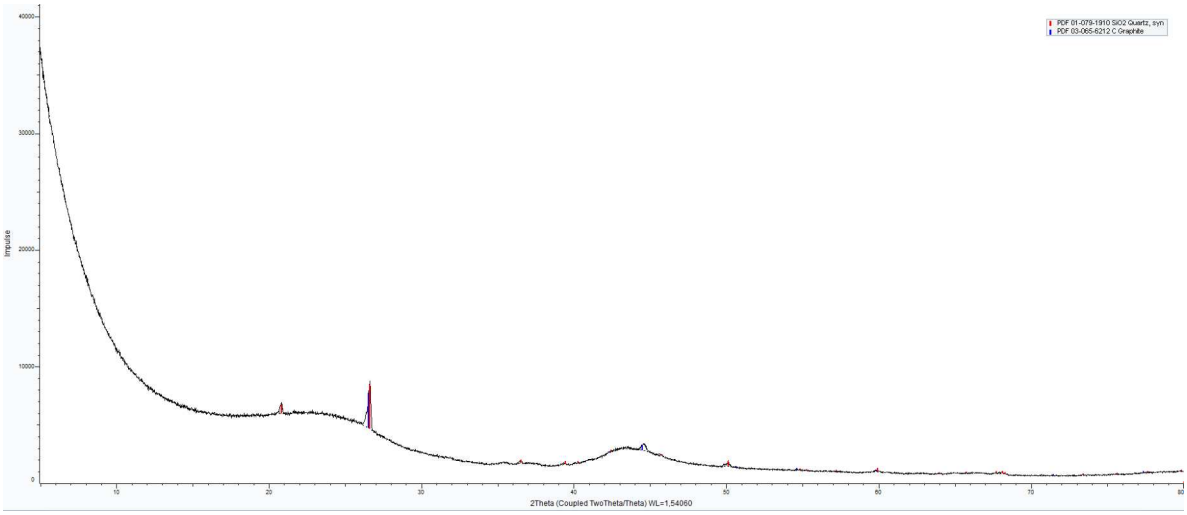

Figure B11: XRD diffractogram of AZ 1050.

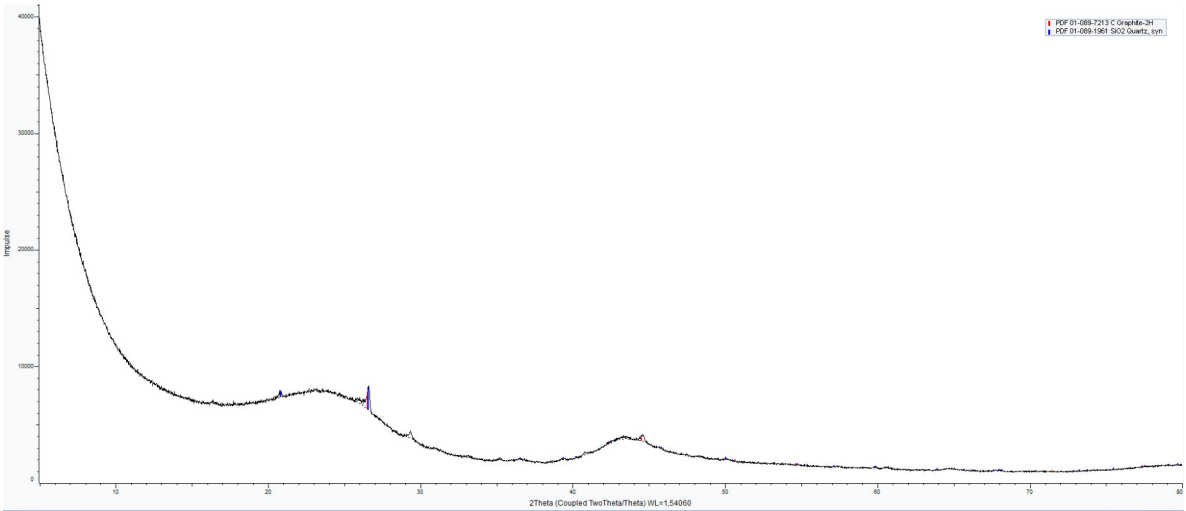

Figure B12: XRD diffractogram of PS WP 235.

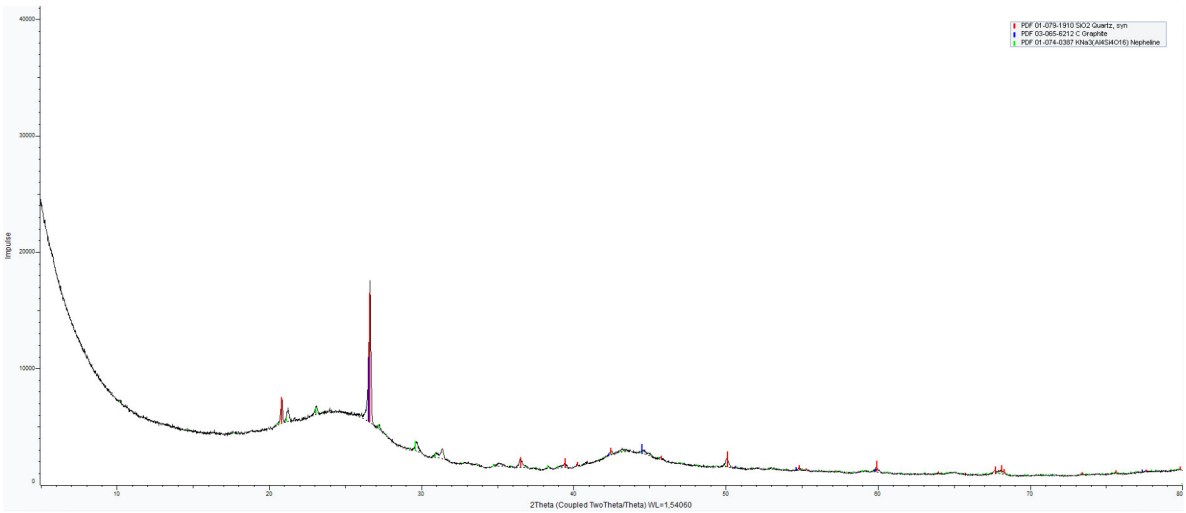

Figure B13: XRD diffractogram of CC 401.

B.3.3 Transmission electron microscopy (TEM)

An FEI Tecnai G² 20 S-TWIN (FEI Company, OR, USA) Transmission Electron Microscope (TEM), operating at 200 kV acceleration voltage and equipped with a LaB6 cathode and EDX, provided TEM images of a granular activated carbon sample of the product Aquasorb 5000G from DonauCarbon. Figures B14 and B15 show inorganic impurities. Furthermore, Figures B16 and B17 depict graphitic structures of the activated carbon.

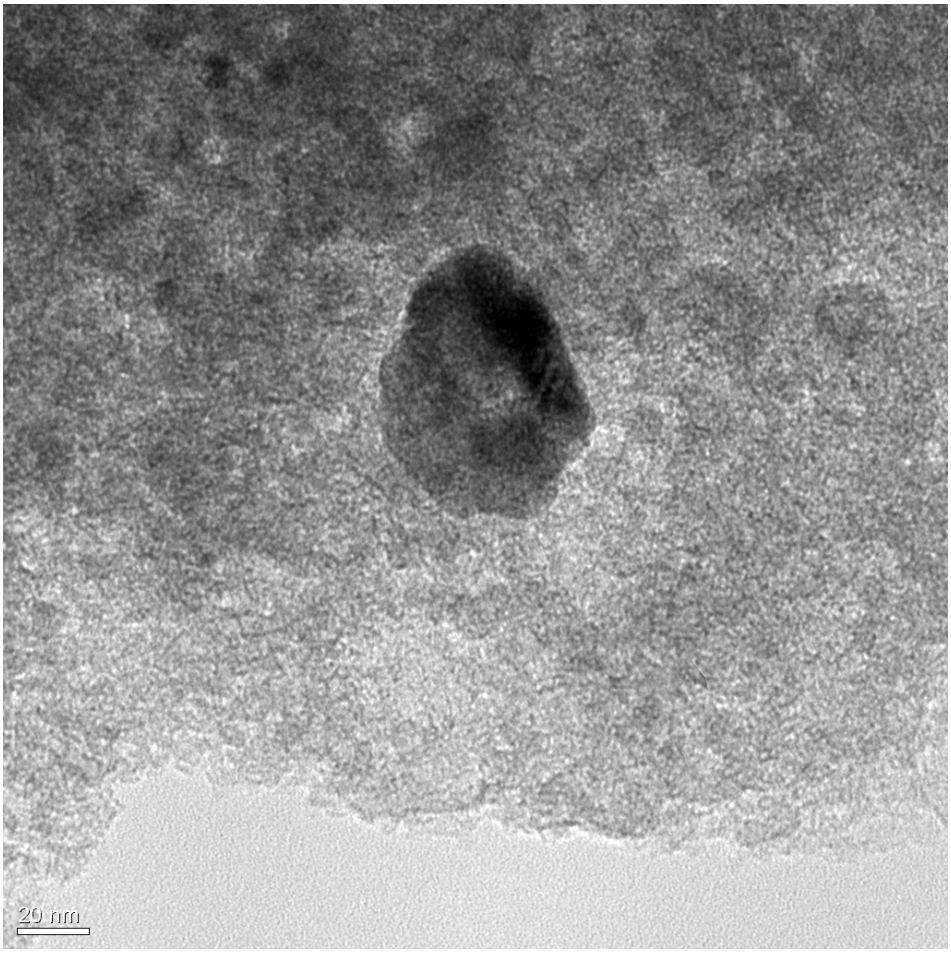

Figure B14: TEM image with inorganic impurities.

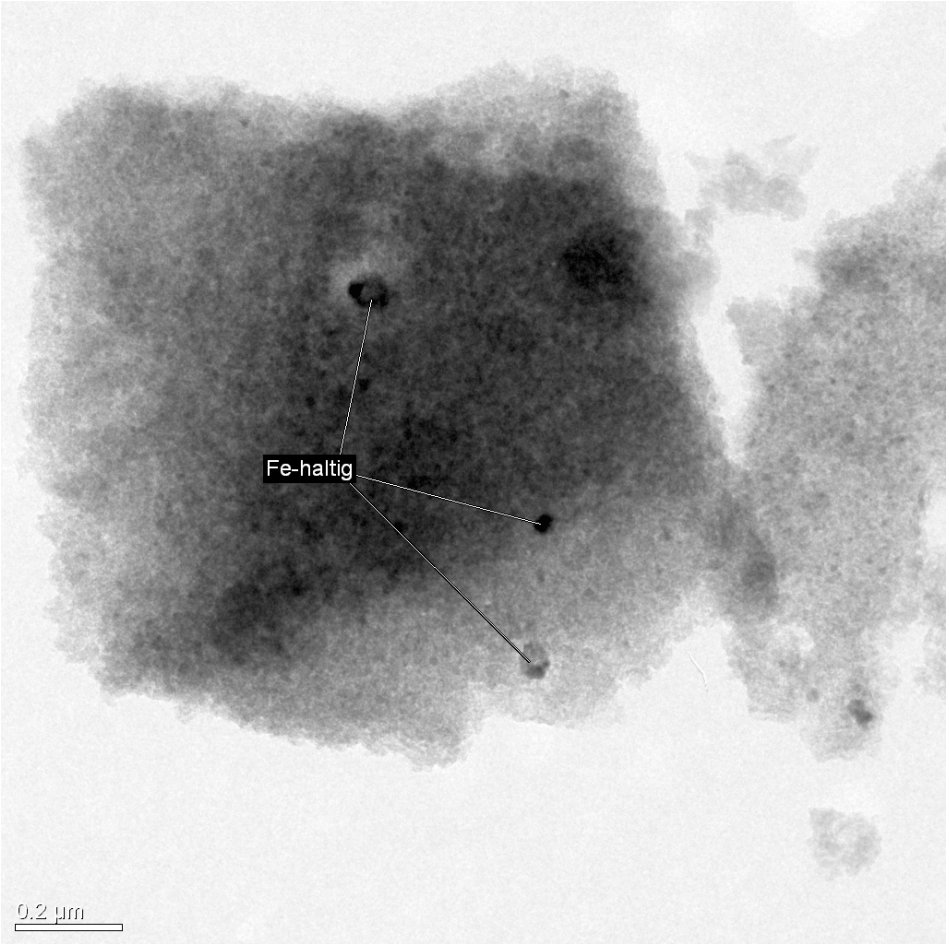

Figure B15: TEM image with highlighted inorganic impurities.

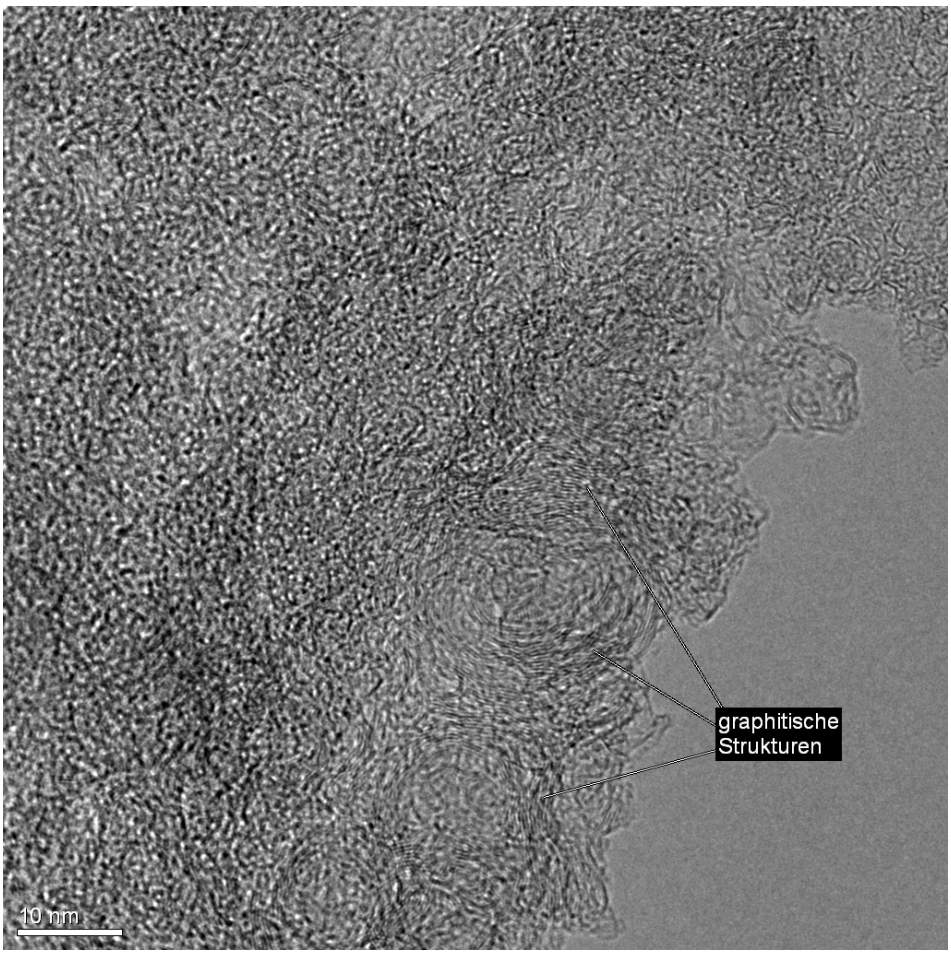

Figure B16: TEM image with highlighted graphitic structures.

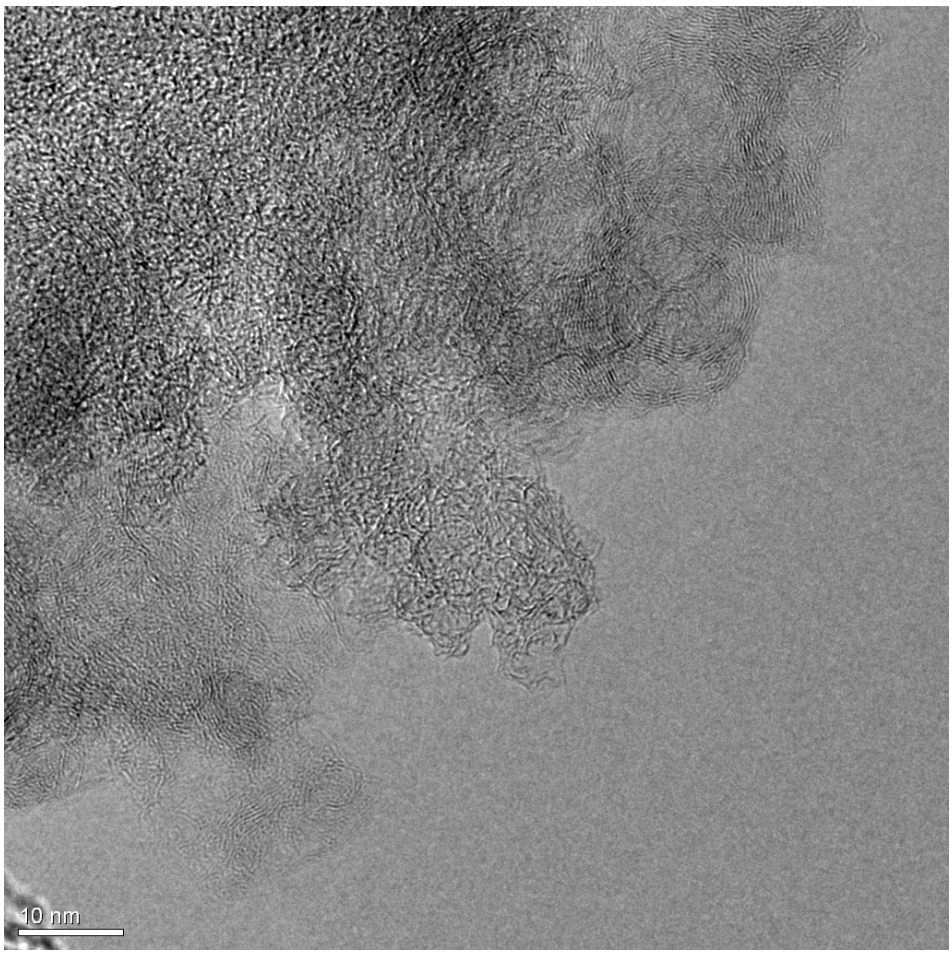

Figure B17: TEM image with graphitic structures.

B.3.4 PCA of XRF data

The score plot is presented within the original research paper in Figure 4, the corresponding loading plots are provided in Figure B18.

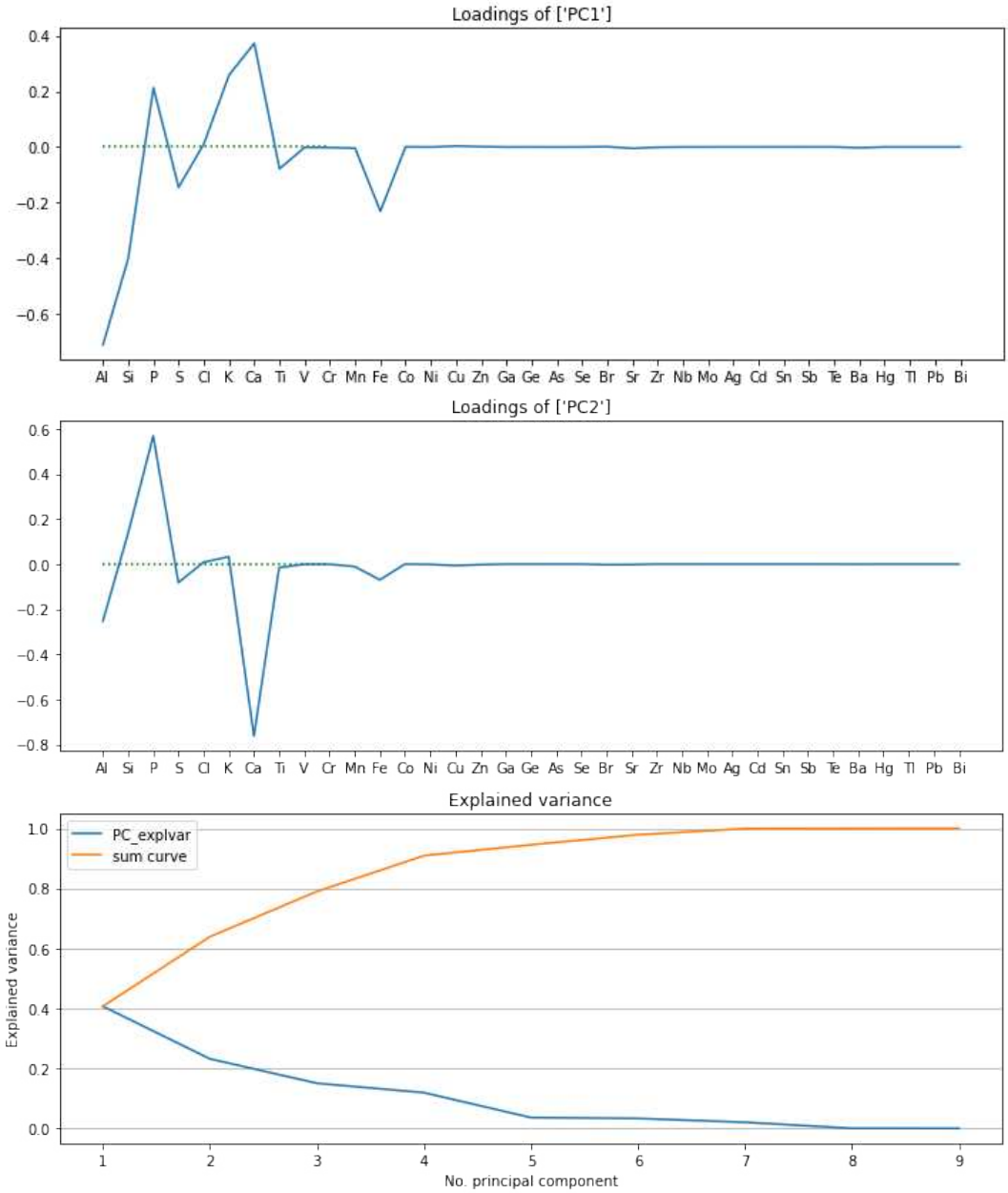

Figure B18: Loading plots of the PCA with row-wise normalized XRF data of the inorganic elemental composition. Principal component (PC) 1 and 2 as well as the explained variance graph are shown.

B.4 Analysis of oxygen and carbon content

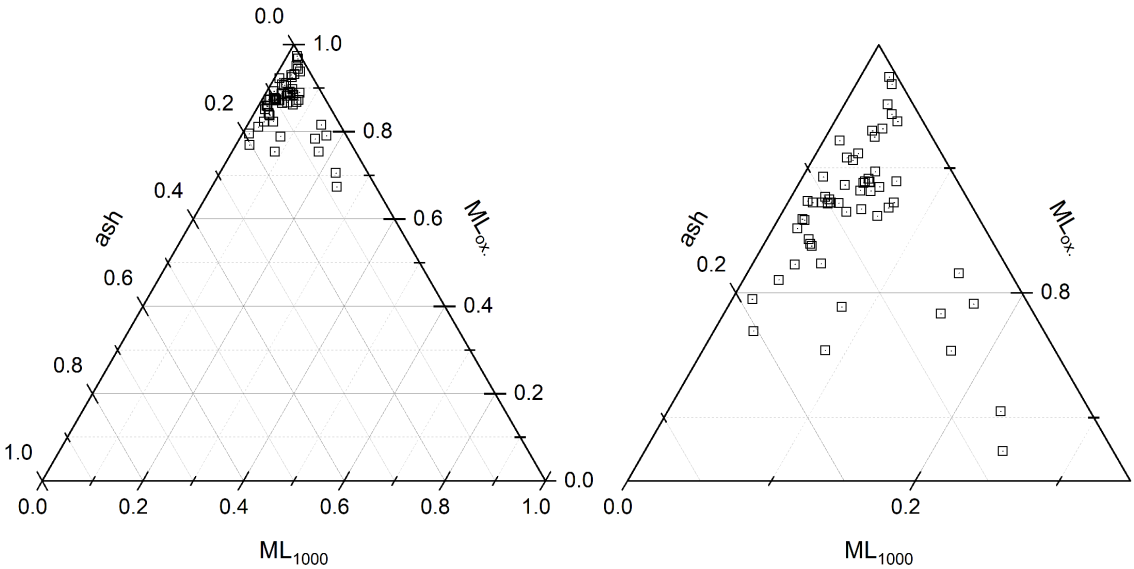

Figure B19: Parameters from TGA measurements shown in a tertiary plot. Left: full scale; Right: scaled to relevant region.

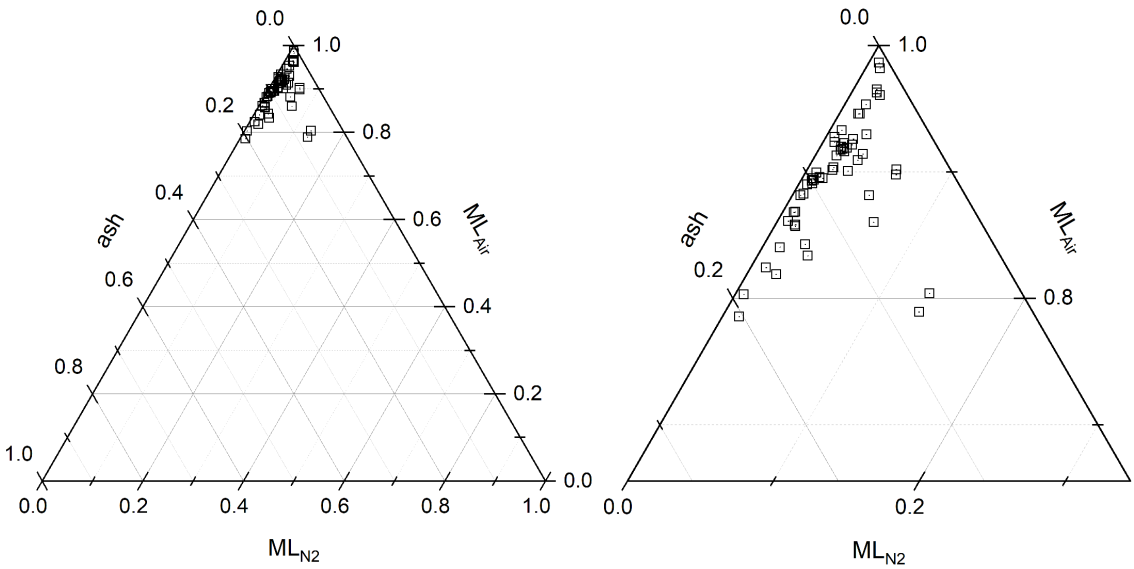

Figure B20: Parameters plot from TGA method according to [10]. Left: full scale; Right: scaled to relevant region.

The obtained three parameters ML_{1000}, $ML_{ox.}$ and ash sum up to 100%. Therefore, they can be visualized by a tertiary plot as shown in Figure B19.

Furthermore, based on the parameters ML_{600} (as ML_{N2}) and ash also an oxidative mass loss (ML_{Air}) can be calculated. According to [10] these parameters annotated in a tertiary plot (Figure B20) can be used to quantify spent activated carbon in activated sludge or in an other organic matrix.

B.4.1 Mass loss profiles (DTG-curves)

Tha mass loss profiles (DTG-curves) of the eight PACs not shown in the original research paper are presented in Figure B21. These samples obtain high mass loss rates due to ongoing carbonization for HK 950 and HKP 1050, inorganic decomposition at about 600 °C for SAE Super and the evolution of aliphatic substances between 300-450 °C from 5000 P-f. However, these profiles are representing the chemical composition of the samples and can be used to compare activated carbons.

Thermogravimetric analysis with TG- and DTG-curves of all 55 samples an partly multiple determinations are available in the alongside published Jupyter notebooks.

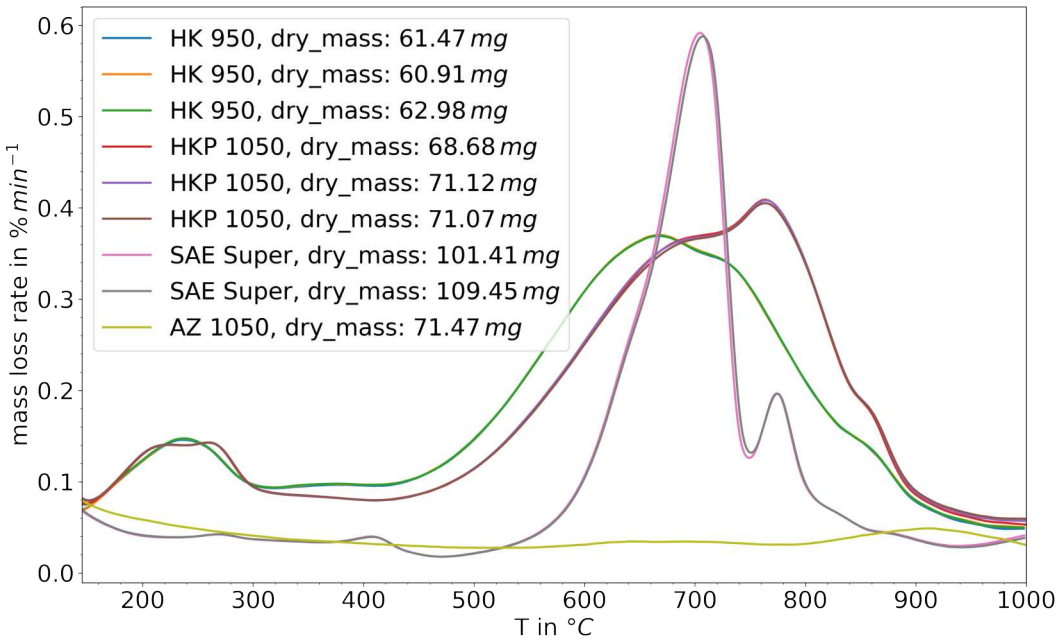

Figure B21: Mass loss rate profiles (DTG) of HK 950, HKP 1050, SAE Super and 5000 P-f from dry temperature 145 °C to 1000 °C in multiple determinations.

B.4.2 Impact of grinding GAC on the oxygen content

The analyzed samples include 18 GACs that have been milled for analysis (cf. Table A1 in Appendix A). ML_{1000} (correlated with the oxygen content) was found to be increased for ground samples compared to the corresponding GACs (Figure B22). In average ML_{1000} increased relatively by 10% (representing 7% oxygen). The whole set of samples comprises 27 GACs and 28 PACs that obtained in average 4.8% ML_{1000} (3.4% oxygen) and 5.9% ML_{1000} (4.1% oxygen), respectively. This indicates that ACs' grain size may influence their oxygen content, perhaps due to the relatively increased outer surface of the particles. Similar effects were obtained by milling PACs for different lengths of time by [272]. Different oxygen-containing functional groups on the inner and outer surface of PAC were also indicated and discussed by [265].

However, it is not clear whether grinding increases the ML_{1000} by oxidation at the fracture surface or whether closed internal pores are opened that could not previously release enclosed oxygen. Further research may be of particular interest since in some experimental setups, GAC grinding is a basic pretreatment, e. g., in rapid small-scale column tests [273, 112].

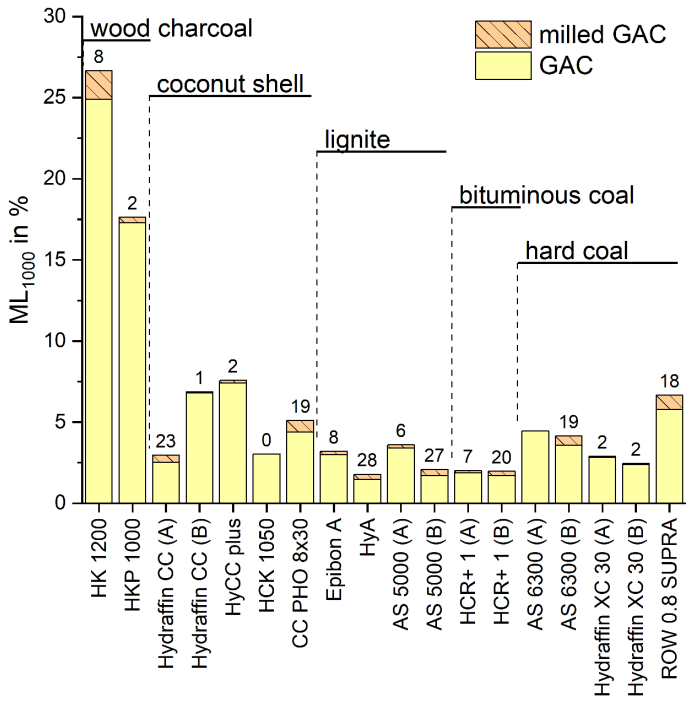

Figure B22: Pyrolytic mass loss up to 1000 °C (ML_{1000}) for 18 GACs and their milled representatives. Number on top of stacked bar show the relative percentage increase of ML_{1000} for the milled GAC.

B.5 Analysis of oxygen-containing functional groups

B.5.1 Surface oxygen groups by TGA-FTIR

Individual surface oxygen groups (SOGs) for the complete set of samples are presented below. Figures B23 and B24 show the obtained SOG quantities for the eight PACs with error bars derived from the robustness testing for the deconvolution fitting. SOGs of all ACs are provided as bar graphs for each type of SOG in Figures B25-B30. The complete TGA-FTIR results with mass loss profiles, release rates and deconvolution plots for all ACs can be found with the published raw data in [202].

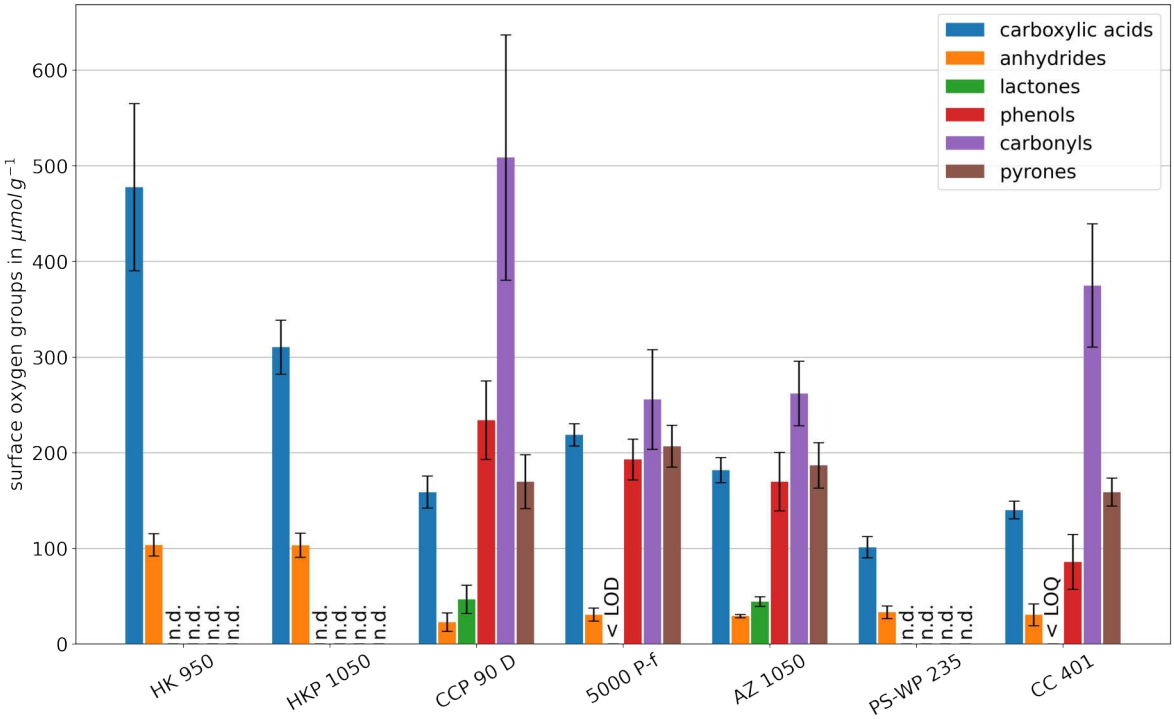

Figure B23: Surface oxygen groups (SOGs) quantified for the eight PACs. Error bars represent the standard deviation obtained by the robustness testing. Release rates of the SAE Super could not be properly deconvoluted and is therefore excluded. HK 950, HKP 1050 and PS WP 235 were analyzed up to 600 °C and therefore only carboxyl and anhydride groups could be determined.

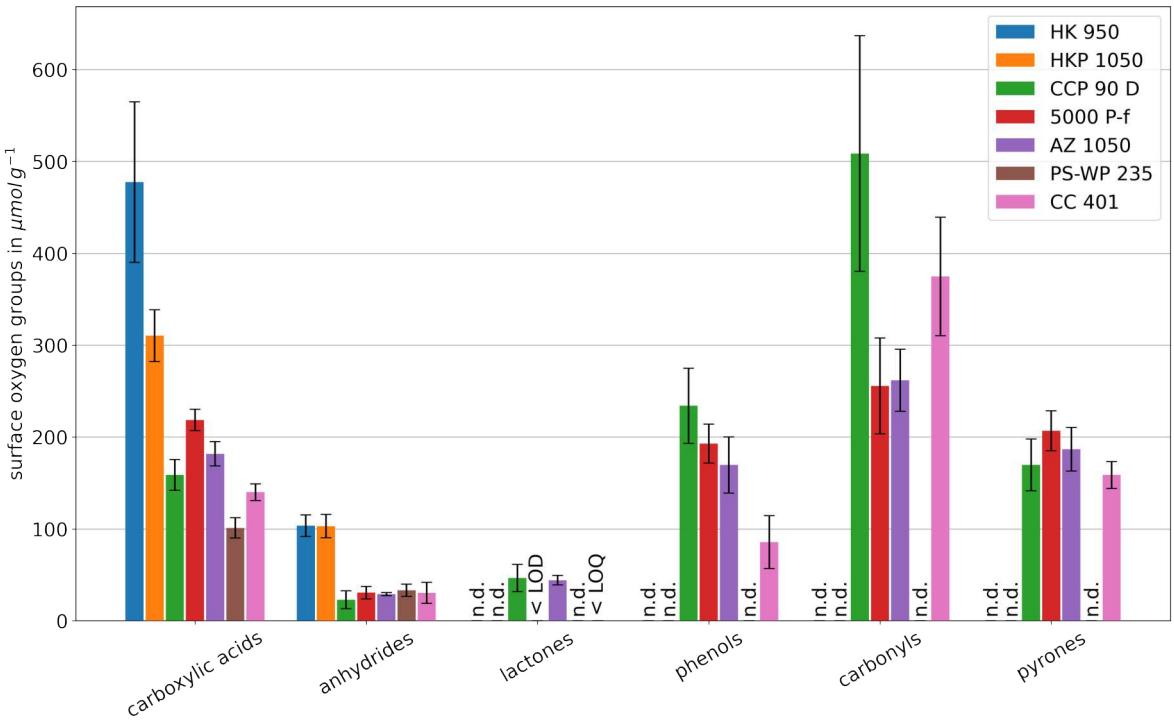

Figure B24: Surface chemistry results grouped by SOGs.

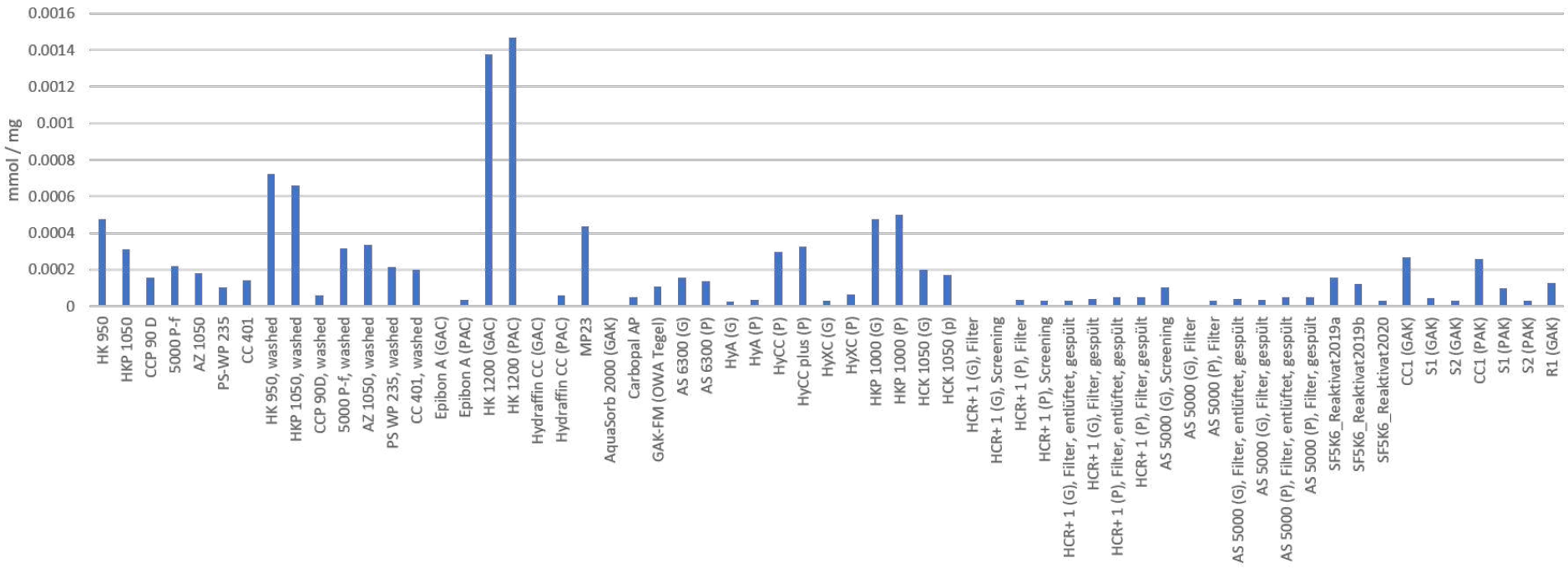

Figure B25: Carboxylic acid SOG quantified for all ACs.

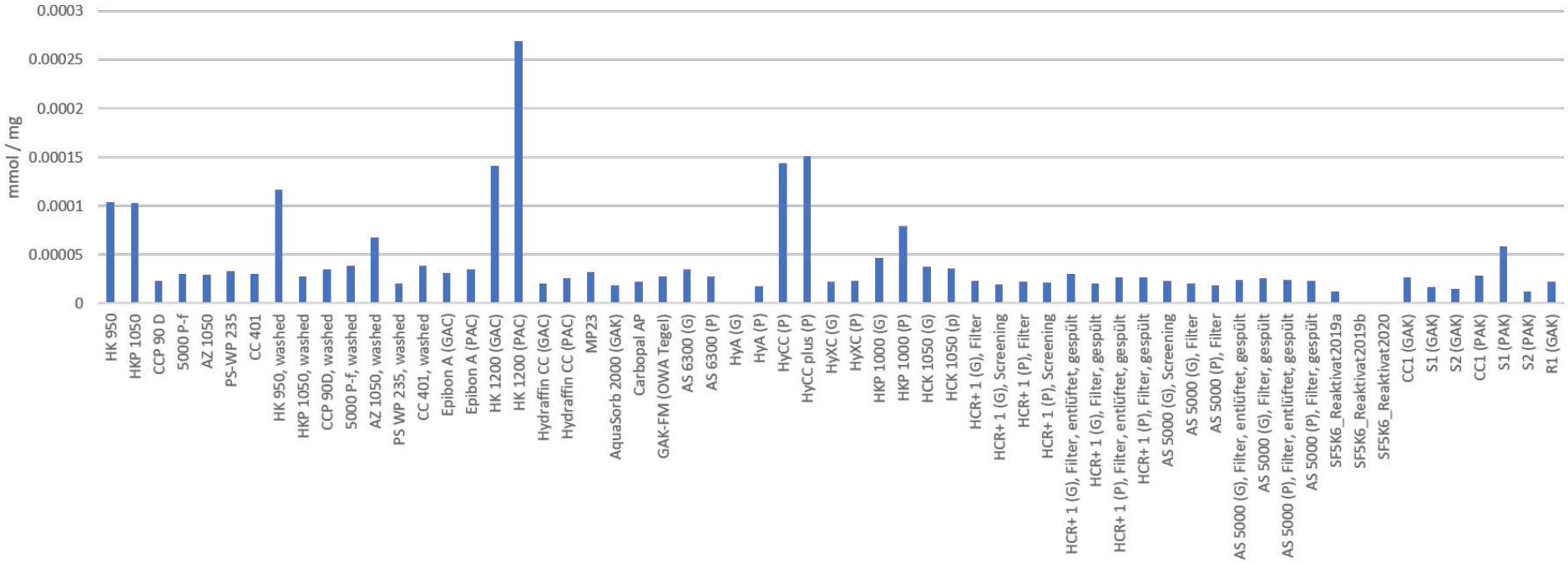

Figure B26: Anhydride SOG quantified for all ACs.

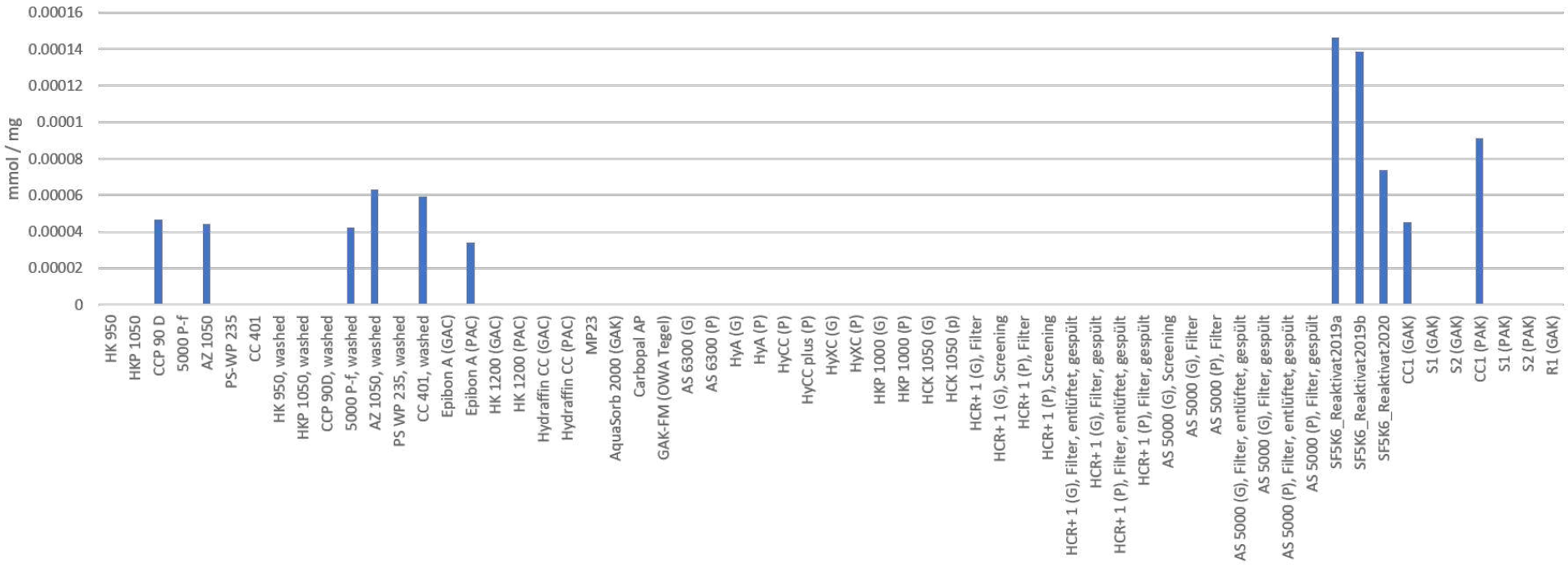

Figure B27: Lactone SOG quantified for all ACs.

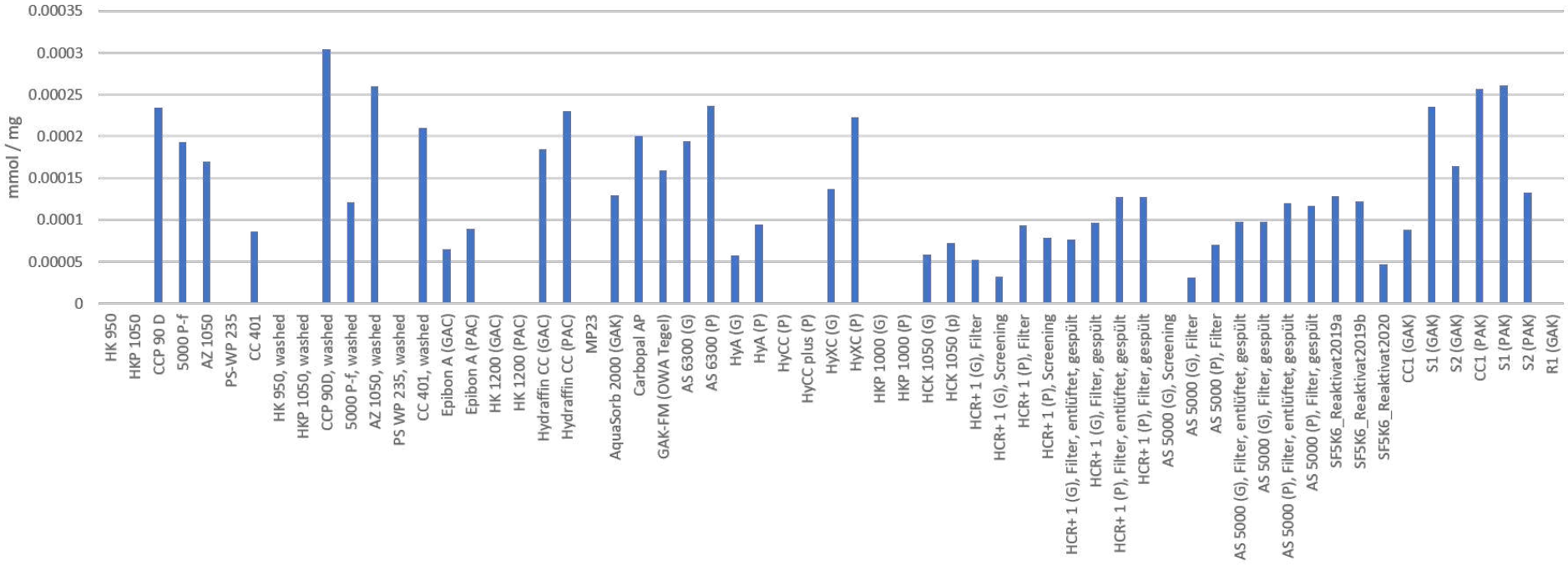

Figure B28: Phenol SOG quantified for all ACs.

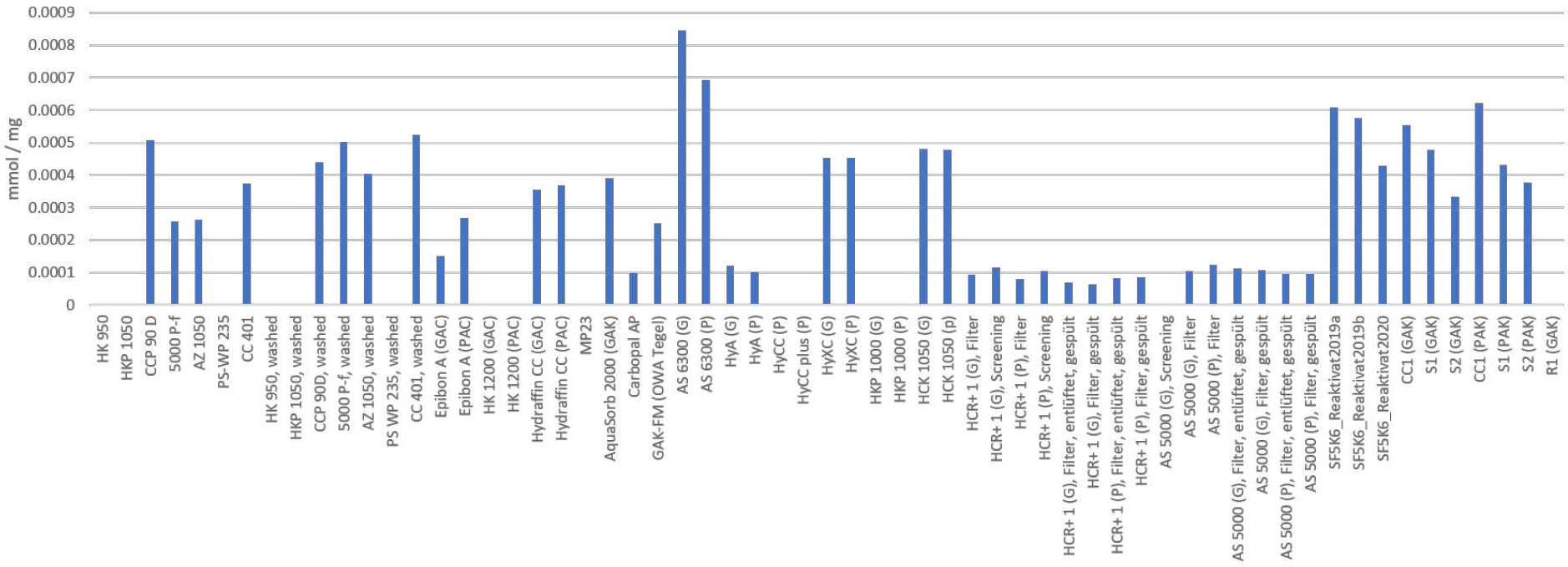

Figure B29: Carbonyl SOG quantified for all ACs.

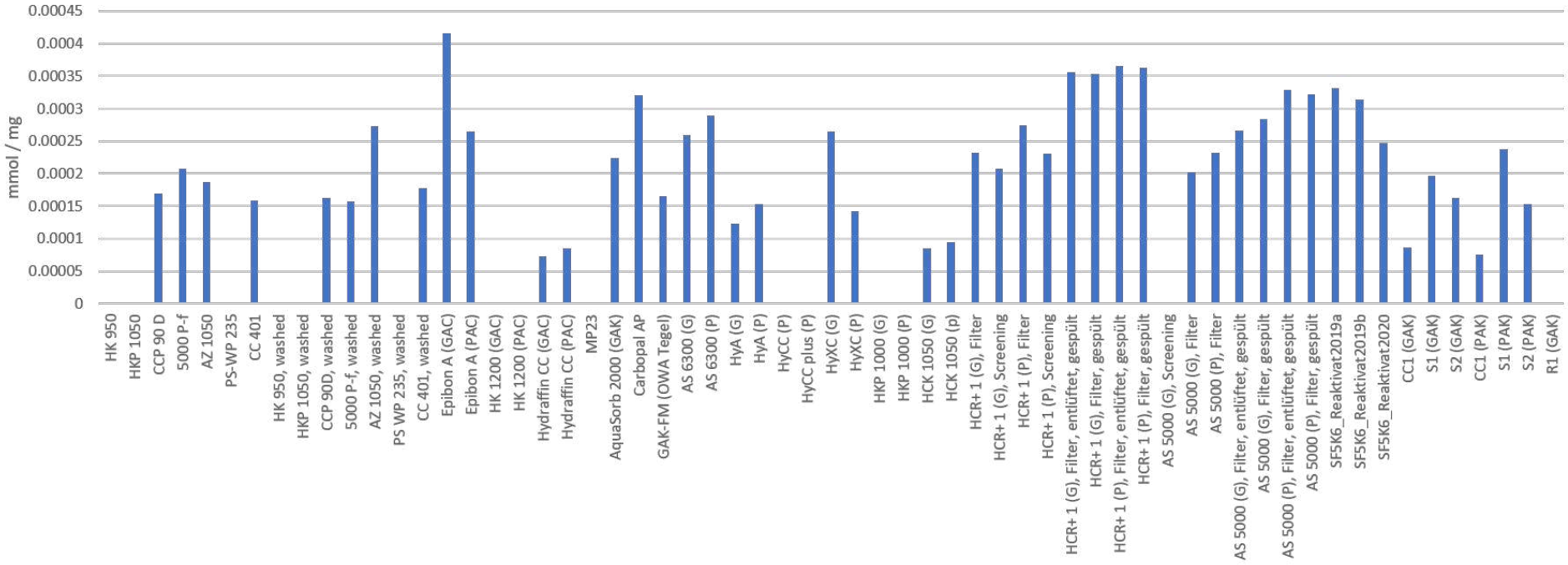

Figure B30: Pyrone SOG quantified for all ACs.

Also effects of the SOGs are discussed by [274] regarding electro-chemical properties as cited by [144]: "Cheng and co-workers reported the relationship between the number of stable CO-desorbing surface oxides titrated by temperature-programmed desorption and the charge storage capability of carbons." and "TPD analyses of oxygen-containing surface complexes pointed out the effective role of CO-desorbing oxides in improving the double-layer capacitance, while CO_2-desorbing groups exhibited a negative effect. As for CO_2-desorbing groups, their presence was proposed to enhance the formation of aggregates that led to a hold-up in the electrochemical response".

B.5.2 PCA of oxygen-containing functional group contents

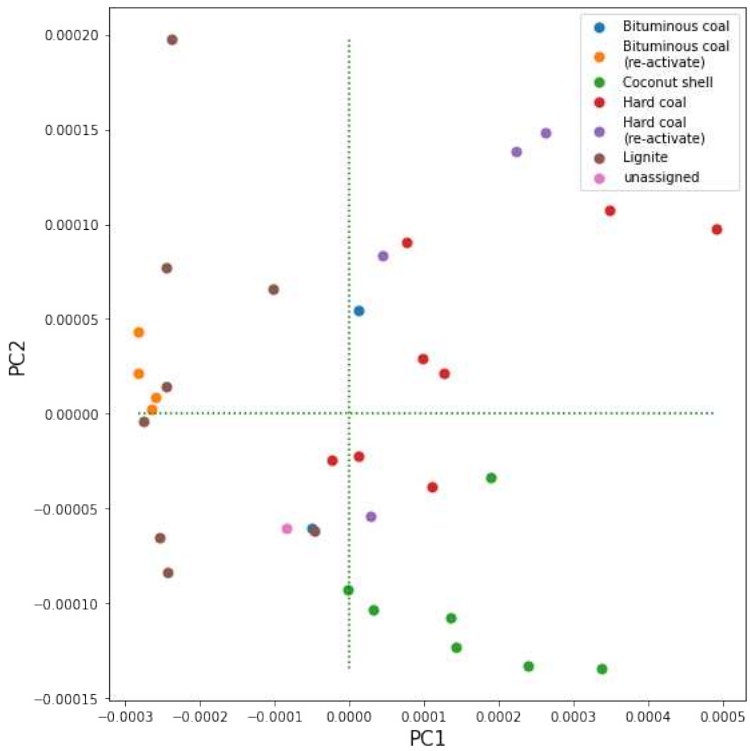

Figure B31: Score plot of the PCA with SOG data not normalized, observed on 34 activated carbon samples, including GAC and PAC, corresponding to loadings plot shown in Figure B32. Colors refer to the raw materials. PC1 is mainly loaded by the quantity of carbonyl groups, PC2 differentiate with positive values high quantities of pyrone groups and with negative values high quantities of carboxylic acid groups.

Two PCA have been applied to the SOG results offering two more perspectives. In both cases, no distinct clustering occurs. However, highlighting of the raw material for each data point (sample) show grouping tendencies on PC1 and PC2.

First on the not normalized data as they are of the same unit and their quantity matters (absolute quantities of SOGs per g of sample are compared). The score plot is presented in Figure B31, the corresponding loading plots are provided in Figure B32. Hard coal and their reactivates are located on the top right hand side, referring to higher amounts of carbonyl and pyrone groups. Lignite, bituminous coal and their reactivates are located on the left hand side, indicating less carbonyl groups. Activated carbons made from coconut shell are located more on the bottom, representing comparable high quantities of carboxylic acid groups.

The second PCA is based on row-wise normalized and centered data from the SOG results (showing relative SOG composition within a sample). This allows the evaluation of the results as a kind of relative pattern of SOGs for each sample (same for PCA on inorganic elemental composition). The score plot with highlighted raw materials is presented in Figure B33 and the corresponding loadings with the explained variance is shown in Figure B34. Lignite and bituminous coal is comprised of clearly more pyrone groups than carbonyl groups. For hard coal and coconut shell it is the other way around whereas activated carbons made of coconut shell additionally show higher carboxylic acid shares.

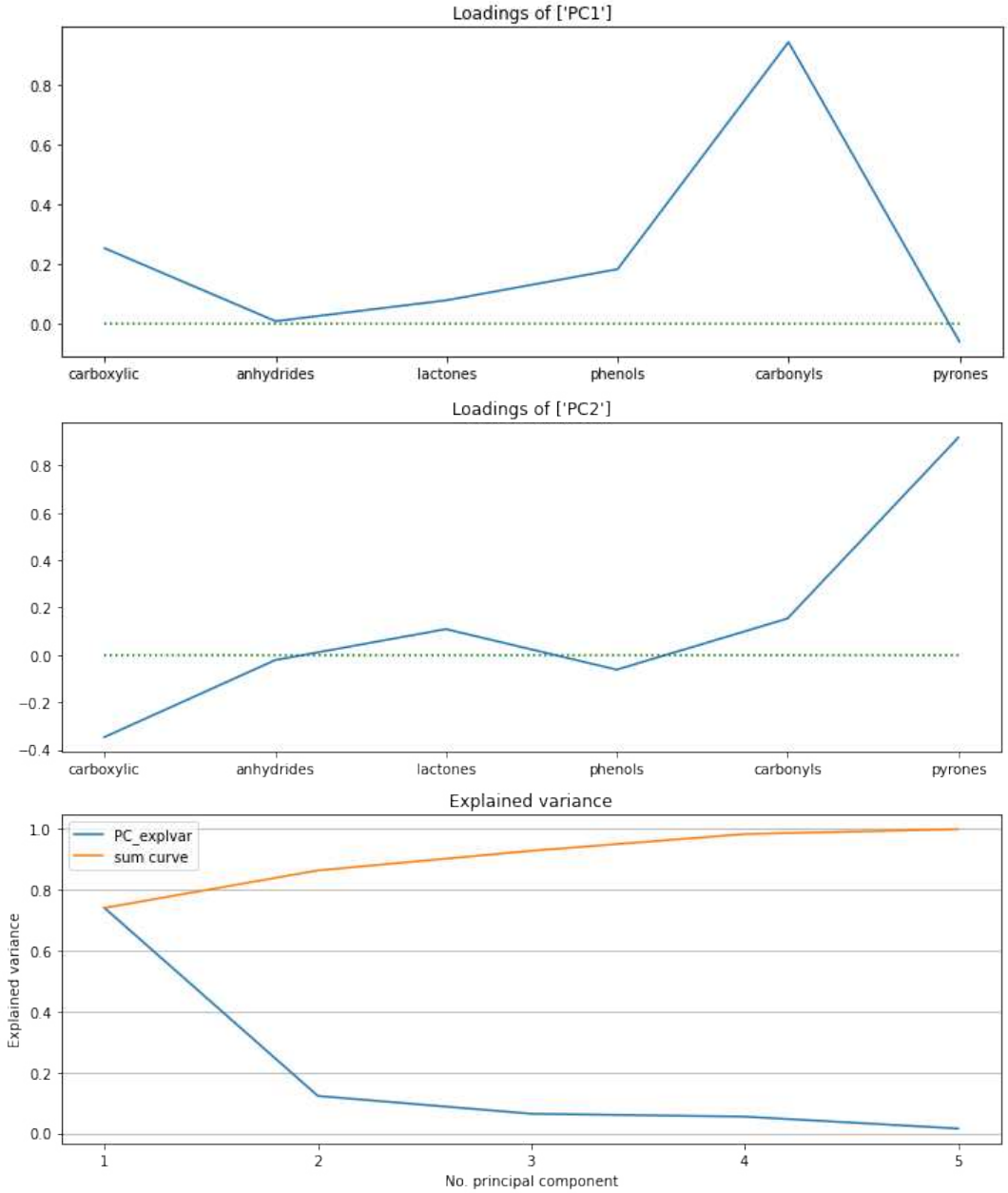

Figure B32: Loading plots of the PCA with not normalized SOG data, corresponding to score plot shown in Figure B31. Principal component (PC) 1 and 2 as well as the explained variance graph are shown.

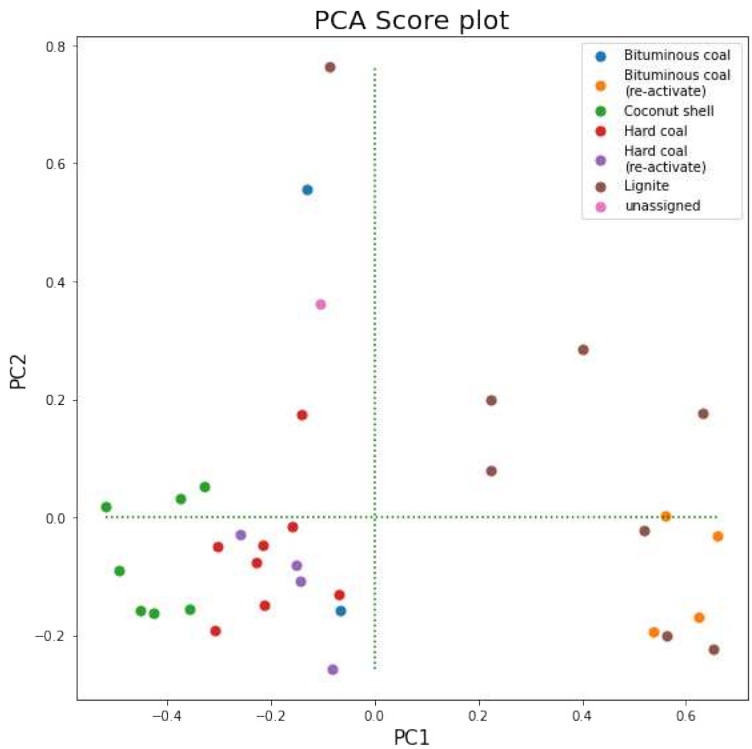

Figure B33: Score plot of the PCA with row-wise normalized SOG data, corresponding to loadings plot shown in Figure B34.

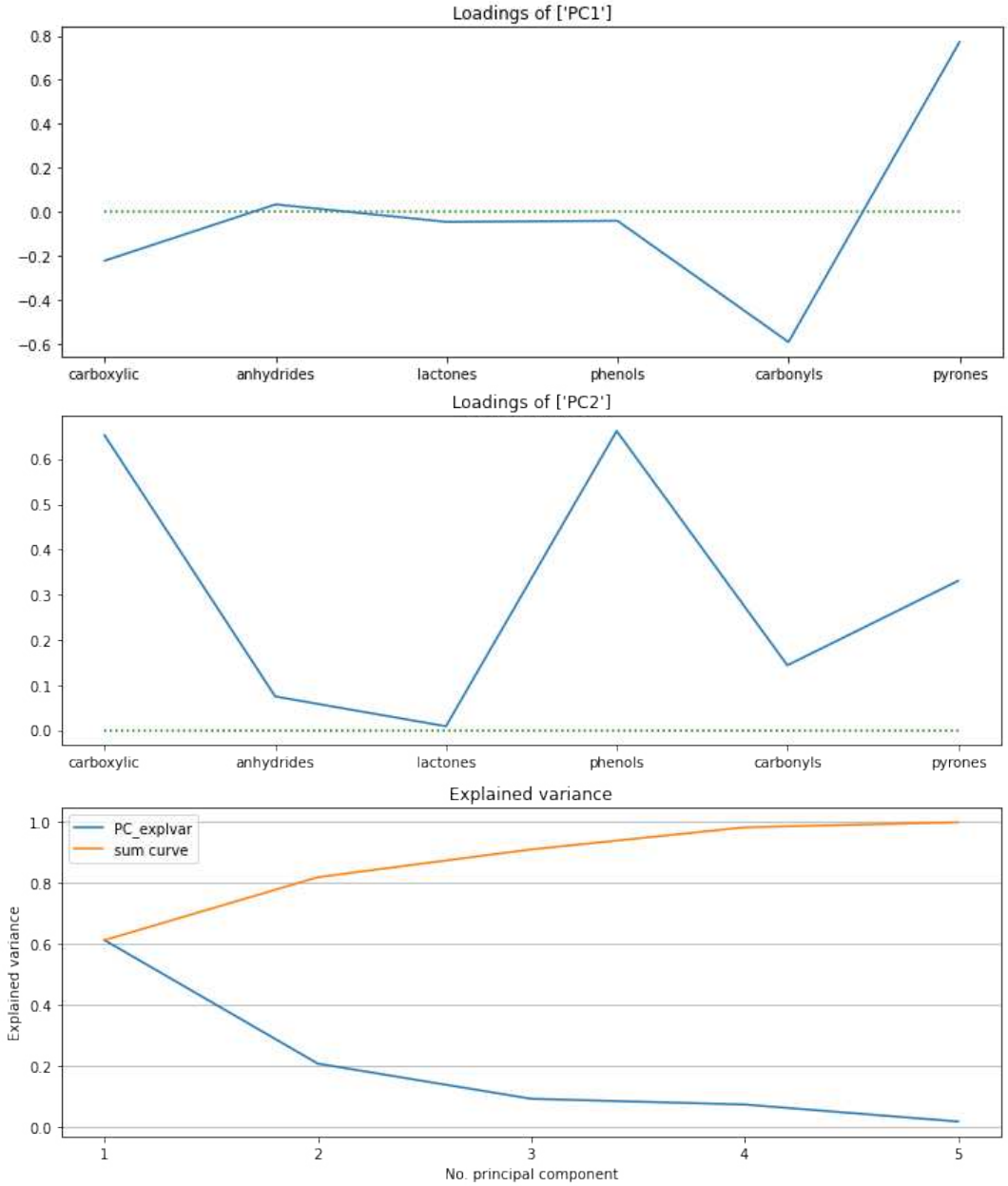

Figure B34: Loading plots of the PCA with row-wise normalized SOG data, corresponding to score plot shown in Figure B33. Principal component (PC) 1 and 2 as well as the explained variance graph are shown.

B.5.3 Comparison with SOGs determined by XPS

Analysis of the outer particle surface by XPS can distinguish three types of carbon-oxygen bonds that are associated with SOGs. XPS analyses indicate greater presence of C–O and C=O bonds (decomposing to CO) compared to O–C=O bonds (decomposing to CO_2). This is generally consistent with the released amounts of CO and CO_2 determined by TGA-FTIR. However, SOGs identified by XPS are not in accordance with the SOGs obtained by TGA-FTIR (Table B2). XPS analyses that only cover the outer surface might not represent the total surface area. As it was indicated by the oxygen content differences between internal and outer surface also may affect the SOG distribution.

B.5.4 X-ray photoelectron spectroscopy (XPS)

Elemental composition of the outer layers of the PAC samples as determined by XPS, is listed in Table B3. Obtained XPS spectra of the analyzed PACs are presented in Figures B35-B48 and corresponding Tables B4-B10, except for 5000 P-f that could not be analyzed due to limited sample mass.

Table B3: Elements determined by XPS in at.% and wt.% of the analyzed PACs.

	unit	**HK**	**HKP**	**CCP**	**SAE**	**P-f**	**AZ**	**PS**	**CC**
C	at.%	86.9	81.1	84.7	83.7	n.d.	86.4	91.6	91.5
O	at.%	11.4	16.0	9.4	11.0	n.d.	8.0	8.4	8.5
Si	at.%	traces	-	5.7	0.1	n.d.	5.6	-	-
Ca	at.%	0.4	0.5	0.1	4.3	n.d.	-	-	-
Na	at.%	-	-	0.1	0.7	n.d.	-	-	-
S	at.%	-	-	-	-	n.d.	-	-	-
Fe	at.%	-	-	-	0.2	n.d.	-	-	-
P	at.%	1.3	2.4	-	-	n.d.	-	-	-
Σ XPS elements	%	100	100	100	100	-	100	100	100
C	wt.%	81	74	76	73	n.d.	78	89	89
O	wt.%	14	19	11	13	n.d.	10	11	11
Si	wt.%	-	-	12	0.2	n.d.	12	-	-
Ca	wt.%	1	2	0.3	12	n.d.	-	-	-
Na	wt.%	-	-	0.2	1	n.d.	-	-	-
S	wt.%	-	-	-	-	n.d.	-	-	-
Fe	wt.%	-	-	-	1	n.d.	-	-	-
P	wt.%	3	6	-	-	n.d.	-	-	-
Σ XPS elements	%	100	100	100	100	-	100	100	100

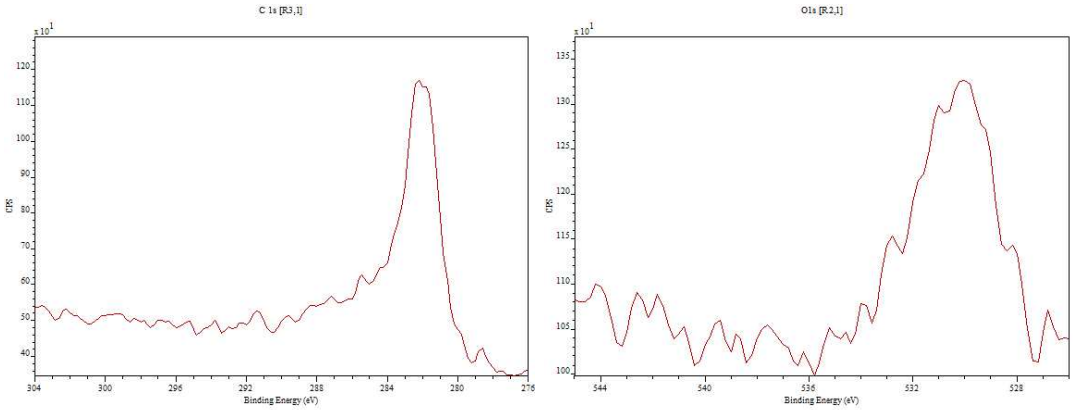

Figure B35: C1s peak (left) and O1s peak (right) of HK 950.

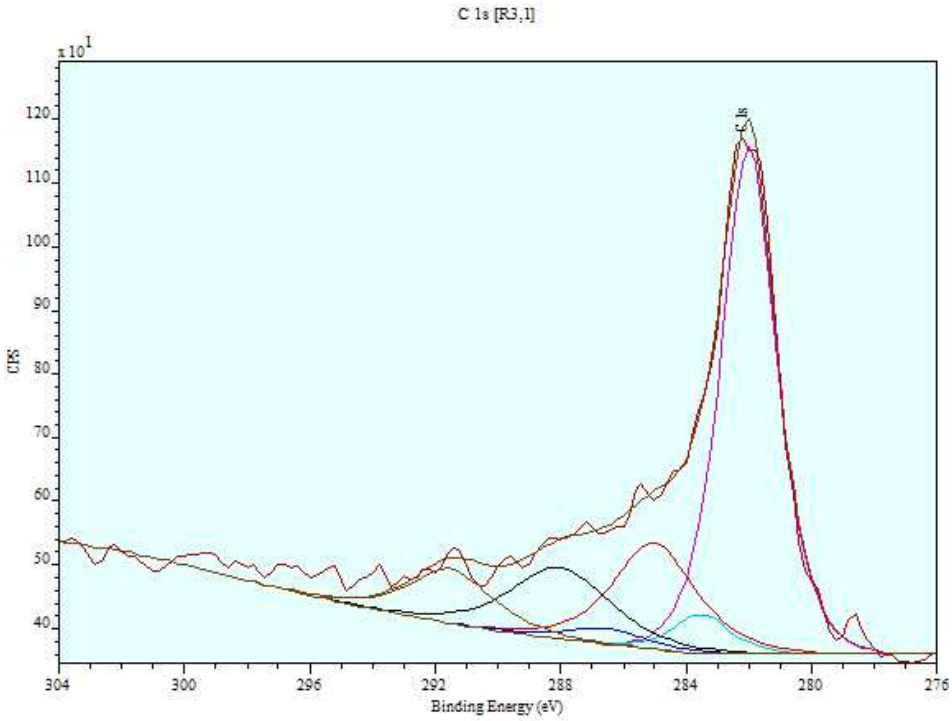

Figure B36: C1s peak of HK 950 with fittings according to Table B4.

Table B4: Fitting of the C1s peak of HK 950, corresponding to Figure B36.

	[C–C]	[C–O]	[C=O]	[O–C=O]	[CO_3^{2-}]	π–π^*
Binding energy in eV	285.0	286.6	288.0	289.5	292.0	295.4
Share in Atom %	54.3	3.1	18.4	1.6	14.2	8.3

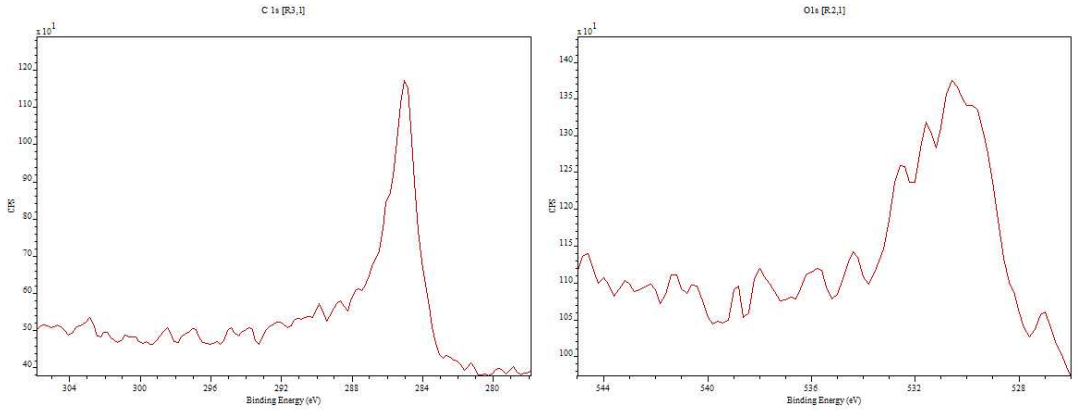

Figure B37: C1s peak (left) and O1s peak (right) of HKP 1050.

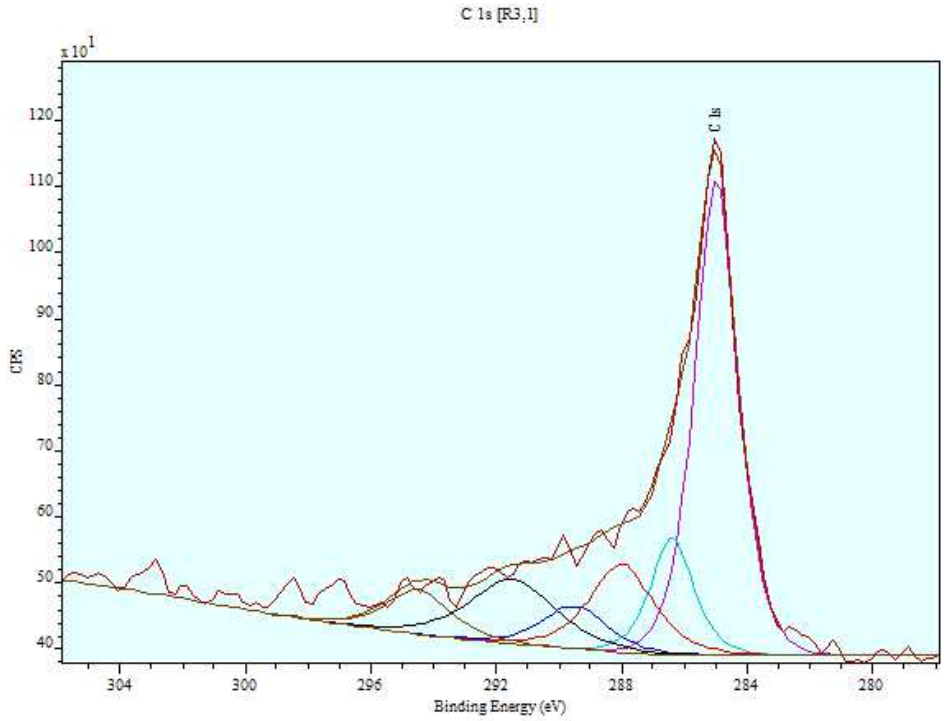

Figure B38: C1s peak of HKP 1050 with fittings according to Table B5.

Table B5: Fitting of the C1s peak of HKP 1050, corresponding to Figure B38.

	[C–C]	[C–O]	[C=O]	[O–C=O]	$[CO_3{}^{2-}]$	π–π^*
Binding energy in eV	285.0	286.6	288.0	289.7	292.5	295.9
Share in Atom %	48.1	9.7	14.0	6.2	13.7	8.3

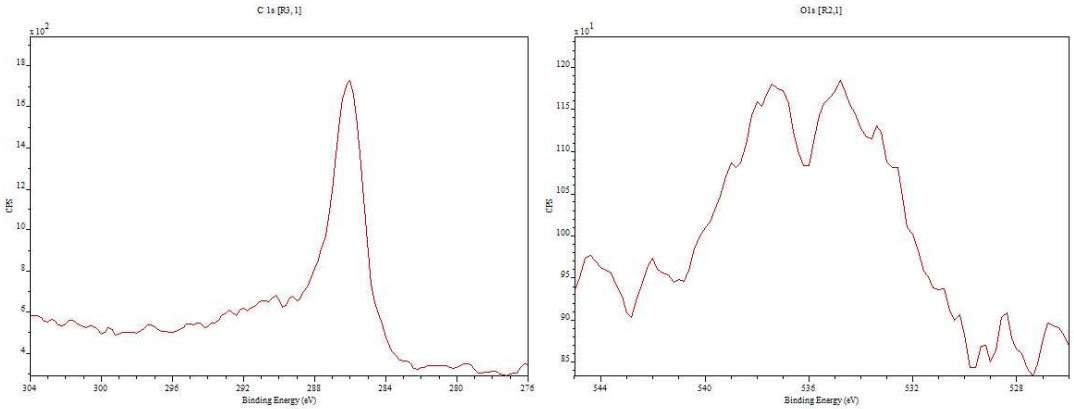

Figure B39: C1s peak (left) and O1s peak (right) of CCP 90D.

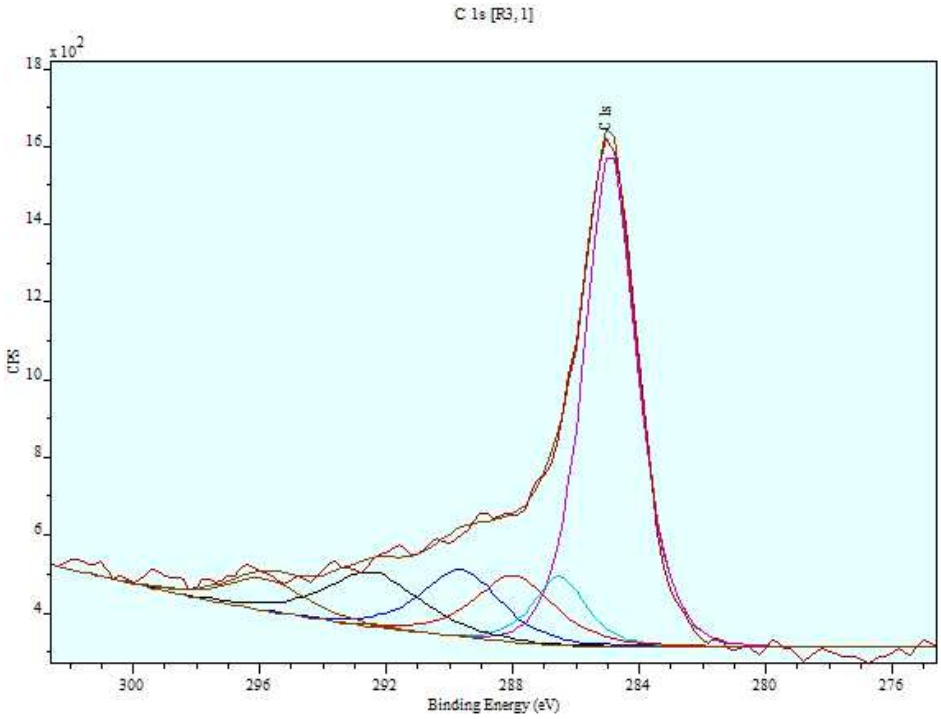

Figure B40: C1s peak of CCP 90D with fittings according to Table B6.

Table B6: Fitting of the C1s peak CCP 90D, corresponding to Figure B40.

	[C–C]	[C–O]	[C=O]	[O–C=O]	[CO_3^{2-}]	π–π^*
Binding energy in eV	285.0	286.6	288.0	289.7	292.5	295.9
Share in Atom %	55.1	7.9	10.0	11.8	10.6	4.4

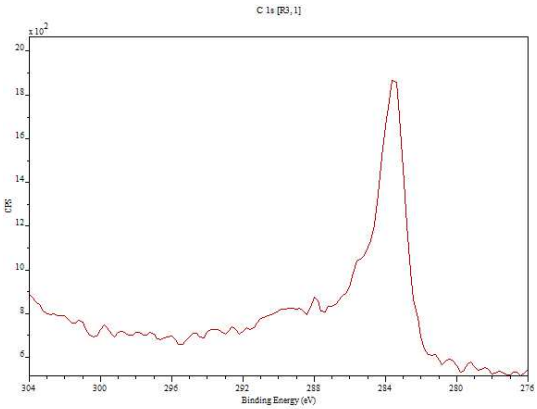

Figure B41: C1s peak of SAE Super.

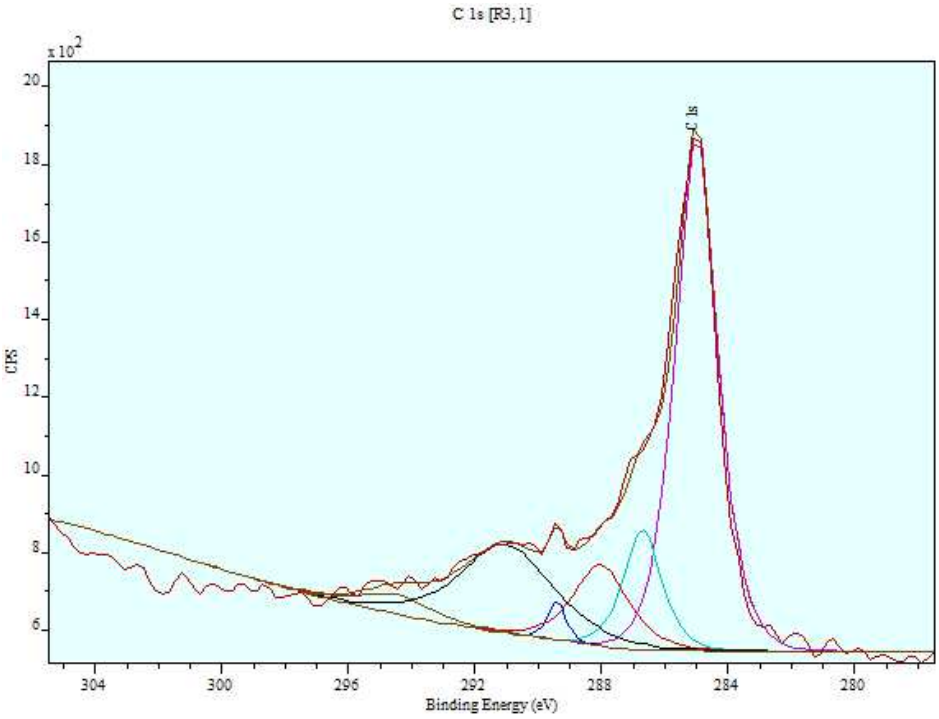

Figure B42: C1s peak of SAE Super with fittings according to Table B7.

Table B7: Fitting of the C1s peak of SAE Super, corresponding to Figure B42.

	[C–C]	[C–O]	[C=O]	[O–C=O]	[CO_3^{2-}]	π–π^*
Binding energy in eV	285.0	286.7	288.0	289.4	291.0	294.5
Share in Atom %	52.1	13.1	10.6	1.5	19.9	2.8

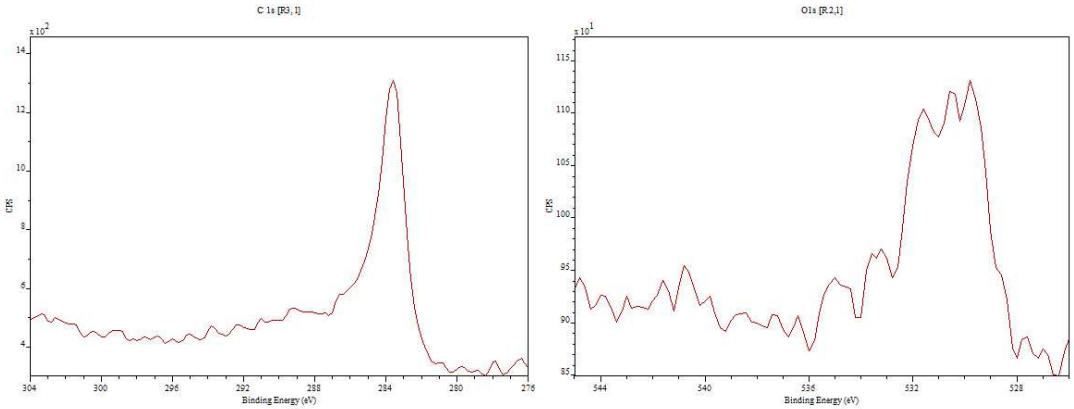

Figure B43: C1s peak (left) and O1s peak (right) of AZ 1050.

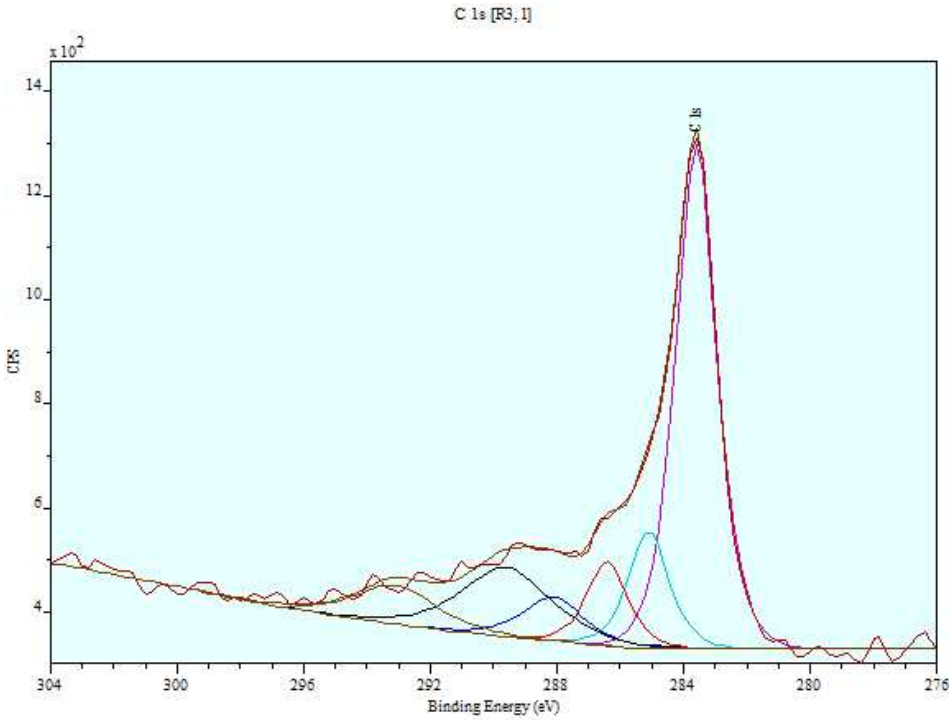

Figure B44: C1s peak of AZ 1050 with fittings according to Table B8.

Table B8: Fitting of the C1s peak of AZ 1050, corresponding to Figure B44.

	[C–C]	[C–O]	[C=O]	[O–C=O]	[CO_3^{2-}]	π–π^*
Binding energy in eV	285.0	286.6	288.0	289.5	292.0	295.4
Share in Atom %	51.2	11.6	7.6	6.4	15.5	7.6

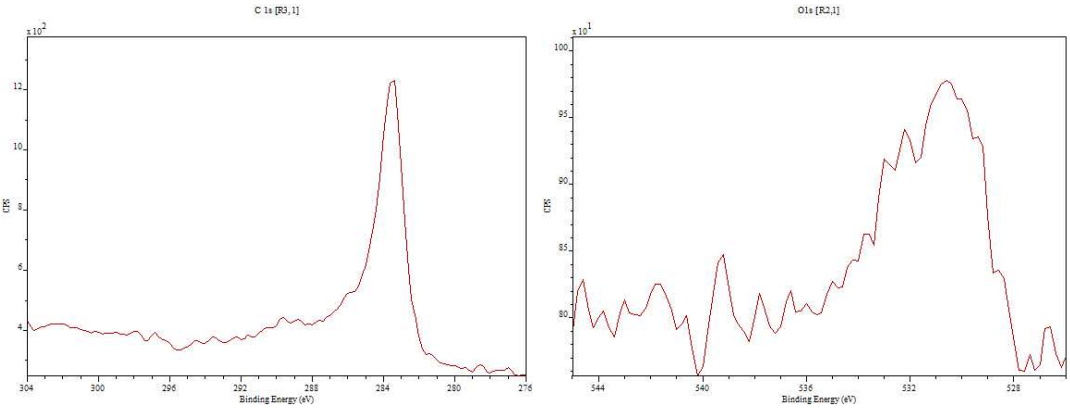

Figure B45: C1s peak (left) and O1s peak (right) of PS WP 235.

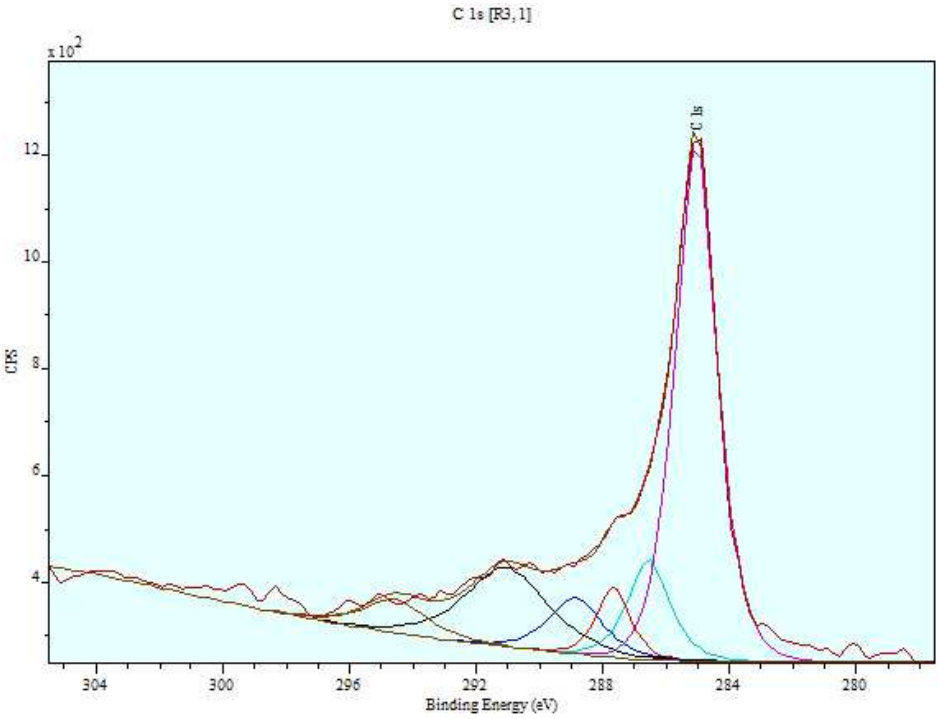

Figure B46: C1s peak of PS WP 235 with fittings according to Table B9.

Table B9: Fitting of the C1s peak of PS WP 235, corresponding to Figure B46.

	[C–C]	[C–O]	[C=O]	[O–C=O]	$[CO_3{}^{2-}]$	π–π^*
Binding energy in eV	285.0	286.8	287.9	289.5	291.0	294.5
Share in Atom %	56.0	8.4	7.4	5.3	16.9	6.0

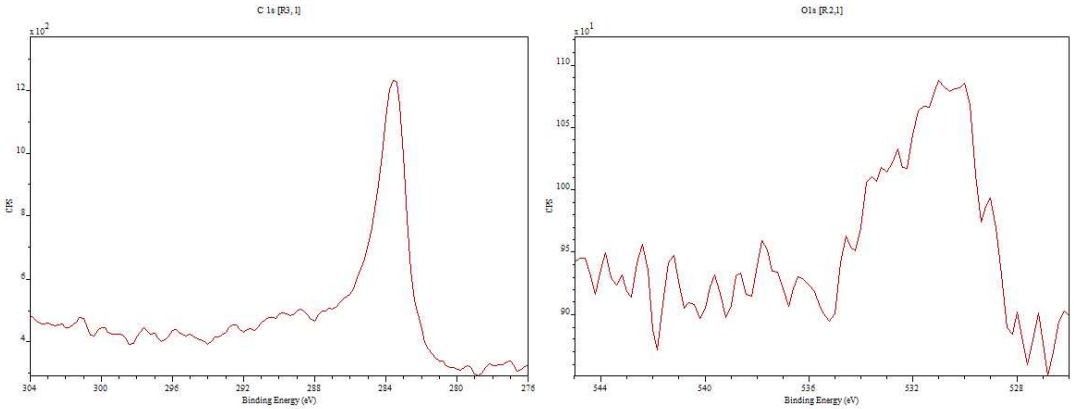

Figure B47: C1s peak (left) and O1s peak (right) of CC 401.

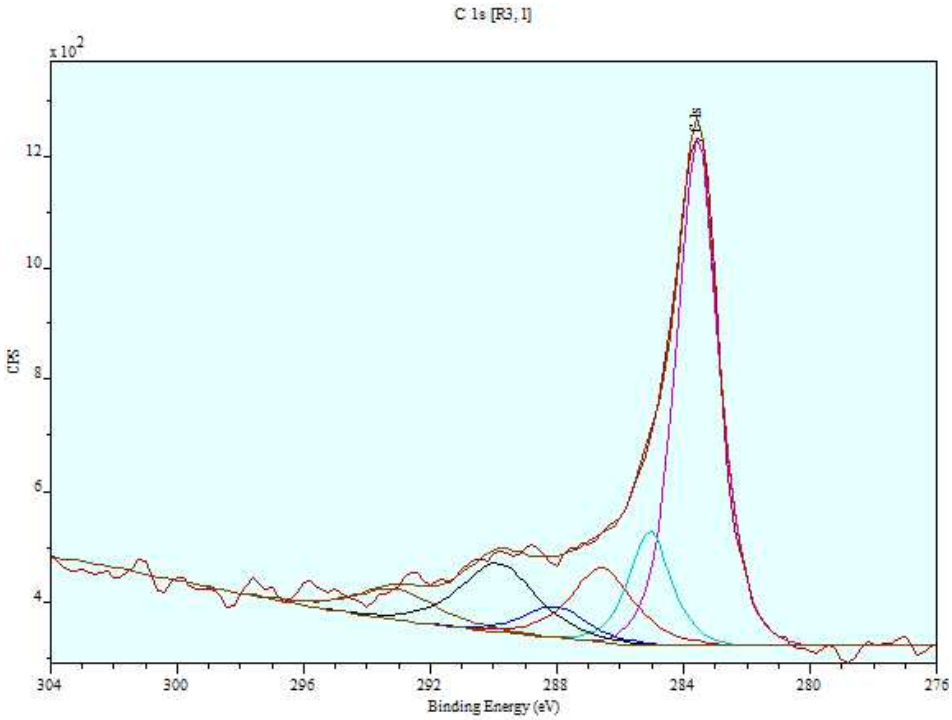

Figure B48: C1s peak of CC 401 with fittings according to Table B10.

Table B10: Fitting of the C1s peak of CC 401, corresponding to Figure B48.

	[C–C]	[C–O]	[C=O]	[O–C=O]	[CO_3^{2-}]	π–π^*
Binding energy in eV	285.0	286.6	288.0	289.7	292.5	295.9
Share in Atom %	53.0	11.7	10.3	5.7	12.1	7.2

C

Supplementary information for "Specific adsorption sites and conditions derived by thermal decomposition of activated carbons and adsorbed carbamazepine"

This appendix is part of chapter 4 and was published in *Scientific Reports* in 2020 [195]. In the original open access publication you find also the spreadsheet named *Structures_by_TED-GC-MS* (provided in XLSX and ODS) containing all information about the decomposition products detected by TED-GC/MS. Additionally, the whole raw data is provided within the zenodo repository [234].

This appendix contains

1 TGA decomposition stages
2 Hydrolysis of isocyanic acid
3 Decomposition products of the 2nd mass loss stage
4 SEM comparisons
5 DRIFTS comparisons

C.1 TGA decomposition stages

The TGA graphs shown in Figures 4.1&4.2a are characterised by two decomposition stages after carbamazepine adsorption. Table C1 provides the temperature ranges and the temperatures of maximum mass loss rate (DTG_{max}) for each mass loss stage. The temperature ranges were used to determine the mass losses in Table 4.2 and to calculate the kinetic parameters shown in Table C2. DTG_{max} temperatures show the shifts of the decomposition stages depending on the activated carbon as graphically assessed in Figure 4.2a.

	1st mass loss stage		2nd mass loss stage	
sample	range in °C	DTG_{max} in °C	range in °C	DTG_{max} in °C
SAE+CBZ-15	150-295	242	295-575	446
HK+CBZ-15	103-222	181	222-502	397
CCP+CBZ-12	120-263	216	263-600	487

Table C1: TGA characteristics for the 1st & 2nd mass loss stage of the systems with the highest carbamazepine loadings.

C.1.1 Influence of sample mass on DTG profiles

The activated carbon HK 950 has a comparable low density and therefore TGA sample mass was 15 mg in the crucibles. This could alter thermal decomposition of samples with 20 mg and parameters like DTG_{max} temperatures in Table C1.

Figure C1 shows the SAE+CBZ-15 system with different sample masses. There is no shift in DTG_{max} temperature of the sample analysed with 15 mg. Therefore, results in Table C1 are not sensitive to the analysed sample masses with slight mass changes.

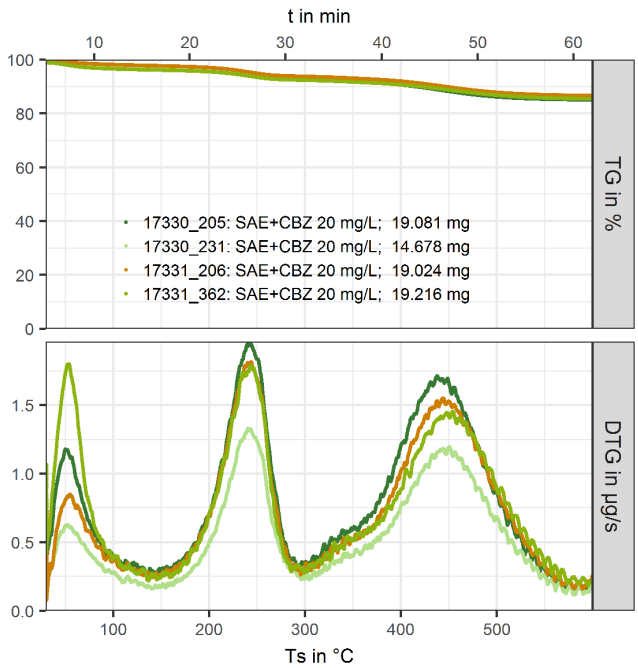

Figure C1: TGA results for the SAE+CBZ-15 system with varying sample masses. No shift in DTG_{max} temperatures can be observed.

C.1.2 Comparison of kinetic parameters

The kinetic parameters determined by TGA ramp-kinetics are provided in Table C2. The results of Pinto et al. (2014)[229] were conducted by heating rates of 2.5, 5, 10 and 15 °C min^{-1}. We assume that the magnitude of the pre-exponential factor (k) differs, due to experimental conditions including carbamazepine investigated as adsorbate or pure powder.

	Activation energy (E_a)	Pre-exponential factor (k)
SAE+CBZ-15	92±2 kJ mol^{-1}	450 min^{-1}
HK+CBZ-15	92±3 kJ mol^{-1}	540 min^{-1}
Carbamazepine[229]	93±2 kJ mol^{-1}	8.6±0.1 min^{-1}

Table C2: Kinetic parameters determined by ramp kinetic experiments for splitting-off isocyanic acid from carbamazepine.

C.2 Hydrolysis of isocyanic acid

Isocyanic acid (HNCO) can be hydrolysed to carbon dioxide and ammonia (Figure C2). This reaction was already described at 80 °C and only with traces of water vapour [275].

$$HNCO + H_2O \longrightarrow CO_2 + NH_3$$

Figure C2: Hydrolysis of isocyanic acid to carbon dioxide and ammonia.

Since we worked with nitrogen as purge gas with 5.0 purity we did not expect noticeable amounts of water. However, we observed the consumption of water in the release rates of TGA-FTIR during HNCO release in SAE+CBZ-15 (yellow line in Figure C3). Simultaneously, the evolution of carbon dioxide and ammonia increased while isocyanic acid decreased.

This was solely found in the TGA-FTIR measurements of the systems with SAE Super, indicating specific catalytic effects by this activated carbon probably by its inorganic inclusions. The amount of water consumed corresponds with the hydrolysis reaction for isocyanic acid. It equals about 0.01% water in the nitrogen purge gas.

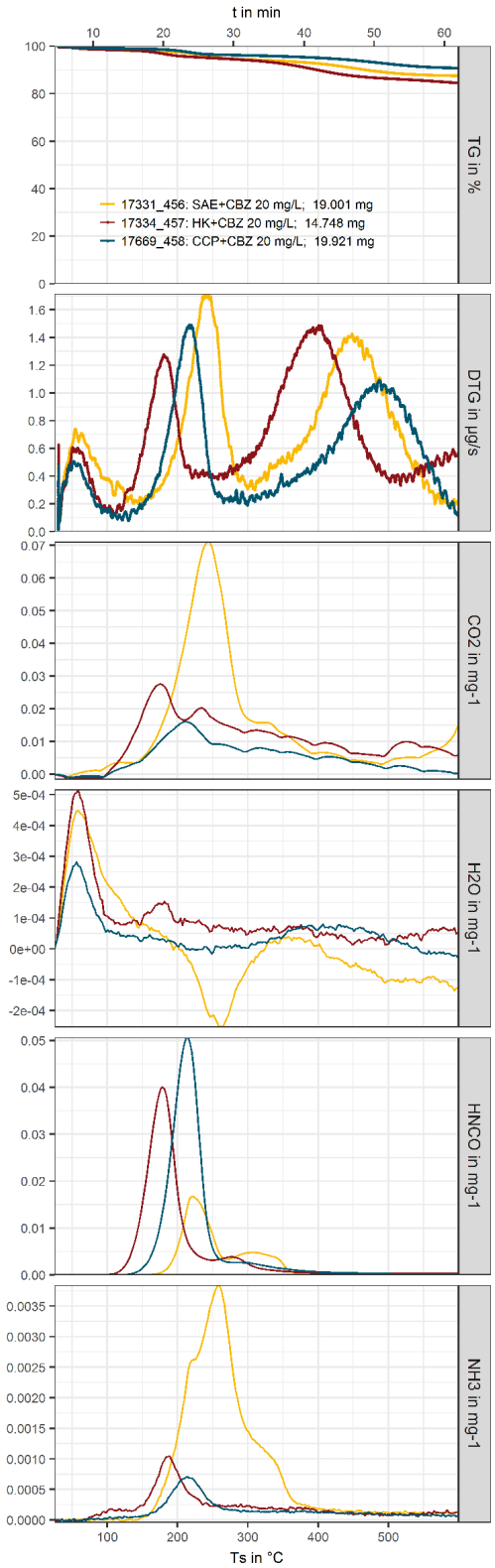

Figure C3: TGA-FTIR results for the highest loadings of carbamazepine on the three activated carbons. The figure corresponds to Figure 4.2(a). Release rates of carbon dioxide, water, isocyanic acid and ammonia are shown normalised to sample mass.

C.3 Decomposition products of the 2nd mass loss stage

The decomposition products observed by TED-GC/MS are provided in the spreadsheet *Structures_by_TED-GC-MS* in the supplementary information files. Figures for comparing the systems with 4.5% carbamazepine mass fraction (like Figure 4.5) and the systems with SAE Super and varying carbamazepine mass fractions (like Figure 4.6) are additionally shown in section C.3.2. First, section C.3.1 shows TGA-FTIR results for the release of hydrogen cyanide.

C.3.1 Release of hydrogen cyanide

A specific characteristic of the systems with HK 950 is the release of significant amounts of hydrogen cyanide (HCN) after carbamazepine adsorption. This was observed by TGA-FTIR and can help to interpret the release of decomposition products observed by TED-GC/MS. Figure C4 shows the TGA-FTIR measurements with HCN release rates of the systems with high carbamazepine loadings. Unloaded activated carbons do not release any HCN at the investigated temperatures.

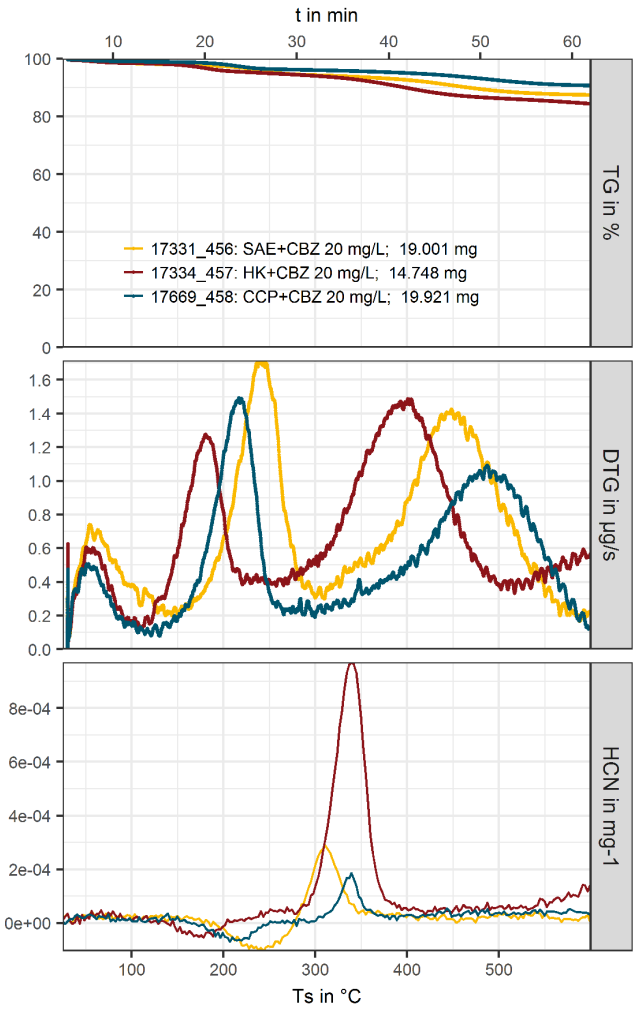

Figure C4: TGA-FTIR results for the highest loadings of carbamazepine on the three activated carbons. The figure corresponds to Figure 4.2(a). Release rates of hydrogen cyanide are shown normalised to sample mass.

C.3.2 Release graphs for all decomposition products of the 2nd mass loss stage

This section covers all decomposition products in the 2nd mass loss stage observed by TED-GC/MS. Data represent double determinations, comparing the three activated carbon systems with 4.5 % carbamazepine and their release from the unloaded adsorbents. Furthermore, the release of the proposed substances from the SAE Super systems depending on the carbamazepine loading, represented by the 2nd stage's mass loss, is provided. Values in the following figures (C5 ... C58) are normalised to sample mass and error bars represent the range of the duplicate determination. Numbering of the substances is based on retention time and can be found the spreadsheet *Structures_by_TED-GC-MS*.

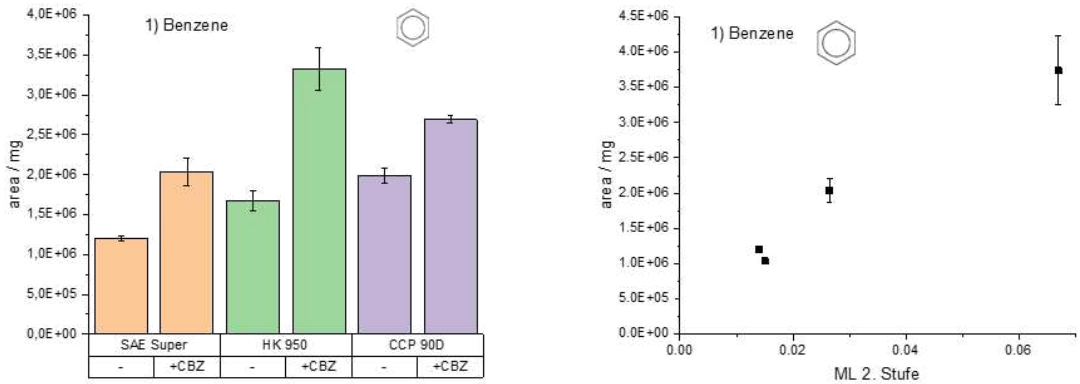

Figure C5: Benzene (1)

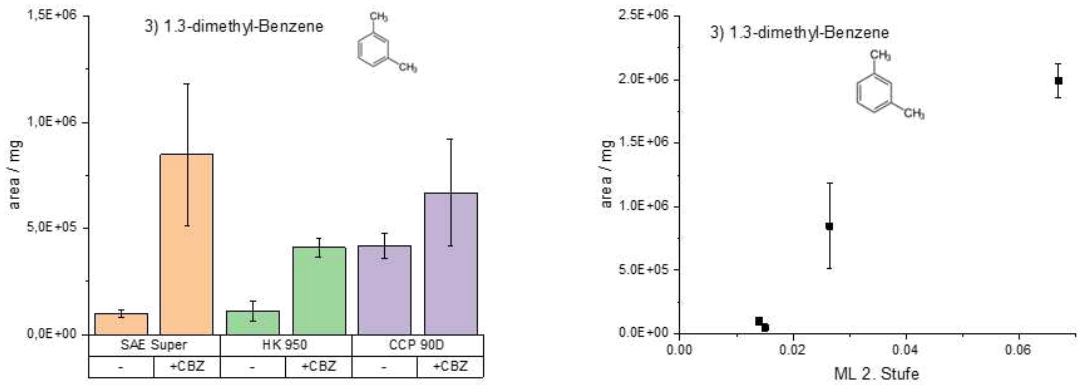

Figure C6: 1,3-dimethyl-Benzene (3)

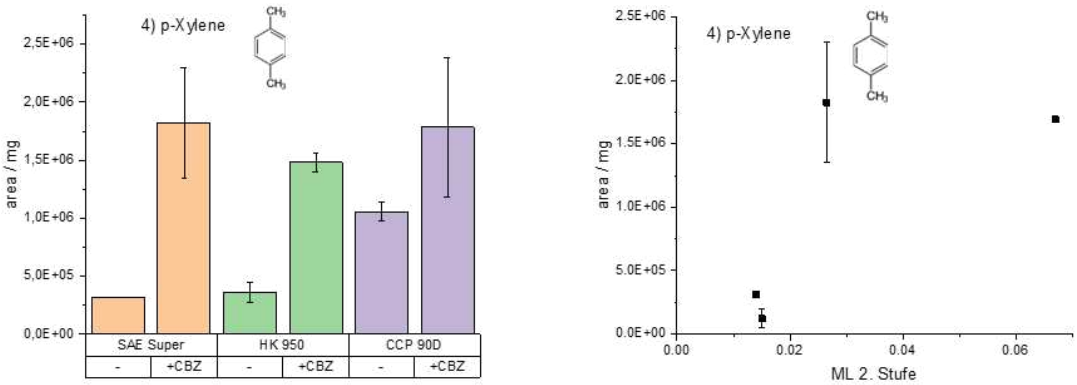

Figure C7: p-Xylene (4)

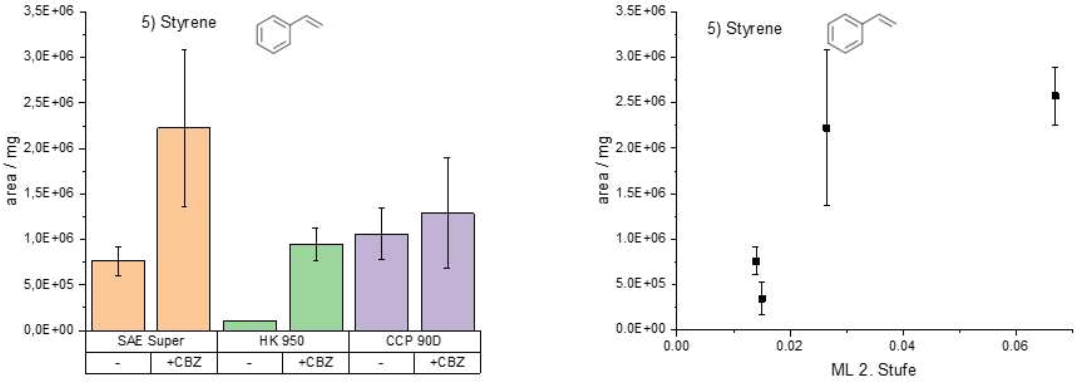

Figure C8: Styrene (5)

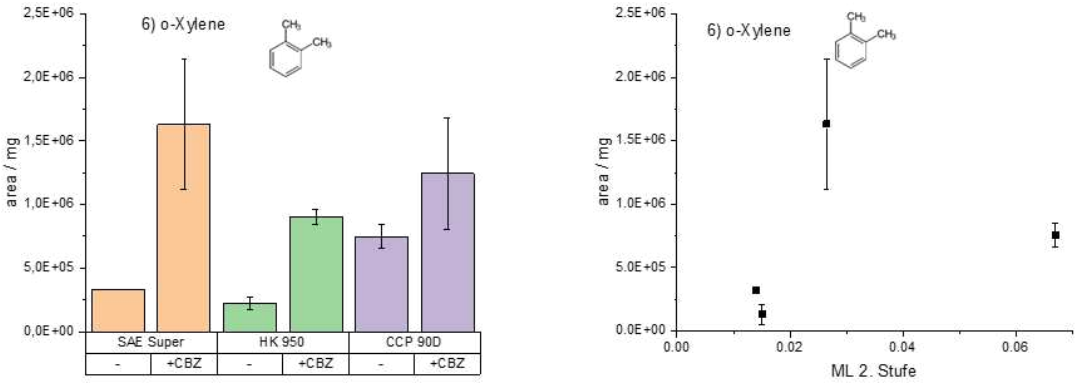

Figure C9: o-Xylene (6)

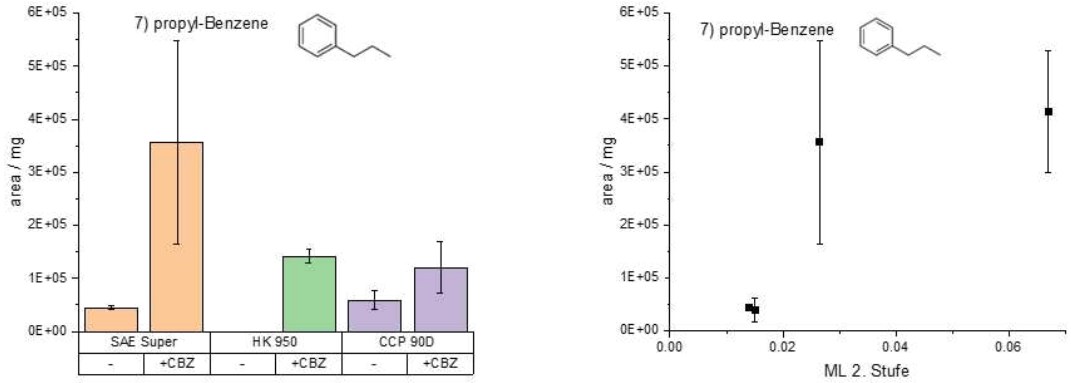

Figure C10: Propyl-Benzene (7)

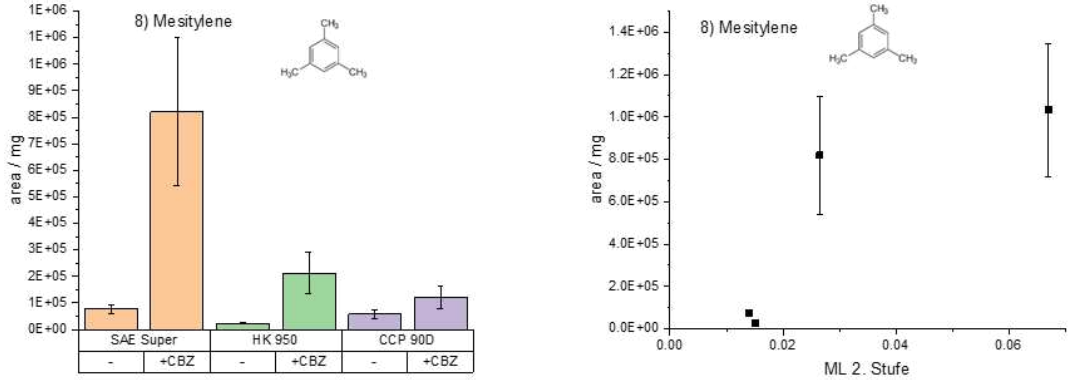

Figure C11: Mesitylene (8)

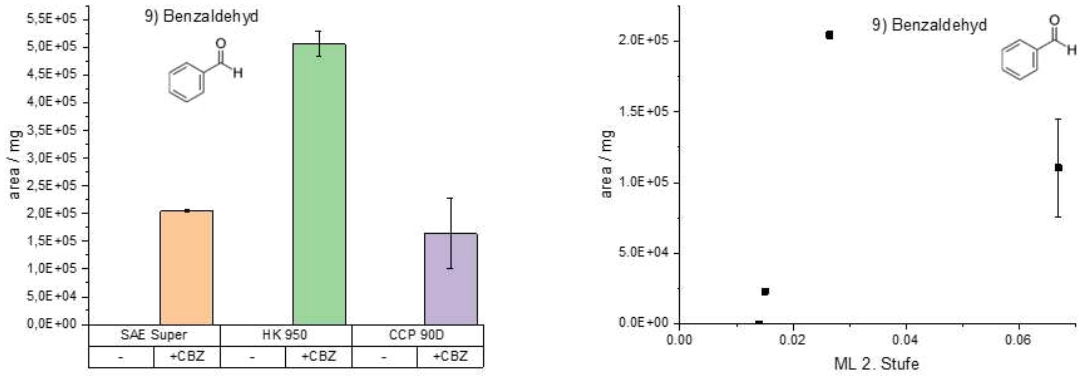

Figure C12: Mesitylene (9)

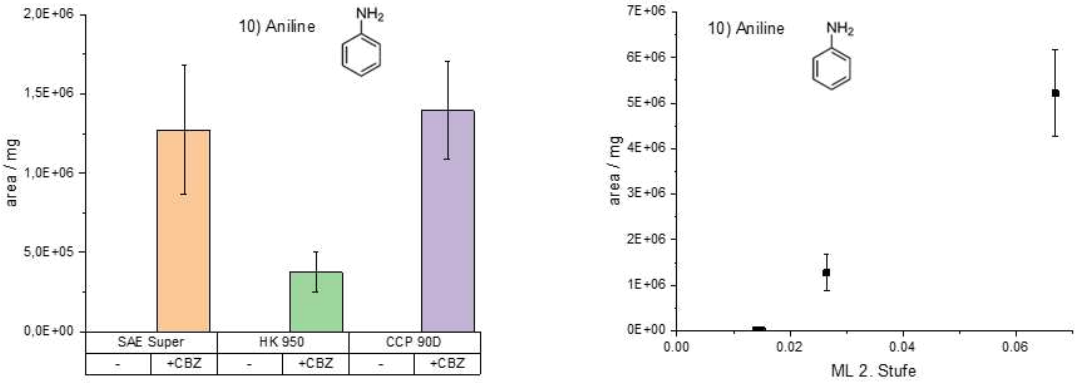

Figure C13: Mesitylene (10)

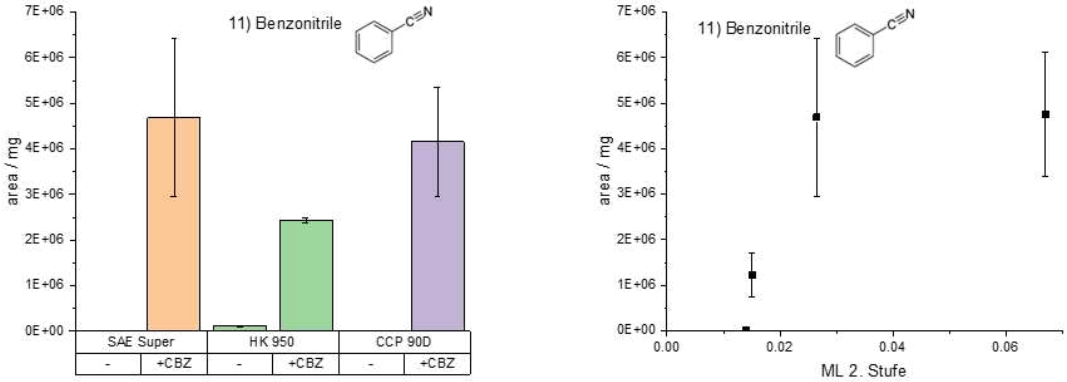

Figure C14: Benzonitrile (11)

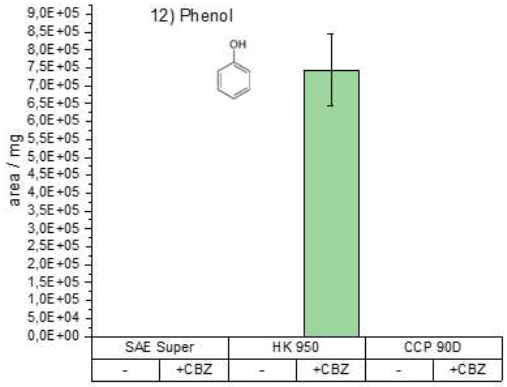

Figure C15: Phenol (12)

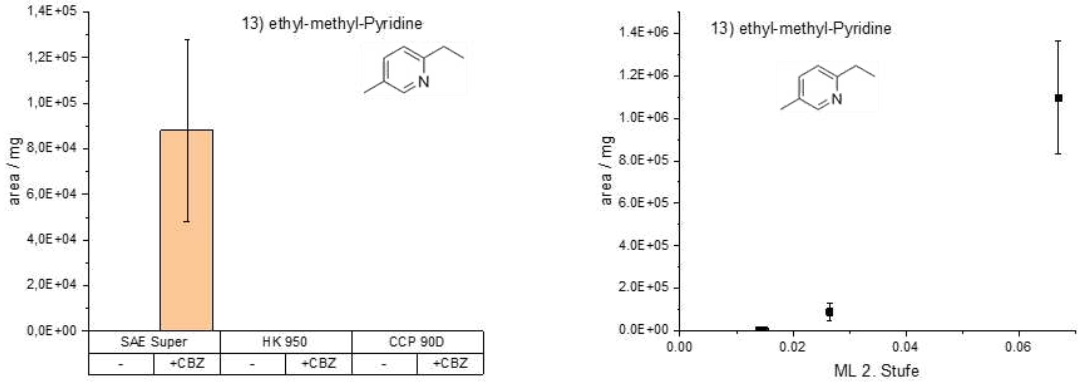

Figure C16: ethyl-methyl-Pyridine or m-Ethylanaline (13)

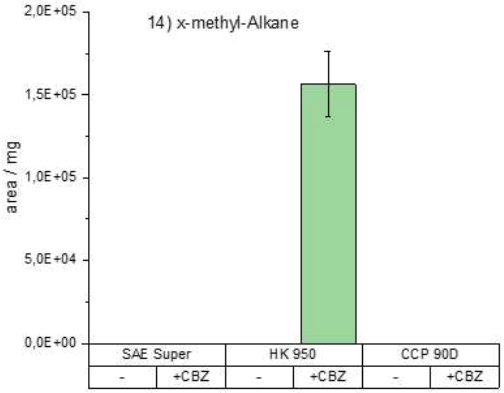

Figure C17: x-methyl-Alkane (14)

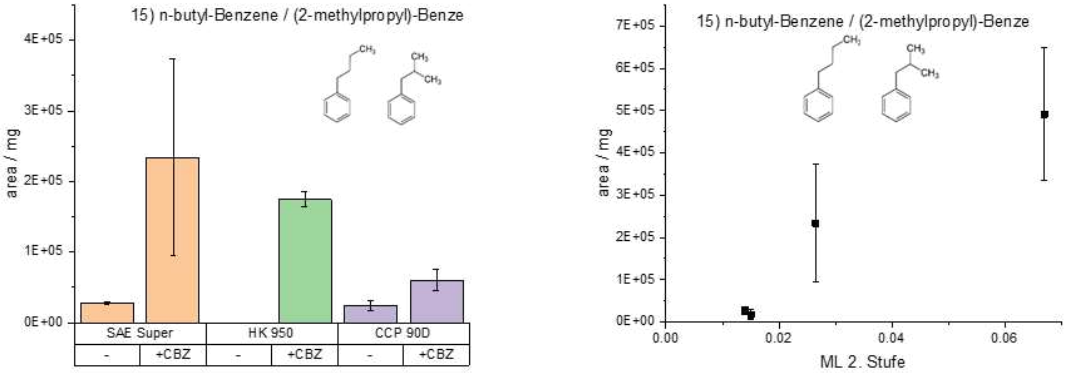

Figure C18: n-butyl-Benzene or (2-methylpropyl)-Benzene (15)

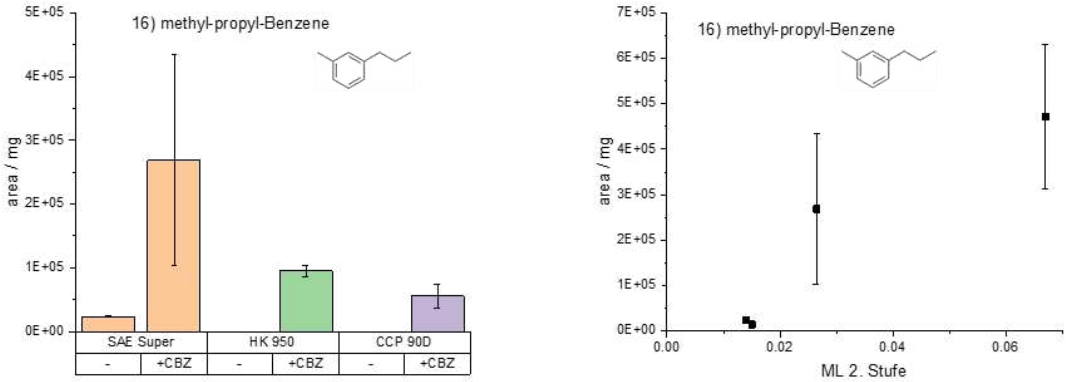

Figure C19: methyl-propyl-Benzene (16)

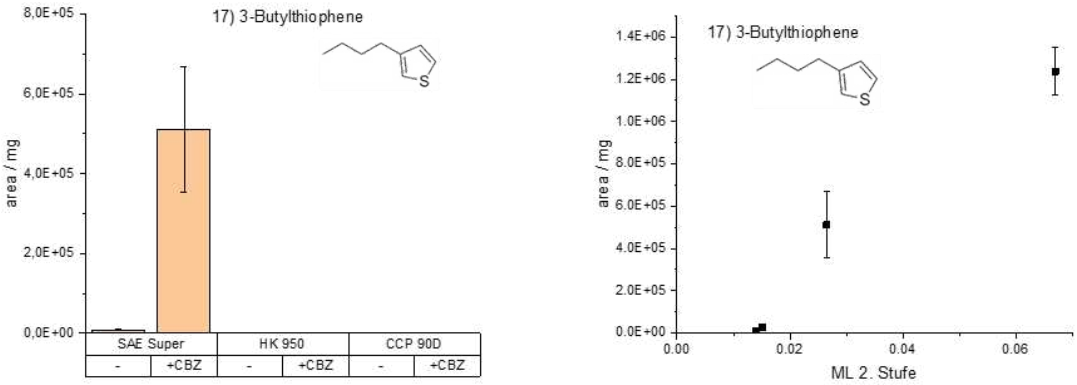

Figure C20: 3-Butylthiophene (17)

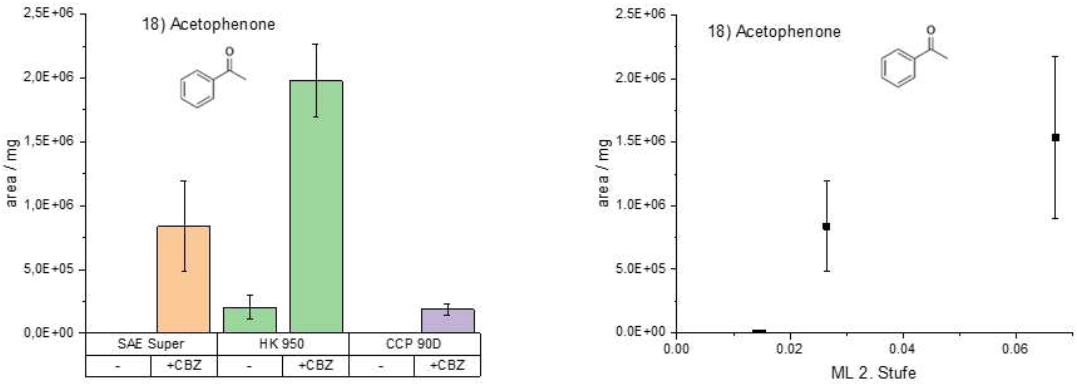

Figure C21: Acetophenone (18)

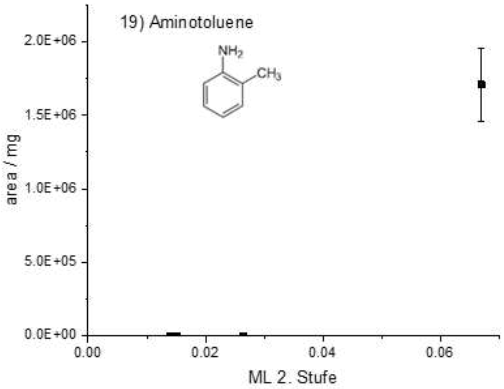

Figure C22: Acetophenone (19)

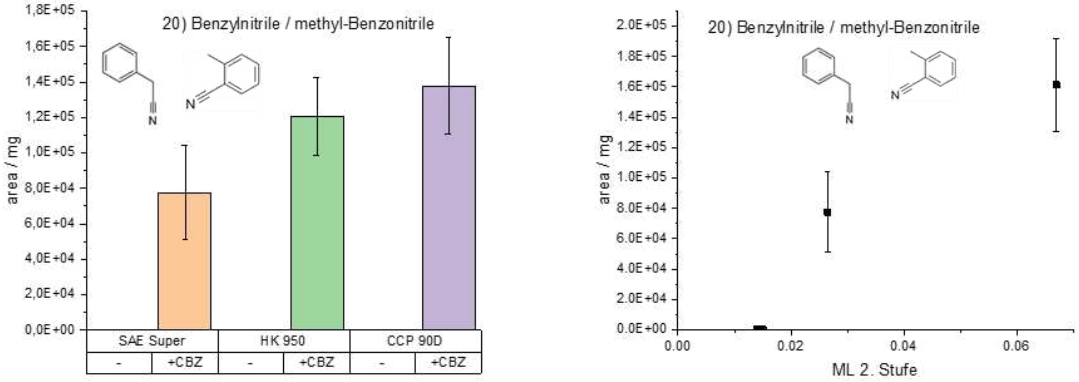

Figure C23: Benzylnitrile or methyl-Benzonitril (20)

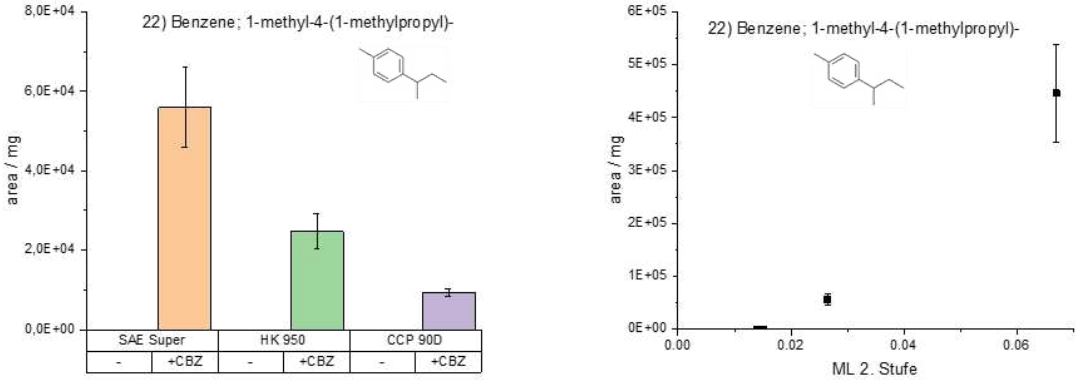

Figure C24: Benzene, 1-methyl-4-(1-methylpropyl)- (22)

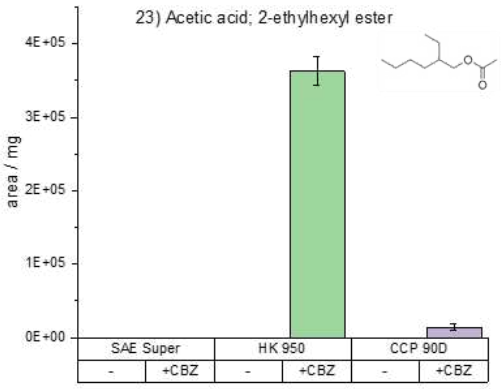

Figure C25: Acetic acid, 2-ethylhexyl ester (23)

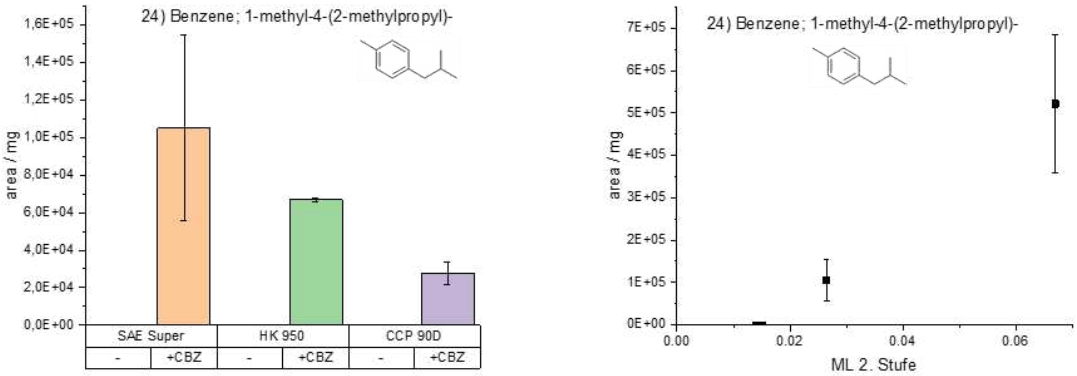

Figure C26: Benzene, 1-methyl-4-(2-methylpropyl)- (24)

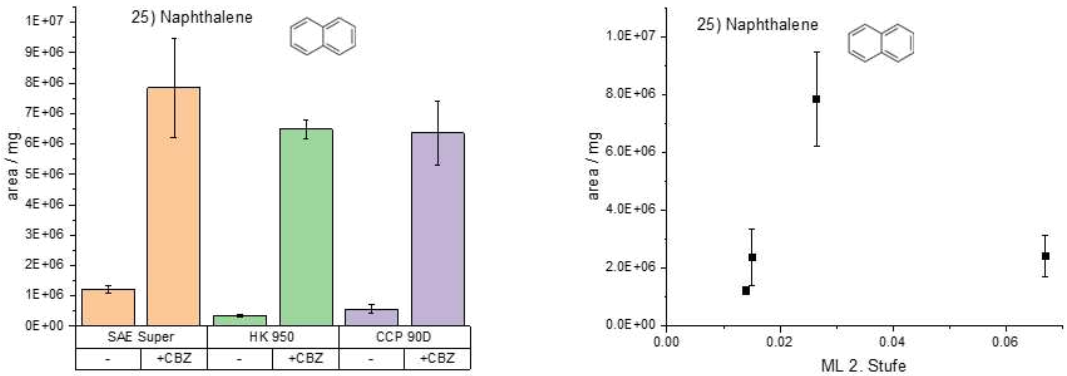

Figure C27: Naphthalene (25)

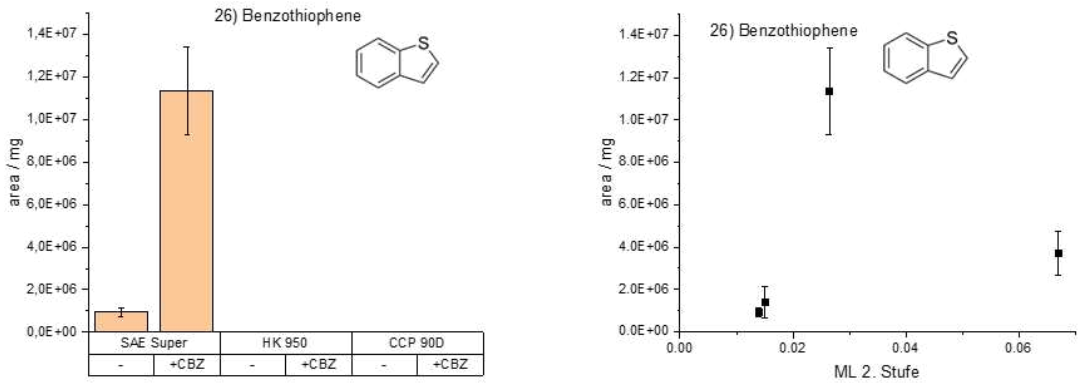

Figure C28: Benzothiophene (26)

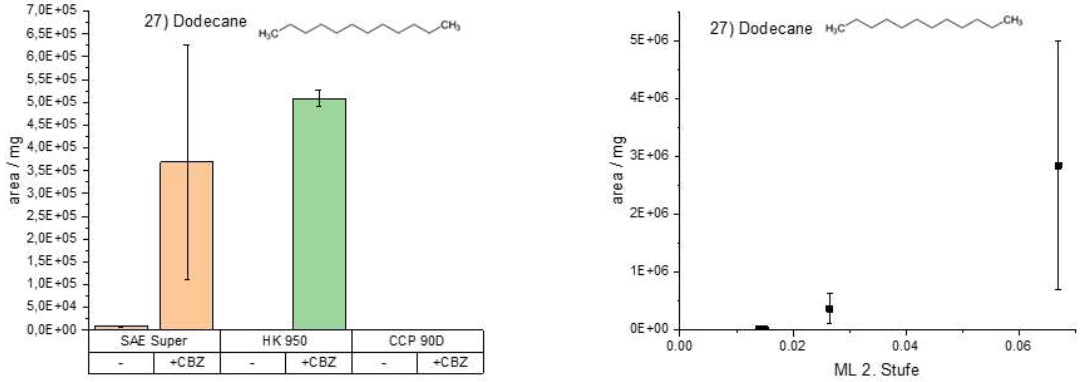

Figure C29: Dodecane (27)

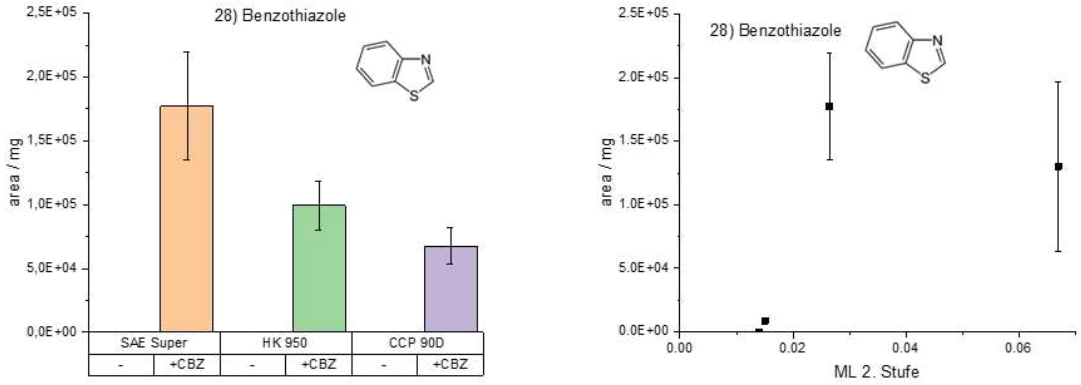

Figure C30: Benzothiazole (28)

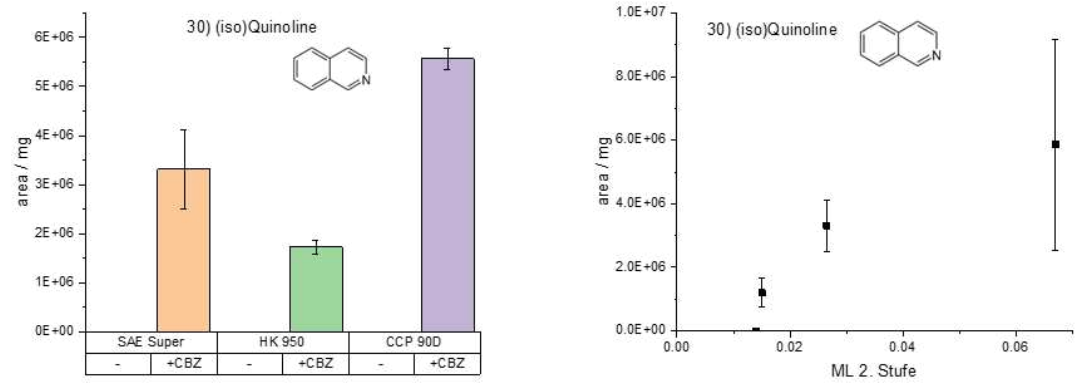

Figure C31: (iso)Quinoline (30)

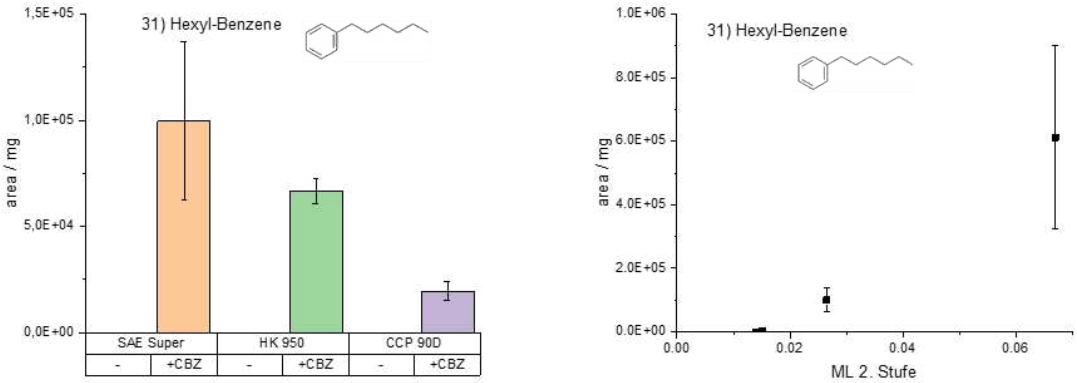

Figure C32: Hexyl-Benzene (31)

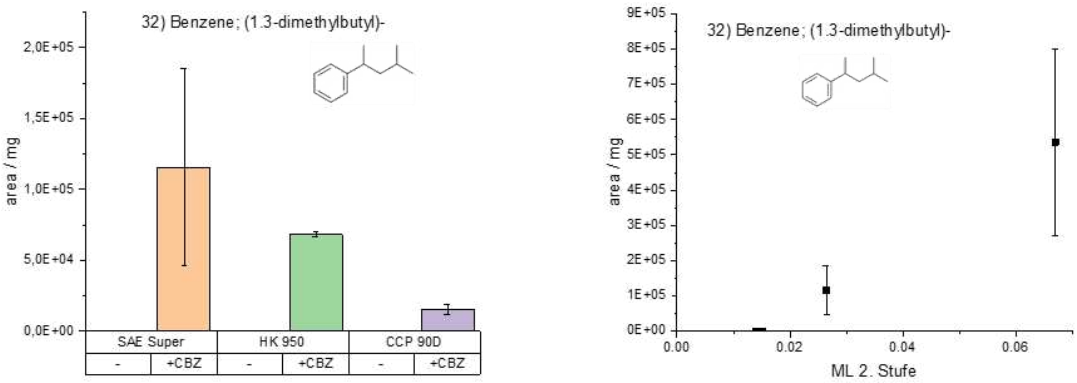

Figure C33: Benzene, (1,3-dimethylbutyl)- (32)

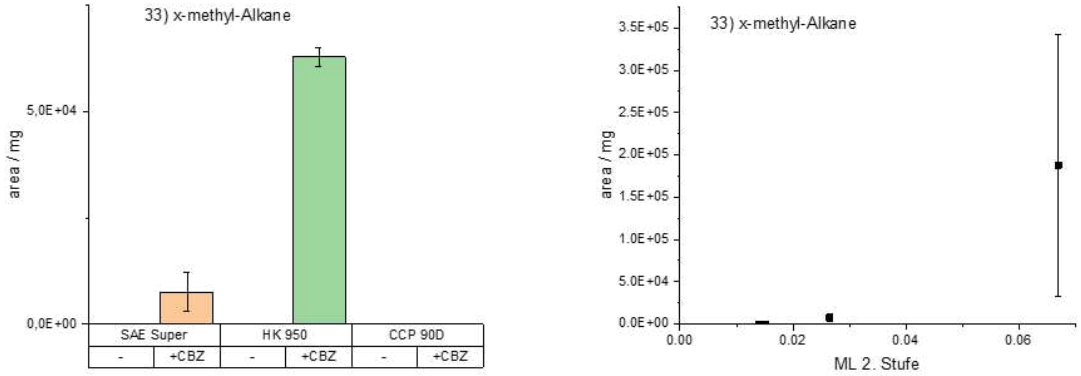

Figure C34: x-methyl-Alkane (33)

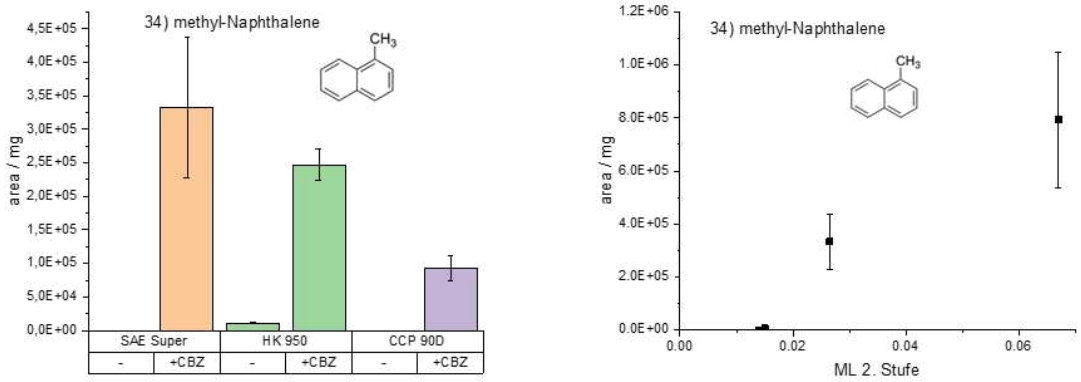

Figure C35: methyl-Naphthalene (34)

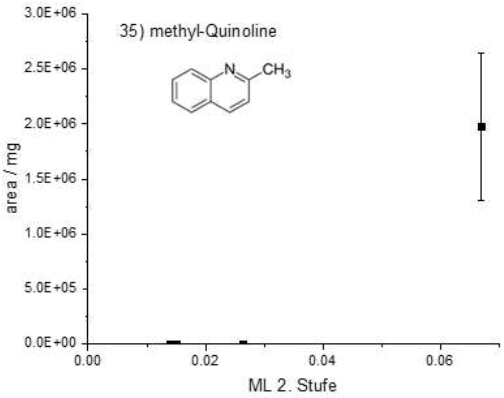

Figure C36: methyl-Quinoline (35)

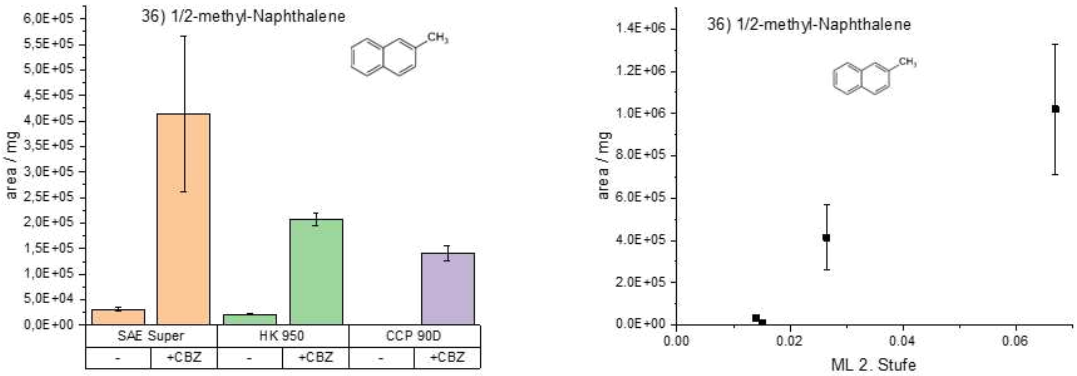

Figure C37: 1- or 2-methyl-Naphthalene (36)

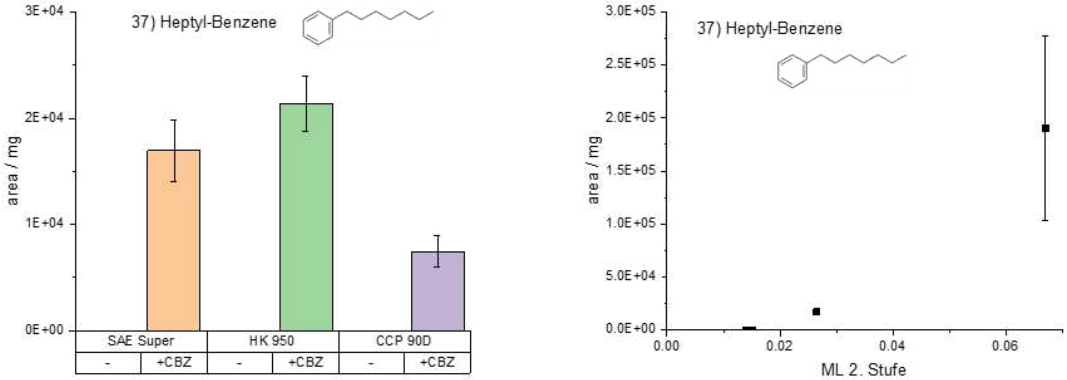

Figure C38: Heptyl-Benzene (37)

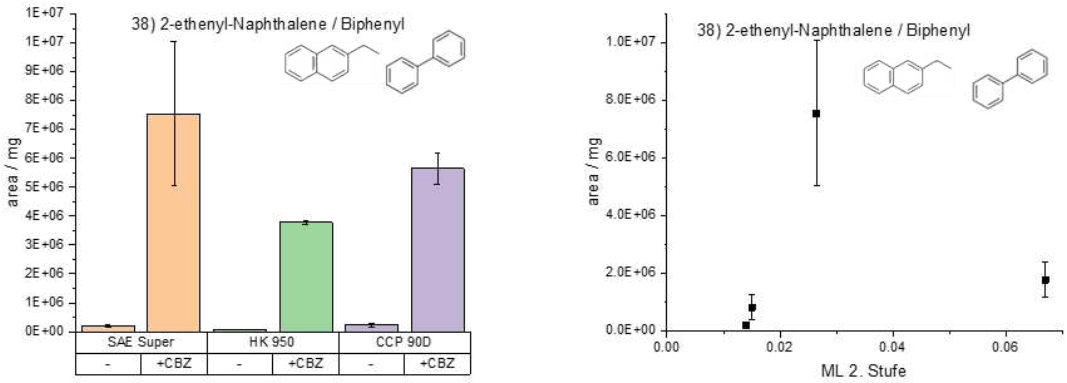

Figure C39: 2-ethenyl-Naphthalene or Biphenyl (38)

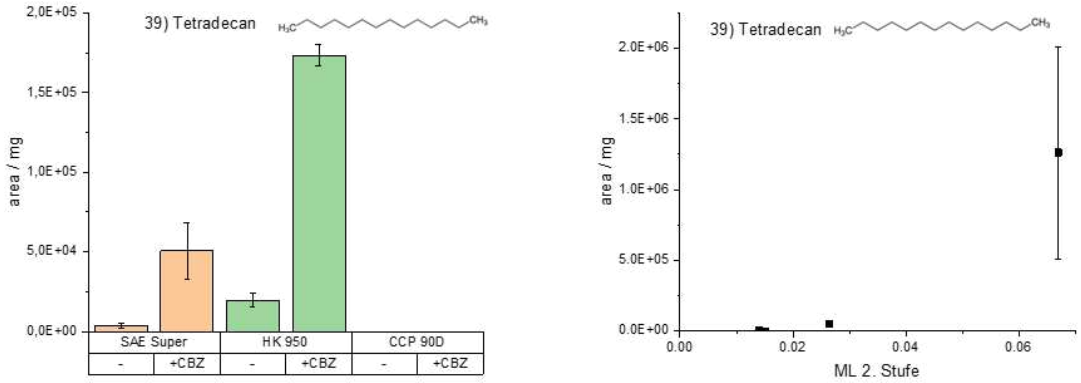

Figure C40: Tetradecane (39)

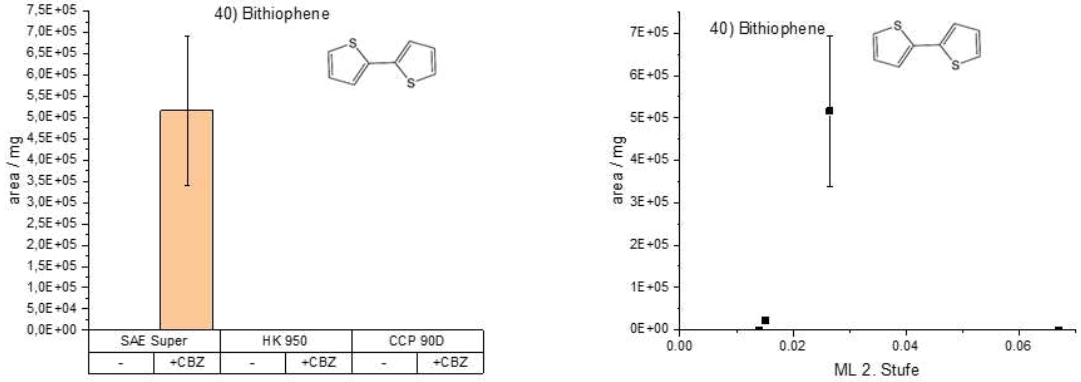

Figure C41: Bithiophene (40)

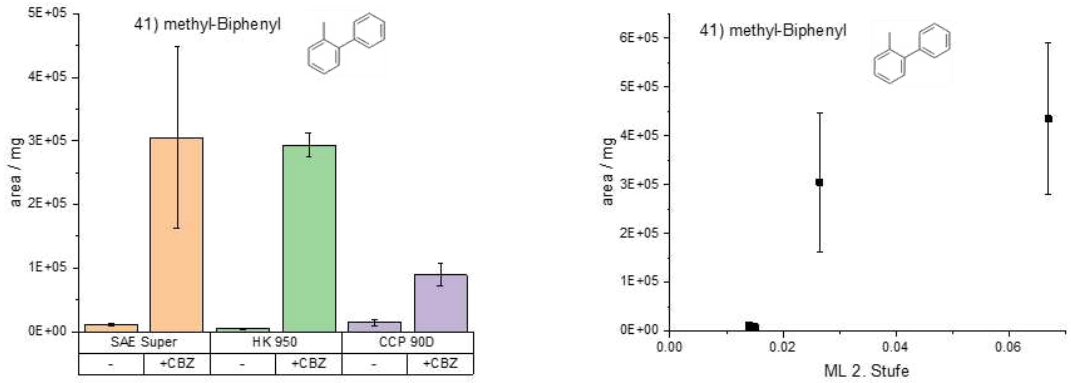

Figure C42: methyl-Biphenyl (41)

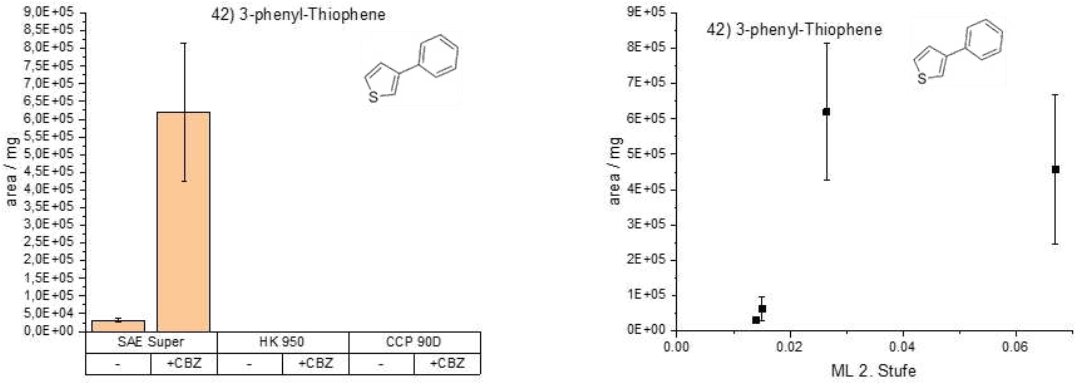

Figure C43: 3-phenyl-Thiophene (42)

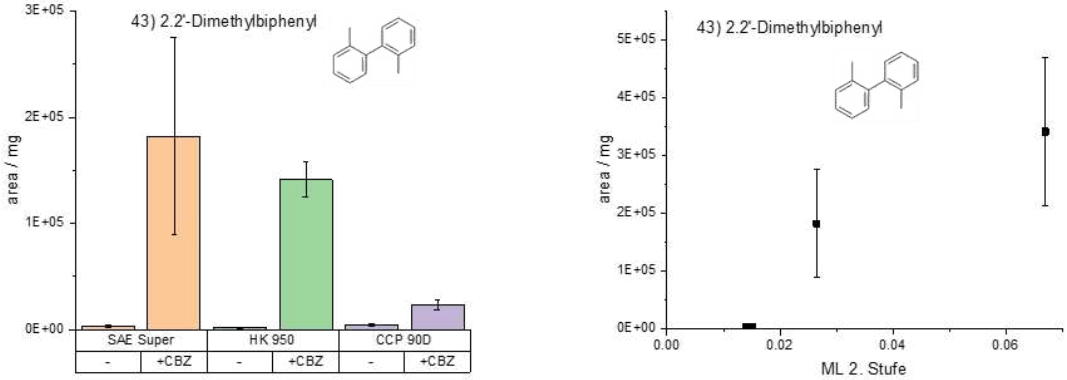

Figure C44: 2,2'-Dimethylbiphenyl (43)

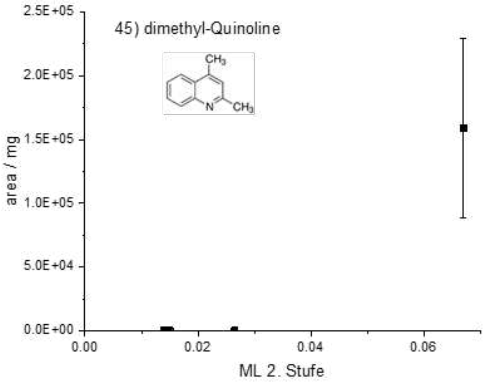

Figure C45: dimethyl-Quinoline (45)

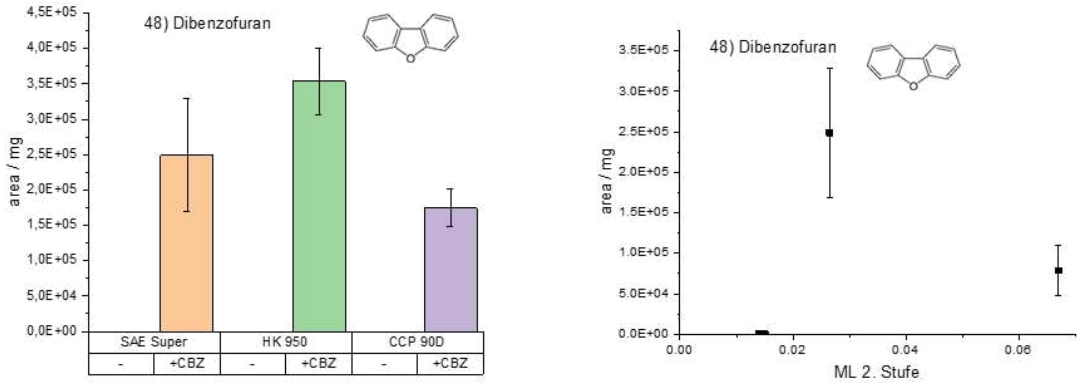

Figure C46: Dibenzofuran (48)

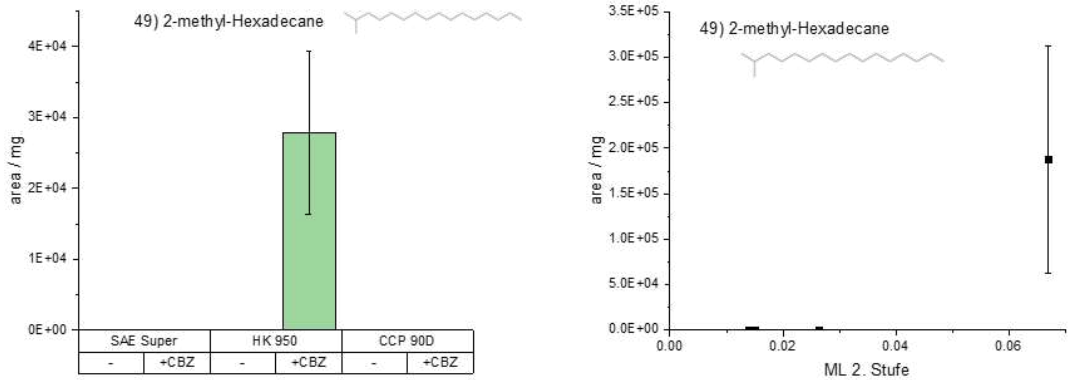

Figure C47: 2-methyl-Hexadecane (49)

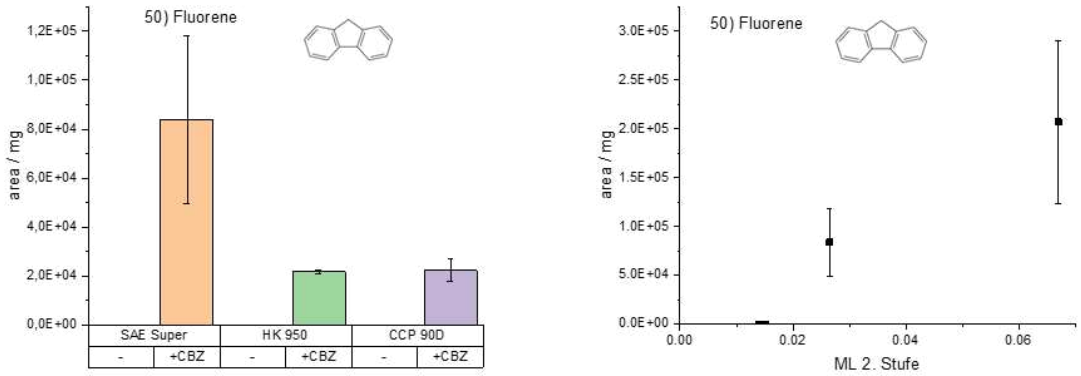

Figure C48: Fluorene (50)

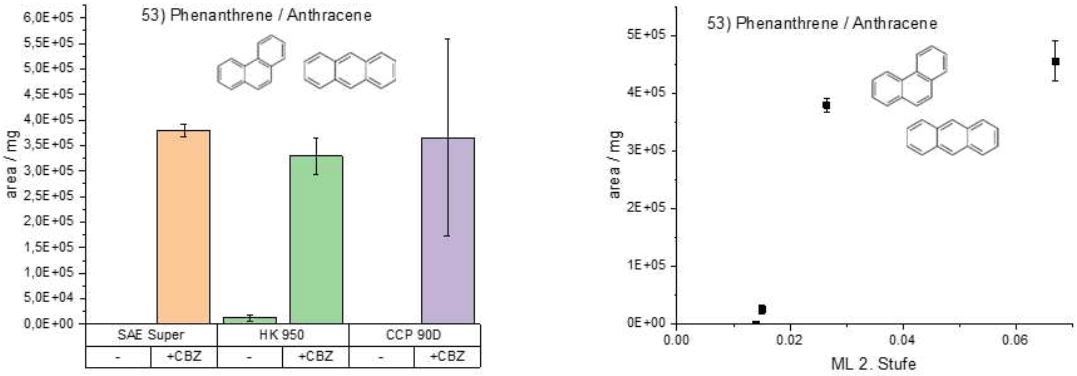

Figure C49: Phenanthrene or Anthracene (53)

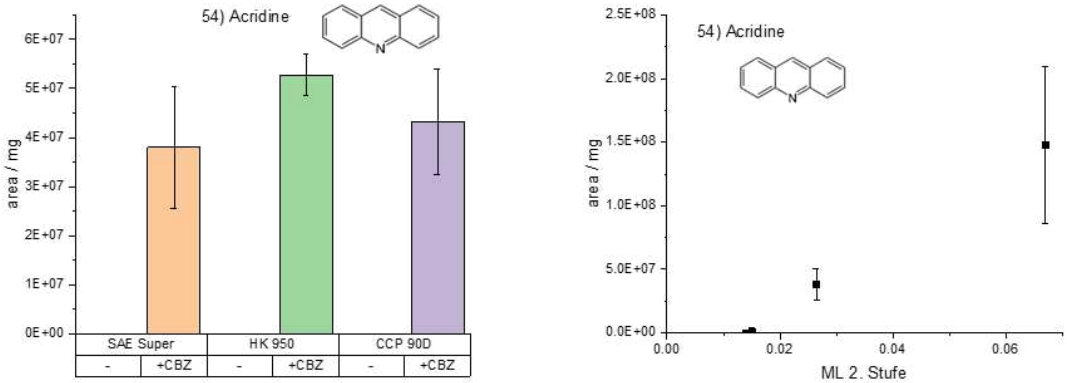

Figure C50: Acridine (54)

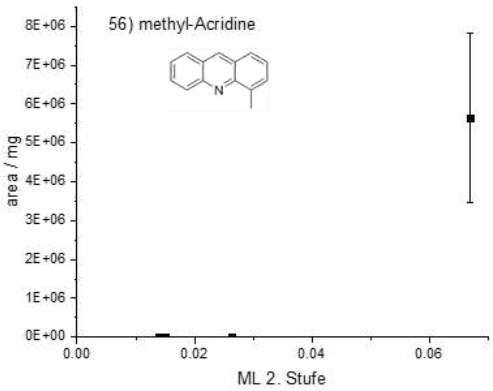

Figure C51: (4-)methyl-Acridine (56)

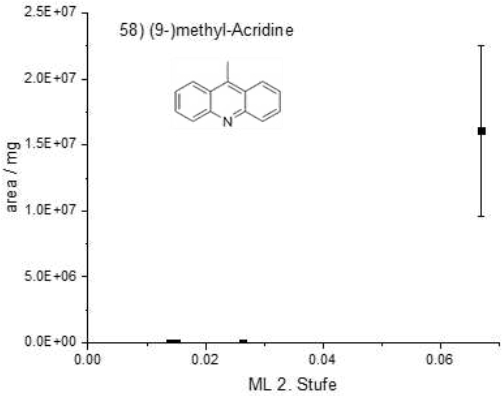

Figure C52: (9-)methyl-Acridine (58)

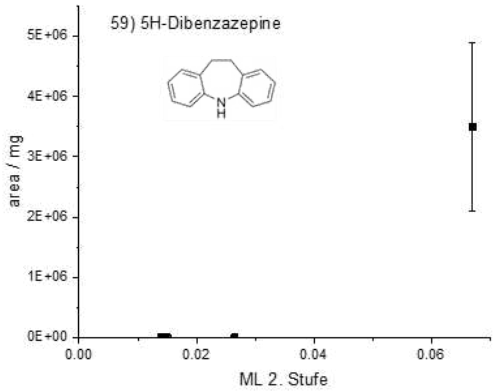

Figure C53: 5H-Dibenzazepine, 10,11-dihydro- (59)

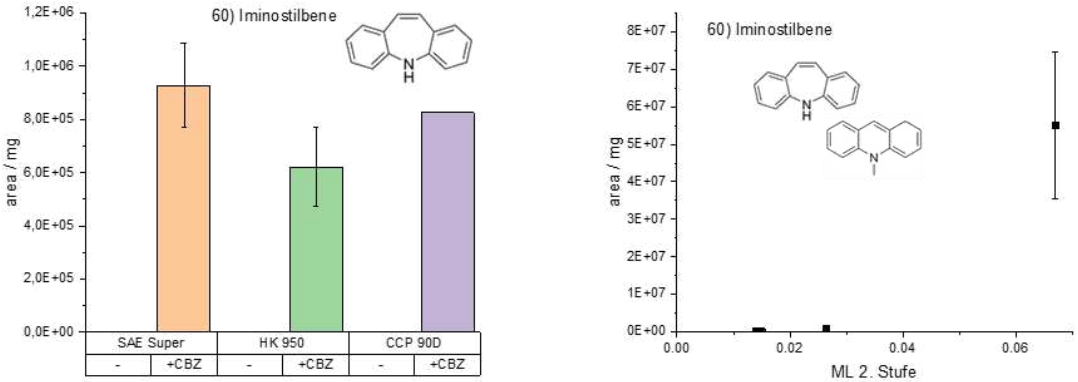

Figure C54: Dibenzazepine, "Iminostilbene" (60)

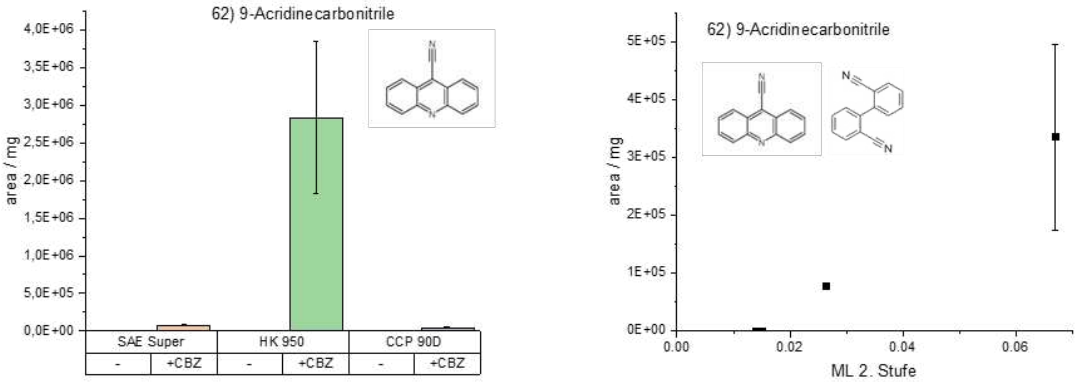

Figure C55: 9-Acridinecarbonitrile or Biphenyldicarbonitrile (62)

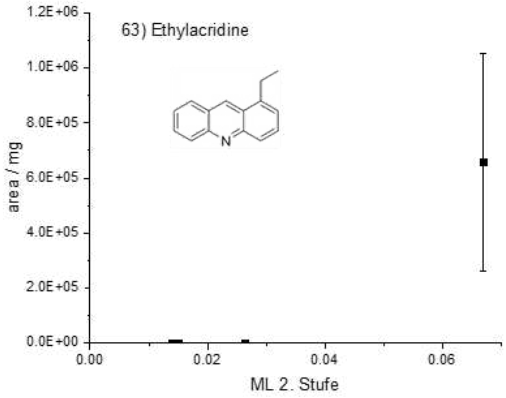

Figure C56: Ethylacridine (63)

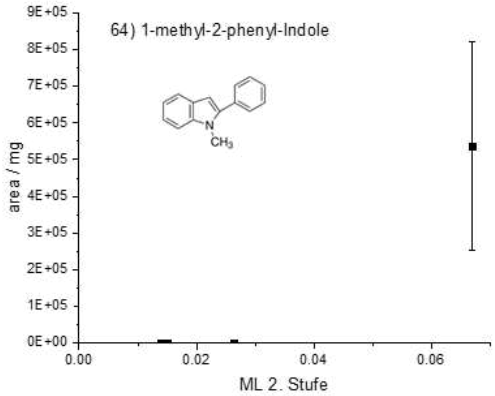

Figure C57: 1-methyl-2-phenyl-Indole (64)

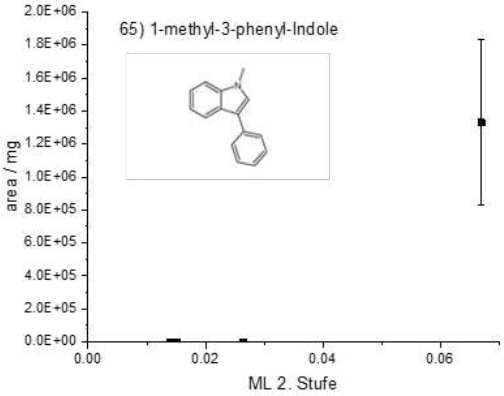

Figure C58: 1-methyl-3-phenyl-Indole (65)

C.4 SEM comparisons

Scanning electron microscopy (SEM) images were recorded of the HK 950 and the CCP 90D systems exemplary for loaded and unloaded samples (Figures C59&C60). The samples were treated identically, but with or without carbamazepine in solution (see Materials and Methods). The images do not show differences in the activated carbon particle's morphology. This confirms that adsorption takes place in the pores, on the inner surface of the particles, even for large amounts of adsorbate.

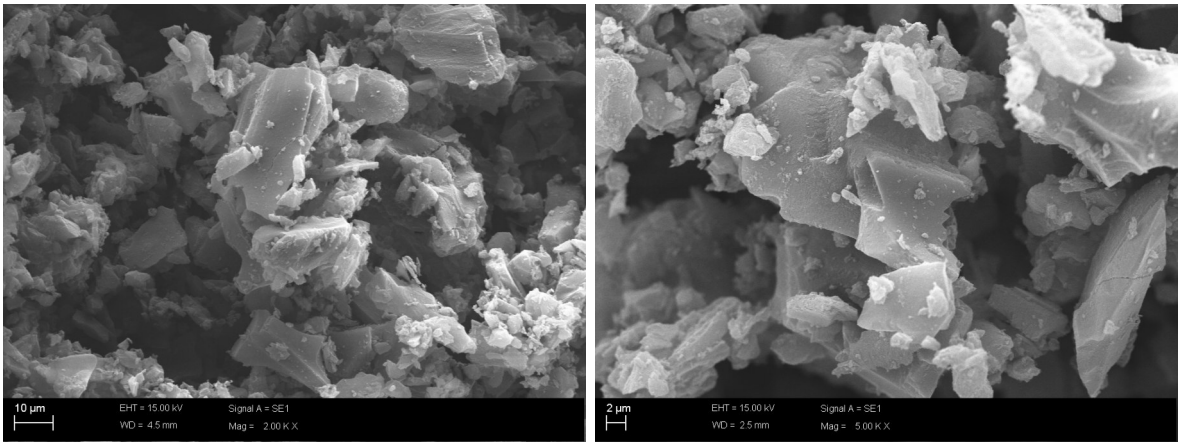

Figure C59: SEM images of HK 950 systems. Left hand side: HK and right hand side: HK+CBZ-15.

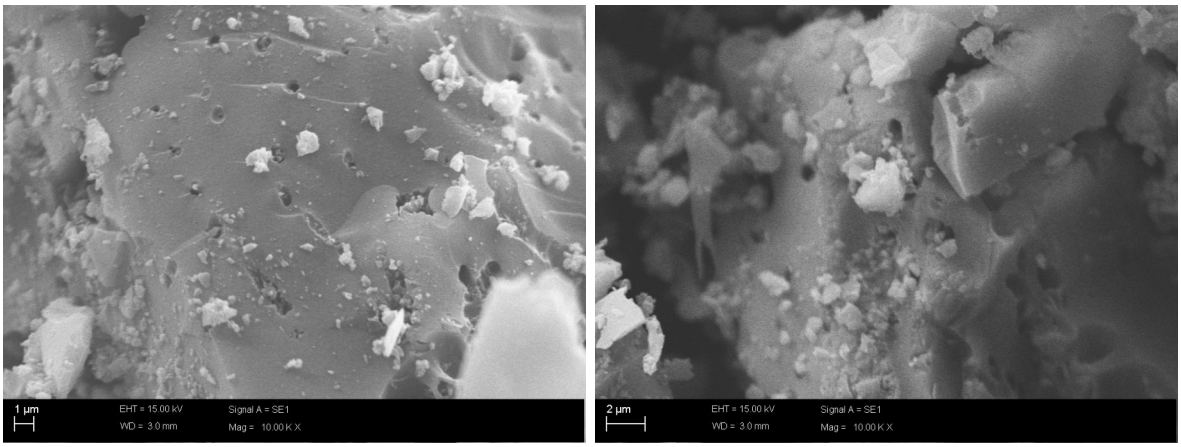

Figure C60: SEM images of CCP 90D systems. Left hand side: CCP and right hand side: CCP+CBZ-12.

C.5 DRIFTS comparisons

Diffuse reflectance infrared fourier transform spectroscopy (DRIFTS) have been applied to all three activated carbons unloaded and loaded with carbamazepine. No differences in the spectra could be observed for the Systems with SAE Super and CCP 90D (Figure C61). The negative bands are spectroscopic effects due to the strong absorption of the activated carbons (about 4 % in KBr). Figure C62a shows the spectra for the HK 950 systems. These spectra are typical for chemical activated, lignocellulose based materials [201]. Furthermore, additional bands occure in the systems loaded with carbamazepine. Figure C62b highlights the wavelength region between 1800 and 650 cm^{-1} with the subtraction sepctrum of loaded and unloaded HK 950 as well as the spectrum of pure carbamazepine. Distinct bands can be found and attributed to intact carbamazepine molecules on the surface of the activated carbon. However, it is related to the spectral properties of HK 950 that carbamazepine is detectable by DRIFTS.

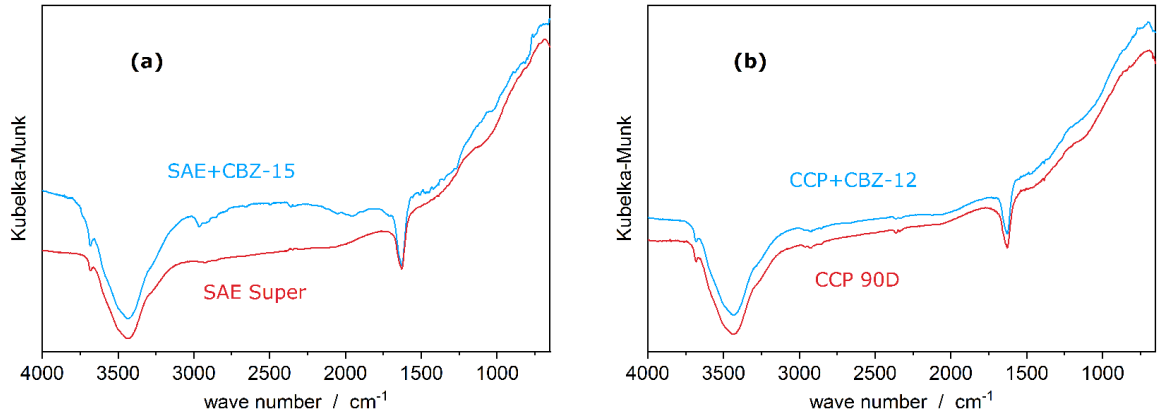

Figure C61: DRIFT spectra of (a) loaded and unloaded SAE Super, (b) loaded and unloaded CCP 90D.

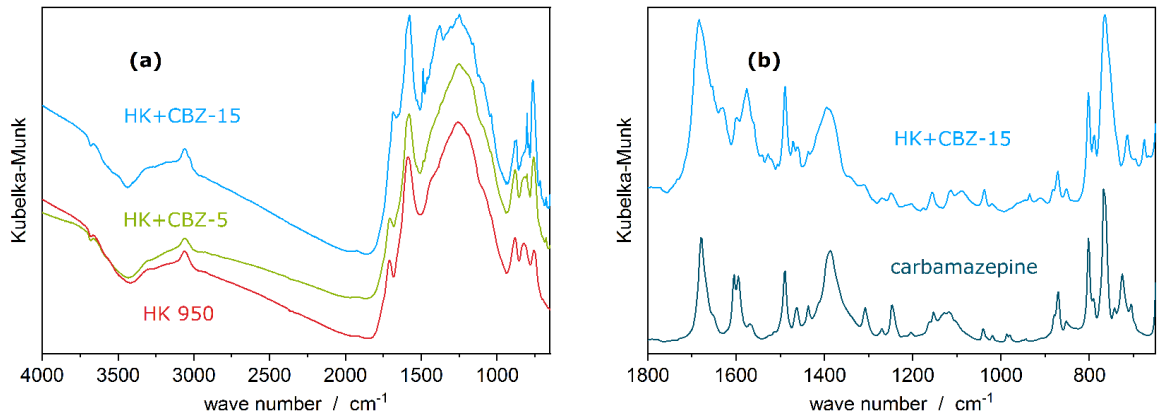

Figure C62: DRIFT spectra of (a) loaded and unloaded HK 950 systems, (b) subtraction spectrum of HK+CBZ-15 and unloaded HK 950 is compared with the spectrum of pure carbamazepine in a qualified wave length region.